SCHOLARLY PUBLICATIONS

A CURRENT AWARENESS BULLETIN
OF RESEARCH OUTPUT

@DTU

(52nd Edition)

APRIL 2017

BY: CENTRAL LIBRARY

DELHI TECHNOLOGICAL UNIVERSITY
(FORMERLY *DELHI COLLEGE OF ENGINEERING)*
GOVT. OF N.C.T. OF DELHI
SHAHBAD DAULATPUR, MAIN BAWANA ROAD
DELHI 110042

PREFACE

This is the **Fifty second** Issue of Current Awareness Bulletin started by Delhi Technological University, Central Library. The aim of the bulletin is to compile, preserve and disseminate information published by the faculty, students and alumni for mutual benefits. The bulletin also aims to propagate the intellectual contribution of Delhi Technological University (DTU) as a whole to the academia.

The bulletin contains information resources available in the internet in the form of articles, reports, presentations published in international journals, websites, etc. by the faculty and students of DTU. The publications of faculty and student which are not covered in this bulletin may be because of the reason that the full text either was not accessible or could not be searched by the search engine used by the library for this purpose.

The learned faculty and students are requested to provide their uncovered publications to the library either through email or in CD, etc to make the bulletin more comprehensive.

This issue contains the information published during **April 2017**. The arrangement of the contents is alphabetical. The full text of the article which is either subscribed by the university or available in the web is provided in this bulletin.

Central Library

CONTENTS

10. Mesoporous silica as amine immobiliser for endowing healing functionality to epoxy resin, ***6.1.Manorama Tripathi***, ***3.Devendra Kumar*** and Prasun Kumar Roya, Applied Chemistry and Polymer Technology, DTU

11. Moderate reagent mixing on an orbital shaker reduces the incubation time of enzyme-linked immunosorbent assay, ***3.Saroj Kumar***, Rajesh Ahirwar, Ishita Rehman and Pradip Nahar, Biotechnology, DTU

12. Phosphate uptake and translocation in a tropical Canna-based constructed wetland, ***3.Anil Kumar Haritash***, ***7.1.Sarbari Dutta*** and ***7.Ashish Sharma***, Environmental Engineering, DTU

13. Spectroscopic studies of Pr3þ doped lithium lead alumino borate glasses for visible reddish orange luminescent device applications***, 6.Nisha Deopa*** , ***3.A.S. Rao***, Dr., Sk. Mahamuda, Mohini Gupta, ***3.M.Jayasimhadri***, D. Haranath and G. Vijaya Prakash, Applied Physics, DTU

1. *Chancellor*

2. *Pro Vice Chancellor* ***2.1.*** *Ex Pro Vice Chancellor*

3. *Faculty* ***3.1.*** *Ex Faculty*

4. *Teaching-cum-Research Fellow* ***4.1.****Asst. Librarian*

5. *Alumni*

6. *Research Scholar* ***6.1.*** *Ex Research Scholar*

7. *PG Scholar* ***7.1.*** *Ex PG Scholar*

8. *Undergraduate Student* ***8.1.*** *Ex Undergraduate Student*

Available online at www.ijapie.org

INTERNATIONAL JOURNAL OF ADVANCED PRODUCTION AND INDUSTRIAL ENGINEERING

IJAPIE-2017-01-122, Vol 2 (1), 82-86

IJAPIE
Connecting Science & Technology with Management.
A Journal for all Products & Processes.

A Review on Design and Stability of Quadrotor to be used in the Precision Agriculture

Krovvidi Srinivas*, Anant Gaurav, Yamika Patel

(Delhi Technological University, Delhi-110042, India)
**Email: srinivaskrovvidi@dtu.ac.in*

Abstract : *Quadcopter otherwise know as the quadrotor is the next generation of aviation devices having greater dynamic stability than the helicopters, Quadrotors are underactuated robots.. They are predominantly used in different areas like civilian purposes such as agriculture, logistics, military exercises, fire sensing and other important areas dealing with complexities such a weight and space constraints. This paper is focused on the dynamic stability and the design of quadcopter. It addresses all the aspects of quadcopter ranging from mechanical design, aerodynamics, materials to be used, applications to the electronics used, The aim of this project is to optimize the quadrotor for Agriculture purposes.*

Keywords: *Quadrotor, Aerodynamics, Design, Stability, Finite Element Analysis, Frame etc.*

I. INTRODUCTION

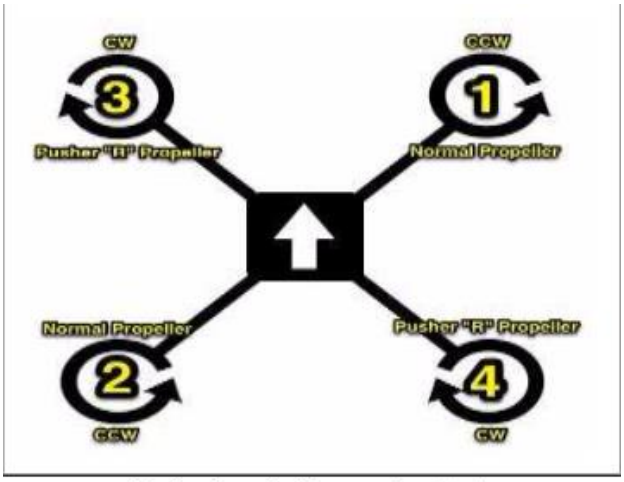

Fig.1. schematic diagram of quadcopter
(FigureSource:http://www.droneybee.com/quadcopter-blade-rotation-lift/)

I. PHYSICAL PRINCIPLES

Physical Principles. Quadcopter is lifted up high in the air with the help of propellers. These propellers convert rotational motion into thrust and this can be explained with the help of Bernoulli's principle and Newton's third law. Every action has equal and opposite reaction.

i. Bernoulli's Principle: Bernoulli's principle states that for an inviscid flow of no conducting fluid, and increase in the speed of fluid occurs simultaneously with a decrease in pressure or a decrease in the fluid's potential energy.

ii.Newtons Second Law: An air foil is the shape of the wing or blade as seen in the cross section, when moved through a fluid produces an aerodynamic force. Due to airfoil shape of the propeller, the air moves faster over the top than under the bottom which results in a greater pressure difference below the airfoil than above it. This pressure difference in turn produces the required thrust.

II. CONTENT

A. Objective:

1. To Study quadrotor Flight dynamics
2. To Study system interactions with the surroundings.
3. Electronic Components Used.
4. Possible Design Prototypes
5. Fabrication Process to utilize
6. Adopting the system as per Agricultural Requirements

B. Frame Selection: Here we are going to utilize the X4 type model for quadrotor as show in the figure 1. The X4 type configuration utilizes the 4 motor and propellers or 8motor and 8 propeller as per requirement providing slightly better control then X4.

C. Material Selection: The whole system is in dynamic motion and rotary arts are involved also landing of the

system can induce impact load on it. Therefore the material shall be so selected that it has high Strength to Weight ratio, this is the paramount property as the weight of aerospace system i.e our quadrotor has to be kept low to keep the power consumption low and to increase the flight time on the same power.

Table 1. Material Selection

Font Size	Material Selection Based on Properties Required		
	Component	Material	Properties
1	Frame/Plate	Carbon Fibre	Vibration Isolation and Absorption.
2	Propeller	Kevlar Epoxy Composite	High weight to Strength ratio.
3	Landing gear	Carbon Fibre	High Impact absorption.

D. Electronic Components used in the quadrotor system

1. Motors: Brushless DC motors also termed as BLDC motors are used in Quadcopters. These motors consist of a permanent magnet which rotates around a fixed armature. They offer several advantages over brushed DC motors which include more torque per weight, reduced noise, increased reliability, longer life time and increased efficiency.

Fig 2: Brushless DC Motor

Motor calculations: The motors should be selected in such a way that it follows following thrust to weight relationship.

Ratio=Thrust / weight =ma / mg

Thus, vertical takeoff and vertical landing (VTOL) is possible only when,(a / g) > 1 or in other words, The total thrust to total weight ratio should be greater than 1 so that the quadcopter can accelerate in the upward direction. In this case, we assumed that

Total Thrust = 2*(Total Weight of the Quadrotor)

Therefore,

Thrust Provided by Each Motors = Total Thrust/4

Electronic Speed Controller: Low voltage and current is provided by the microcontroller and this is not sufficient to drive motors. To drive the motors at specific speed, we require a motor driver to supply specific amount of voltage and current required by them and this work is done by Electronic speed controller.

Propeller: Propeller is a type of fan that converts rotational motion into thrust. Generally, propellers are classified on the basis of their diameter and pitch and are represented in terms of product of diameter and pitch. For e.g. 10 *4 449 × 255 7, 10*4.5, etc. The diameter of propeller indicates the virtual circle that the prop generates whereas the pitch indicates the amount of travel per single rotation of propeller. In order to counter motor torque, Quadcopter require two clockwise and two anticlockwise rotating propellers. All the propellers used in quadcopter should have same diameter and pitch. Many motors come with propeller specifications so as to have optimum power consumption. If propeller specifications are not mentioned on motor then we have to use trial and error method.

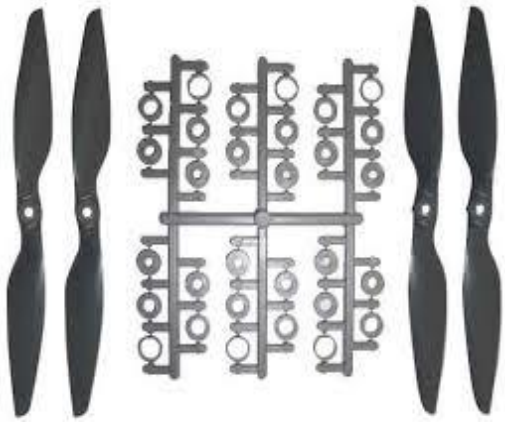

Fig 3: Propellers

Battery: Lithium Polymer (Li-Po) batteries are used in quadcopter. These batteries are rechargeable and also have low weight and high voltage capacity as compared to other type of batteries. Battery chargers are required for charging the battery

Battery calculations

Max. Current withdrawal by motors = no. of motors* maximum current withdrawal by single motor = 4*15 = 60 A

The discharge current of battery should be higher than the maximum current withdrawn by motors. Where, discharge current= Capacity in ampere * discharge rate. If we assume a constant current draw of 20A, then flight time for quadcopter is calculated as follows,

Flight time = (Capacity in amperes/Current draw) * 60

Flight Controller: To maintain balance, the quadcopter should continuously take measurements from the sensors and

make adjustment accordingly to the speed of the rotors to keep the body level. Flying capabilities and cost are the two main factors to be considered while selecting flight controller. Flying capabilities consists of following basic factors-

- Gyro stabilization: It is the ability to keep the copter stable and level under the pilot control.
- Self-leveling: It is the ability to automatically adjust itself during any orientation so that the copter stays level.
- Altitude hold: It is the ability to hover at a certain distance from ground without having to manually adjust the throttle.

6. Transmitter and receiver : The Transmitter (Tx) and Receiver (Rx) system allows the Quadcopter to be remotely controlled through a wireless signal. The aircraft controls would typically include throttle, pitch, roll, yaw, and mode settings.2.4GHz TX and RX system is used for its better performance, because it will not experience signal conflicts from other radio frequency (RF) controllers. Receiver used is having 6C 2.4 Ghz system which perfectly bonded with the 2.4Ghz transmitter.

E. Interaction with the surroundings.

The surrounding air in which the quadrotor operates is assumed to be a low Reynold no. flow i.e the flow is laminar in nature and the problem of low damping is imminent in the case of quadrotors as the friction provided by the air is almost negligible therefore the control has to

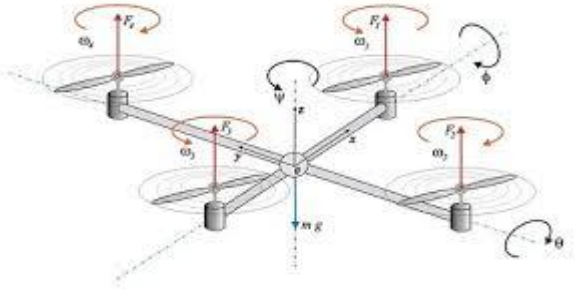

Fig 4: Degrees of Freedom of Quadrotor
(FigSource:http://www.azorobotics.com/Article.aspx?ArticleID=187)

E. Motions and their Manipulations

The quadrotor is an underactuated robot, ie the degree of free are more than the input sources, also it has move in frictionless undamped medium. therefore the to have exact motion tracing is a difficult task but can be achieved.

Vertical Take Off: The force required for this motion is known as lift force and generated by thrust produced by four propellers rotating at same speed.

Yaw Motion (ψ): This motion is attained by increasing speed of appropriate set of motors. By generating couple of force from two neighbour motors, yawing can be achieved.

Pitch Motion (ɵ): This motion can be attained by generating couple of forces from the set of motors in the direction of the movement (Front and rear motor).

Roll Motion (Φ): This motion can be attained by generating couple of forces from the set of motors in the direction other than the direction of motion (Left and Right side motor.

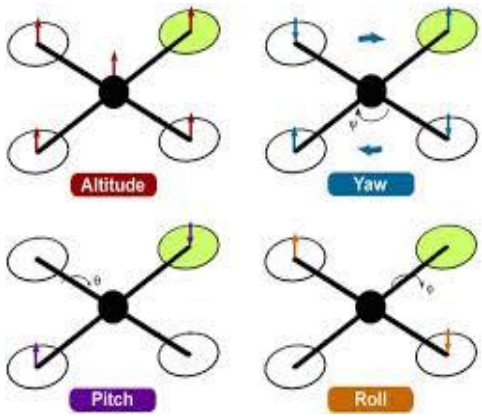

Fig 5: Motions of Quadrotor

(Figure Source: http://uav-society.blogspot.in/2014/06/quadcopter-mechanics.html)

F. Precision Agriculture

Goal of precision agriculture is to combine technology with agriculture to increase outcomes in agriculture, through database management of input variables and operation conditions, this data can be used for various reasons such as forecasting, inventory managements.

Fig 6: Smart Farming

(Figure Source:< https://www.smart-akis.com/index.php/network/what-is-smart-farming/>)

In precision Agriculture we optimize the bests of Economics, Environmental data, Management strategies and technological advancements.

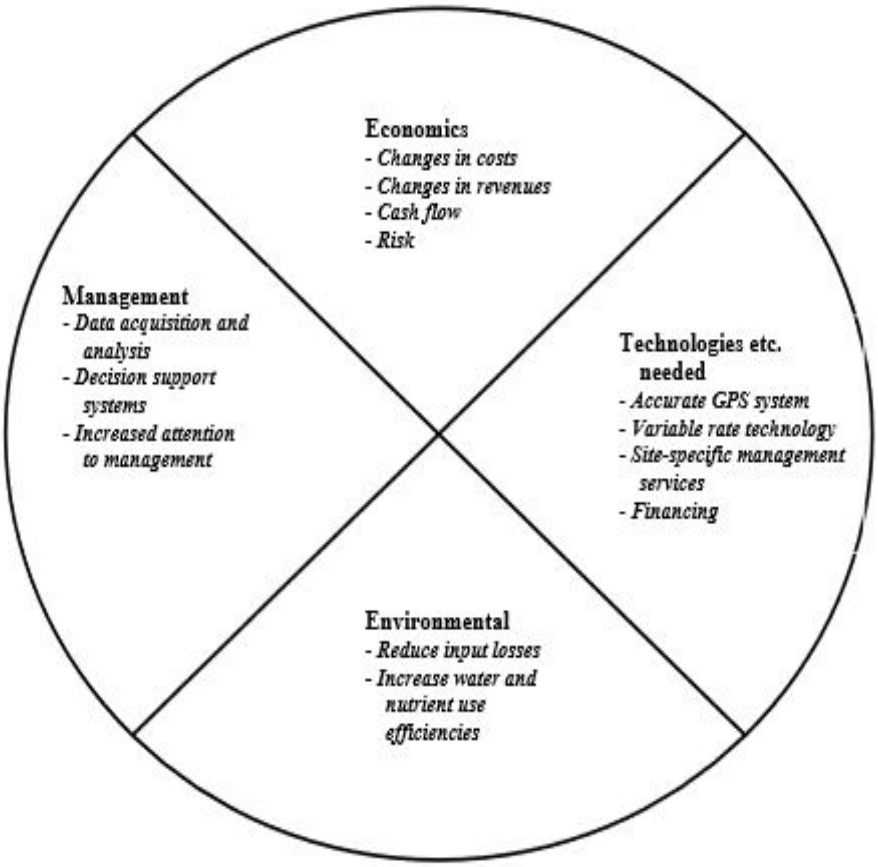

Fig 7: Input and Impact of Precision Agriculture.

G. Literature Review

A.V. Javir (2015) [1] In this paper safety of the quadrotor is discussed, safe design of the quadrotor is done by designing a quadrotor model on a CAD software and doing its analysis on Ansys 15.0 Workbench, the thrust generated by the propellers to lift the system and its effect on the surrounding and the effect of vibration generated on the system itself.

Ahmad Khushairy Makhtar (2012) [2] This paper discusses the various different configurations of the quadcopter and provides a basis to chose a quadrotor model over other various model such as fixed wing type model. The pros mentioned in the paper are greater flight stability and VTOL feature. Addition to that its ability to hover closer to specified targets. Sometime however hovering is unstable, making the navigation difficult and use for precision usage. The purpose of this research was to fix this hover stability issue and fix the control system, but fully customisable to suit its users' needs. The results of the hardware implementation show that the quadcopter has a stable hover with an error of ±2 cm for a total flight time of 5 minutes with a total implementation cost of USD 24.

Hardik Modh (2014) [4] This paper takes the quadrotor from the engineering perspective and the problems associated with them in whole and also the the weight reduction of the complete system is the target. Our main goal is to design and fabricate a Quadrotor which can be used for various application in market, defense, commercial and infrastructure applications like Traffic obverse and control, disaster management operation, weather and height estimation, concourse management, Locating forest fire or frost conditions in farmlands, Weather forecasting, post natural disaster, Object identification and Reconnaissance. With the help of our project guides, we have the resources and technical knowledge to successfully complete this project. We chose the UAV Quadrotor for project because of its flexibility, high learning opportunity and potential of future research. The project tries to beyond the conventional ways of how we use quadrotors today, how we can incorporate it with daily usage, making it more robust, reliable and user friendly. This project will be definitely useful to implement new function of high weight lifting in the account of UAVs.

Amir Abbas Bakhtiari (2013) [5] Precision farming is a data-based management and a way of agricultural production, which takes into account the in-field variability. Precision agricultural technologies, such as Global Positioning Systems,Geographic Information Systems, remote sensing, yield monitors, mapping, and guidance systems for variable rate application, made it possible to manage within-field variation on large scales. The objectives of this perusal are to collect information about precision farming technology and

its opportunities, challenge and difficulty. It can be concluded by results of the study that there numerous opportunities and problems in adopting the precision farming across the world specially in south-asia which is mainly agriculture dependent and yield when compared to western world is low. Different mode of precisions can be used in the different parts of the world depending on the creativity of users.

NITI Ayog, Government of India [6] This paper aims on discussing important set of policy issues and challenges faced by Indian Agriculture and to come up with total solutions to bring about second Green Revolution and this time not concentrated to just some part of the name but rather to be pan India and maintain that levels of growth, maitaing the growth is also challenge. Five key issues are determined: measures necessary to raise productivity, policies ensuring remunerative prices for farmers, reforms necessary in the area of land leasing and titles, a mechanism to bring quick relief to farmers hit by natural disasters, and initiatives necessary to spread Green Revolution to eastern states. While measures that have been outlined are essential for rejuvenation of agriculture as well as ensuring a decent life for farmers, we must not lose sight of the fact that relief to farmers will remain incomplete without the creation of job opportunities for them in non-agricultural sectors. With industry and services able to grow much faster than agriculture—the fastest that agriculture has grown over a continuous ten-year period in the post independence era is 4.7% during the 1980s—the share of agriculture in the GDP will continue to decline. Already, this share is down to approximately 15% while it supports 49% of the workforce. In order that today's farmer families can share in the faster growth occurring in industry and services, it is essential that some of them be able to find good jobs in these sectors. As some of the farm families move out of agriculture, the opportunities for consolidating and enlarging land holdings will open up as well. In turn, this will allow greater use of modern machinery and farm techniques allowing productivity and wages to rise rapidly in agriculture as well. The following offers a summary of policy recommendation.

ALEX McBRATNEY (2015) [7] We have to be careful that we do not get stuck in a limited paradigm, such as zone management. Different kind of aim should be there for different kind of countries, developing or developed or based on there requirements, there should be no hard and fast rule for making a quadrotor . Challenges or conflicts in designing as per the requirements should be noted and resolved .Concerted and co-ordinated research effort is needed in the following six areas.

(1) Appropriate criteria for the economic assessment of PA.
(2) Recognition and quantification of temporal variation.
(3) Whole-farm focus.
(4) Crop quality assessment method
(5) Product tracking and quality assurance.
(6) Environmental auditing.

Amy T. Winstead and Shannon H. Norwood [8]

Evidence from the 2009 Alabama Precision Ag and Field Crops Conference indicated that sequential adoption of precision agriculture technologies exist, especially regarding yield monitors and GPS guidance. It was clear that precision agriculture technologies have been more readily adopted by farms with larger acreage rather than small-acre farms. It was also clear that users of precision agriculture technologies rely upon the university/Extension system for information.The perception of land value as a function of variable or uniform application indicates one incentive to adopt precision agriculture

CONCLUSIONS

The core intention of our project is to study the complete designing process of quadrotor from the engineering perspective and to fabricate a working model of UAV-Quadrotor with improvement in its weight carrying capacity. Our main goal is to fabricate a Quadrotor which can be used for multipurpose application in market, military, commercial and industrial applications like Traffic monitoring and management, Search and rescue operation, Temperature and altitude estimation, Crowd management, Locating forest fire or frost conditions in farmlands, Weather forecasting, post natural disaster, Object identification and Reconnaissance. With the help of our project guides, we have the resources and technical knowledge to successfully complete this project. We chose the UAV Quadrotor for project because of its flexibility, high learning opportunity and potential of future research. This project can go further in variety of research work to integrate various technologies with UAVs to get various useful outputs. This project will be definitely useful to implement new function of high weight lifting in the account of UAVs.

REFERENCES

[1] A.V Javir, Design Analysis and Fabrication of Quadrotor, Journal of International Association of Advanced technology and Science ISSN-3347-4482, Vol-16 March 2015
[2] Bernard Tat meng Leong et al, Journal of International Symposium on Robotics and intelligent sensors 2012(IRIS2012)
[3] Hardik Modh "Quadrotor – An Unmanned Aerial Vehicle" in journal IJEDR Volume 2, Issue 1 pp. 1299-1303 in 2014
[4] Amir Abbas Bhaktiari "Precision Farming Technology, Opportunities and Difficulty" ternational Journal for Science and Emerging Technologies with Latest Trends ISSN No. (Online):2250-364
[5] NITI Ayog, Government of India 16 December 2015
[6] Future Directions of Precision Agriculture by ALEX McBRATNEY, Precision Agriculture, 6, 7–23, 2005 Ó 2005 Springer Science+Business Media Inc. Manufactured in The Netherlands
[7] Adoption And Use Of Precision Agriculture Technologies By Practitioners by Amy T. Winstead and Shannon H. Norwood Engineer's Aerodynamics by S. M. Yahya, John wiley & sons publication.

ISSN 2277-3061
Volume 15 Number 7
International Journal of Computer and Technology

COLOURED IMAGE SEGMENTATION USING K-MEANS ALGORITHM

Ishita Vishnoi[1], Nikunj Khetan[2], Dr. S. Indu[3]
[12]Department of Computer Engineering, Delhi Technological University, New Delhi, India
[3]Department of Electronics & Communication Engineering, Delhi Technological University, New Delhi, Indiia
[1]ishita95.2010@gmail.com, [2]nikunjkhetan123@gmail.com, [3]s.indu@dce.ac.in

ABSTRACT

Hand gestures are natural means of communication for human beings and even more so for hearing and speech impaired people who communicate through sign language. Unfortunately, most people are not familiar with sign language and an interpreter is required to translate dialogues. Hence, there is a need to develop a low cost, easily implementable and efficient means to recognize sign language gestures to eliminate the interpreter and facilitate easier communication. The proposed work achieves a satisfactory recognition accuracy using in-built laptop webcam using combination of 3 skin color models(HSV,RGB,YCbCr) and background subtraction to eliminate noise from webcam low quality images to recognize sign language for helping the hearing and speech impaired in real-time without requiring too much computational power or any other device as it can be implemented in any laptop with a webcam.

Keywords

Background subtraction, Hand gesture recognition, HSV, RGB, YCbCr, Multi-class SVM

Academic Discipline And Sub-Disciplines

Computer Science, Computer Engineering, Human Computer Interaction

SUBJECT CLASSIFICATION

Image Processing, Machine Learning, Computer Vision

TYPE (METHOD/APPROACH)

Experimentation, Empirical studies, Computer Simulation

1. Introduction

Hand Gesture Recognition system is an active research area in computer vision due to its broad application in human computer interaction(HCI),sign language, augmented reality,gaming,etc. Hand gesture is a natural means of communication between humans and vision-based systems to provide a user interface that can help people convey their feelings and information satisfactorily.

In genereal,there are two types of gestures-static and dynamic. Static gestures are expressed in single frames whereas dynamic gestures span over multiple frames incorporating temporal variability. To recognize these gestures there are three basic processing stages- hand segmentation, feature extraction and classification. Hand segmentation contributes greatly to the accuracy of gesture recognition which poses many difficulties because hand segmentation is easily affected by illumination changes, skin color differences between humans, presence of other background elements having similar skin color and low camera quality. To solve this issue of effective hand segmentation many methods have been proposed. In [1-2] gloves and colored markers are used to segment the hand and also obtain additional information such as orientation and position of palm and fingers.

The color space that is used plays a significant role in the successful segmentation but, color spaces are sensitive to lighting changes, hence, there is a tendency to use chrominance components while neglecting the luminance components. We use a combination of three color models-HSV,BGR,YCbCr[11], to segment skin pixels and background subtraction[12] to negate effects of illumination changes and complex background.

Feature extraction is done using SIFT [9] and used Bag of Features model to map the space incompatible SIFT keypoints using K-means clustering as in [10].

We have used a multiclass SVM classifier to minimize computational complexity, dataset and show real-time behavior without delayed response.

The paper is organized as: Section A describes the image preprocessing, Section B illustrates the training stage and Section C illustrates the testing stage.

2. State Of The Art

In [3] infrared camera and in [4] Microsoft Kinect depth sensor was used. Both these methods give good accuracy but are expensive methods because both the infrared camera and Kinect sensor are costly to acquire. [5] uses two fixed cameras to real-time calculate the hand position and recognize gesture information, this method doesn't achieve good accuracy results and also increases complexity due to usage of two cameras. [6] uses 3D information provided by a range camera. This method can be used only for very simple gestures and has low segmentation and tracking speed.

For classification many methods have been used,[7] uses the Dynamic Time Approach(DTW) approach which requires large number of templates for a range of variations and cannot handle undefined patterns, [8] uses Hidden Markov Model(HMM)to recognize dynamic gestures with a high accuracy but requires high computational power and has a delayed response to detection of gestures. Neural Network classifier has been applied for gestures classification [14][15] but it is time consuming and when the dataset increases, the time needed for classification is increased too. Another type of feed-forward NNs were used called the Convolutional Neural Networks (CNN, or ConvNet) [16] to recognize hand gestures. The method also used Kinect Sensor along with GPU acceleration to achieve high accuracy but, requires high computational power and is costly. [17] also uses CNNs to achieve high classification rate under varying conditions of intensity and illumination changes but, also involves high computational power and is expensive.

3. Problem Formulation

This paper proposes a method to recognize static hand gestures in complex background images that represent alphabets and numbers of the standard Polish Sign Language. The Polish Sign Language has been chosen as it uses only single handed gestures as compared to the Indian Sign Language that uses both hands for sign language gestures. The individual gestures once recognized accurately, can be further used to identify meaningful words and sentences.

4. Materials And Methods

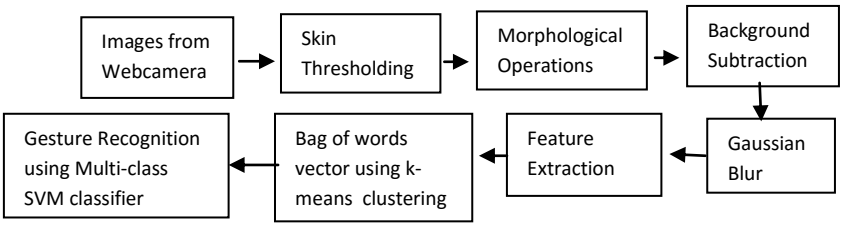

Figure 1. Method used in this paper for hand gesture recognition

Image Capture:

The following two devices were used to capture images for this work

-Canon EOS Rebel T3 DSLR Camera

-Usb 2.0 UVC HD Webcam

The images are taken under various illumination and intensity conditions. One input image(Figure 2(a)) is shown.

4.1 Image Preprocessing

Preprocessing phase of the proposed system consists of different operations: Skin Thresholding, Morphological Operations, Background Subtraction, Gaussian Blur.

I. **Skin Thresholding**: The objective of skin thresholding is to segment skin color pixels in the webcam image. Three color models are used RGB,HSV,YCbCr and the bounding rules of the components of these color models are derived from [11].See Figure 2(b).

II. **Morphological Operations**: Morphological filtering operations-dilation and erosion are used to reduce object noise from the binary image and as a result get a smooth, complete and closed segmented hand gesture after skin thresholding. See Figure 2(c)

III. **Background Subtraction**: It is a Gaussian Mixture-based Background/Foreground Segmentation Algorithm[12] that selects the appropriate number of gaussian distribution for each pixel. It provides better adaptibility to varying scenes due illumination changes etc. It eliminates background objects having similar skin color. See Figure 2(d)

IV. **Gaussian Blur**: It is a very useful filter to eliminate noise from the image. Gaussian filter convolves each point in input array with Gaussian kernel and thereafter sums them all to give the output array. See Figure 2(e)

2(a)Input Image 2(b)Skin Thresholding 2(c)Dilation-Erosion 2(d)Background Subtraction 2(e)Gaussian Blur

Figure 2(a)-2(e)

4.2 Training Stage

For building the training set, a total of 120 images of different hand gestures of different people under various illumination conditions are taken to provide a more realistic and accurate training to the system. For training the system, we have taken 6 different gestures and assigned the labels as shown in Fig 3(a)-3(f).

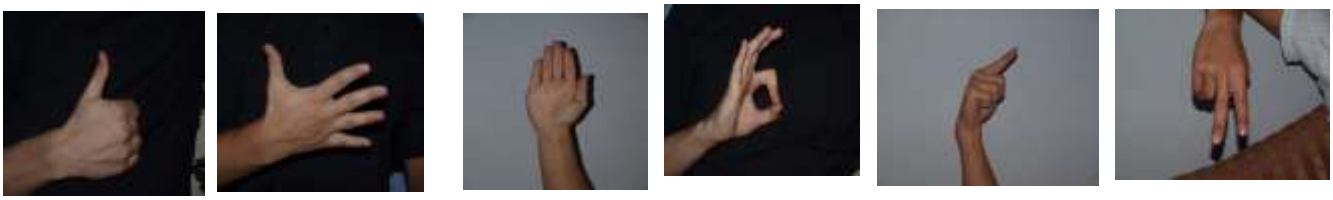

3(a)One 3(b)Five 3(c)B 3(d)O 3(e)U 3(f)D

Figure 3(a)-3(f)

The training dataset consists both of images taken against uniform background and images taken by a webcam agianst a more noisy background. The training images are used to build the bag of words vocabulary and to train the SVM classifier. Table 1 below shows the class labels assigned to gestures.

Table 1. Some Sign Language Gestures and their class labels

(Polish Sign Language)

Gesture (Sign Language)	Corresponding Class Label
One	Class 1
Five	Class 2
B	Class 3
O	Class 4
U	Class 5
D	Class 6

I. Extracting SIFT Keypoints

Keypoints are salient image patches that include rich local information of an image. Keypoints are detected by a robust feature detection method,namely SIFT, in this paper. SIFT, gives is found to give accurate results for the gesture recognition task at hand as it is invariant to changes in scale, orientation and illumination.

The steps that are involved to generate the set of image features are as follows:

1. **Scale-space extrema detection**: This first stage consists of carrying out computation that searches all scales and image locations. It is implemented efficiently by utilizing a difference-of-Gaussian function to identify potential interest points that are invariant to orientation and scale.

2. **Keypoint localization**: At each candidate location, a detailed model is apt to resolve scale and location. Keypoints are selected based on measures of their stability.

3. **Orientation assignment**: One or more orientations are appointed to each keypoint location which is based on local image gradient directions. All future operations that are performed on image data has been transformed relative to the appointed orientation, location, and scale for each feature, providing invariance to these transformations.

4**. Keypoint descriptor**: The local image gradients are measured by selecting scale in the region around each keypoint. These are then transformed into a representation which then allows for significant levels of local shape distortion and change in illumination.

A training images with its keypoints is shown in figure 4.

Figure 4. Keypoints in an image

II. K-Means Clustering And Bag Of Words Vocabulary

A clustering procedure is applied to group key points from all training images into a large number of clusters, with the center of each cluster corresponding to a different visual word. The number of clusters is to be pre-defined as the vocabulary size and depends on the structure of data used. Here it is estimated by the maximum number of keypoints extracted for an image that may also include other objects in the background.In this work, the maximum number of keypoints are for the palm gesture ,around 85,but for a webcam image with a cluttered background, this number increases due to keypoints from other objects too.We have taken the size of clusters to build the vocabulary as 700.

In k-means clustering, the vector space is divided into k randomly located centroids and the keypoints extracted from each of the images are assigned to the nearest cluster.The centroids are then shifted to the mean position of its keypoints and this process is continued till the assignments become constant. Each of the keypoints(feature vectors) are then assigned to the nearest cluster center based on Euclidian distance.Therefore, the keypoints extracted from images are used to build the clusters which are then used to build the vectors of the vocabulary used for training.The cluster model builds k vectors,equal to the number of centroids, each of which has 128 components ie. the length of each keypoint.These keypoint vectors of each of the training images are then fed into the k-means clustering model where every image with n keypoints (n x 128) is reduced to 1 x k (bag of words) where k is the number of clusters.

Each keypoint (vector) that is extracted from a training image is represented by one component in the generated vector (bag-of-words) and is assigned the index value of the cluster centroid with the nearest Euclidean distance. The generated vector is grouped along with all the generated vectors of other training images that have the same hand gesture and that are also labeled with the same class number.

Visual representation of clusters and centroids are shown below in Figure 5.

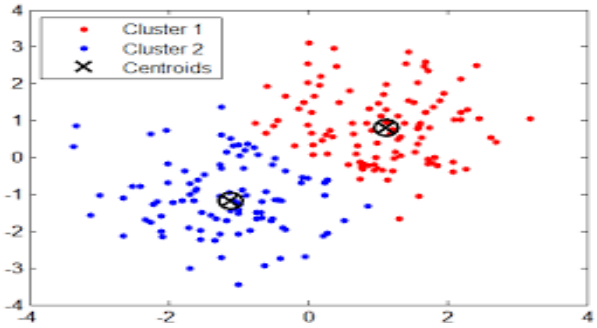

Figure 5. K-means Clustering

(http://mines.humanoriented.com/classes/2010/fall/csci568/portfolio_exports/mvoget/cluster/cluster.html)

III. Multi-Class SVM Training Classifier

The bag of words vector constructed for every training image, along with its class label is used as input for training the multiclass SVM training classifier model. A Support Vector Machine (SVM) is a discriminative classifier that is defined by a separating hyperplane i.e., given labeled training data (supervised learning), the algorithm outputs an optimal hyperplane which categorizes new examples. The optimal hyperplane is computed as shown below:

Let's introduce the notation used to define formally a hyperplane:

$$F(x)=\beta_0 + \beta^T x,$$

where β is known as the *weight vector* and β0 as the *bias.*

The optimal hyperplane can be represented in an infinite number of different ways by scaling of β and β0. Conventionally among all the possible representations of the hyperplane, the one chosen is

$$\beta_0 + \beta^T x=1$$

where x symbolizes the training examples closest to the hyperplane. Training examples that are closest to the hyperplane are called **support vectors**. This representation is known as the **canonical** hyperplane.

Now, we use the result of geometry that gives the distance between a point $\mathbf{x}$ and a hyperplane (β, β0)

$$\textbf{Distance}=|\beta_0+\beta^T x|/||\beta||$$

In particular, for the canonical hyperplane, the numerator is equal to one and the distance to the support vectors is

$$\text{Distance}_{\text{support vectors}}=|\beta_0+\beta^T x|/||\beta||=1/||\beta||$$

Recall that the margin introduced in the previous section, here denoted as M, is twice the distance to the closest examples:

$$M=2/||\beta||$$

Finally, the problem of maximizing M is equivalent to the problem of minimizing a function **L(β)** subject to some constraints. The constraints model the requirement for the hyperplane to classify correctly all the training examples $\mathbf{x_i}$. Formally,

Min $\mathbf{L(\beta)=0.5||\beta||^2}$ **subject to** $y_i(\beta_0+\beta^T x_i)>=1$ ∀i,

β, β_0

where $\mathbf{y_i}$ represents each of the labels of the training examples.

This is a problem of Lagrangian optimization that can be solved using Lagrange multipliers to obtain the weight vector **β** and the bias β_0 of the optimal hyperplane.

The SVM once trained, can predict with some accuracy the label of the class for a test image.

4.3 Testing Stage

In this part of the system, the six hand gestures for which the multi class SVM classifier was trained, are tested. The images are taken from a webcam (50 images) and from the DSLR camera (50 images) to simulate realistic behaviour, are taken under various light and background conditions. The keypoints are extracted from the testing images and after applying the k-means clustering model on them, are mapped to the bag of words vocabulary created in the testing stage. Each feature vector in the keypoints is represented by one component in the generated vector (bag of words) with value equal to the index of centroid in the cluster model with the nearest Euclidean distance. Then, the generated vector (Bag-of-Words) is used as input to the multi-class SVM training classifier model that was built in the training stage which predicts the most accurate matching class label for each testing image. Thus, the pre-defined hand gestures can be recognized from the class labels. The average time taken for testing and predicting the class of 50 images is 10 seconds.

5. Results

The training dataset used to train the classifier consists of a total of 100 images of which 50 images are taken by the DSLR camera with a good resolution and uniform background, and other 50 images are taken using a webcam. The training images taken under different scale, orientation and illumination conditions for each gesture make the system robust to changes in these factors. Moreover, the skin thresholding and pre-processing eliminates the extra objects and noise in the background.

The testing dataset is made up of 100 images of each hand gesture, 50 taken from the camera and 50 from webcam. The accuracy of the present system is an average 90% for images taken from the DSLR camera in uniform background and 80% for images taken from the web camera as shown in Table 2.

The accuracy level is high when images are taken from a good resolution camera as compared to webcam images where it suffers due to low quality of images with a lot of background noise. Moreover, it was observed during the experiment that in the present system, the accuracy levels drop when the hand gestures are somewhat similar in the number of fingers or shape. Keeping in mind these constraints, the system can still be trained for more gestures, provided there is sufficient training data set for each of those hand gestures. The model described in this paper, however, responds fairly well to the specific distinct hand gestures in different conditions and is time efficient.

Table 2. Testing Results of Images

Gesture (Sign Language)	Corresponding Class Label	ACCURACY(%)	
		Canon EOS RebelT3 Images	Webcam Images
One	Class 1	90	81
Five	Class 2	92	85
B	Class 3	93	79
O	Class 4	95	83
U	Class 5	85	75
D	Class 6	87	76

6. Conclusion

Our proposed work has a good accuracy of recognition of sign language gestures of the Polish Sign Language, 90% for uniform background images and 80% in the case of webcam images. The satisfactory recognition accuracy using in-built laptop webcam makes it easily implementable and useful to recognize hand gestures hence, sign language recognition for helping the hearing and speech impaired can be done in real-time without requiring too much computational power or any other device as it can be implemented in any laptop with a webcam. This work can further be extended to form and identify meaningful words and statements from the individual alphabets and numbers of the sign language, to be displayed as subtitled text for the sign language in real time to aid the physically impaired.

7. Conflicts of interest

The authors declare that there is no conflict of interest regarding the publication of this manuscript.

ACKNOWLEDGMENTS

Our thanks to the experts who have contributed towards development of the template.

REFERENCES

[1] D. J. Sturman and D. Zeltzer, “A survey of glove-based input,” IEEE Computer Graphics and Applications, vol. 14, no. 1, pp. 30–39, Jan. 1994

[2] N. Ibraheem, M. Hasan, R. Khan, P. Mishra, (2012). “comparative study of skin color based segmentation techniques”, Aligarh Muslim University, A.M.U., Aligarh, India.

[3] Xingyan Li. (2003). “Gesture Recognition Based on Fuzzy C-Means Clustering Algorithm”, Department of Computer Science. The University of Tennessee Knoxville.

[4] Yingying She, Qian Wang, Yunzhe Jia, Ting Gu, Qun He, Baorong Yang[2014], “A Real-time Hand Gesture Recognition Approach Based on Motion Features of Feature Points”,Software School ,Xiamen University Xiamen, China..

[5] Tong-de Tan, Zhi-min Guo ,“Research of Hand Positioning and Gesture Recognition Based on Binocular Vision “,Information and Engineering School, Zhengzhou University ,Zhengzhou, China

[6] Hervé Lahamy ,Derek Litchi ,” REAL-TIME HAND GESTURE RECOGNITION USING RANGE CAMERAS “, Department of Geomatics Engineering, University of Calgary,Calgary,Alberta.

[7] Hong Cheng, Jun Luo,Xuewen Chen,” A WINDOWED DYNAMIC TIME WARPING APPROACH FOR 3DCONTINUOUS HAND GESTURERE COGNITION”.

[8] Zhong Yang,Yi Li,Weidong Chen,Yang Zheng(2012),” Dynamic Hand Gesture Recognition Using Hidden Markov Models”.

[9] D. G. Lowe. Distinctive image features from scale-invariant keypoints. Int. J. Comput. Vision, 60(2):91-110, 2004.

[10] Nasser Dardas, Qing Chen, Nicolas D. Georganas,Emil M. Petriu, Fellow(2010),"Hand Gesture Recognition Using Bag-of-Features and Multi-Class Support Vector Machine".

[11] Nusirwan Anwar bin Abdul Rahman, Kit Chong Wei and John See," RGB-H-CbCr Skin Colour Model for Human Face Detection".

[12] Z.Zivkovic, "Improved adaptive Gausian mixture model for background subtraction" in 2004 and "Efficient Adaptive Density Estimation per Image Pixel for the Task of Background Subtraction" in 2006.

[13] C.-C. Chang and C.-J. Lin. LIBSVM: a library for support vector machines,2001.

[14] Simei G. Wysoski, Marcus V. Lamar, Susumu Kuroyanagi, Akira Iwata, (2002). "A Rotation Invariant Approach On Static-Gesture Recognition Using Boundary Histograms And Neural Networks," IEEE Proceedings of the 9th International Conference on Neural Information Processing, Singapura.

[15] Kouichi M., Hitomi T. (1999) "Gesture Recognition using Recurrent Neural Networks" ACM conference on Human factors in computing systems: Reaching through technology (CHI '91), pp. 237-242. doi: 10.1145/108844.108900

[16] L.Pigou,S.Dieleman,P.-J.Kindermans and B.Schrauwen, Sign language recognition using convolutional neural networks. In ECCVW, 2014.

[17]Pavlo Molchanov, Shalini Gupta, Kihwan Kim, and Jan Kautz Hand Gesture Recognition with 3D Convolutional Neural Networks. In CVPRW, 2015.

Author' biography with Photo

Ishita Vishnoi,

Undergraduate,

Department of Computer Science,

Delhi Technological University

Nikunj Khetan,

Undergraduate,

Department of Computer Science,

Delhi Technological University

Dr. S. Indu,

Associate Professor,

Department of Electronics & Communication,

Delhi Technological University

Applied Thermal Engineering 120 (2017) 560–567

Contents lists available at ScienceDirect

Applied Thermal Engineering

journal homepage: www.elsevier.com/locate/apthermeng

Research Paper

Development of an innovative polygeneration process in hybrid solar-biomass system for combined power, cooling and desalination

U. Sahoo [a,b], R. Kumar [a,*], P.C. Pant [b], R. Chaudhary [a]

[a] Department of Mechanical Engineering, Delhi Technological University, New Delhi 110042, India
[b] National Institute of Solar Energy, Ministry of New and Renewable Energy, Govt. of India, Gurgaon, Haryana 122003, India

HIGHLIGHTS

- Heat utilization from solar and biomass resources are considered for hybridization.
- Modeling of polygeneration process in hybrid solar-biomass power plant is considered.
- Thermodynamic evaluation are performed to identify the effect of various parameters.
- Primary Energy Saving of polygeneration process is determined.

ARTICLE INFO

Article history:
Received 7 November 2016
Accepted 8 April 2017
Available online 11 April 2017

Keywords:
Polygeneration
Hybrid solar-biomass
Energy
Exergy
Primary energy savings

ABSTRACT

In the polygeneration process simultaneous production of power, vapor absorption refrigeration (VAR) cooling and multi-effect humidification and dehumidification (MEHD) desalination system from different heat sources in hybrid solar-biomass (HSB) system with higher energy efficiency take place. It is one of the solutions to fulfill energy requirements from renewable sources and also helps in the reduction of carbon dioxide emissions. The VAR cooling system operates using the extracted heat taken from turbine and condenser heat of the VAR cooling system is used in desalination system for production of drinking water as per demand requirement. Though the production of electricity decreases due to extraction of heat from turbine for VAR cooling and desalination, the complete system meets the energy requirements & increases the primary energy savings (PES). The thermodynamic evaluation and optimization of HSB system in polygeneration process for combined power, cooling and desalination is investigated to identify the effects of various operating parameters. Primary energy savings (PES) of polygeneration process in HSB system is achieved to 50.5%. The energy output is increased to 78.12% from this system as compared to simple power plant.

1. Introduction

The energy demand for cooling and process heat/desalination applications are increasing continuously due to increase in the electricity requirements for industries, office campuses, institutions. Globally, in industrial sector about two-thirds of total consumption of energy is used for process heat applications. In India, the increase in huge electricity demand for industry, institutions, office complexes, commercial establishments, etc has resulted in higher consumption of conventional energy e.g. coal, fossil fuel (41% covered by petroleum and 40% by natural gas) [1,2], as well as increasing the greenhouse gas (GHG) emissions and negative impact of climate change. To meet the higher electricity demand, renewable energy sources i.e. solar thermal energy and biomass heat (during non-availability of sunshine hours) are one of the best options to operate thermally driven power systems in place of conventional power [3]. The average intensity of Direct Normal Irradiance (DNI) received in most of the parts of India is 4–5.5 kWh/m^2/day [4]. Although solar thermal has good potential for power generation in this country but due to daily & seasonal variations it cannot be utilised continuously to generate constant power as per required demand. So, hybridization of solar thermal power plant (STPP) is most important to meet power requirements [5]. Biomass can be one of the options for contributing toward partial and full load energy requirements during low/non sunshine hours and supplement with each other seasonally [6]. Over 500 million tons (MT) of biomass is produced every year in different states in India [7]. Solar thermal technology drives the thermal power system in peak sunshine hours [8] and biomass heat drives

* Corresponding author.
E-mail address: dr.rajeshmits@gmail.com (R. Kumar).

http://dx.doi.org/10.1016/j.applthermaleng.2017.04.034
1359-4311/

Nomenclature

g	specific gravitational force (m/sec^2)
T	temperature (°C or K)
h	specific enthalpy (kJ/kg)
s	specific entropy (kJ/kg K)
W	rate of work transfer (kW)
Q	rate of heat transfer (kW)
E_x	exergy (kW)
E	energy (kW)
C_p	specific heat (kJ/kg K)
Q_b	total heat produced from biomass (kW)
Q_{solar}	solar energy falling on PTC field (kW)
$V_{i,e}$	bulk velocity of the working fluid at inlet & outlet (m/s)
W_{net}	net-work output of the HSB plant (kW)
$Z_{i,e}$	altitude of the stream above the sea level at inlet & outlet (m/s)

p	pump
e	evaporator
ab	absorber
fw	feed water
Dw	distilled water
Bw	brackish water
HE	heat exchanger
i, e	exergy flowing stream at inlet and outlet
j	heat source of each state points of the system
$P1$ & $P2$	pump 1 and 2
PTC	parabolic trough collector
SPP	simple power plant
w	water
o	surrounding (or reference environment) condition
1–29, $c, a, x\&y$	state points of the system

Subscripts

c	condenser
g	generator

in short transient during the day and at night time to generate constant power. There is a huge potential for combined power, cooling and process heat applications using polygeneration process in many industries. This means that VAR cooling system can be operated by using the turbine heat of HSB power plant and desalination system can also be operated using the cooling condenser heat. Polygeneration process in hybrid solar thermal power plant can improve the overall efficiency, reliability and reduce the amount of CO_2 emissions [9]. India has lot of potential to use polygeneration system for sustainability of HSB power plant and meeting the energy requirements of various users. This paper mainly focuses on the thermodynamics analysis (i.e. energy and exergy) of HSB power plant in polygeneration process for combined electricity, VAR cooling and desalination. Yuan et al. [10] developed a cooling system with desalination in cogeneration process. The desalination system operates by utilizing the rejected heat from the condenser of cooling system. The performance analysis of combined distillation and air-conditioning system has been studied. The proposed system was simulated to predict distillate output from cooling coil for the system. The system was also optimized to meet the cooling load of 5.4 kW and distilled water of 100 L/day [11].

Dincer and Zamfirescu [12] discussed on multigeneration energy system using the renewable energy heat source and also compared thermodynamic performance & payback period. Ahmadi et al. [13] discussed the thermodynamics analysis i.e. exergy efficiency and optimized the cost of multi generation energy system based on a micro gas turbine. The system generates power, cooling and hot water simultaneously. Mago and Hueffed [14] explained the heating, cooling and power system for a large office building and discussed the primary energy savings and economic costs. Many researchers explained about the performance evaluation of VAR systems in their required temperature ranges and most of the research work has been done on combined cooling, heating and power which are able to provide more than one product commodity [15–20] but very little research work has been carried out for polygeneration process. In order to meet the energy demand from renewable energy sources, polygeneration process (energy & exergy) in hybrid solar thermal power plant for combined power, cooling & desalination is developed and accessed the performance of the system as shown in Fig. 1. It is the next generation energy production technique with a potential to overcome intermittence of renewable energy. This system can deliver electricity with lesser impact on environment compare to conventional fossil fuel based power generating system. It has potential of improving network efficiencies and assess to electricity to a large section of population. Increasing deployment of this innovative system also enhances the diversity of energy supply and, therefore energy security of any nation by reducing fuel risks.

2. System description

The hybridized solar thermal and biomass system produces steam at pressure of 60 bar and temperature of 500 °C and supplies it to turbine at mass flow rate of 5 kg/s (state point 5). The selection of solar thermal technology is a real challenges to meet the heat requirement for power generation due to variation of DNI in most places of the country. The cost of solar thermal collector field is determined primarily by its size and technology, which will affect the cost of the energy generation from the system. The implementation of the technology depends on the cost effective conversion of the solar energy into useful thermal energy. From the literature survey, PTC & paraboloid dish technology are recognized as the most efficient systems and best suited technologies for generation of power in India [21]. PTC technology has been deployed in this HSB system to supply primary heat, however, biomass boiler is considered to supply secondary heat in intermittency of the day and full load capacity at night cycle (4-c-a) as shown in Fig. 2. In this case, steam is bled and expanded at specific steam flow rate to an intermediate stage and supplied to generator of VAR cooling system (State point 6–6′). And remaining steam is expanded at low pressure and medium temperature at state point 7. The bled steam at point 6′ is sent to feed water heater. Condensed water is pumped to the feed water heater at pressure of 5 bar (State point 2) and mixed with bled steam in feed water heater. In generator, the heat of extracted steam from the turbine (State point 6) is added and boils off the weak solution of LiBr-water. The solution (LiBr-water) splits into LiBr and water vapor. Refrigerant water vapor flows to the condenser (State point 16) where heat is rejected as the refrigerant condensate (State point 17 & 18) and strong LiBr-water solution returns back to the absorber through HE-1 and EV-1 (State points 13–14–15). The condensate liquid from the HE-2 is supplied (State point 18) to the evaporator

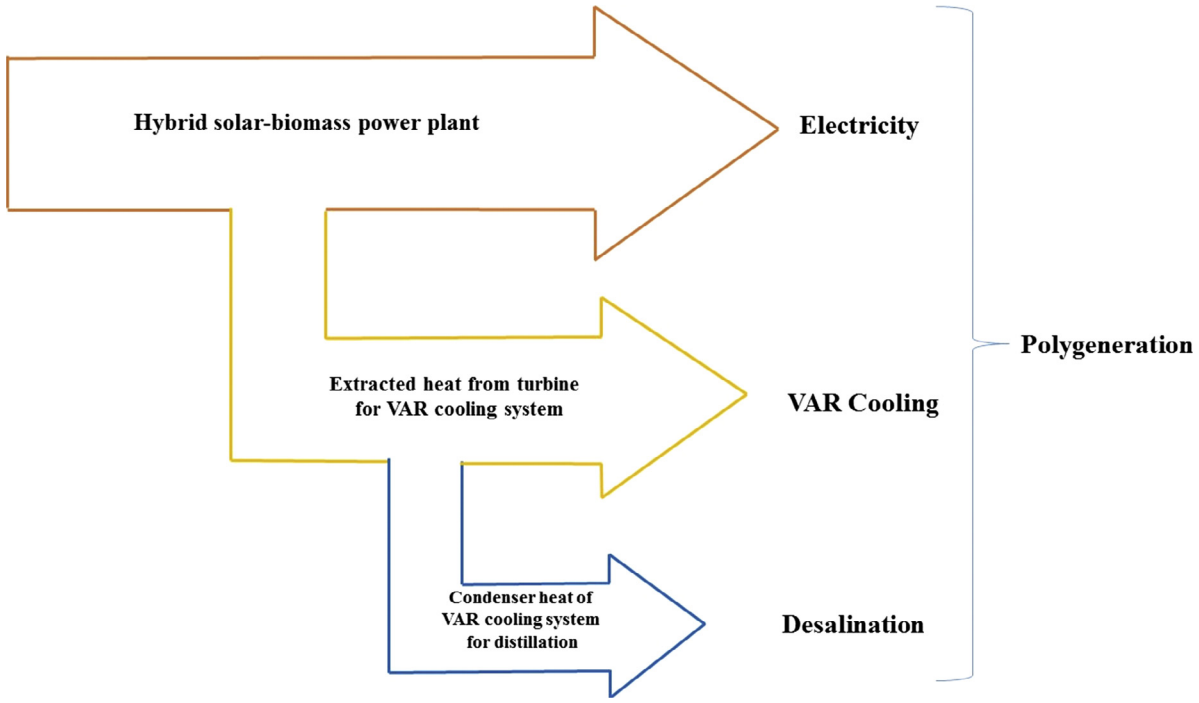

Fig. 1. Flow diagram of proposed cooling system with process heat applications.

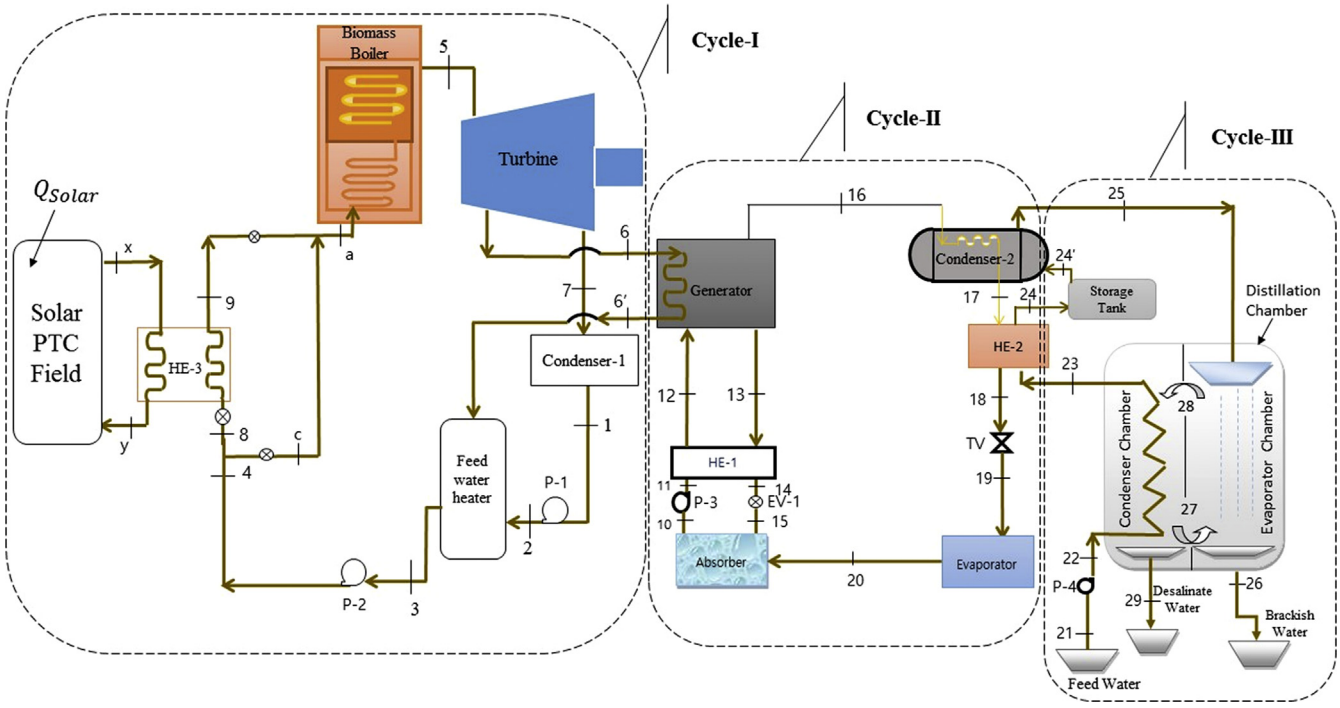

Fig. 2. Schematic diagram of hybrid solar-biomass power plant with cooling and desalination in polygeneration process.

through throttle valve (State point 19). Water vapor formed from the evaporator is absorbed (State point 20) by the strong LiBr-water solution sprayed in the absorber maintaining low pressure in the evaporator. As strong LiBr-water solution absorbs water vapor, it becomes weak solution of LiBr-water and then pumped to the generator through HE-1 (State points 10–11–12). The VAR cooling system has been designed such that the heat of condenser-2 and HE-2 can be used to heat the preheated water of condenser chamber of multi effect dehumidification (MED) system (State points 16–17–18).

In MED system, the feed water is pumped (State points 21–22) to condenser chamber (State points 22–23) of distillation chamber for preheating and supplied to the HE-2 (State point 23). The preheated water is getting further heated and supplied to the

condenser of VAR cooling system through storage tank (State point 24–24′) and then the hot water is sprayed on to the top of the evaporator chamber at a desired mass flow rate (State point 25). The humidified hot air from evaporator chamber is drifted toward the condenser chamber by natural convection. Then the air gets partially dehumidified in the condenser chamber and brought back to the evaporator chamber. The water vapor gets condensed in condenser chamber and collected the water droplet in desalination water collection tank. The production of three output (i.e. Electricity → cooling → desalination) is termed as *polygeneration* process.

3. Modeling and thermodynamic analysis

The technical modeling and thermodynamic analysis (i.e. energy and exergy) of polygeneration process in HSB thermal power plant for combined power, cooling and desalination has been analyzed and optimized. Specifically, the energy and exergy analysis are taken to better understand the performance of polygeneration process in HSB system. The specifications of major equipment are shown in Table 1. The following assumptions are made for the thermodynamics analyses:

- Steady-state, steady-flow operating conditions are considered.
- The Pressure drops in pipes and heat losses are negligible.
- All components are well insulated and are considered adiabatic.
- Kinetic and potential energy changes are negligible.

3.1. Energy analysis

3.1.1. HSB power plant (Cycle-I)

The mass and energy balance equations has been applied on each components of the hybrid system.

$$\sum_i m_i = \sum_e m_e \tag{1}$$

$$Q_{solar} + Q_b + m\left(h_i + \frac{V_i^2}{2} + gZ_i\right) = m\left(h_e + \frac{V_e^2}{2} + gZ_e\right) + W_{net} \tag{2}$$

The energy balance equations of parabolic trough collector and major components of HSB power plant (cycle-I) are expressed in [22].

Table 1
System specifications of major components of the polygeneration system.

Equipment	Input parameters	Value
PTC Field	Total numbers of collector assembly	26
	Length of PTC assembly	120 m
	With of mirror	5.75 m
	Aperture area, A_{ap}	18,000 m^2
	Optical efficiency, η_{opt}	65%
	a_1	0.1 W/m^2 °C
	a_2	0.001 W/m^2 °C^2
	Mirror reflectance	94%
	Flow rate of heat transfer fluid	25 kg/s
Turbine isentropic efficiency		96%
Pump isentropic efficiency		88%
Biomass boiler thermal efficiency		80%
Condenser effectiveness		86%
Generator effectiveness		100%
Absorber effectiveness		100%
Evaporator effectiveness		100%
Heat exchanger-1, 2 & 3 effectiveness		86%
Storage tank capacity		163.77 m^3/h
$(Cp)_{air}$		1.004 kJ/kg K
$(Cp)_v$		1.872 kJ/kg K
R_{air}		0.287 kJ/kg K
R_v		0.461 kJ/kg K

3.1.2. VAR cooling system (Cycle-II)

The following energy balance equation of major components of cooling system are expressed as:

$$\text{Generator}: \; Q_g = m_{13}\cdot h_{13} + m_{16}\cdot h_{16} - m_{12}\cdot h_{12} \tag{3}$$

$$\text{Condenser-2}: \; Q_{c2} = m_{16}\cdot h_{16} + m_{24'}\cdot h_{24'} - m_{17}\cdot h_{17} - m_{25}\cdot h_{25} \tag{4}$$

$$\text{Evaporator}: \; Q_e = m_{20}\cdot h_{20} - m_{19}\cdot h_{19} \tag{5}$$

$$\text{Pump 3}: \; W_{p_3} = m_{11}\cdot h_{11} - m_{10}\cdot h_{10} \tag{6}$$

$$\text{HE-2}: \; Q_{HE-2} = m_{17}\cdot h_{17} + m_{23}\cdot h_{23} - m_{18}\cdot h_{18} - m_{24}\cdot h_{24} \tag{7}$$

The coefficient of performance of the single effect VAR cooling system is expressed as

$$COP = \frac{Q_e}{(Q_g + W_{P3})} \tag{8}$$

3.1.3. MEHD desalination system (Cycle-III)

The energy balance equations for distillation chamber can be written as

$$m_{fw}(h_{22} + h_{25}) = m_{fw}h_{23} + m_{Bw}h_{26} + m_{Dw}h_{29} \tag{9}$$

$$m_{Dw} = 0.001 \times (w_{28} - w_{27}) \times m_{air} \tag{10}$$

$$m_{Bw} = m_{fw} - [0.001 \times (w_{28} - w_{27}) \times m_{air}] \tag{11}$$

Amount of heat transfer required (Q_d) for heating the preheating water at state point ′23′

$$Q_d = m_{fw}\cdot c_{p,fw}\cdot (T_{25} - T_{23}) \tag{12}$$

The heat transfer of feed water in the humidification process is defined as

$$Q_{25-26} = m_{fw}h_{25} - m_{Bw}h_{26} \tag{13}$$

The heat transfer of saturated air in the humidification process is defined as

$$Q_{28-27} = m_{air}(h_{28} - h_{27}) \tag{14}$$

The energy efficiency of humidification process is expressed as

$$\eta_{energy,humidification} = \frac{Q_{28-27}}{Q_{25-26}} \tag{15}$$

By using pinch technology, T_{26} and T_{28} can be determine.

The heat transfer of feed water in the dehumidification process is expresses as

$$Q_{DH,22-23} = m_{fw}(h_{23} - h_{22}) \tag{16}$$

The heat transfer of saturated air in the dehumidification process can be calculated as

$$Q_{DH,28-27} = m_{air}(h_{28} - h_{27}) \tag{17}$$

The energy efficiency of dehumidification process is expressed as

$$\eta_{energy,dehumidification} = \frac{Q_{DH,22-23}}{Q_{DH,28-27}} \tag{18}$$

By using pinch technology [23] T_{23} and T_{27} can be determine.

The energy efficiency of MEHD distillation system is expressed as

$$\eta_{energy,distillation} = \frac{m_{Dw}\times h_{fg}}{Q_d} \tag{19}$$

where h_{fg} is latent heat of vaporization of feed water (kJ/kg).

3.2. Energy efficiency of polygeneration process in HSB system

The energy efficiency of polygeneration process in HSB power plant ($\eta_{E,polygeneration}$) is expressed as:

$$\eta_{E,polygeneration} = \frac{W_{net} + Q_e + (m_{Dw} \times h_{fg})}{Q_{solar} + Q_b} \tag{20}$$

3.3. Exergy analysis

3.3.1. HSB power plant (Cycle-I)

The steady-state process, respective balances for exergy can be written as [24]

$$\sum_i E_{xi} + \sum_j \left[1 - \frac{T_o}{T_j}\right] Q_j = \sum_e E_{xe} + W_{net} + E_{xD} \tag{21}$$

Exergy of the flowing stream at each state point of hybrid system (E_x) may be expressed as

$$E_x = [(h - h_o) - T_o(s - s_o)] \tag{22}$$

The exergy analysis for balance equations of parabolic trough collector and major components of HSB power plant (cycle-I) are expressed in [22].

3.3.2. VAR cooling system (Cycle-II)

$$\text{Generator}: \; E_{x,g} = Q_g\left(1 - \frac{T_o}{T_g}\right) \tag{23}$$

$$\text{Condenser-2}: \; E_{x,c2} = Q_{c2}\left(1 - \frac{T_o}{T_{c2}}\right) \tag{24}$$

$$\text{Evaporator}: \; E_{x,e} = m_{20}[(h_{19} - h_{20}) - T_o(s_{19} - s_{20})] \tag{25}$$

$$\text{Absorber}: \; E_{x,ab} = m_{15}(h_{15} - T_o s_{15}) + m_{20}(h_{20} - T_o s_{20}) - m_{10}(h_{10} - T_o s_{10}) \tag{26}$$

The exergy coefficient of performance of the single effect VAR cooling system is expressed as

$$E_{x,COP} = \frac{E_{x,e}}{(E_{x,g} + W_{P3})} \tag{27}$$

3.3.3. MEHD distillation system (Cycle-III)

The exergy balance equations of the system is expressed as;

$$m_{fw}(Ex_{22} + Ex_{25}) = m_{fw}Ex_{23} + m_{Bw}Ex_{26} + m_{Dw}Ex_{29} \tag{28}$$

The exergy of feed water in humidification process:

$$Ex_{25-26} = m_{fw}Ex_{25} - m_{Bw}Ex_{26} \tag{29}$$

The exergy on water vapor at state point 27 & 28 in humidification is defined as:

$$Ex_{28-27} = m_{air}(Ex_{28} - Ex_{27}) \tag{30}$$

The exergy at point n (i.e. point 27 and 28) is also calculated by [25]

$$Ex_{27,28} = [(C_p)_{air} + \omega_n(C_p)_v](T_n - T_0) - T_0\left\{[(C_p)_{air} + \omega_n(C_p)_v]\ln\left(\frac{T_n}{T_0}\right) - (R_{air} + \omega_n R_v)\ln\left(\frac{P_n}{P_0}\right)\right\} + T_o\left[(R_{air} + \omega_n R_v)\ln\left(\frac{1 + 1.6078\omega^o}{1 + 1.6078\omega_n}\right) + 1.6078\omega_n R_{air}\ln\left(\frac{\omega_n}{\omega^o}\right)\right] \tag{31}$$

where d is calculated as;

$$\omega = 622\left(\frac{\phi P_v}{P - \phi P_v}\right) \tag{32}$$

where ϕ relative humidity is defined as;

$$\phi = \frac{P_v}{P_{vs}} \tag{33}$$

The exergy efficiency of humidification process is defined as;

$$\eta_{ex,humidification} = \frac{Ex_{28-27}}{Ex_{25-26}} \tag{34}$$

The exergy on the sprayed water in dehumidification process;

$$Ex_{DH,22-23} = m_{fw}(Ex_{23} - Ex_{22}) \tag{35}$$

The exergy on saturated air in the dehumidification process;

$$Ex_{DH,28-27} = m_{air}(h_{28} - h_{27}) \tag{36}$$

The exergy efficiency of the system by dehumidification process is written as;

$$\eta_{ex,dehumidification} = \frac{Ex_{DH,22-23}}{Ex_{DH,28-27}} \tag{37}$$

The exergy efficiency of MEHD distillation system is expressed as

$$\eta_{exergy,distillation} = \frac{m_{Dw} \times (h_{fg} - T_o \times s_{fg})}{Q_{ex,d}} \tag{38}$$

where $Q_{ex,d}$ is exergy on heat transfer required for heating the pre-heating water.

3.4. Exergy efficiency of polygeneration process in HSB system

The exergy efficiency of polygeneration process in HSB power plant is expressed as:

$$\eta_{Ex,polygeneration} = \frac{W_{net} + E_{x,e} + E_{x,Dw}}{E_{xSolar} + E_{xb}} \tag{39}$$

where E_{xb} and E_{xSolar} are the exergy of biomass and solar [22].

4. PES

The total output in polygeneration process is expressed as

$$W_{Polygeneration} = W_{net} + Q_e + Q_{Dw} \tag{40}$$

The (PESPP) can be expressed [26] as on the basis of following equations.

$$PES = 1 - \left(\frac{1}{\frac{\eta_{heat}}{\eta_{Ref.,heat}} + \frac{\eta_{electrical}}{\eta_{Ref.,electrical}}}\right) \times 100 \tag{41}$$

$$\eta_{heat} = \text{Heat efficieicency in Polygeneration process} = \frac{Q_e + Q_{Dw}}{Q_{solar} + Q_b} = \frac{\text{Useful heat output}}{\text{Heat Input to the polygeneration process}} \tag{42}$$

$$\eta_{ref,heat} = \text{Efficiency reference value for separate heat production} = 0.9$$

$$\eta_{electrical} = \text{Electrical efficieicency of Polygeneration system} = \frac{W_{net}}{Q_{solar} + Q_b} = \frac{\text{Useful Electrical Output}}{\text{Heat Input to the polygeneration system}} \tag{43}$$

$\eta_{ref,electrical}$ = Efficiency reference value for separate electricity production through solar-biomass = 0.25

and

$$\eta_{electrical} = \frac{W_{net}}{Q_{solar} + Q_b} \quad (44)$$

The percentage % increase of equivalent electricity production in polygeneration process as compared to simple power plant is expressed as;

$$(\%) \text{ increased} = \frac{W_{Polygeneration} - W_{SPP}}{W_{SPP}} \quad (45)$$

where W_{SPP} is the work output of simple power plant at temperature and pressure of 60 bar and 500 °C.

5. Result and discussions

In this paper, the thermodynamic (i.e. Energy and exergy) modeling and optimization of HSB power plant with cooling and desalination in polygeneration process are presented. The different parametric study is carried out to simulate the results of various useful outputs by varying various input points such as direct normal irradiance, generator heat of VAR system. For the proposed subsystem, various parametric state points of the system are given in Table 2.

The PTC field provides the heat as per availability of DNI and biomass boiler provides the remaining heat to fulfill the heat requirement for continuous running the power plant. Figs. 3 and 4 show the monthly daily average percentage utilization of heat from solar and biomass. It is seen that, in the month of November solar radiation decreases compared to May due to cosine effect. In this case, remaining heat can be taken to maintain the heated water to superheated condition from biomass boiler.

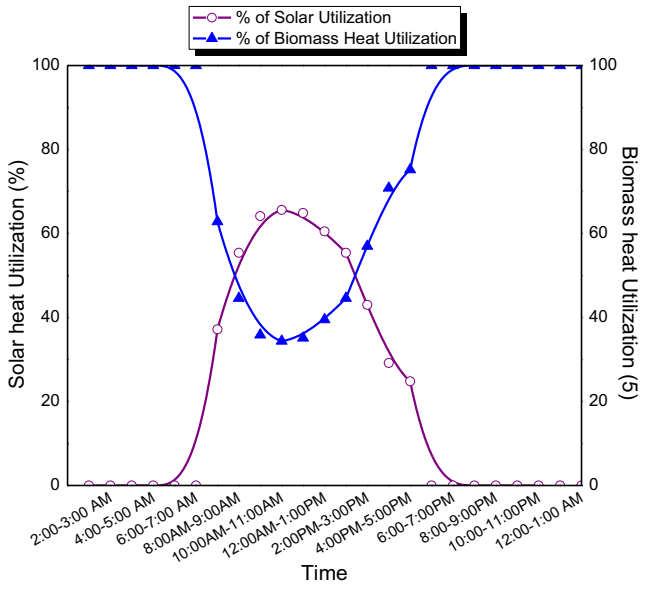

Fig. 3. Daily hourly average of heat utilization from solar and biomass for the month of May.

Figs. 5 and 6 show the variation of DNI on solar-biomass heat, turbine inlet heat, boiler heat, PTC heat, energy efficiency of PTC field, energy and exergy efficiency of polygeneration in HSB system. It is observed that energy & exergy efficiencies of PTC increases with increase of DNI. With the increase of PTC energy efficiency, the PTC heat increases but the overall efficiency of the HSB system in polygeneration decrease due to less efficiency of PTC field compared to biomass boiler. The PTC energy efficiency increases to 51.62% whereas the biomass boiler efficiency remains constant at 80%. So, the heat taken from solar field is less than the

Table 2
State point properties of the hybrid polygeneration system.

State points	Fluid	Pressure (bar)	Temperature (°C)	Enthalpy (kJ/kg K)	Mass flow rate (kg/s)
1	Water	0.1	45.8	191.8	5.0
2	Water	5	45.8	191.8	5.0
3	Water	5	105.9	444.2	5.0
4,c	Water	60	106.3	450	5.0
5	Water	60	500	3422	5.0
6	Water	7.1	201.5	2927	4.35
6′	Water	7.1	138.5	701.6	4.35
7	Water	0.1	45.8	2329	4.15
8	Water	60	106.3	450	5.0
9,a	Water	60	275.6	1250	5.0
X	Therminol VP-1	12	391.8	2588	25.0
Y	Therminol VP-1	12	240	2154	25.0
10	LiBr-Water	0.001313	37	81.43	21.47
11	LiBr-Water	0.08453	37	81.43	21.47
12	LiBr-Water	0.08453	138.1	301.5	21.47
13	LiBr	0.08453	142	353.8	18.05
14	LiBr	0.08453	40.1	91.99	18.05
15	LiBr	0.001313	40.1	91.99	18.05
16	Water	0.08453	142	2753	3.421
17	Water	0.08453	95	398	3.421
18	Water	0.08453	40	167.6	3.421
19	Water	0.001313	11	398	3.421
20	Water	0.001313	11	2521	3.421
21	Water	0.1	35	192.4	45.49
22	Water	0.1	35	146.7	45.49
23	Water	0.1	37.5	157.1	45.49
24	Water	0.1	50	209.4	45.49
25	Water	0.1	88.1	368.8	45.49
26	Water	0.1	50.2	210.4	43.98

[a]These above data are generated by Enginesering Equations Solver (EES) software.

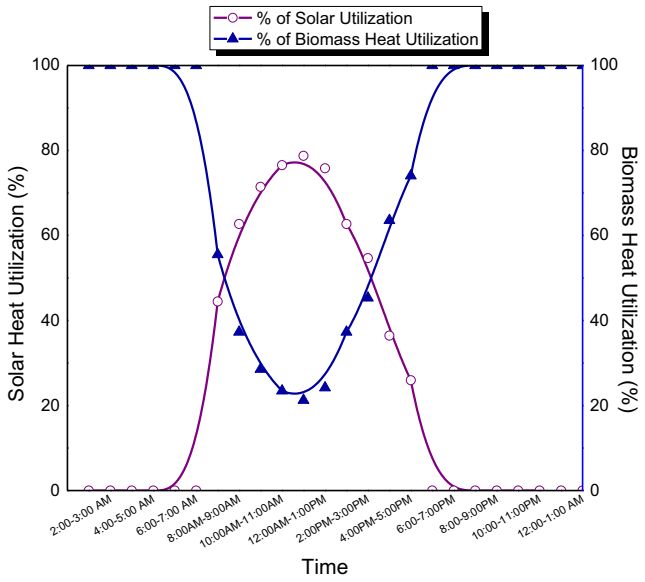

Fig. 4. Daily hourly average of heat utilization from solar and biomass for the month of November.

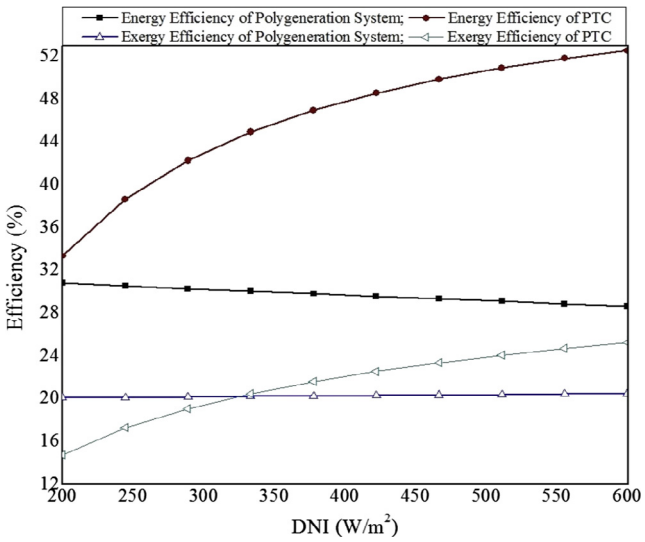

Fig. 5. Variation of DNI on efficiency of PTC and HSB system in polygeneration process.

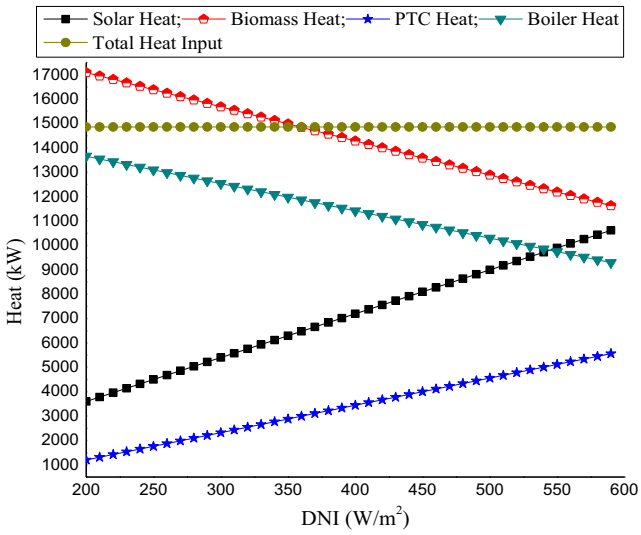

Fig. 6. Variation of DNI on various parameters of HSB system in polygeneration process.

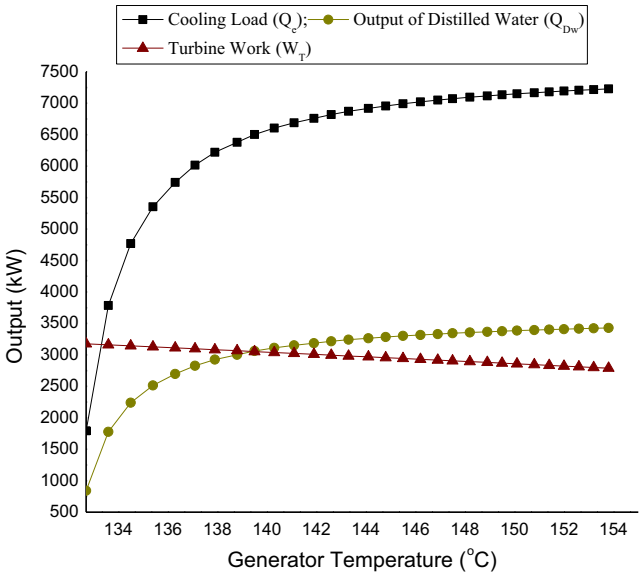

Fig. 7. Variation of turbine work, cooling load and output of distilled water of the HSB system in polygeneration process on various generator temperature.

heat taken from the biomass boiler. The biomass heat increases result in increasing the overall efficiency of system when the DNI decreases. It is clearly indicated that the heat input sources from solar and biomass is very important for improving the overall efficiency of system and these supplement with each other. From this study it becomes apparent that the heat utilization from solar and biomass is considered as 37.34% (8100 kW) and 62.65% (13,588 kW) respectively for modeling of HSB system in polygeneration process. The maximum energy and exergy efficiencies of HSB system in polygeneration process for combined power, cooling & desalination are 30.81% and 20.47% respectively.

Fig. 7 shows the variation of turbine work, evaporator load and output of distilled water of the HSB system in polygeneration process on various generator temperatures. It can be seen that the increase in the generator temperature results in decrease in the turbine work output of HSB power plant. The evaporator load, output of distilled water continuously increases at a faster rate up to a generator temperature of 142 °C, thereafter the rate of increase in the evaporator load and output distillation declines with increase in generator temperature while keeping other parameters of the system as constant. For better understanding the effect of generator temperature (i.e. generator temperature taken from extracted heat from turbine) on cooling load and distilled water output, we should concentrate on the effect of temperature on work output, VAR cooling and distilled water output. It is clearly indicated from the Figure that though the production of electricity decreases due to extraction of heat from turbine for generator heat of VAR cooling system, the complete system meets the energy requirements and its overall efficiency increases.

Fig. 8 shows the energy and exergy efficiencies with change in extraction pressures in turbine at various fraction of steam (i.e.0.1, 0.3, 0.5, 0.7 & 0.9). The energy efficiency increases slightly from 24.69% to 27.77% at extraction pressure and fraction of steam from 390 to 600 kPa and 0.1 respectively. It is also seen that, the

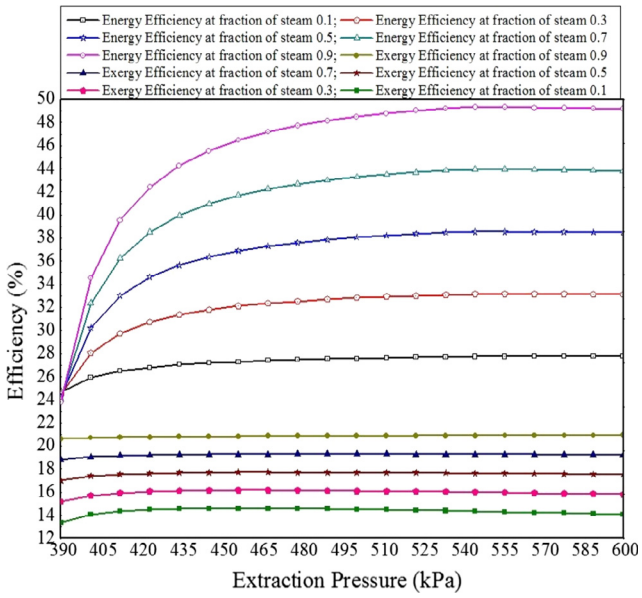

Fig. 8. Energy and exergy efficiencies with change in extraction pressure from turbine at various fraction of steam (i.e. 0.1, 0.3, 0.5, 0.7 & 0.9).

maximum energy efficiency increases to 49.35% at extraction pressure of 555 kPa and fraction of steam of 0.9. The profile of exergy efficiency follows the same trend as energy efficiency against extraction pressure in turbine at these five fractions of steam.

6. Conclusion

Polygeneration process in HSB thermal power plant for combined power, cooling and desalination offer an opportunity to increase further efficiency through proper thermodynamic arrangement of different processes or end products as compared to simple power plant. The thermodynamic evaluation (energy and exergy) and optimization of polygeneration process in HSB system for combined power, cooling and desalination system provides the useful information. The system has achieved a maximum energy efficiency of 49.35% at various decision variable of extraction pressure, fraction of steam and desalination inlet heated water temperature of 555 kPa, 0.9 & 81.08 °C of the polygeneration process in HSB thermal power plant. The exergy efficiency of the system is increased to 20.94%. The equivalent electricity generation from polygeneration process in HSB thermal power plant increased to 78.12% as compared to a simple thermal power plant and the PES is 50.5%. The HSB system in polygeneration process is ideal for industries, office campuses, institutions to fulfill the energy requirements for various applications i.e. electricity, space cooling and drinking water. Developments in these regards have taken place over the past two decades are quite encouraging. It is expected that in the near future HSB power plant in polygeneration process will constitute one of the competitive options of electricity generation.

Acknowledgement

The Authors express their deep gratitude to Shri. S.K. Singh, Director General, National Institute of Solar Energy, Ministry of New and Renewable Energy, Government of India for assisting in identifying and formulating the research problem. His valuable suggestion and advice gave us the confidence to overcome the challenges in formulation of this manuscript.

References

[1] N. Kalkan, E.A. Young, A. Celiktas, Solar thermal air conditioning technology reducing the footprint of solar thermal air conditioning, Renew. Sustain. Energy Rev. 16 (2012) 6352–6383.
[2] Solar Heat for Industrial Processes, IEA-ETSAP and IRENA 2015.
[3] F. Assilzadeh, S.A. Kalogirou, Y. Ali, K. Sopian, Simulation and optimization of a LiBr solar absorption cooling system with evacuated tube collectors, Renew. Energy 30 (2005) 1143–1159.
[4] Solar Radiation Energy over India. Indian Meteorological Department and Ministry of New and Renewable Energy, Govt. of India, 2008.
[5] Technology Roadmap: Solar Heating and Cooling, IEA, 2013.
[6] U. Sahoo, R. Kumar, P.C. Pant, R. Chaudhury, Scope and sustainability of hybrid solar–biomass power plant with cooling, desalination in polygeneration process in India, Renew. Sustain. Energy Rev. 51 (2015) 304–316.
[7] J. Singh, B.S. Panesar, S.K. Sharma, Energy potential through crop biomass using geographical information system-a case study of Punjab, Biomass Bioenergy 32 (2008) 301–307.
[8] V. Raja Boopathi, V. Shanmugam, A review and new approach to minimize the cost of solar assisted absorption cooling system, Renew. Sustain. Energy Rev. 16 (2012) 6725–6731.
[9] L.M. Serra, M.A. Lozano, J. Ramos, A.V. Ensinas, S.A. Nebra, Polygeneration and efficient use of natural resources, Energy 34 (2009) 575–586.
[10] G. Yuan, L. Zhang, H. Zhang, Experimental research of an integrative unit for air-conditioning and desalination, Desalination 182 (2005) 511–516.
[11] K. Ghali, N. Ghaddar, A. Alsaidi, Experimental and theoretical study of an optimized integrated solar desalination and air conditioning unit, Int. J. Green Energy 8 (2011) 81–99.
[12] I. Dincer, C. Zamfirescu, Renewable energy based multigenerational systems, Int. J. Energy Res. 36 (2012) 1403–1415.
[13] P. Ahmadi, I. Dincer, M.A. Rosen, Thermodynamic modeling and multi objective evolutionary-based optimization of a new multigeneration energy system, Energy Convers. Manage. 76 (2013) 282–300.
[14] J. Mago Pedro, Anna K. Hueffed, Evaluation of a turbine driven CCHP system for large office buildings under different operating strategies, Energy Build. 42 (2010) 1628–1636.
[15] C.P. Jawahar, R. Saravanan, J.C. Bruno, A. Coronas, Simulation studies on GAX based Kalina cycle for both power and cooling applications, Appl. Therm. Eng. 50 (2013) 1522–1529.
[16] M. Rivarolo, A. Cuneo, A. Traverso, A.F. Massardo, Design optimization of smart poly-generation energy districts through a model based approach, Appl. Therm. Eng. 99 (2016) 291–301.
[17] P. Bosch, A. Modarresi, A. Friedl, Comparison of combined ethanol and biogas polygeneration facilities using exergy analysis, Appl. Therm. Eng. 37 (2012) 19–29.
[18] A. Khaliq, R. Kumar, Thermodynamic performance assessment of gas turbine trigeneration system for combined heat cold and power production, J. Eng. Gas Turbines Power 130 (2008), 024501-024501-4.
[19] A. Buonomano, F. Calise, G. Ferruzzi, L. Vanoli, A novel renewable polygeneration system for hospital buildings: design, simulation and thermo-economic optimization, Appl. Therm. Eng. 67 (2014) 43–60.
[20] A. Piacentino, F. Cardona, An original multi-objective criterion for the design of small-scale polygeneration systems based on realistic operating conditions, Appl. Therm. Eng. 28 (2008) 2391–2404.
[21] U. Sahoo, S.K. Singh, R. Kumar, P.C. Pant, P. Saxena, Evaluation of Solar Thermal Technologies and Applications in India, Adv. Energy Res. 21 (2015) 141–189.
[22] U. Sahoo, R. Kumara, P.C. Pant, R. Chaudhary, Resource assessment for hybrid solar-biomass power plant and its thermodynamic evaluation in India, Sol. Energy 139 (2016) 47–57.
[23] S.B. Hou, SQ. Ye, HF. Zhang, Performance optimization of solar humidification-dehumidification desalination process using Pinch technology, Desalination 183 (2005) 143–149.
[24] T.J. Kotas, The Exergy Method of Thermal Plant Analysis, first ed., New York, 1995.
[25] I. Dincer, A.Z. Sahin, A new model for thermodynamic analysis of a drying process, Heat Mass Transf. 47 (2004) 645–652.
[26] The directive 2004/8/EC of the European Parliament and of the council, Official Journal of the European Union, 2004. <http://www.zoldforrasenergia.hu/docs/2004-08-EC.pdf> (assessed 11.08.2016).

Swarm and Evolutionary Computation xxx (xxxx) xxx–xxx

Contents lists available at ScienceDirect

Swarm and Evolutionary Computation

journal homepage: www.elsevier.com/locate/swevo

Effectual recommendations using artificial algae algorithm and fuzzy c-mean

Rahul Katarya*, Om Prakash Verma

Department of Computer Science & Engineering, Delhi Technological University, Delhi, India

ARTICLE INFO

Keywords:
Recommender system
Collaborative filtering
Artificial algae algorithm
Fuzzy c-mean
Recommendations

ABSTRACT

Recommender systems play a significant role in e-commerce applications. The primary motive of a recommender system is to recommend some items or products to the users based on their previous ratings of other products in the online environment. In this article, we presented a hybrid collaborative filtering based recommender system that improved the accuracy of the recommendations. In our work, we adopted fuzzy c-mean (FCM) and a recent bio-inspired approach, which is artificial algae algorithm (AAA). We have used advanced multilevel Pearson correlation coefficient (PCC) to find the similarity between two users. Moreover, we discovered the rating which the user will most likely give to the movies which he has not given any ratings yet. By applying above-mentioned procedures, the quality of the recommendations is improved significantly. The proposed system succeeded to provide recommendations of better quality and accuracy when compared to other alternatives. We have experimented and evaluated our proposed recommender system on four real data sets: Movielens 100,000, Movielens 1 million, Jester and Epinion. We concluded that our proposed recommender system delivered better recommendations for all four datasets. The efficiency of the system was estimated by evaluation metrics such as mean absolute error (MAE), precision and recall and showed impressive results. This proposed system delivered best results as compared to our previous work (Katarya and Verma, 2016) [1].

1. Introduction

Recommender systems (RSs) are the most popular information filtering systems for e-commerce applications [2–6]. RSs use heterogeneous web data and deliver the accurate information to people such as ratings of products, user profile history, location information (check-in, time), content and features for items for ranking and social relationships (for example in Facebook or LinkedIn) among online users. Recommender systems analyze the various patterns and available information and find a favorite collection of items or products for the users [7–11]. Recommender systems heavily depend on the information database, and they use that big database by applying certain filtering algorithms to find out what a user will like mostly [12,13]. Collaborative filtering (CF) based recommender systems help the users to select the products based on the experiences of other users who have similar kind of interests or those who have already purchased the same kind of items in the past. Collaborative filtering significantly relies on a database of ratings submitted by each user for an item or a product, and then the ratings of different users are compared to each other using suitable similarity method to provide recommendations to the users. It includes identifying the similar users, i.e. the users who have given a similar rating to other products and then the constant function is applied to get the average rating of the product. CF has been widely accepted by many electronic commerce companies such as eBay [14–16], Netflix [17,18] and Amazon [19,20], and this is due to its reliability and effectiveness. In addition to collaborative filtering, there are various other recommendation methods, which can be used to make recommendations. It includes content based filtering, which is based on item metadata, i.e. we get information about the item [21]. In the method, the user gives, a set of information and preferences and the recommender system makes use of this extra information to get accurate recommendations. A knowledge-based recommender system is another approach that uses interpretations about user preferences and interests and knowledge about the domain and uses it to give recommendations to the user [22]. In our earlier work [1], we have presented an efficient collaborative recommender system which was based on the data mining and bio-inspired approach. K-means delivered the initial parameters to particle swarm optimization (bio-inspired algorithm) with the utilization of Movielens dataset. Particle swarm optimization offered initial seed and optimized the Fuzzy c-means (FCM). The PSO-KM-FCM based collaborative recommender system delivered better results when we compared it with other

* Corresponding author.
E-mail address: rahulkatarya@dtu.ac.in (R. Katarya).

http://dx.doi.org/10.1016/j.swevo.2017.04.004
Received 15 June 2016; Received in revised form 7 April 2017; Accepted 15 April 2017

several existing systems. In our approach, we used collaborative filtering method that aims to improve the accuracy of the recommendations. As used in most of the collaborative recommendations systems, we also used similarity function (Pearson correlation coefficient (PCC)), to find the similarity between two users [23]. PCC range varies from −1 to +1, where +1 means they are very similar and −1 means they are not similar at all. We allocated the users into clusters using fuzzy c-mean (FCM) and then adopted a recent bio-inspired algorithm that is artificial algae algorithm (AAA). This technique divides the users into various clusters depending on their similarity. To find the similarity between the two users, we used PCC with some minor modification. Our primary aim is to provide better recommendations to the users. By applying above-mentioned techniques, the quality of the recommendations is enhanced. The recommender system efficiency and performance are enhanced by adopting a latest bio-inspired algorithm which is artificial algae algorithm. The proposed system attempts to make recommendations of better quality and accuracy when compared to other systems. The major contributions of this article are:

1. We presented an efficient collaborative recommender system with the utilization of Swarm intelligence algorithm and data clustering approach.
2. A recent bio-inspired algorithm, artificial algae algorithm [24–26] is employed, and fuzzy c-mean [27–29] is also adopted for clustering.
3. We allocated the users into clusters using fuzzy c-mean (FCM) and then adopted a recent bio-inspired algorithm, which is artificial algae algorithm (AAA).
4. We performed various experiments to evaluate our proposed system using four real data sets: Movielens 100 K, Movielens 1 million, Jester and Epinion.
5. We compared our proposed system with our previous work [1] and existing work [30] by using various evaluation metrics such as mean absolute error (MAE), precision and recall.
6. Our proposed system delivered superior results for almost all four datasets. This shows that our proposed system is both practical and efficient.
7. The proposed recommender system also performed excellently with respect to time when compared with already existing systems.

The rest of this research article is organized as follows: Section 2 explains the related work and methods; Section 3 is based on proposed work. Section 4 describes the experimental evaluation and Section 5 contains the conclusion and future aspects of our work.

2. Related work and methods

In this section, we will illuminate the various methodologies that were implemented previously in the field of collaborative filtering. These collaborative filtering techniques were applied to different datasets and users to rate the various items or services. Many collaborative filtering techniques are broadly used in e-commerce applications such as movies recommendation and products recommendation. A query based recommender system was offered which employed the small latent factor and solved the issues related to the cold start and context situations [31]. Another recommender system was provided for the group recommendation in which primary focus was based on the group profiles and participants involvement and checked the presence of each group member by segregating the item space [32]. One of the most famous attacks in the recommender system is shilling attack, and in this regard, a method was proposed for recommender system in which researchers noticed the shilling attacks with the utilization of support vector machine and target items [33]. Users profiles have great importance for suggesting the quality of recommendations, and by considering the user's profile features a method was proposed in which authors removed the profiles which do not have importance [34]. Machine learning and computational intelligence are providing a gateway to the recommender systems and in this respect three-way decision and random forest were employed to design a recommender system [35]. Authors used both misclassification cost and teacher cost in which misclassification was dedicated to the incorrectly recommended performances, and teacher cost was based on the user preferences. Nowadays most of the recommender system are based on the contextual situations such as locations and surrounding conditions. A hybrid recommender system was offered by the researchers in which they used the location of users in the social networks such as Foursquare [36]. A recommender system was presented who considered the ontology and genetic algorithm and examined the top-n recommendations and solved the cold start problem [37]. Evolutionary computation is an emerging trend towards the recommender system, and a genetic algorithm was employed for recommendations [38]. Authors used a mixture of recommendation techniques and suggested a cost-reduced framework for recommender systems. Job searching is always hectic work in the online portal, so some authors helped the job seekers and offered a personalized job-resume match-making recommender system that presented an innovative online job search process [39]. Collaborative filtering is the most exciting technique which has solved many problems of recommender system such as a novel framework was offered which handled the one-class recommendation difficulties of social media by developing the rich content information with Matrix Factorization (MF) technique [40]. Similar collaborative filtering based recommender systems were presented with effective results by various researchers [41–45]. Fuzzy c-mean clustering technique has shown great importance in the big data and e-commerce such as recommender system, medical domain, and web mining applications [46–49]. To generate recommendations for a particular user, we require *k*-nearest neighbors of that user. A similarity function provides the expected neighbors by calculating the similarity between two users at a time. Then, the k numbers of users, which are most similar to the specified users, are computed which are characterized as k-nearest neighbors of that user and for the identification of k-nearest neighbors we need a similarity function, and PCC is such a function. The ratings of two users are compared in PCC and defined in Equation 1. $Sim(a, b)$ is the similarity value between users a and b, $r_{a,p}$is the rating user a has given for item p and $r_{b,p}$is the rating user b, has given for item p, and $\bar{r}a$ and $\bar{r}b$ represent the average ratings of user a and b respectively. Moreover, "P" is the set of all the elements. Additionally, the similarity value lies in the range −1 to 1. More the similarity value more is the similarity of choices between the two users.

$$Sim_{a.b}^{PCC} = \frac{\sum p \in P(r_{a,p} - \bar{r}a)(r_{b,p} - \bar{r}b)}{\sqrt{\sum p \in P(r_{a,p} - \bar{r}a)^2}\sqrt{\sum p \in P(r_{b,p} - \bar{r}b)^2}} \quad (1)$$

After calculating similarity values, the k-nearest neighbors are identified, and the rating prediction process is applied to the items prediction. Further, the item with the highest rating is predicted and suggested to the specified user. PCC inspired several other methods to calculate the similarity, one of such approach is the weighted PCC (WPCC) [50]. WPCC is solely based on PCC with an addition of calculating the similarities by T numbers of the co-rated item. The similarity measure computation method estimates the similarity between two items which are commonly co-rated by the both the users. The main objective of T is that if the number of co-rated items between the users is superior to or equal to T, then recommendations from these users are preferred. If the value is less than T, then the regular PCC similarity function is used. The WPCC is defined in Eq. (2).

$$Sim_{a,b}^{WPCC} = \begin{cases} \frac{|Ia \cap Ib|}{T} \cdot Sim_{a,b}^{PCC}, & \text{if } |Ia \cap Ib| < T \\ Sima, b^{PCC}, & \text{otherwise} \end{cases} \quad (2)$$

Ia is a number of items rated by user "a" and Ib is number of items rated by user "b" and Ia ∩ Ib is number of items, which are rated by

both users “a” and “b”. A similar method for the similarity calculation is scalable Pearson Correlation Coefficient algorithm (SPCC) [51]. In this approach, the exponential function is used. The greater number of co-rated items make the higher similarity value of the two users. SPCC is defined in Eq. (3).

$$Sim_{a,b}^{SPCC} = \frac{1}{1 + \exp(-|Ia \cap Ib|/2)} \bullet Sim_{a,b}^{PCC} \tag{3}$$

Another approach is a hybrid, which introduces the concept of multi-level function in similarity function. It is a multi-level collaborative filtering method [52]. It enhances the process of k-nearest neighbors by finding a large margin with the application of PCC, as this approach adds various new factors that result in high efficiency and accuracy. This is explained using four levels in Eq. (4).

$$Sim_{a,b}^{Nikolaos} = \begin{cases} Sim_{a,b}^{PCC} + x, & \text{if} \frac{|Ia \cap Ib|}{T} \geq t1 \text{ and } Sim_{a,b}^{PCC} \geq y \\ Sim_{a,b}^{PCC} + x, & \text{if} \frac{|Ia \cap Ib|}{T} < t1 \text{ and } \frac{|Ia \cap Ib|}{T} \geq t2 \text{ and } Sim_{a,b}^{PCC} \geq y \\ Sim_{a,b}^{PCC} + x, & \text{if} \frac{|Ia \cap Ib|}{T} < t2 \text{ and } \frac{|Ia \cap Ib|}{T} \geq t3 \text{ and } Sim_{a,b}^{PCC} \geq y \\ Sim_{a,b}^{PCC} + x, & \text{if} \frac{|Ia \cap Ib|}{T} < t3 \text{ and } \frac{|Ia \cap Ib|}{T} \geq t4 \text{ and } Sim_{a,b}^{PCC} \geq y \\ 0, & \text{otherwise} \end{cases} \tag{4}$$

The Eq. (4) is divided into the four levels. T is the overall number of co-rated items. Here x and y are positive real numbers such that x∈R and y∈R. At each level the number of co-rated items is checked. If they are superior to the pre-specified thresholds (t1, t2, t3, t4), then they can move to the next stage to test the comparison value, which is derived from the two users from PCC. If users have an adequate number of co-rated items with PCC, then their similarity value is calculated. If similarity value is greater than a pre-specified threshold (y), then a list of recommendations are returned. Otherwise, for users who do not have a sufficient number of co-rated items, then zero value is returned. Finally, t1, t2, t3, and t4 are computed which are natural numbers and represent the number of co-rated items for each level (t1 ∈ N, t2∈N, t3∈N, t4∈N∧t4 > t3 > t2 > t1).

3. Proposed method

The collaborative filtering based algorithms for recommender systems predict the items for the users based on their experiences. In this section, we will explain our proposed system. Our primary concern is to design an efficient CF based recommender system with improved multi-level CF and similarity measure regarding the accuracy and efficiency. In our method initially, we applied FCM (Fuzzy c-mean) clustering approach [28,29]. FCM is the most widely used and efficient method for cluster formation for a given dataset. We provided a rating matrix (user X item) to FCM with appropriate dataset constants. FCM calculated the distance between users iteratively and produced cluster’s number for each user. We applied PCC using FCM clusters and get intermediate similarities of users. Then we implemented AAA (Artificial Algae Algorithm) optimization approach [24,25]. It takes input as rating matrix (user X item). In AAA initially, all algae are distributed randomly in different colonies and the appropriate colony is computed for algae. It was based on distances between two algae cell in three-dimension space. AAA provides colony’s numbers for all users who were used for co-rated items count. FCM’s result was assimilated with AAA colonies. The result of intermediate similarities was compared with previously calculated FCM’s similarity. After that, multi-level filters were applied to get the users similarities. We introduced similarity function to get co-rated items as in PCC, which is defined in Eq. (5).

Algorithm 1:

```
Input: User id ‘U1’ /*id for a user*/
       Item id /*all items ratings which are rated by user*/
       Cluster’s array /*using Fuzzy C-Mean*/
       Colony’s array /*Artificial Algae Algorithm*/
Output: Similarity Array for U1 from other users

Calculate Avg. Rating for U1
 for each User ‘U2’ from the user set
Initialization of variables numerator and denominator.
    if U1 and U2 are in the same cluster
       for each item i (int i=1;i<=total items;i++)
          if both U1 and U2 rated that item
             co-rated items incremented
             Calculate numerator and denominator of Eq. (1)
          end
       end
    end
    if numerator or denominator =0
       assign similarity of U1 and U2 is 0
    else
       assign similarity of U1 and U2 from Eq. (1)
    end

    if U1 and U2 are in the same colony
       for each item i (int i=1;i<=total items;i++)
          if both U1 and U2 rated that item
             co-rated items incremented
             Calculate numerator and denominator of Eq. (1)
          end
       end
    end
    if numerator or denominator =0
       Res=0 (similarity of U1 and U2)
    else
       Res= similarity of U1 and U2 from Eq. (1)
    end
    Recalculate similarity using Eq. (6)
   Use function is written in Eq. (5)
End
```

Fig. 1. Computation of user similarity.

$$Sim_{a,b}^{Proposed} = \begin{cases} Sim_{a,b}^{AAA} + x1, & \text{if} \frac{|Ia \cap Ib|}{T} \geq t1 \text{ and } Sim_{a,b}^{AAA} \geq y \\ Sim_{a,b}^{AAA} + x2, & \text{if} \frac{|Ia \cap Ib|}{T} < t1 \text{ and} \frac{|Ia \cap Ib|}{T} \geq t2 \text{ and } Sim_{a,b}^{AAA} \geq y \\ Sim_{a,b}^{AAA} + x3, & \text{if} \frac{|Ia \cap Ib|}{T} < t2 \text{ and} \frac{|Ia \cap Ib|}{T} \geq t3 \text{ and } Sim_{a,b}^{AAA} \geq y \\ Sim_{a,b}^{AAA} + x4, & \text{if} \frac{|Ia \cap Ib|}{T} < t3 \text{ and} \frac{|Ia \cap Ib|}{T} \geq t4 \text{ and } Sim_{a,b}^{AAA} \geq y \\ 0, & \text{if} \frac{|Ia \cap Ib|}{T} < t4 \end{cases} \tag{5}$$

In Eq. (5), $Sim_{a,b}^{AAA}$ denotes the similarity between user ‘a’ and user ‘b’ and ‘T’ stands for total co-rated items. The t1, t2, t3, and t4 are the predefined thresholds of co-rated items for user similarity $Sim_{a,b}^{AAA}$ in four levels. Here x1, x2, x3, x4 and y are positive real numbers such that x1∈R, x2∈R, x3∈R, x4∈R and y∈R . We took t1=50, t2=20, t3=10, t4=5 and x1=0.5, x2=0.375, x3=0.25, x4=0.125 and y=0.33 in which t1∈N, t2∈N, t3∈N, t4∈N∧t1 > t2 > t3 > t4. Eq. (5) checks the similarity given by AAA using ‘y’ and number of co-rated items. If co-rated items are less than particular level’s ‘t’, then shift to next lower level and so on until appropriate level is found. If $Sim_{a,b}^{AAA}$ is less than ‘y’ then Eq. (5)'s similarity is zero. The algorithms are systematically explained in Fig. 1 and Fig. 2, which represents user similarity computation and recommended items respectively. In Fig. 1, a detailed description of our approach is mentioned. The algorithm takes user id and item id for each previously rated items by the user as input. It also takes cluster’s array (created by FCM approach) and colony’s array formed by AAA method. Algorithm initiates with particular user U2 from total users, and iteratively covers all users. If our user and U2 belongs to same cluster number, then an iteration of all items starts and co-rated items are counted along with numerator and denominator value of Eq. (1). Moreover, if they do not belong then U2 is not considered for similarity

Algorithm 2.

Input: User id 'U1' /*id for a user*/
SA /*Similarity Array for U1 from other users from algorithm 1*/
K /*no. of similar neighbors of U1*/
Output: A set of recommended items for U1

```
Find k best similar neighbour of U1 using SA
for (int i=1;i<=total items;i++)
    for (int j=1;j<=k;j++)
        if U1 and kth user rating >0
            get the product of both user's ratings
            total =total+product
            count no. of products
        end
    end
    if the rating of U1 is not 0
        if product count is not 0
            rate this item as a round of total/product count
        else
            rate this item 0
        end
    else
            rate this item 0
    end
end
```

Fig. 2. Item recommendations to the user.

computations and similarity becomes zero and loop will go to next U2 user. By using Eq. (1), we calculated the $Sim_{a,b}^{FCM}$. Movielens 100k dataset has 943 users; we divided different users into 20 clusters. AAA picks a user at random and tries to allocate its best possible algae colony. It checks whether user U1 and user U2 belong to same colony number, then the iteration of all items starts and co-rated items are counted along with numerator and denominator value of Eq. (1). And if they do not belong then U2 is not considered for similarity computations and similarity 0 is given then loop goes to next user U2. After using Eq. (1), we calculated similarity. This procedure is repeated for every user and the main outer loop iterates twice the numbers of times of item count (i.e., 0.1682). A similar process was implemented with Movielens 1 M dataset, which has 6000 users. We distributed different users in 25 clusters. The process is repeated for each user and the main loop iterates twice the number of times of item count (i.e., 0.4000). Jester dataset has 59,132 users that we divided into 30 clusters for artificial algae algorithm processing. As AAA's is repeated for, each user and outer loop run 300 times (i.e. twice the times of the total item count). Above AAA's processing for Epinions dataset has also implemented, which has 49,290 users in total. Moreover, we allow a different user in 20 different clusters. Mainly it checks whether both selected users and user U2 belongs to the same cluster or not, according to that further computation takes place. Then algorithm examines the number of items in order to decide if it should iterate twice or not. In this stage, we use colony's array for calculation of $Sim_{a,b}^{AAA}$. Then we check the condition that if our user and U2 belongs to the same colony than we iterate all items, and co-rated items are counted, using Eq. (1), we calculate $Sim_{a,b}^{AAA}$. The similarity is given 0 if they did not belong to same colony and loop continues. After that, for taking advantage of both FCM and AAA approaches we calculate relative average of $Sim_{a,b}^{FCM}$ and $Sim_{a,b}^{AAA}$ using Eq. (6) and reassign it to $Sim_{a,b}^{AAA}$ written below.

$$Sim_{a,b}^{AAA} \Rightarrow \frac{(Sim_{a,b}^{FCM} \times \text{co-rated items in FCM}) + (Sim_{a,b}^{AAA} \times \text{co-rated items in AAA})}{Co-rated\ items\ in\ FCM + Co-rated\ items\ in\ AAA} \quad (6)$$

In the last stage, we use our Eq. (5) for more efficient similarities of user's. It uses the $Sim_{a,b}^{AAA}$ similarity and with the help of different level filters by co-rated item number and optimum similarity, it gives $Sim_{a,b}^{Proposed}$. That is our desired similarities for items recommendations.

In AAA initially, all algae (users) are distributed randomly in different colonies (clusters) and computes the final or appropriate colony for algae, which is based on distances between two algae cell in three-dimension space. It provides the colony's numbers for all users who were used in counting the co-rated items. AAA with FCM (Fuzzy c-mean) provides clusters of users, which have similarities. So, AAA is used in a generalized way for all the datasets for clustering purpose with the utilization of FCM.

Figs. 1 and 2 elaborates the steps involved in item recommendation to the user. It takes input of user id,$Sim_{a,b}^{Proposed}$ and a number of similar neighbors 'k.' Initially, we find k best similar neighbor for a particular user and then iterates all items one by one. Then we initialize the loop for each similar neighbor and compute the summation of multiplication result of item rating given by k user and initial user. After that, we check the condition of ratings of initial user, total count and if condition satisfied then we calculate a rating for a particular item for our user. Moreover, if the condition fails, then the rating is zero. Finally, we recommend totally best-rated items to a particular user which is our desired goal.

Fig. 3 shows flow chart representation of our proposed approach. It initiates with a user U we choose to provide item recommendation to it. If users belong to the same clusters, then the similarity is calculated with co-rated items. According to membership, similarities are assigned and then using similarity, we can find similar users. Then items

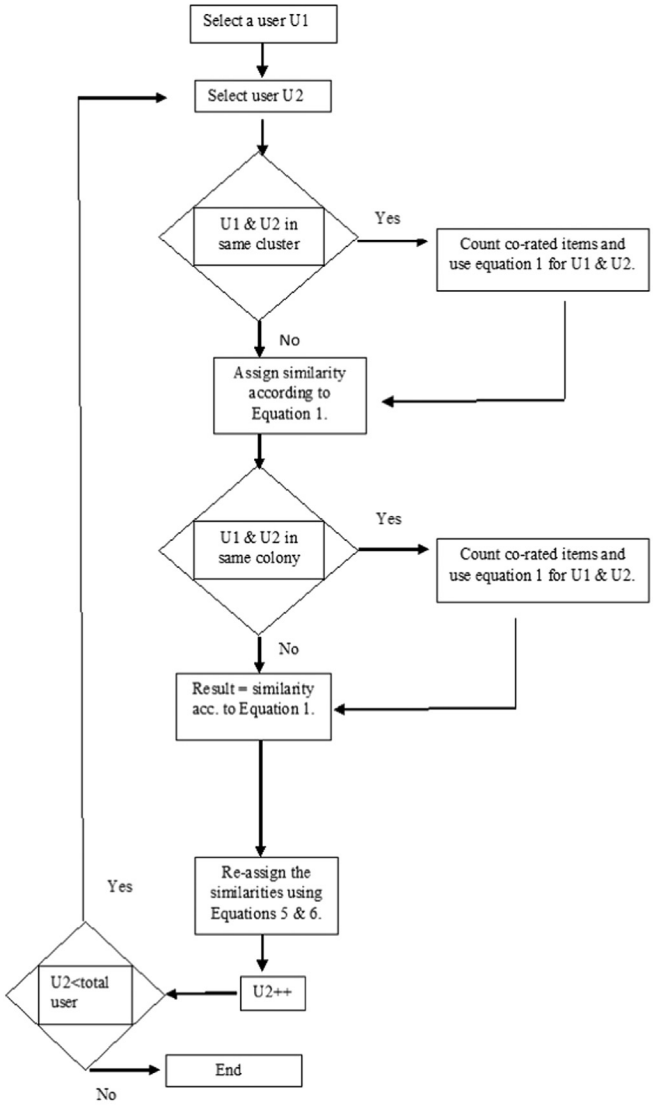

Fig. 3. Flow chart of proposed recommender system.

are recommended using similar users.

4. Experiments and results

In this section, we conducted a set of experiments to examine the effectiveness of our new proposed system in collaborative filtering environment. The results are based on four authentic datasets and some widely used metrics with different parameters. The experimentation took place on a system with a configuration of Intel i5 2.7 GHz, 4 GB RAM, Windows 10 and all the algorithms were implemented in the C++ programming language and results are visualized using MS Excel.

4.1. Datasets

In this research article, four real datasets are used to observe the results under different parameters such as a number of users and items. The four datasets are the MovieLens 100,000, MovieLens 1 million, Jester dataset and Epinions.

- **MovieLens 100,000**: MovieLens 100,000 is a real dataset, which contains 1682 movies, 943 users and 100,000 ratings. The data was composed through the MovieLens website (movielens.umn.edu) during the seven-month period from September 19th, 1997 through April 22, 1998, and is publicly available for experimental evaluation. All ratings are in the range of 1–5.
- **MovieLens 1 million**: These files contain 1,000,209 anonymous ratings of approximately 3900 movies made by 6040 MovieLens users who joined MovieLens in 2000. All the ratings are made on a 5-star scale 1–5). Each user has at least 20 ratings. There are four features available in this dataset such as [UserID], [MovieID], [Rating] and [Timestamp].
- **Jester**: This is a publicly available dataset developed at the University of California, Berkeley and has over 1.7 million ratings of 150 jokes from 59,132 users. The data from the dataset are associated to their online joke recommendation system. Like the two previous datasets, this one has been used widely for logged off experimental evaluation of collaborative filtering recommender systems and the data in each row is formatted as [userid] [itemid] [rating]. All the ratings are continuous in the range of −10 to 10.
- **Epinion**: This dataset was crawled from Epinions.com and it is freely available for download. The data in the dataset are in the form [userid] [itemid] [rating]. All the rating values are on the scale 1–5. The dataset has 664,824 ratings from 49,290 users on 139,738 items.

4.2. Comparisons

We have utilized the following collaborative filtering recommendation methods in the comparisons.

•**PCC**: This method is used to calculate the statistical correlation between the mundane ratings of two users to determine the closest attribute between them. The output will give a value between +1 and −1 inclusive, where 1 is a total positive correlation, 0 is no correlation, and −1 is a total negative correlation.

•**WPCC:** This is a method based on PCC. The difference is that the algorithm considers a pre-defined number of prevalent ratings between users. Moreover, if the number of prevalent ratings is not sufficient, then it switches to classical PCC.

•**SPCC**: This is modified similarity method which is based on PCC and sigmoid function. SPCC is effective to commonly rated items.

•**Multi-level CF**: This method is predicated on multiple levels, from top-to-bottom, with each of these qualities having a number of constraints. The constraints provide a higher corresponding attribute value between users that have items that are more prevalent and a PCC similarity value above a certain threshold.

The methods mentioned above have been compared against our proposed method. Our proposed method uses Fuzzy c-means (FCM) to cluster the user. Fuzzy c-means (FCM) is a data clustering procedure in which a dataset is gathered into n clusters with the individual data point in the dataset fitting to every cluster to a certain degree. We used the artificial algae algorithm (AAA) which is Bio-inspired optimization algorithm. The algorithm is based on evolutionary process, adaptation process and the movement of microalgae. AAA with FCM produced abundant and balanced results over different datasets.

4.3. Measures

To measure the accurateness of the recommendations provided by the above-said methods, we used the widely accepted mean absolute error (MAE) metric. MAE is defined in the Eq. (7).

$$MAE = \frac{1}{n}\sum_{i=1}^{n}|pi - ri| \tag{7}$$

where pi represents the predicted rating and ri is the actual rating. This method is used for the computation of the deviation between the predicted ratings and the actual ratings. It should also be noted that lower values are better for results. In information retrieval systems, such as recommender systems, some metrics can measure the quality of the top-N recommendations. These metrics are precision and recall. For these metrics, higher values are better. Precision metric, which is the amount of relevant recommendations found in the retrieved set of recommendations, is defined below in Eq. (8).

$$precision = \frac{\text{correctly recommended items}}{\text{total recommended items}} \tag{8}$$

Moreover, recall is the amount of relevant recommendations that have been retrieved successfully is defined in Eq. (9).

$$recall = \frac{\text{correctly recommended items}}{\text{relavent items}} \tag{9}$$

4.4. Results and discussion

Given below are the experimental results obtained for different datasets under varying parameters. In the results, k represents the number of nearest neighbors.

The MAE results for the MovieLens 100 k dataset are shown in Fig. 4. It is observed that when k is small, up to 16 neighbors, our proposed method outperforms all the other recommendation methods. When the number of neighbors is getting higher, i.e., 32 or more, we can see that our proposed method performs decently. On an average, our proposed method performed 21% better.

The MAE results for the MovieLens 1 million dataset are shown in Fig. 5. It is observed that our proposed method outperforms the other methods. We can see that the larger the neighborhood grows the results

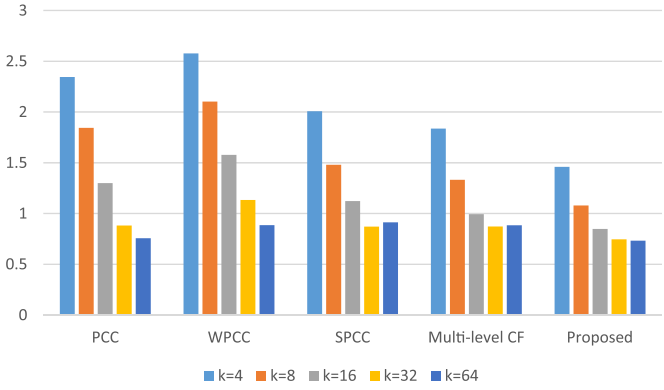

Fig. 4. Presentation of MAE for MovieLens 100,000.

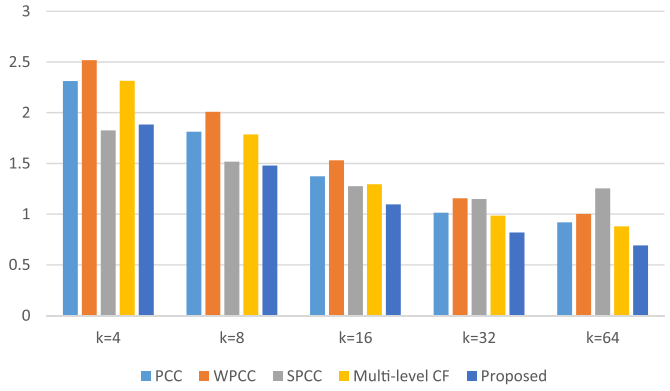

Fig. 5. Presentation of MAE for MovieLens 1 Million.

become better for all methods. Our method performs 17.6% better on an average.

The MAE results for the Jester dataset are shown in Fig. 6. The results of our proposed method are better than existing methods, specially when k is lower, i.e. less than 32. However, when k becomes large, i.e. 32 or greater, then SPCC performs better. However, still, on average our approach performed 19.2% better.

The MAE results for the Epinions dataset are shown in Fig. 7. Here also our method performed well when k is less than or equal to 32. Unfortunately, when k becomes large, our proposed method does not perform well. On average SPCC performed 7.3% better than our proposed approach.

In Fig. 8, we can see the results obtained by using the precision metric. Our proposed approach gives better result in the case of MovieLens 1 million datasets. Also on an average, our approach performed 3.4% better results.

In Fig. 9, we can see the results obtained by using the Recall metric. Our proposed approach gives better result in the case of Jester dataset. Also on an average, our approach performed 1.5% better results. We have presented a novel recommender system with the utilization of AAA and FCM. All four datasets have numbers of attributes such as user ID, item ID, rating, and timestamp. The attributes of MovieLens 100k dataset are user id, item id, rating, and timestamp and we identified k-nearest neighbors for each user and employed PCC (Pearson Correlation Coefficient) to compare two users. We computed mean absolute error, precision, recall for every dataset, and experimentally demonstrated that our proposed system performed well as compared to existing systems.

In Fig. 10 and Fig. 11, the comparison of our proposed system with other already existing systems has been demonstrated by means absolute error and speed. The four different dataset behaved differently for different systems. K-means [53,54] is most popular data clustering technique which was applied on all four datasets and showed satisfactorily response with PCA-Kmeans, PCA-GAKM, GAKM-cluster, and KM-PSO-FCM. But proposed system performed well in such a way that for the Movielens100k and Movielens1M dataset's MAE was less than 1. Some others systems such as SOM, UPCC, and PCA-SOM also performed lower than proposed system. The MAE for K-means was 0.66, and when a system with PCA and K-means was evaluated on Movielens 100k, then MAE was 0.67 for the PCA-Kmeans. For the SOM, UPCC, and PCA-SOM the MAE was 0.79, 0.82 and 1.3 respectively. A genetic algorithm has also shown an effective response in recommender systems. MAE for PCA-GAKM and GA-KM was 0.92 and 0.78 respectively. Particle swarm optimization with K-mean and FCM resulted into the 0.76 MAE. But our proposed recommender system delivered the MAE as 0.73.

Our approach, on average has performed better as compared to other existing methods. We have increased efficiency and accuracy when it comes to recommending items to various users. The results are better by a great factor, and it reflects in all the three metrics namely

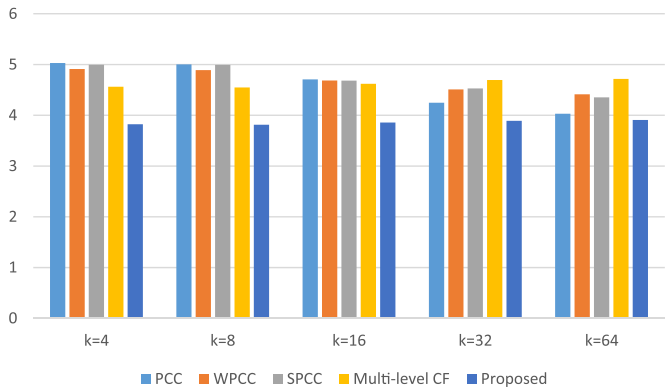

Fig. 6. Presentation of MAE for Jester dataset.

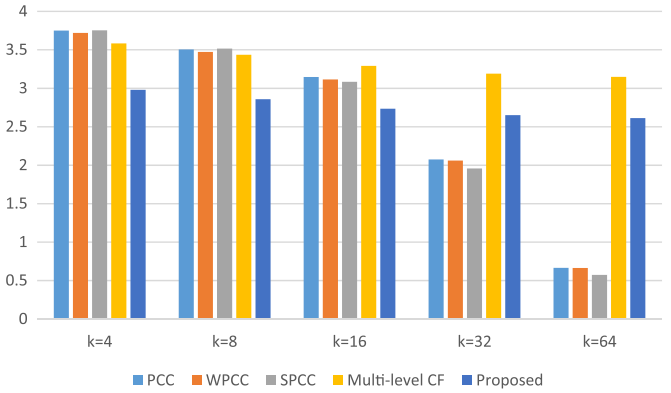

Fig. 7. Presentation of MAE for Epinions dataset.

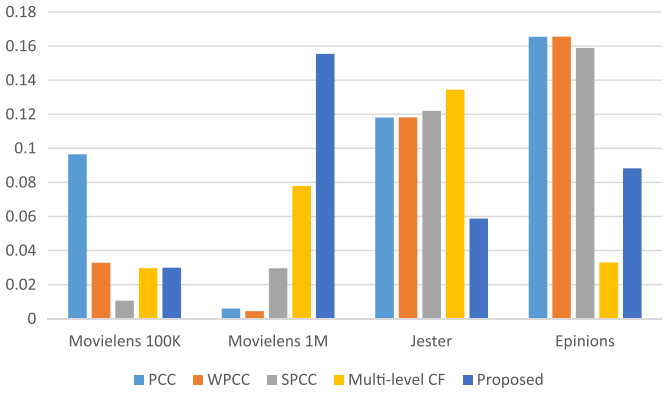

Fig. 8. Presentation of precision for four datasets.

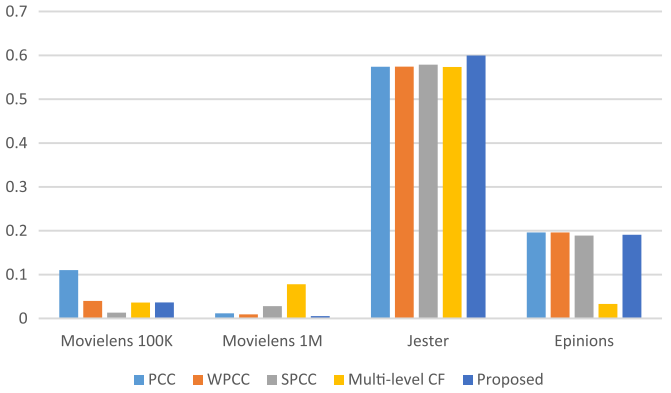

Fig. 9. Presentation of recall for four datasets.

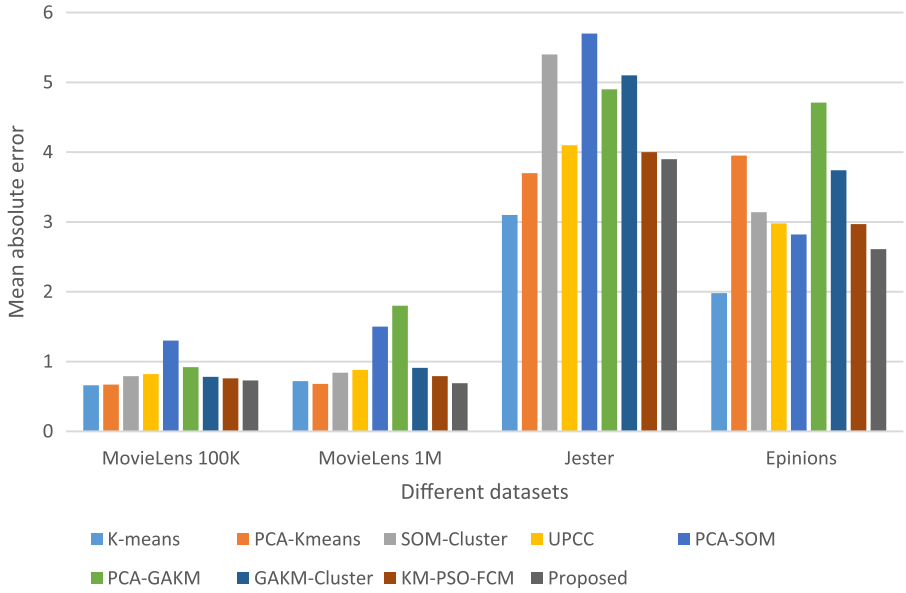

Fig. 10. Comparison of mean absolute error (MAE) for different systems.

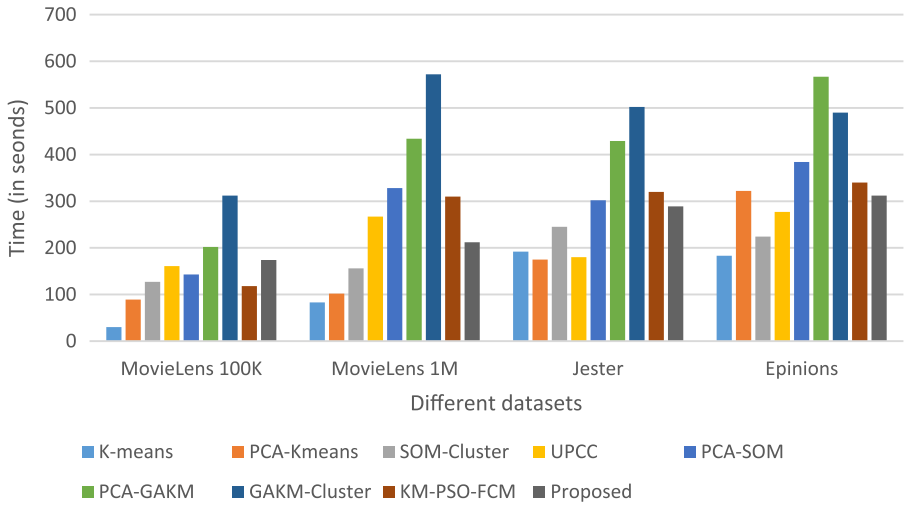

Fig. 11. Comparison of speed of different systems.

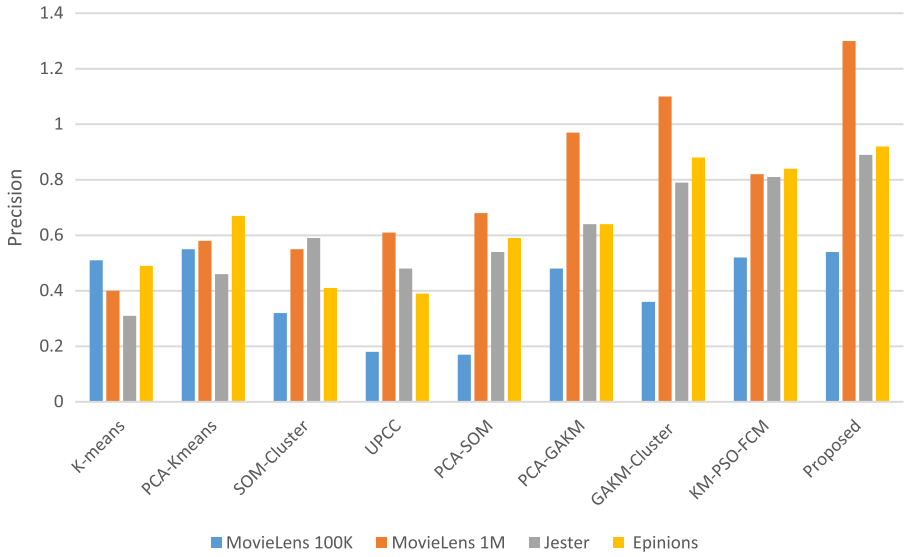

Fig. 12. Comparison of precision for different systems.

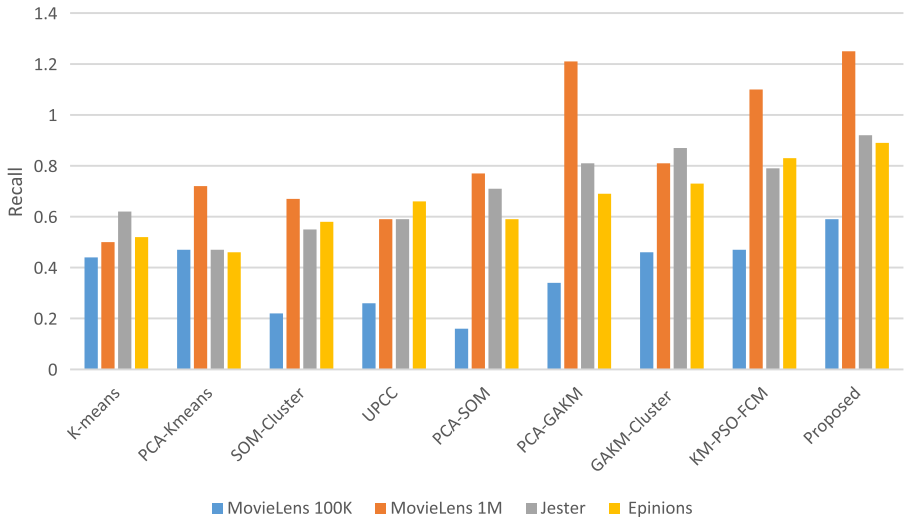

Fig. 13. Comparison of recall for different systems.

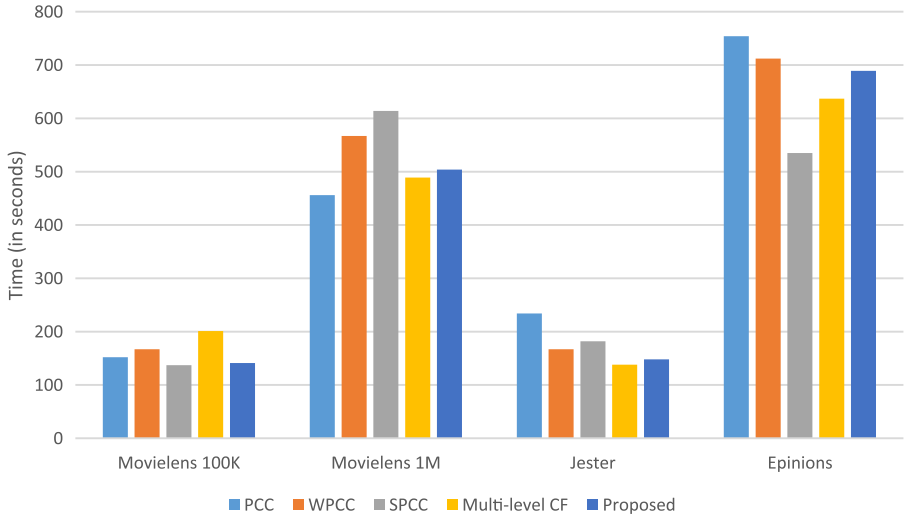

Fig. 14. Comparison of performance of different systems with time.

MAE, Precision, and Recall. First, let us take notice at the MAE metric. In MovieLens 100k dataset, it is observed that when k is small, up to 16 users, our proposed method outperforms all the other recommendation methods. When the number of neighbors is getting higher, i.e., 32 or more, we can see that our proposed method shows satisfactory outcomes. On an average, our proposed method performed 21% better. In the case of 1 million datasets, we observed that our proposed method outperforms the other methods. However, here it is visible that the larger the neighborhood grows, the better the results become for all methods. Our method performs 17.6% better on an average in this dataset. For Jester dataset, a trend is observed that our proposed method performed better than the other methods when k is lower, i.e. less than 32. However, when k becomes large, i.e. 32 or greater SPCC performs better. However, still, on average our approach performed 19.2% better. Moreover, at last, for the Epinions dataset also, our method performed well when k is less than or equal to 32. When k becomes large, our proposed method showed an acceptable response. On average SPCC performed 7.3% better than our proposed approach. However, if we consider the average MAE for all the datasets used, we can state that our proposed method performed better than rest of the procedures. Now we consider the precision metric. For MovieLens 100k, our approach showed a better result than SPCC and multi-level CF approach. For MovieLens 1 M, our approach came out to be best of them all and showed a better result than all the approaches. For Epinions also, our approach showed the better result as compared to multi-level CF approach. However, for Jester dataset, it did not perform well. On an average, our approach showed 3.4% had a better result for precision metric. The third and last metric we used to compare the different methods is the recall metric. By using MovieLens 100k dataset, our approach showed a better result than SPCC and multi-level CF. Using Jester dataset, our method performed phenomenally, and the result is better than all the rest procedures. For Epinions dataset, our approach's result is better than SPCC and multi-level CF and almost comparable to PCC and WPCC. For MovieLens 1 M dataset, our method performs satisfactorily. However, still, on an average, our method performs 1.5% better result than other methods for Recall metric.

In Figs. 12–13, the performance of various systems is compared by taking two evaluation metrics such as precision and recall. We have also compared the performance with respect to time in Fig. 14.

5. Conclusion and future work

In this research article, we presented a novel recommender system, which was based on the artificial algae algorithm and fuzzy c-mean clustering algorithm with new similarity method. The performance of proposed recommender system was compared with already existing systems such as K-means, PCA-Kmeans, SOM, UPCC, PCA-SOM, PCA-

GAKM, GAKM and KM-PSO-FCM. We employed four real datasets such as MovieLens 100 K, MovieLens 1 M, Jester, and Epinions. The performance was evaluated on precision, recall, mean absolute error with time. Therefore, we can conclude that our proposed recommender system performed efficiently as compared with already existing systems. Also, we can say that we improved the multi-level CF approach by a huge factor and proposed system's recommendations are more accurate than other recommended systems. The next challenge of our proposed recommender system is to use context, sentiments and social-based features with big data for recommendations. Data with typical attributes such as locations, trust, tag, and emotions can enhance the quality of the proposed recommender system.

References

[1] R. Katarya, O.P. Verma, A collaborative recommender system enhanced with particle swarm optimization technique, Multimed. Tools Appl. 75 (2016) 1–15. http://dx.doi.org/10.1007/s11042-016-3481-4.
[2] B. Barragáns-Martínez, E. Costa-Montenegro, J. Juncal-Martínez, Developing a recommender system in a consumer electronic device, Expert Syst. Appl. 42 (2015) 4216–4228. http://dx.doi.org/10.1016/j.eswa.2015.01.052.
[3] J. Beel, B. Gipp, S. Langer, C. Breitinger, Research-paper recommender systems: a literature survey, Int. J. Digit. Libr. (2015). http://dx.doi.org/10.1007/s00799-015-0156-0.
[4] L. Chen, G. Chen, F. Wang, Recommender systems based on user reviews: the state of the art, Use. Model. Use.-Adapt. Interact. 25 (2015) 99–154. http://dx.doi.org/10.1007/s11257-015-9155-5.
[5] J. Bobadilla, F. Ortega, A. Hernando, A. Gutiérrez, Recommender systems survey, Knowl.-Based Syst. 46 (2013) 109–132. http://dx.doi.org/10.1016/j.knosys.2013.03.012.
[6] R. Katarya, O.P. Verma, Recent developments in affective recommender systems, Phys. A Stat. Mech. Appl. 461 (2016) 182–190. http://dx.doi.org/10.1016/j.physa.2016.05.046.
[7] R. Katarya, O.P. Verma, Restaurant Recommender System Based on Psychographic and Demographic Factors in Mobile Environment, in: Proceedings of the IEEE International Conference Green Computing and of Internet Things 2015, 2015, pp. 907–912.
[8] R. Katarya, I. Jain, H. Hasija, An interactive interface for instilling trust and providing diverse recommendations, in: Proceedings of the IEEE International Conference Computer Communication Technology ICCCT-2014: 2014, pp. 17–22.
[9] R. Katarya, O.P. Verma, I. Jain, User behaviour analysis in context-aware recommender system using hybrid filtering approach, in: Proceedings of the IEEE International Conference on Computer Communication Technology ICCCT 2013, 2013, pp. 222–227. http://dx.doi.org/10.1109/ICCCT.2013.6749631.
[10] R. Katarya, O.P. Verma, An effective web page recommender system with fuzzy c-mean clustering, Multimed. Tools Appl. (2016). http://dx.doi.org/10.1007/s11042-016-4078-7.
[11] R. Katarya, O.P. Verma, An effective collaborative movie recommender system with cuckoo search, Egypt. Inform. J. (2016). http://dx.doi.org/10.1016/j.eij.2016.10.002.
[12] R. Katarya, O.P. Verma, Recommender system with grey wolf optimizer and FCM, Neural Comput. Appl. (2016). http://dx.doi.org/10.1007/s00521-016-2817-3.
[13] R. Katarya, O.P. Verma, Efficient music recommender system using context graph and particle swarm, Multimed. Tools Appl. (2017). http://dx.doi.org/10.1007/s11042-017-4447-x.
[14] B. Van Der Heide, B.K. Johnson, M.H. Vang, The effects of product photographs and reputation systems on consumer behavior and product cost on eBay, Comput. Human. Behav. 29 (2013) 570–576. http://dx.doi.org/10.1016/j.chb.2012.11.002.
[15] N. Walia, F.M. Zahedi, Success strategies and web elements in online marketplaces: a moderated-mediation analysis of seller types on ebay, IEEE Trans. Eng. Manag 60 (2013) 763–776. http://dx.doi.org/10.1109/TEM.2013.2272194.
[16] D. van Heijst, R. Potharst, M. van Wezel, A support system for predicting eBay end prices, Decis. Support Syst. 44 (2008) 970–982. http://dx.doi.org/10.1016/j.dss.2007.11.004.
[17] C.A. Gomez-uribe, N. Hunt, The netflix recommender system: algorithms, business value, and innovation, ACM Trans. Manag. Inf. Syst. 6 (2015). http://dx.doi.org/10.1145/2843948.
[18] J.A. Villarroel, J.E. Taylor, C.L. Tucci, Innovation and learning performance implications of free revealing and knowledge brokering in competing communities: insights from the Netflix Prize challenge, Comput. Math. Organ. Theory 19 (2013) 42–77. http://dx.doi.org/10.1007/s10588-012-9137-7.
[19] C. Koçaş, C. Akkan, A system for pricing the sales distribution from blockbusters to the long tail, Decis. Support Syst. 89 (2016) 56–65. http://dx.doi.org/10.1016/j.dss.2016.06.008.
[20] G. Linden, B. Smith, J. York, Amazon.com recommendations: item-to-item collaborative filtering, IEEE Internet Comput. 7 (2003) 76–80. http://dx.doi.org/10.1109/MIC.2003.1167344.
[21] A.A. Kardan, M. Ebrahimi, A novel approach to hybrid recommendation systems based on association rules mining for content recommendation in asynchronous discussion groups, Inf. Sci. 219 (2013) 93–110. http://dx.doi.org/10.1016/j.ins.2012.07.011.
[22] L.O. Colombo-Mendoza, R. Valencia-García, A. Rodríguez-González, G. Alor-Hernández, J.J. Samper-Zapater, RecomMetz: a context-aware knowledge-based mobile recommender system for movie showtimes, Expert Syst. Appl. (2014). http://dx.doi.org/10.1016/j.eswa.2014.09.016.
[23] C. Yu, L. Huang, CluCF: a clustering CF algorithm to address data sparsity problem, Serv. Oriented Comput. Appl. (2016) 1–13. http://dx.doi.org/10.1007/s11761-016-0191-8.
[24] S.A. Uymaz, G. Tezel, E. Yel, Artificial algae algorithm with multi-light source for numerical optimization and applications, Biosystems 138 (2015) 25–38. http://dx.doi.org/10.1016/j.asoc.2015.03.003.
[25] S.A. Uymaz, G. Tezel, E. Yel, Artificial algae algorithm (AAA) for nonlinear global optimization, Appl. Soft Comput. J. 31 (2015) 153–171. http://dx.doi.org/10.1016/j.asoc.2015.03.003.
[26] X. Zhang, C. Wu, J. Li, X. Wang, Z. Yang, J.-M. Lee, et al., Binary artificial algae algorithm for multidimensional knapsack problems, Appl. Soft Comput. 43 (2016) 583–595. http://dx.doi.org/10.1016/j.asoc.2016.02.027.
[27] R.J. Hathaway, J.C. Bezdek, Fuzzy c-means clustering of incomplete data, IEEE Trans. Syst. Man. Cybern. B. Cybern. 31 (2001) 735–744. http://dx.doi.org/10.1109/3477.956035.
[28] T.C. Havens, J.C. Bezdek, C. Leckie, L.O. Hall, M. Palaniswami, Fuzzy c-Means algorithms for very large data, IEEE Trans. Fuzzy Syst. 20 (2012) 1130–1146. http://dx.doi.org/10.1109/TFUZZ.2012.2201485.
[29] J.C. Bezdek, R. Ehrlich, W. Full, FCM: the fuzzy c-means clustering algorithm, Comput. Geosci. 10 (1984) 191–203. http://dx.doi.org/10.1016/0098-3004(84)90020-7.
[30] Z. Wang, X. Yu, N. Feng, Z. Wang, An improved collaborative movie recommendation system using computational intelligence, J. Vis. Lang. Comput. 25 (2014) 667–675. http://dx.doi.org/10.1016/j.jvlc.2014.09.011.
[31] C.-L. Liu, X.-W. Wu, Large-scale recommender system with compact latent factor model, Expert Syst. Appl. 64 (2016) 467–475. http://dx.doi.org/10.1016/j.eswa.2016.08.009.
[32] W. Wang, G. Zhang, J. Lu, Member contribution-based group recommender system, Decis. Support Syst. (2016). http://dx.doi.org/10.1016/j.dss.2016.05.002.
[33] W. Zhou, J. Wen, Q. Xiong, M. Gao, J. Zeng, SVM-TIA a shilling attack detection method based on SVM and target item analysis in recommender systems, Neurocomputing (2016) 1–9. http://dx.doi.org/10.1016/j.neucom.2015.12.137.
[34] R. Saia, L. Boratto, S. Carta, A semantic approach to remove incoherent items from a user profile and improve the accuracy of a recommender system, J. Intell. Inf. Syst. (2016) 1–24. http://dx.doi.org/10.1007/s10844-016-0406-7.
[35] H.-R. Zhang, F. Min, Three-way recommender systems based on random forests, Knowl.-Based Syst. 91 (2016) 275–286. http://dx.doi.org/10.1016/j.knosys.2015.06.019.
[36] J. Capdevila, M. Arias, A. Arratia, GeoSRS: a hybrid social recommender system for geolocated data, Inf. Syst. 57 (2016) 111–128. http://dx.doi.org/10.1016/j.is.2015.10.003.
[37] G. Lv, C. Hu, S. Chen, Research on recommender system based on ontology and genetic algorithm, Neurocomputing 187 (2016) 92–97. http://dx.doi.org/10.1016/j.neucom.2015.09.113.
[38] E.Q. Da Silva, C.G. Camilo-Junior, L.M.L. Pascoal, T.C. Rosa, An evolutionary approach for combining results of recommender systems techniques based on collaborative filtering, Expert Syst. Appl. 53 (2016) 204–218. http://dx.doi.org/10.1016/j.eswa.2015.12.050.
[39] S. Guo, F. Alamudun, T. Hammond, RésuMatcher: a personalized résumé-job matching system, Expert Syst. Appl. 60 (2016) 169–182. http://dx.doi.org/10.1016/j.eswa.2016.04.013.
[40] T. Yuan, J. Cheng, X. Zhang, Q. Liu, H. Lu, Enriching one-class collaborative filtering with content information from social media, Multimed. Syst. 22 (2016) 51–62. http://dx.doi.org/10.1007/s00530-014-0392-y.
[41] F. Ortega, A. Hernando, J. Bobadilla, J.H. Kang, Recommending items to group of users using matrix factorization based collaborative filtering, Inf. Sci. 345 (2016) 313–324. http://dx.doi.org/10.1016/j.ins.2016.01.083.
[42] M. Nasiri, B. Minaei, Increasing prediction accuracy in collaborative filtering with initialized factor matrices, J. Supercomput. 72 (2016) 2157–2169. http://dx.doi.org/10.1007/s11227-016-1717-8.
[43] A. Shahmohammadi, E. Khadangi, A. Bagheri, Presenting new collaborative link prediction methods for activity recommendation in Facebook, Neurocomputing (2016) 1–10. http://dx.doi.org/10.1016/j.neucom.2016.06.024.
[44] Y. Carmel, B. Patt-Shamir, Comparison-based interactive collaborative filtering, Theor. Comput. Sci. 1 (2016) 1–10. http://dx.doi.org/10.1016/j.tcs.2016.03.010.
[45] N. Pappas, A. Popescu-Belis, Adaptive sentiment-aware one-class collaborative filtering, Expert Syst. Appl. 43 (2015) 23–41. http://dx.doi.org/10.1016/j.eswa.2015.08.035.
[46] H. Izakian, W. Pedrycz, I. Jamal, Clustering spatiotemporal data: an augmented fuzzy C-means, IEEE Trans. Fuzzy Syst. 21 (2013) 855–868. http://dx.doi.org/10.1109/TFUZZ.2012.2233479.
[47] H. Koohi, K. Kiani, User based collaborative filtering using fuzzy C-means, Measurement (2016). http://dx.doi.org/10.1016/j.measurement.2016.05.058.
[48] K. Treerattanapitak, C. Jaruskulchai, Exponential fuzzy C-means for collaborative filtering, J. Comput. Sci. Technol. 27 (2012) 567–576. http://dx.doi.org/10.1007/s11390-012-1244-x.
[49] C. Birtolo, D. Ronca, Advances in clustering collaborative filtering by means of fuzzy C-means and trust, Expert Syst. Appl. 40 (2013) 6997–7009. http://dx.doi.org/10.1016/j.eswa.2013.06.022.
[50] J. Herlocker, J. Konstan, An algorithmic framework for performing collaborative filtering, in: SIGIR '99 Proceedings of 22nd Annual International ACM SIGIR Conference on Research Development in Information Retrieval, 1999: pp. 8.

http://dx.doi.org/10.1145/312624.312682.

[51] M. Jamali, M. Ester, TrustWalker: a random walk model for combining trust-based and item-based recommendation, in: Proceedings of the 15th ACM SIGKDD International Conference on Knowledge Discovery and Data Mining, 2009, pp. 397–406. doi:citeulike-article-id:5151320.

[52] N. Polatidis, C.K. Georgiadis, A multi-level collaborative filtering method that improves recommendations, Expert Syst. Appl. 48 (2015) 100–110. http://dx.doi.org/10.1016/j.eswa.2015.11.023.

[53] T. Kanungo, D.M. Mount, N.S. Netanyahu, C.D. Piatko, R. Silverman, a.Y. Wu, An efficient k-means clustering algorithm: analysis and implementation, IEEE Trans. Pattern Anal. Mach. Intell. 24 (2002) 881–892. http://dx.doi.org/10.1109/TPAMI.2002.1017616.

[54] J.A. Hartigan, M.A. Wong, A K-means clustering algorithm, J. R. Stat. Soc. 28 (1979) 100–108.

Arab J Sci Eng
DOI 10.1007/s13369-017-2500-8

RESEARCH ARTICLE - COMPUTER ENGINEERING AND COMPUTER SCIENCE

Electronically Tunable Fractional Order Filter

Rakesh Verma[1] · **Neeta Pandey**[1] · **Rajeshwari Pandey**[1]

Received: 31 August 2016 / Accepted: 9 March 2017

Abstract In this paper, an electronically tunable resistorless fractional order filter (FOF) based on operational transconductance amplifier (OTA) is presented. It uses two fractional capacitors (FC) of same order and provides fractional order low-pass filter and fractional order band-pass filter responses simultaneously. Mathematical formulations are outlined for various critical frequencies and transfer function sensitivities for presented FOF. The FCs of orders 0.5 and 0.9 are considered for illustrating the proposal. The FCs are realized using the fourth-order continued fraction expansion-based RC ladder and are characterized using SPICE simulations. Functional verification of presented FOF with FC of orders 0.5 and 0.9 is exhibited through SPICE simulations. The OTA is implemented using 0.5 μm CMOS technology model parameters. Electronic tunability of half power and right-phase frequencies of presented FOF is achieved through bias current variation of OTA. The transfer functions' sensitivity with respect to various circuit parameters is also examined through simulations, and it is found that the values remain well within unity for most of the circuit parameters. Furthermore, the presented FOF is attractive from integration viewpoint as it achieves tunability via bias current variation in contrast to tuning through resistor variation in existing FOFs.

Keywords Fractional order · Fractance · Filter · OTA

1 Introduction

The processes in nature and real objects can be modeled more precisely by using fractional calculus than classical integer-order methods [1–3]. The voltage–current relation in a semi-infinite transmission line [1], flow of fluid in a porous media and conduction of heat in a semi-infinite slab [2] are some of the illustrations where the governing equations can be modeled more accurately by fractional order differential or integral operators. Similarly, the charging and discharging of lossy capacitors inherently follow fractional order dynamics [4]. This has attracted the focus of researchers and designers toward development and design of fractional order system applications relating to control systems [3,5–7], biomedical instrumentation [8,9] and signal processing [4,10]. Embedding the concept of fractional order systems into analog signal processing has resulted in the emergence of FOF as is evident from the recent literature [11–38] and references cited therein.

An extensive literature review suggests that the available FOFs have been implemented either using all passive components [11,13,14,23] or are designed around active elements along with passive components [15–22,24–31, 33,34,36,37]. Later class of FOFs either makes use of FCs [12,15–22,24,25,33,34,36,37] to achieve FO behavior or employ an appropriate integer-order function to approximate FO transfer function and then obtain a functional block diagram (FBD) [26–31]. It is further observed that active FOFs based on FCs have been designed using Op-Amp [12,15–17,19,20,24,25,33,34,36,37] and second-generation current conveyor (CCII) [18,21,22,25]. These FOF topologies are derived from conventional integer-order filters such as Sallen–Key [15–17], Tow–Thomas (TT) [19–21] and Kerwin–Huelsman–Newcomb (KHN) [15–17,21, 22,33,34] biquads, respectively. Multiple-amplifier biquad

✉ Neeta Pandey
n66pandey@rediffmail.com

[1] Department of Electronics and Communication Engineering, Delhi Technological University Delhi, Delhi, India

Published online: 05 April 2017

(MAB) [25], generalized impedance converter (GIC) [12,25, 36,37] and frequency-dependent negative resistor (FDNR) [25] based FOF realizations have also been presented. These FOFs along with their various features are comprehended in Table 1.

Following are the observations based on Table 1:

- All FOFs use resistors.
- Refs. [12,20,24,25,36,37] use both capacitors and FCs to obtain desired functionality whereas [15–19,21,22,33, 34] employ only FCs.
- The FOF filter performance is compared with integer-order filter in [15,18,20,34,36] whereas [12,16,17,19, 21,22,24,25,33,37] have not presented the same.
- Sensitivity analysis is presented in [18,33,36,37] while [12,15–17,19–22,24,25,34] did not address this.
- Stability analysis is given for available FOFs except [12].
- In existing literature, electronic tunability of FOF parameters is not available.

The above review suggests that a limited number of FOFs are available which use either op-amp (voltage mode) or CCII (current mode) active blocks. It is well known that signal processing in current mode offers advantages like wider bandwidth, higher slew rate and lower power consumption and gives simpler architecture due to ease in addition/subtraction of current signals. A comprehensive review of current mode active blocks is available in [39]. The OTA is one among those active blocks which has been used widely for developing signal processing [40–43] and generating [43–47] applications. The OTA-based applications are generally designed using transconductance-C method which is much suited for integrated applications as it consumes lesser silicon area. This also enables electronic tuning of various parameters of the designed applications.

Considering the advantages of OTA, importance of FOF and observing from Table 1 that existing FOFs do not provide electronic tuning; the authors aim at presenting an OTA-based FOF which provides electronically tunable FLPF and FBPF responses simultaneously. The remaining paper is organized as follows: The basics of fractional order element and FOF design equations are placed in Sect. 2. The OTA-based FOF (with generic fractional order α) and mathematical formulation of its various critical frequencies are presented in Sect. 3. This section also includes transfer functions' sensitivity with respect to order of FC, passive components and active parameters used. The proposal is verified by designing FOF using FCs of order 0.5 and 0.9. Functional verification of the proposed FOF through SPICE simulation is put forward in Sect. 4. Conclusions are drawn in Sect. 5.

2 Preliminaries

In this section, basic terminology related to FOF is briefly described. Generic description of fractance element is presented first followed by design equations and various critical frequencies.

2.1 Fractional Order Element

In fractional order analog circuit design, a fundamental fractional order element (FOE) is employed. The FOE is also termed as fractance element and is denoted as F. The impedance of F can be expressed as $Z(s) = \text{as}^{\alpha}$ [12] where α represents the fractional order of the fractance. The fractance element with $0 < \alpha < 1$ represents fractional inductor (FI) and $-1 < \alpha < 0$ corresponds to fractional capacitor (FC). For specific value of α as $-1/\ 0/1$, the fractance turns into classical element capacitor/resistor/inductor, respectively, whereas $\alpha = -2$ corresponds to frequency-dependent negative resistance (FDNR). The phase angle for an ideal fractance element is constant and is independent of operating frequency; therefore, it is also termed as constant phase element. It however depends on fractional order.The use of FOE increases the range of responses that can be obtained from a system, from narrow integer subset to more general fractional domain. The fractance element is not commercially available though its behavior can be simulated by finding an appropriate rational approximation [48] of its impedance function.

2.2 Design Equations of FOF and Critical Frequencies

The generic FOF transfer function using two FCs of different orders, represented by α and β, respectively, can be expressed as

$$T(s) = \frac{N(s)}{D(s)} = \frac{b_2 s^{(\alpha+\beta)} + b_1 s^{\alpha} + b_0}{s^{(\alpha+\beta)} + a_1 s^{\alpha} + a_0} \tag{1}$$

where coefficients b_0, b_1, b_2, a_0, a_1 are the constant terms. Various FO responses may be obtained if coefficients are selected according to scheme given in Table 2.

Considering $\alpha = \beta$, (1) modifies to

$$T(s) = \frac{N(s)}{D(s)} = \frac{b_2 s^{2\alpha} + b_1 s^{\alpha} + b_0}{s^{2\alpha} + a_1 s^{\alpha} + a_0} \tag{2}$$

and may be referred FOF filter transfer function constituted by two FCs of same order.

The magnitude of the characteristic equation of (2) [21] can be obtained as

Table 1 Features of active realization of FOFs employed by FC in available literature

Ref. No.	Active Element / Circuit	Filter Realization	No. of passive components			Electronic Tuning	Verification		Comparison with conventional integer order filter	Performance parameters for Filter Analysis				Sensitivity (A / NA)	Stability (A / NA)
			R	C	FC		Numerical/ MATLAB Simulation/ Analysis for theoretical results	PSPICE/ ADS Simulation/ Hardware for experimental results		Critical Frequencies			Q-factor		
										$\omega_{max/min}$ / ω_{osc}	ω_{3dB}	ω_{rp}			
[12]	Op-Amp	Fractional Resonance based FOF	4 to 5	0 to 1	2 to 3	No	MATLAB simulation of FLPF, FHPF for order (α+β)=1.1, 1.5, 1.9 and FBPF, FNF for order (α+β)=1.5, 1.9 when β=1	FLPF for order (α+β)=1.1, 1.5, 1.9 and FNF for order (α+β)=1, 1.4 when α=0.5	No	Yes	Yes	No	Yes	NA	NA
[15]	Op-Amp	FO-Sallen Key	4 to 5	0	2	No	FLPF, FHPF, FBPF, FNF,FAPF of order 0.4, 1, 1.6	PSPICE simulation of FLPF of order 0.4, 1, 1.6	Yes	Yes	Yes	Yes	Yes	NA	A
		FO-KHN filter	6	0	2										
[16]	Op-Amp	FO-Sallen Key filter	4	0	2	No	Butterworth FLPF for α ≠ β	ADS simulation of butterworth FLPF for α ≠ β	No	No	Yes	No	No	NA	A
		FO-KHN filter	6	0	2										
[17]	Op-Amp	FO-KHN filter	6	0	2	No	FLPF for dependent order case (β=kα)	Kit of NI ELVIS II from National Instruments used for order (α, β)=(0.6, 1.2)	No	Yes	No	No	No	NA	A
		FO-Sallen Key filter	4	0	2										
[18]	CCII	FLPF	2	0	2	No	FLPF for order α=β=0.8, 1, 1.2	SPICE and Hardware implementation on Kit of NI ELVIS II from National Instruments used for order α = β = 0.8	Yes	Yes	Yes	No	No	A	A
[19]	Op-Amp	FO-Chebyshev filter based on TT biquad circuit	6	1	1	No	FLPF of order 1+α, 2+α, 3+α with step 0.1	FLPF of order 1.2, 1.5, 1.8	No	No	No	No	No	NA	A
[20]	Op-Amp	FO - TT filter	6	1	1	No	FLPF and FBPF of order 1.1, 1.5, 1.9	FLPF and FBPF of order 1.1, 1.5, 1.9	Yes	No	No	No	No	NA	A
[21]	CCII with FC	FO-KHN filter	6	0	2	No	FLPF for α ≠ β	ADS simulation of FLPF for α ≠ β	No	Yes	Yes	Yes	No	NA	A
		FO - TT filter	4	0	2										

Table 1 continued

Ref. No.	Active Element / Circuit	Filter Realization	No. of passive components			Electronic Tuning	Verification		Comparison with conventional integer order filter	Performance parameters for Filter Analysis				Sensitivity (A / NA)	Stability (A / NA)
			R	C	FC		Numerical/ MATLAB Simulation/ Analysis for theoretical results	PSPICE/ ADS Simulation/ Hardware for experimental results		Critical Frequencies			Q-factor		
										$\omega_{max/min}$ / ω_{osc}	ω_{3dB}	ω_{rp}			
[22]	CCII	FO - KHN filter	7	0	2	No	FLPF, FHPF, FBPF for for (α, β)=(1.5, 2.25), (1.2, 1.8), (0.8, 1.2)	ADS simulation for (α, β)=(1.5, 2.25), (1.2, 1.8), (0.8, 1.2)	No	Yes	Yes	No	No	NA	A
[24]	Op-Amp	FO-Inverse Chebyshev LP Filter on multiple input biquad (MIB) circuit	8	1	1	No	(1+α) order FLPF with fractional steps from α=0.1 to α=0.9	SPICE simulation of 1.2, 1.5 and 1.8 order FLPF	No	No	No	No	No	NA	A
[25]	Op-Amp	High Q and Asymmetric -slope 2α order FBPF	4 to 7	2	1	No	FBPF when FC has order α=0.1, 0.5, 0.9	Experimental and Spice results for α=0.1, 0.5 order FC	No	Yes	Yes	No	Yes	NA	A
	CCII		4	2	1										
[33]	Op-Amp	FO-KHN Biquad Filter	6	0	2	No	FLPF, FHPF, FBPF for α=0.86 and β=0.46	PSPICE and Experimental results of FLPF, FHPF, FBPF for α=0.86 and β=0.46	No	Yes	Yes	No	Yes	A	A
[34]	Op-Amp	FO-KHN Biquad Filter	6	0	2	No	FLPF, FHPF, FBPF having dependent order FCs β=kα	ADS simulation of FLPF, FHPF, FBPF having dependent order FCs β=kα	Yes	Yes	Yes	Yes	Yes	NA	A
[36]	Op-Amp	FBPF and FNF developed on FO parallel resonator (FOPR) circuit	8	2	2	No	FNF of (1+α+β)= 2.1 order FO filter when α=0.68 and β=0.42 order FCs	Hardware Experiment for (1+α+β)= 2.1 order FO filter when α=0.68 and β=0.42 order FCs	Yes	Yes	Yes	No	Yes	A	A
[37]	Op-Amp	FBPF	4 to 5	0 to 1	2	No	FBPF of order (α+β=2) where α<1 and β>1	Experimental results of FBPF for order (α, β)=(0.67, 0.21), (0.56, 0.153),(0.56, 0.129)	Yes	Yes	Yes	No	Yes	A	A

Table 2 Conditions for fractional order responses

Condition	Response
$b_2 = 0, b_1 = 0$	FO low-pass filter (FLPF)
$b_1 = 0, b_0 = 0$	FO high-pass filter (FHPF)
$b_2 = 0, b_0 = 0$	FO band-pass filter (FBPF)
$b_1 = 0$	FO band-stop filter (FBSF)

$$|D(s)| = \left[\omega^{4\alpha} + 2a_1\omega^{3\alpha}\cos\alpha\pi/2 + \left(a_1^2 + 2a_0\cos\alpha\pi\right)\omega^{2\alpha} + 2a_1a_0\omega^{\alpha}\cos\alpha\pi/2 + a_0^2\right]^{1/2} \quad (3)$$

In general, three critical frequencies [21] are used to characterize FOF which are defined below:

ω_m: the maximum/minimum frequency point at which $|T(j\omega)|$ is maximum/minimum
ω_h: the half power frequency point
ω_{rp}: the right-phase frequency corresponding to angle = $\pm\pi/2$

3 OTA-Based FOF Realization

The OTA is current mode active building block (ABB), and circuit symbol of OTA is given in Fig. 1. The OTA may be modeled as a differential voltage-controlled current source with current output given by

$$I_0 = \pm g_m(V_+ - V_-), \quad (4)$$

where g_m represents transconductance of OTA and its value depends on bias current (I_b). Thus, electronic tunability of the circuit parameters can be introduced through I_b variation. Circuit symbol of OTA is given in Fig. 1.

In this work, OTA-based filter topology [49] is adapted for FO domain and resulting topology is depicted in Fig. 2. It uses two FCs (C_1, C_2) of order α each and provides electronically tunable FLPF and FBPF responses simultaneously. The

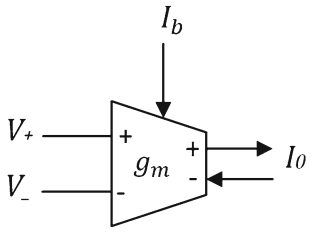

Fig. 1 Circuit symbol of OTA

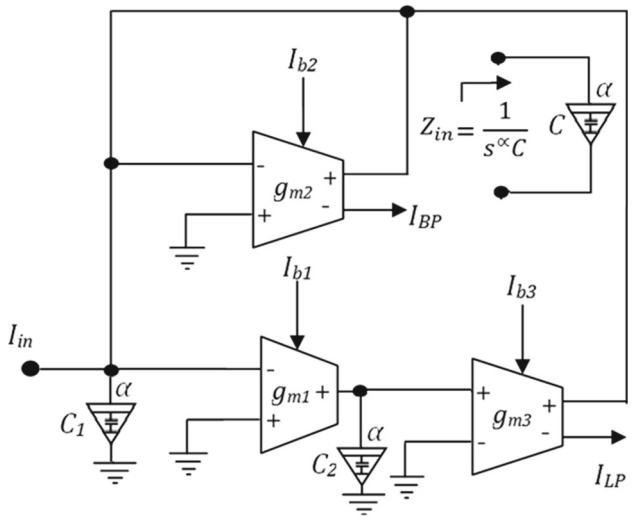

Fig. 2 OTA-based current mode circuit configuration

routine analysis results in the following filter transfer functions:

$$T(s)^{2\alpha}_{FLPF} = \frac{g_{m1}g_{m3}/C_1C_2}{D(s)} \quad (5)$$

$$T(s)^{2\alpha}_{FBPF} = \frac{s^{\alpha}g_{m2}/C_1}{D(s)} \quad (6)$$

$$\text{where} \quad D(s) = s^{2\alpha} + s^{\alpha}g_{m2}/C_1 + g_{m1}g_{m3}/C_1C_2 \quad (7)$$

In order to determine the critical frequencies of the proposed FLPF and FBPF, the magnitudes of $T_{FLPF}(s)$ and $T_{FBPF}(s)$ are computed, respectively, as

$$|T(j\omega)|_{FLPF} = \frac{\frac{g_{m1}g_{m3}}{C_1C_2}}{\left[\omega^{4\alpha} + 2\frac{g_{m2}}{C_1}\omega^{3\alpha}\cos\alpha\pi/2 + \left(\frac{g_{m2}^2}{C_1^2} + 2\frac{g_{m1}g_{m3}}{C_1C_2}\cos\alpha\pi\right)\omega^{2\alpha} + 2\frac{g_{m1}g_{m3}}{C_1C_2}\frac{g_{m2}}{C_1}\omega^{\alpha}\cos\alpha\pi/2 + \left(\frac{g_{m1}g_{m3}}{C_1C_2}\right)^2\right]^{1/2}} \quad (8)$$

$$|T(j\omega)|_{FBPF} = \frac{\frac{g_{m2}}{C_1}\omega^{\alpha}}{\left[\omega^{4\alpha} + 2\frac{g_{m2}}{C_1}\omega^{3\alpha}\cos\alpha\pi/2 + \left(\frac{g_{m2}^2}{C_1^2} + 2\frac{g_{m1}g_{m3}}{C_1C_2}\cos\alpha\pi\right)\omega^{2\alpha} + 2\frac{g_{m1}g_{m3}}{C_1C_2}\frac{g_{m2}}{C_1}\omega^{\alpha}\cos\alpha\pi/2 + \left(\frac{g_{m1}g_{m3}}{C_1C_2}\right)^2\right]^{1/2}} \quad (9)$$

The frequencies $\omega_{m(FLPF)}$ and $\omega_{m(FBPF)}$ are determined by differentiating magnitudes of $T_{FLPF}(s)$ and $T_{FBPF}(s)$ by (8) and (9) with respect to ω^{α} and equating to zero. Applying this to (8) and (9) results, respectively, in

$$\omega_{m(FLPF)}^{3\alpha} + 3\frac{g_{m2}}{2C_1}\omega_{m(FLPF)}^{2\alpha}\cos\alpha\pi/2 + \left[2\left(\frac{g_{m2}}{2C_1}\right)^2 + \frac{g_{m1}g_{m3}}{C_1C_2}\cos\alpha\pi\right]\omega_{m(FLPF)}^{\alpha} + \frac{g_{m2}}{2C_1}\frac{g_{m1}g_{m3}}{C_1C_2}\cos\alpha\pi/2 = 0 \tag{10}$$

$$\left(\omega_{m(FBPF)}^{2\alpha} - \frac{g_{m1}g_{m3}}{C_1C_2}\right)\left(\omega_{m(FBPF)}^{2\alpha} + 2\omega_{m(FBPF)}^{\alpha}\frac{g_{m2}}{2C_1}\cos\frac{\alpha\pi}{2} + \frac{g_{m1}g_{m3}}{C_1C_2}\right) = 0 \tag{11}$$

The numerical values of $\omega_{m(FLPF)}$ and $\omega_{m(FBPF)}$ can be determined by solving (10) and (11), respectively. In case of FBPF, one of the $\omega_{m(FBPF)}$ value is given by $\omega_{m1} = \left(\frac{g_{m1}g_{m3}}{C_1C_2}\right)^{1/2\alpha}$ and its corresponding peak magnitude is computed as

$$\left|T(j\omega_{m1(FBPF)})\right| = \frac{\frac{g_{m2}}{2C_1}}{\left|\frac{g_{m2}}{2C_1} + \sqrt{\frac{g_{m1}g_{m3}}{C_1C_2}}\cos\alpha\pi/2\right|} \tag{12}$$

The half power frequency for FLPF($\omega_{h(FLPF)}$) may be determined by equating magnitude of (8) to $1/\sqrt{2}$. The corresponding expression is computed as

$$\omega_{h(FLPF)}^{4\alpha} + 4\frac{g_{m2}}{2C_1}\omega_{h(FLPF)}^{3\alpha}\cos\alpha\pi/2 + \left[4\left(\frac{g_{m2}}{2C_1}\right)^2 + 2\frac{g_{m1}g_{m3}}{C_1C_2}\cos\alpha\pi\right]\omega_{h(FLPF)}^{2\alpha} + 4\frac{g_{m2}}{2C_1}\frac{g_{m1}g_{m3}}{C_1C_2}\omega_{h(FLPF)}^{\alpha}\cos\alpha\pi/2 - \left(\frac{g_{m1}g_{m3}}{C_1C_2}\right)^2 = 0. \tag{13}$$

Similarly, the expression for computing half power frequency for FBPF ($\omega_{h(FBPF)}$) is given by

$$\omega_{h(FBPF)}^{4\alpha} + 4\frac{g_{m2}}{2C_1}\omega_{h(FBPF)}^{3\alpha}\cos\frac{\alpha\pi}{2} - \left[4\left(\frac{g_{m2}}{2C_1}\right)^2 - 2\frac{g_{m1}g_{m3}}{C_1C_2}\cos\alpha\pi + 8\frac{g_{m1}g_{m3}}{C_1C_2}\cos^2\frac{\alpha\pi}{2} + 16\frac{g_{m2}}{2C_1}\sqrt{\frac{g_{m1}g_{m3}}{C_1C_2}}\cos\frac{\alpha\pi}{2}\right]\omega_{h(FBPF)}^{2\alpha} + 4\frac{g_{m2}}{2C_1}\frac{g_{m1}g_{m3}}{C_1C_2}\omega_{h(FBPF)}^{\alpha}\cos\alpha\pi/2 + \left(\frac{g_{m1}g_{m3}}{C_1C_2}\right)^2 = 0 \tag{14}$$

The numerical values of $\omega_{h(FLPF)}$ and $\omega_{h(FBPF)}$ can be determined by solving (13) and (14), respectively.

The right-phase frequency for FLPF and FBPF is expressed by (15) and (16), respectively.

$$\omega_{rp(FLPF)} = \left(\frac{-\frac{g_{m2}}{2C_1}\cos\frac{\alpha\pi}{2} - \sqrt{\left(\frac{g_{m2}}{2C_1}\right)^2\cos^2\frac{\alpha\pi}{2} - \frac{g_{m1}g_{m3}}{C_1C_2}\cos\alpha\pi}}{\cos\alpha\pi}\right)^{1/\alpha} \tag{15}$$

$$\omega_{rp(FBPF)} = \left(\frac{-\frac{g_{m2}}{2C_1} \pm \sqrt{\left(\frac{g_{m2}}{2C_1}\right)^2 - \frac{g_{m1}g_{m3}}{C_1C_2}\cos^2\frac{\alpha\pi}{2}}}{\cos\frac{\alpha\pi}{2}}\right)^{1/\alpha} \tag{16}$$

The critical frequencies of FLPF and FBPF responses depend upon transconductance (g_m) of OTAs which can be tuned electronically through bias current variation. Therefore, various critical frequencies of OTA-based FOF can be electronically tuned. It is relevant to mention here that tuning of filter parameters is achieved through potentiometer in [36].

3.1 Stability Analysis

It is well known that for a linear time invariant (LTI) system to be stable, all roots of its characteristic equation should lie in the left half of complex plane. However, this constraint is relaxed in FO systems and roots may exist on the right

Table 3 Stability constraints with ω_0 and Q of $D(s)$ for all positive a_i

Parameter $k = 4\left(g_{m1}g_{m3}C_1/g_{m2}^2C_2\right)$	Stability condition	Root location	Pole-frequency ω_0	Q
$k \le 1$	$\alpha < 2$	$r_{1,2} = \frac{-g_{m2}/C_1 \pm \sqrt{(g_{m2}/C_1)^2 - 4\left(\frac{g_{m1}g_{m3}}{C_1C_2}\right)}}{2} = g_{1,2}e^{j\pi}$	$g_{1,2}^{1/\alpha}$	$\frac{-1}{2\cos\pi/\alpha}$
$k > 1$	$\alpha < 2\delta/\pi$, $\delta = \cos^{-1}(-1/\sqrt{k}) > \pi/2$	$r_{1,2} = \sqrt{\frac{g_{m1}g_{m3}}{C_1C_2}}e^{\pm j\delta}$	$\left(\frac{g_{m1}g_{m3}}{C_1C_2}\right)^{1/2\alpha}$	$\frac{-1}{2\cos\delta/\alpha}$

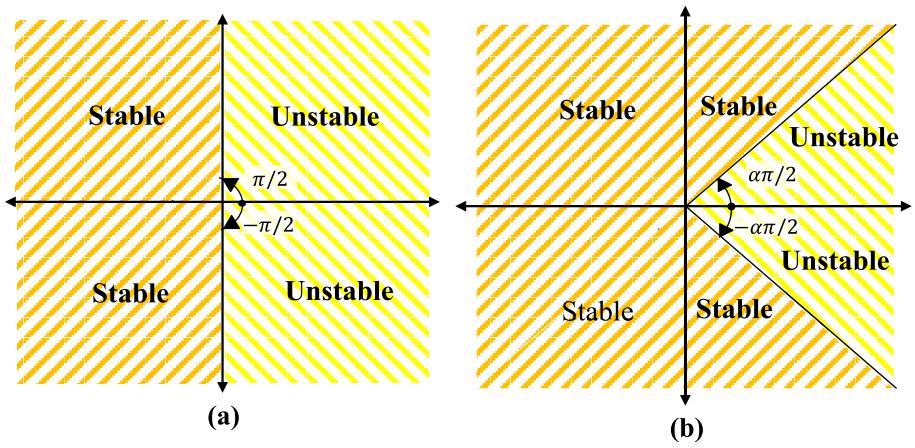

Fig. 3 Stability region in complex (**a**) s-plane; (**b**) s^{α} plane

half of complex plane. The stability analysis of FO domain is well explained in [35] and has been adapted in the present work. The stability of presented FOF depends on coefficients of $s^{i\alpha}(i = 1, 0)$ in (7). In this work, all coefficients of (7) are positive and conditions for different parameters [15] are mentioned in Table 3 where $k = 4\left(g_{\mathrm{m1}}g_{\mathrm{m3}}/g_{\mathrm{m2}}^2\right)$

It may be noted from Table 3 that FOF is stable for $|\delta| > \alpha\pi/2$ for α ranging between 0 and 1 whereas integer-order filter is stable for $|\delta| > \pi/2$. This fact is pictorially represented in Fig. 3 [35] wherein from it may be concluded that stability region for FOF is extended as compared to integer-order filter.

3.2 Sensitivity Analysis

The significance of sensitivity analysis of FOFs is to indicate the relative change in filters responses with respect to the circuit parameters used. In this subsection, sensitivities of both the FOF transfer functions have been computed to enumerate the effect of FO, FC value and g_{m} and are expressed, respectively, as

$$S_{\alpha}^{\mathrm{TF_{FLPF}}} = -\frac{\alpha s^{\alpha}\ln(s)\left(2s^{\alpha} + g_{\mathrm{m2}}/C_1\right)}{s^{2\alpha} + s^{\alpha}g_{\mathrm{m2}}/C_1 + g_{\mathrm{m1}}g_{\mathrm{m3}}/C_1C_2} \tag{17}$$

$$S_{C_1}^{\mathrm{TF_{FLPF}}} = -\frac{s^{2\alpha}}{s^{2\alpha} + s^{\alpha}g_{\mathrm{m2}}/C_1 + g_{\mathrm{m1}}g_{\mathrm{m3}}/C_1C_2} = S_{C_1}^{\mathrm{TF_{FBPF}}} \tag{18}$$

$$S_{C_2}^{\mathrm{TF_{FLPF}}} = -\frac{s^{2\alpha} + s^{\alpha}g_{\mathrm{m2}}/C_1}{s^{2\alpha} + s^{\alpha}g_{\mathrm{m2}}/C_1 + g_{\mathrm{m1}}g_{\mathrm{m3}}/C_1C_2} = -S_{g_{\mathrm{m1}}}^{\mathrm{TF_{FLPF}}} = -S_{g_{\mathrm{m3}}}^{\mathrm{TF_{FLPF}}} \tag{19}$$

$$S_{g_{\mathrm{m2}}}^{\mathrm{TF_{FLPF}}} = -\frac{s^{\alpha}g_{\mathrm{m2}}/C_1}{s^{2\alpha} + s^{\alpha}g_{\mathrm{m2}}/C_1 + g_{\mathrm{m1}}g_{\mathrm{m3}}/C_1C_2} \tag{20}$$

$$S_{\alpha}^{\mathrm{TF_{FBPF}}} = \frac{\alpha s^{\alpha}\ln(s)\left[-s^{2\alpha} + g_{\mathrm{m1}}g_{\mathrm{m3}}/C_1C_2\right]}{s^{2\alpha} + s^{\alpha}g_{\mathrm{m2}}/C_1 + g_{\mathrm{m1}}g_{\mathrm{m3}}/C_1C_2} \tag{21}$$

$$S_{C_2}^{\mathrm{TF_{FBPF}}} = \frac{g_{\mathrm{m1}}g_{\mathrm{m3}}/C_1C_2}{s^{2\alpha} + s^{\alpha}g_{\mathrm{m2}}/C_1 + g_{\mathrm{m1}}g_{\mathrm{m3}}/C_1C_2} = S_{g_{\mathrm{m1}}}^{\mathrm{TF_{FBPF}}} = S_{g_{\mathrm{m3}}}^{TF_{\mathrm{FBPF}}} \tag{22}$$

$$S_{g_{\mathrm{m2}}}^{\mathrm{TF_{FBPF}}} = \frac{s^{2\alpha} + g_{\mathrm{m1}}g_{\mathrm{m3}}/C_1C_2}{s^{2\alpha} + s^{\alpha}g_{\mathrm{m2}}/C_1 + g_{\mathrm{m1}}g_{\mathrm{m3}}/C_1C_2} \tag{23}$$

Equations (17)–(23) show that the transfer functions' sensitivity depends on FO, FC value and g_{m} of OTA. Therefore, graphs need be plotted to observe the exact effect of various parameters.

4 Simulation Results

Workability of proposed OTA-based FOF is verified through SPICE simulations for $\alpha = 0.5$ and 0.9. The CMOS-based schematic of OTA [49] with 0.5 µm CMOS process parameters provided by MOSIS (AGILENT) is used.The FC

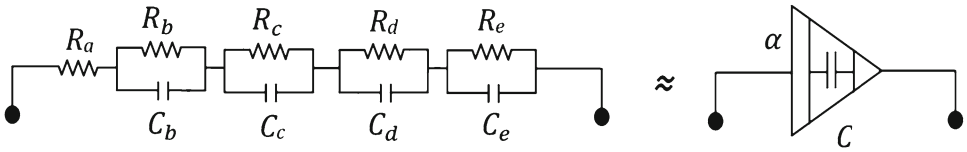

Fig. 4 A fourth-order RC ladder circuit [12]

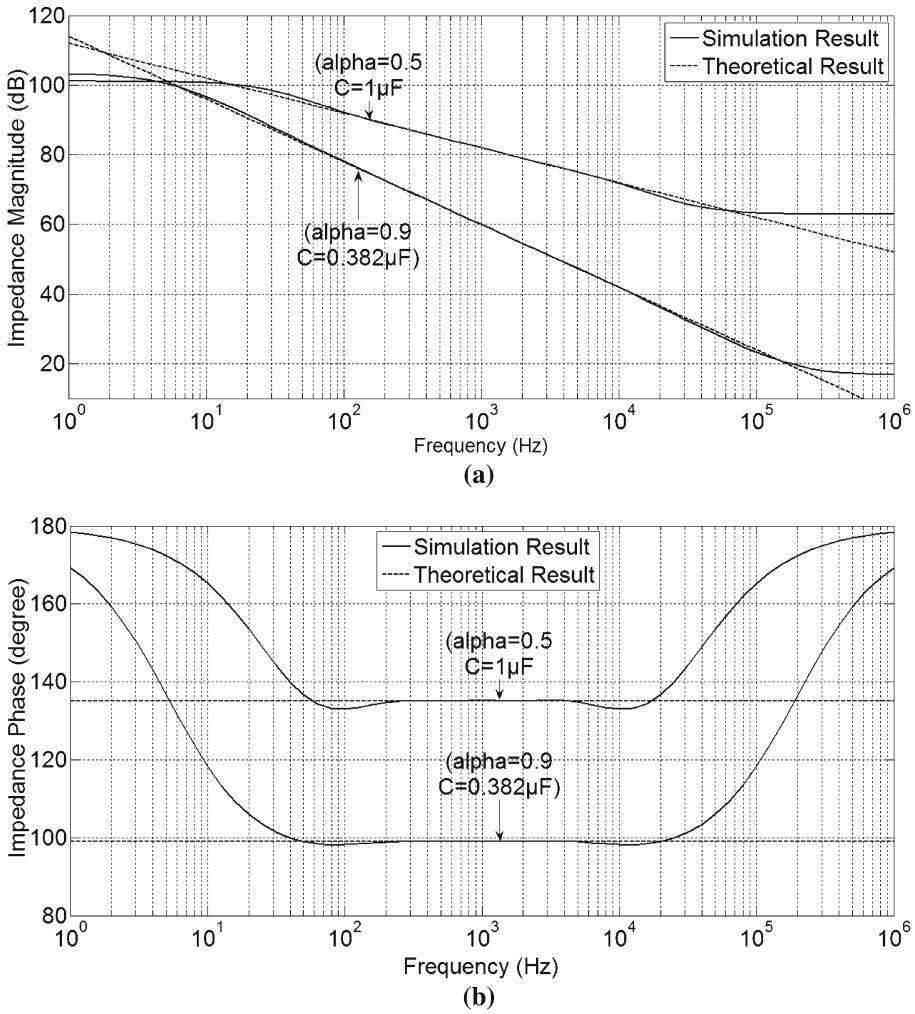

Fig. 5 **a** Impedance magnitude, **b** phase responses of FC

employed in FOF cannot be directly simulated in SPICE; therefore, in this work it is realized using finite ladder circuit based on the fourth-order CFE approximation model [12] (Fig. 4). The magnitude and phase of FC impedance function are $1/(\omega^{\alpha}C)$ and $(-\alpha\pi/2$ or, $(180-\alpha\pi/2))$, respectively. Therefore, the magnitude response of FC of order α would show a negative slope of $\left(-20\alpha\log_{10}\omega\right)$ while its phase remains constant. SPICE simulations have been carried out for examining behavior of FCs of order 0.5 and 0.9 with a center frequency of 1 kHz. The corresponding theoretical and simulated magnitude and phase responses are shown in Fig. 5. It may be observed that there is close agreement in theoretical and simulated magnitude and phase responses in frequency range (9 Hz–105 kHz) and (180 Hz–5.5 kHz), respectively, for $\alpha = 0.5$ and the corresponding range for $\alpha = 0.9$ is (4 Hz–230 kHz) and (150 Hz–7.5 kHz) with a deviation of ± 1.5 dB and $\pm 0.3^0$ for magnitude and phase responses, respectively. It may be noted that the range improves with increase in FO.

The responses of OTA-based FOF with FC of order 0.5 and 0.9 are shown in Figs. 6 and 7, respectively, for simulation settings of Table 4. The supply voltages are taken as ± 1.8 V. It may be noted from Table 4 that since $k > 1$ and $\alpha < 2\delta/\pi$ therefore the stability criteria given in Table 3 is satisfied.

It is observed from Figs. 6b and 7b that right-phase frequency exists only for FLPF of order 0.9 which is in sync with (15) and (16), respectively. Performance parameters for proposed FLPF and FBPF are listed in Table 5 and 6, respectively, along with corresponding conventional filter ($\alpha = 1$) parameters. There is a close match between theoretical and simulated values. It is also found that the value of critical frequencies increases with decrease in FO.

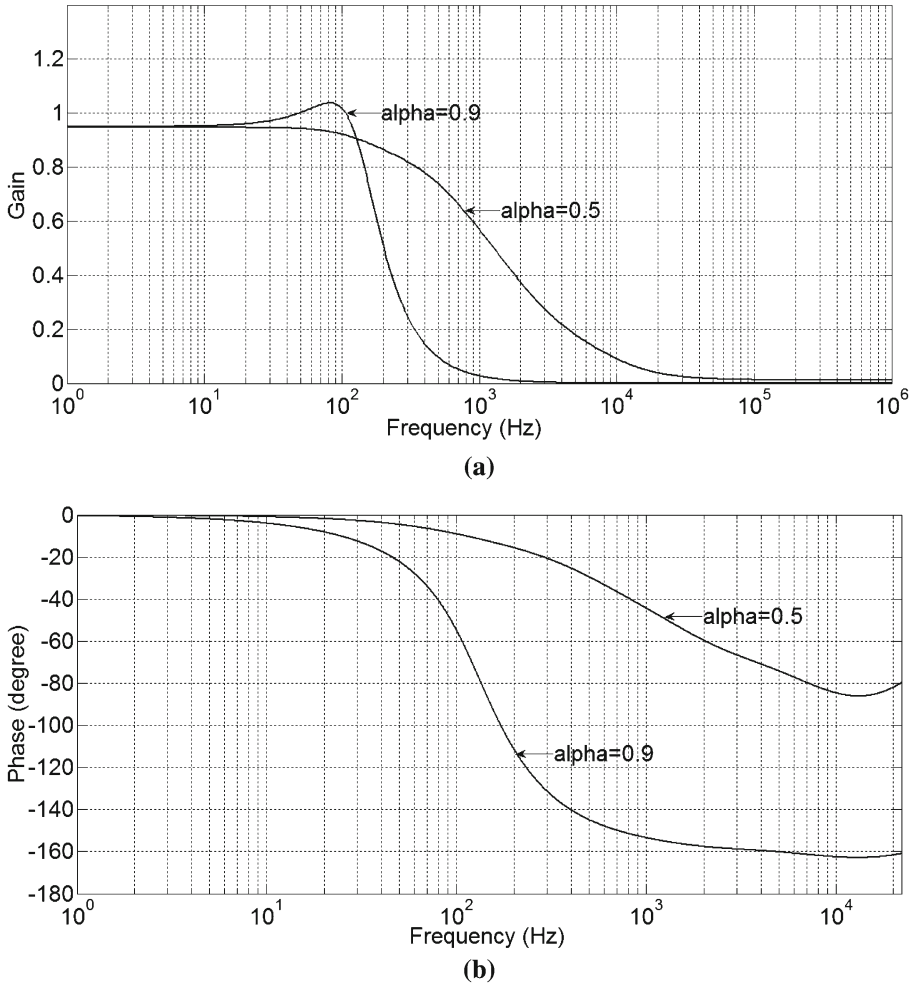

Fig. 6 Simulated frequency response (**a**) magnitude and (**b**) phase for proposed FLPF

The FLPF ($\alpha = 0.5$ and 0.9) is tested for electronic tunability of half power frequency by varying I_{b2} while keeping the other settings same as listed in Table 4. The results are plotted in Fig. 8. The right-phase frequency variation with respect to I_{b2} for FLPF with $\alpha = 0.9$ is plotted in Fig. 9. It may be observed that both half power and right-phase frequencies show downward trend with increasing bias current.

Equations (17)–(23) are plotted in Fig. 10 to investigate the effect of FO, FC value and g_m of OTA on the transfer functions' sensitivity, wherein data are acquired at 1 kHz. The value of g_{m2} is taken as 25 μA/V (data 1), 50 μA/V (data 2) and 80 μA/V (data 3) for all plots except those given in Fig. 10e, i. The values of g_{m1} and g_{m3} are kept equal at 25 μA/V (data 1), 50 μA/V (data 2) and 80 μA/V (data 3) while observing sensitivity variation with respect to g_{m2} (Fig. 10e, i). Sensitivities with respect to α, C_1 and C_2 are plotted while keeping g_{m1} and g_{m3} equal to 25 μA/V and g_{m2} at 25 μA/V. The values of α, C_1 and C_2 are kept at 0.5, 1 and 1 μF, respectively, in all the plots for the cases where these parameter are not varied for observation. The transfer functions' sensitivity with respect to FC value and g_m of OTA remain well within unity while both FLPF and FBPF are sensitive to FO variation.

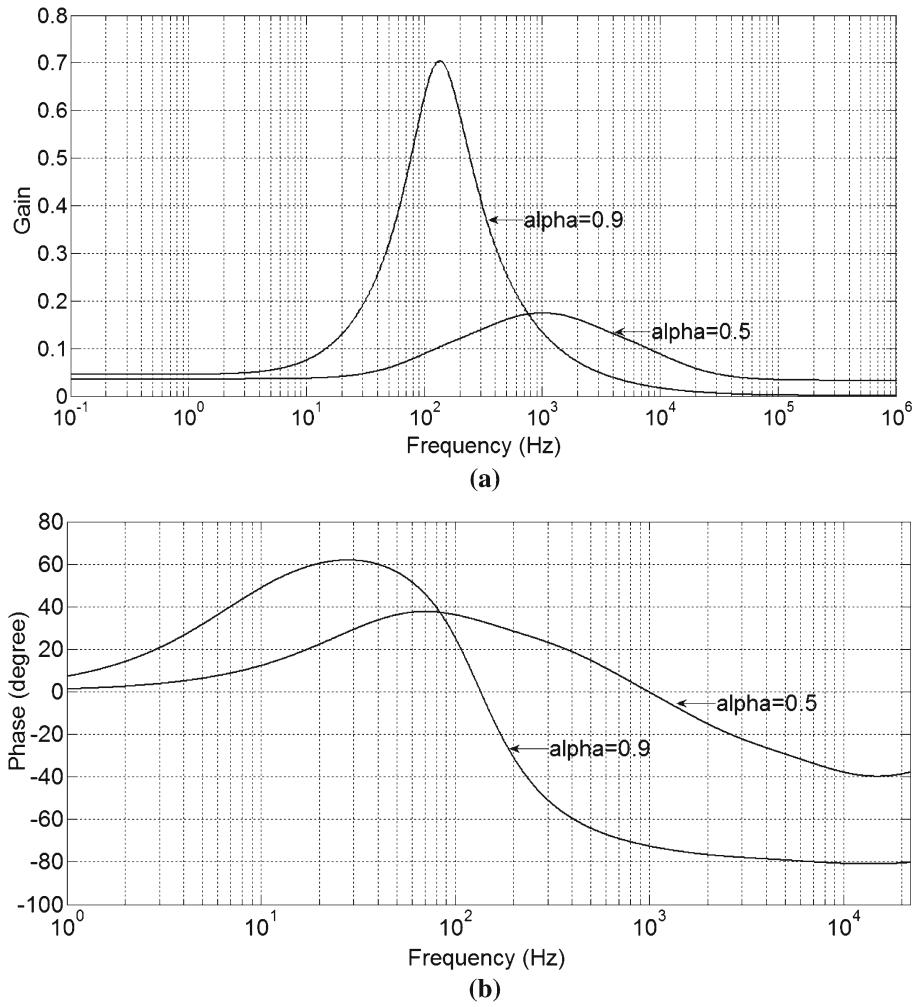

Fig. 7 Simulated frequency response (**a**) magnitude and (**b**) phase for proposed FBPF

Table 4 Simulation setting for proposed FOF

Order (α)	C (μF)	$I_{b1} = I_{b3}$(μA)	I_{b2}(μA)	$g_{m1} = g_{m3}$(μA/V)	g_{m2} (μA/V)	a_0	a_1	k	$2\delta/\pi$
0.5	1	17.4	2.47	79.311	23.942	6290.235	23.942	43.894	1.096
0.9	0.382	98	57.73	165	134.7	186569.572	352.618	6	1.268

Table 5 Performance parameters for FLPF for α = 0.5, 0.9 and 1.0

Parameters measured	$C = 1\,\mu$F				$C = 0.382\,\mu$F			
	Simulation results		Theoretical results		Simulation results		Theoretical results	
	$\alpha = 0.5$	$\alpha = 1.0$	$\alpha = 0.5$	$\alpha = 1.0$	$\alpha = 0.9$	$\alpha = 1.0$	$\alpha = 0.9$	$\alpha = 1.0$
Dc gain	0.95	0.995	1	1	0.95	0.985	1	1
Half power frequency (Hz)	681	19.31	628	19.3	156.33	94.3	163.946	94
Max/min frequency (Hz)	none	12.3	none	12.338	79.228	55.45	80.58	56.1

Table 6 Performance parameters for FBPF for $\alpha = 0.5$, 0.9 and 1.0

Parameters measured	$C = 1\mu F$				$C = 0.382\mu F$			
	Simulation results		Theoretical results		Simulation results		Theoretical results	
	$\alpha = 0.5$	$\alpha = 1.0$	$\alpha = 0.5$	$\alpha = 1.0$	$\alpha = 0.9$	$\alpha = 1.0$	$\alpha = 0.9$	$\alpha = 1.0$
Lower cutoff frequency (Hz)	211	10.73	224	10.8	76.77	45.91	75.37	46.2
Higher cutoff frequency (Hz)	4.7 k	14.68	4.47 k	15	245	102.3	242	105.45
Center frequency (Hz)	1.08 k	12.6	1.001 k	12.62	136	69.4	135	68.78
Gain at center frequency	−15.169 dB	0.89	−15 dB	1	0.705	0.95	0.723	1

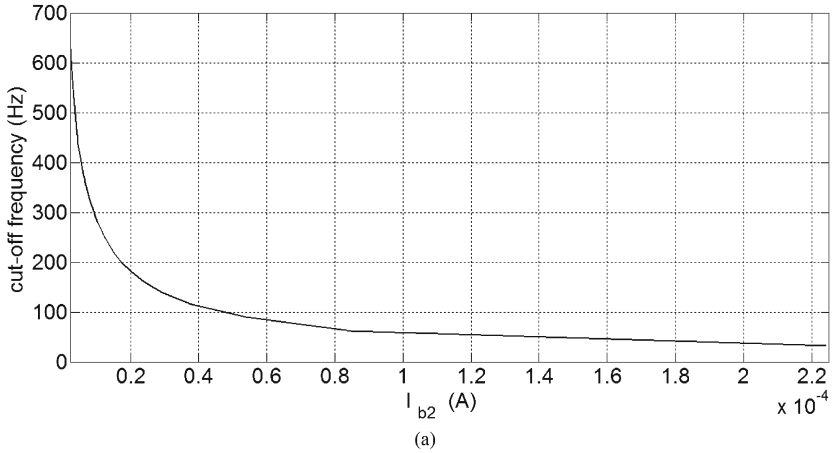

(a)

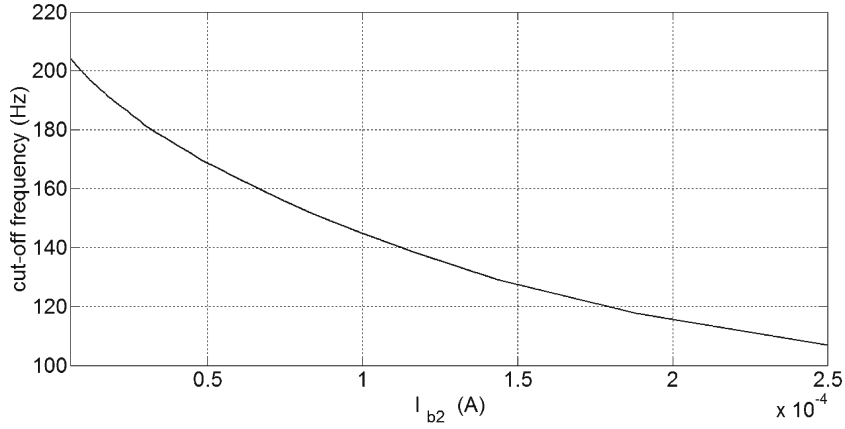

(b)

Fig. 8 Electronic tunability of cutoff frequency of proposed FLPF having $\alpha =$ **a** 0.5, **b** 0.9

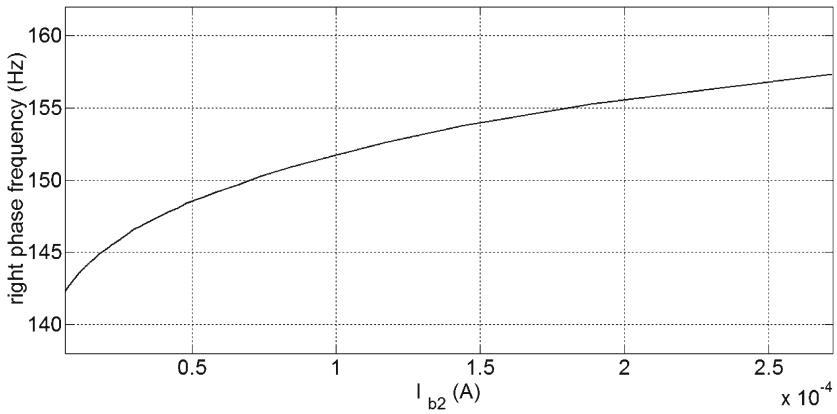

Fig. 9 Electronic tunability of right-phase frequency of proposed FLPF having $\alpha = 0.9$

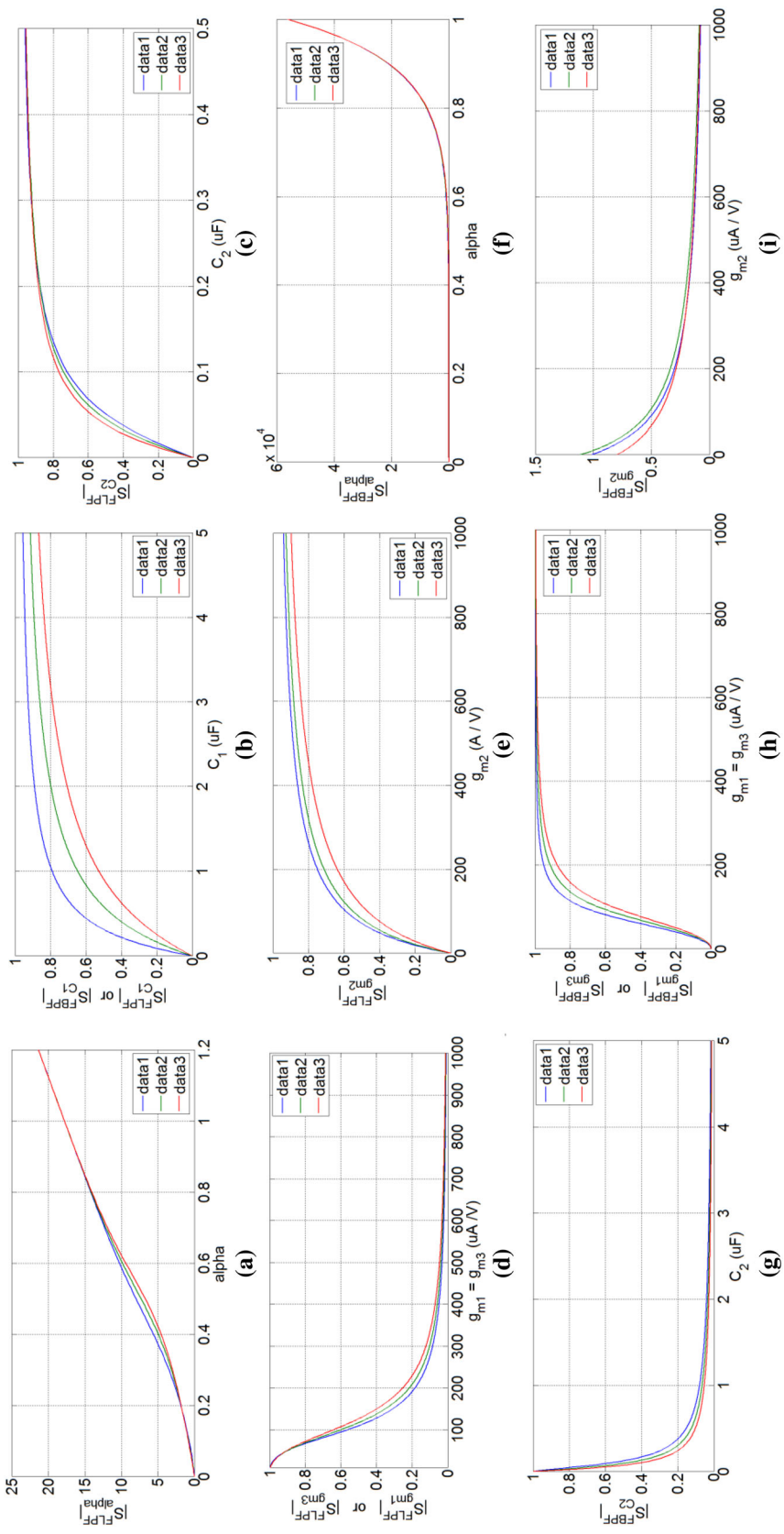

Fig. 10 Sensitivity: **a** $|S_{\alpha}^{\mathrm{FLPF}}|$ versus α; **b** $|S_{C1}^{=\mathrm{FLPF}}|$ versus C_1 and $|S_{C1}^{\mathrm{FBPF}}|$ versus. C_1; **c** $|S_{C2}^{\mathrm{FLPF}}|$ versus C_2; **d** $|S_{g_{\mathrm{m1}}=g_{\mathrm{m3}}}^{\mathrm{FLPF}}|$ versus $g_{\mathrm{m1}} = g_{\mathrm{m3}}$; **e** $|S_{g_{\mathrm{m2}}}^{\mathrm{FLPF}}|$ versus g_{m2}; **f** $|S_{\alpha}^{\mathrm{FBPF}}|$ versus α; **g** $|S_{C2}^{\mathrm{FBPF}}|$ versus C_2; **h** $|S_{g_{\mathrm{m1}}=g_{\mathrm{m3}}}^{\mathrm{FBPF}}|$ versus $g_{\mathrm{m1}} = g_{\mathrm{m3}}$; **i** $|S_{g_{\mathrm{m2}}}^{\mathrm{FBPF}}|$ versus g_{m2}

5 Conclusion

An electronically tunable FOF design using OTA is presented in this paper which provides FLPF and FBPF responses simultaneously. The design uses two fractional capacitors (FC) of same order. Mathematical expressions for various critical frequencies and transfer functions' sensitivity for OTA-based FOF are derived. SPICE simulations are included to characterize FC of orders 0.5 and 0.9, verify functionality of presented FOF and to show electronic tunability of half power frequency, right-phase frequency. Transfer function sensitivities are also examined. The simulated results are found to be in close agreement with theoretical ones, hence verifying the workability of OTA-based FOF.

References

1. Debnath, L.: Recent applications of fractional calculus to science and engineering. Int. J. Math. Math. Sci. **2003**(54), 3413–3442 (2003)
2. Elwakil, A.S.: Fractional-order circuits and systems: an emerging Interdisciplinary research area. IEEE Circuit Syst. Mag. **10**(4), 40–50 (2010)
3. Chen, Y.Q.; Petras, I.; Xue, D.: Fractional order control—a tutorial. In: Proceeding American Control Conference (ACC), pp. 1397–1411 (2009)
4. Das, S.; Pan, I.: Fractional order signal processing—introductory concepts and applications. In: Springer Briefs in Applied Sciences and Technology (2012)
5. Dorcak, L.; Valsa, J.; Gonzalez, E.; Terpak, J.; Petras, I.; Pivka, L.: Analogue realization of fractional-order dynamical systems. Entropy **15**(10), 4199–4214 (2013)
6. Podlubny, I.; Petras, I.; Vinagre, B.M.; Leary, P.O.; Dorcak, L.: Analogue realizations of fractional-order controllers. Nonlinear Dyn. **29**(4), 281–296 (2012)
7. Suksang, T.; Loedhammacakra, W.; Pirajnanchai, V.: Implement the fractional-order, half integrator and differentiator on the OTA based $PI^{\lambda}D^{\mu}$ controller circuit. In: IEEE Conference on ECTICON (2012). doi:10.1109/ECTICON.2012.6254136
8. Geddes, L.A.; Baker, L.E.: Principles of Applied Biomedical Instrumentation, 3rd edn. Wiely, New York (1989)
9. Faria, A.C.; Veiga, J.; Lopes, A.J.; Melo, P.L.: Forced oscillation, integer and fractional-order modeling in asthma. Comput. Methods Programs Biomed. **128**, 12–26 (2016)
10. Sheng, H.; Chen, Y.Q.; Qiu, T.S.: Fractional Processes and Fractional-Order Signal Processing: Techniques and Applications. Springer, New York (2011)
11. Radwan, A.G.; Soliman, A.M.; Elwakil, A.S.: First-order filters generalized to the fractional domain. J. Circuits Syst. Comput. **17**(1), 55–66 (2008)
12. Freeborn, T.J.; Maundy, B.; Elwakil, A.: Fractional resonance-based $RL_{\beta}C_{\alpha}$ filters. Math. Probl. Eng. **2013**, 1–10 (2013)
13. Soltan, A.; Radwan, A.G.; Soliman, A.M.: Butterworth passive filter in the fractional-order. Int. Conf. Microelectron. (ICM) **23**, 1–5 (2011)
14. Radwan, A.: Stability analysis of the fractional-order $RL_{\beta}C_{\alpha}$ circuit. J. Fract. Calc. Appl. **3**(1), 1–15 (2012)
15. Radwan, A.; Elwakil, A.; Soliman, A.: On the generalization of second-order filters to the fractional order domain. J. Circuits Syst. Comput. **18**(2), 361–386 (2009)
16. Ali, A.S.; Radwan, A.G.; Soliman, A.M.: Fractional order butterworth filter: active and passive realizations. IEEE J. Emerg. Sel. Top. Circuits Syst. **3**(3), 346–354 (2013)
17. Soltan, A.; Radwan, A.G.; Soliman, A.M.: Fractional order sallen-key and KHN filters stability and poles allocation. Circuits Syst. Signal Process. **34**(5), 1461–1480 (2014)
18. Said, L.A.; Ismail, S.M.; Radwan, A.G.; Madian, A.H.; El-Yazeed, M.F.A.; Soliman, A.M.: On The Optimization of Fractional Order Low-Pass filters. Circuits Syst. Signal Process. **35**(6), 2017–2039 (2016)
19. Freeborn, T.; Maundy, B.; Elwakil, A.S.: Approximated fractional order Chebyshev lowpass filters. Math. Probl. Eng. **2015**, 1–7 (2015)
20. Freeborn, T.J.; Maundy, B.; Elwakil, A.: Fractional-step Tow-Thomas biquad filters, nonlinear theory and its applications. IEICE (NOLTA) **3**(3), 357–374 (2012)
21. Soltan, A.; Radwan, A.G.; Soliman, A.M.: CCII based fractional filters of different orders. J. Adv. Res. **5**(2), 157–164 (2014)
22. Soltan, A.; Radwan, A.G.; Soliman A.M.: CCII based KHN fractional order filter. In: IEEE-Midwest Symposium on Circuits and Systems (MWSCAS), pp. 197–200 (2013)
23. AbdelAty, A.M.; Soltan, A.; Ahmed, W.A.; Radwan A.G.: Low pass filter design based on fractional power Chebyshev polynomial. In: IEEE International Conference on Electronics, Circuits, and Systems (ICECS) (2015). doi:10.1109/ICECS.2015.7440236
24. Freeborn, T.J.; Elwakil, A.S.; Maundy, B.: Approximated fractional-order inverse Chebyshev lowpass filters. Circuits Syst. Signal Process. **35**(6), 1973–1982 (2016)
25. Ahmadi, P.; Maundy, B.; Elwakil, A.S.; Belostostski, L.: High-quality factor asymmetric-slope band pass filters: a fractional-order capacitor approach. IET Circuits Devices Syst. **6**(3), 187–197 (2012)
26. Tsirimokou, G.; Laoudias, C.; Psychalinos, C.: 0.5-V fractional-order companding filters. Int. J. Circuit Theory Appl. (2014). doi:10.1002/cta.1995
27. Tsirimokou, G.; Psychalinos, C.: Ultra-low voltage fractional order differentiator and integrator topologies an application for handling noisy ECGs. Analog Integerated Circuits Signal Process. **81**(2), 393–405 (2014)
28. Maundy, B.; Elwakil, A.S.; Freeborn, T.J.: On the Practical realization of higher order filters with fractional stepping. Signal Process. **91**(3), 484–491 (2011)
29. Jerabek, J.; Sotner, R.; Dvorak, J.; Langhammer, L.; Koton, J.: Fractional-order high-pass filter with electronically adjustable parameters. In: IEEE International Conference on Applied Electronics (2016). doi:10.1109/AE.2016.7577253
30. Tsirimokou, G.; Psychalinos, C.; Elwakil, A.S.: Fractional-order electronically controlled generalized filters. Int. J. Circuit Theory Appl. (2016). doi:10.1002/cta.2250
31. Khateb, F.; Kubanek, D.; Tsirimokou, G.; Psychalinos, C.: Fractional-order filters based on low-voltage DDCCs. Microelectron. J. **50**, 50–59 (2016)
32. Li, M.: Approximating ideal filters by systems of fractional order. Comput. Math. Methods Med. **2012**, 1–6 (2012)
33. Tripathy, M.C.; Biswas, K.; Sen, S.: A design example of a fractional-order Kerwin-Huelsman-Newcomb biquad filter with two fractional capacitors of different order. Circuits Syst. Signal Process. **32**, 1523–1536 (2013)
34. Soltan, A.; Radwan, A.G.; Soliman, A.M.: Fractional order filter with two fractional elements of dependant orders. Microelectron. J. **43**(11), 818–827 (2012)
35. Radwan, A.G.; Soliman, A.M.; Elwakil, A.S.; Sedeek, A.: On the stability of linear systems with fractional-order elements. Chaos Solitons Fract. **40**(5), 2317–2328 (2009)

36. Adhikary, A.; Sen, S.; Biswas, K.: Practical realization of tunable fractional order parallel resonator and fractional order filters. IEEE Trans. Circuits Syst. I **63**(8), 1142–1151 (2016)
37. Tripathy, M.C.; Mondal, D.; Biswas, K.; Sen, S.: Experimental studies on realization of fractional inductors and fractional-order bandpass filters. Int. J. Circuit Theory Appl. **43**(9), 1183–1196 (2014)
38. Helie, T.: Simulation of fractional-order low-pass filters. IEEE/ACM Trans. Audio Speech Lang. Process. **22**(11), 1636–1647 (2014)
39. Biolek, D.; Senani, R.; Biolkova, V.; Kolka, Z.: Active elements for analog signal processing: classification, review, and new proposals. Radioengineering **17**(4), 15–32 (2008)
40. Ranjan, R.K.; Yalla, S.P.; Sorya, S.; Paul, S.K.: Active comb filter using operational transconductance amplifier. Act. Passiv. Electron. Compon. (2014). doi:10.1155/2014/587932
41. Ananda Mohan, P.V.: VLSI Analog Filters: Active RC, OTA-C and SC. Birkhauer, Boston (2013)
42. Kamat, D.V.: Ananda Mohan, P.V.; Gopalakrishna Prabhu, K.: Active-RC filters using two-stage OTAs with and without feed-forward compensation. IET Circuits Devices Syst. **5**(6), 527–535 (2011)
43. Li, Y.A.: Electronically tunable current-mode biquadratic filter and four-phase quadrature oscillator. Microelectron. J. **45**(3), 330–335 (2014)
44. Li, Y.N.: On the systematic synthesis of OTA-based wien oscillators. AEU Int. J. Electron. Commun. **67**(9), 754–760 (2013)
45. Sotner, R.; Jerabek, J.; Herencsar, N.; Vrba, K.; Dostal, T.: Features of multi-loop structures with OTAs and adjustable current amplifier for second-order multiphase/ quadrature oscillators. AEU Int. J. Electron. Commun. **69**(5), 814–822 (2015)
46. Senani, R.; Gupta, M.; Bhaskar, D.R.; Singh, A.K.: Generation of equivalent forms of operational transconductance amplifier-RC sinusoidal oscillators: the nullor approach. IET J. Eng. (2014). doi:10.1049/joe.2013.0200
47. Senani, R.; Bhaskar, D.R.; Gupta, M.; Singh, A.K.: Canonic OTA-C sinusoidal oscillators: generation of new grounded-capacitor versions. Am. J. Electr. Electron. Eng. **3**(6), 137–146 (2015)
48. Krishna, B.T.: Studies on fractional-order differentiators and integrators: a survey. Signal Process. **91**(3), 386–426 (2011)
49. Sumi, Y.; Tsukutani, T.; Tsunetsugu, H.; Yabuki, N.: Electrical tunable multiple-mode universal biquadratic circuits. In: International Conference on Computer Application and Industrial Electronics (2010). doi:10.1109/ICCAIE.2010.5735109

Int J Syst Assur Eng Manag
DOI 10.1007/s13198-017-0612-x

ORIGINAL ARTICLE

Engineering and validating security to make cloud secure

Shruti Jaiswal[1] · **Daya Gupta**[1]

Received: 18 September 2016 / Revised: 17 March 2017

Abstract With ever increasing demand for cloud computing services, the rate for the security threats has amplified drastically and this cannot be overlooked. Cloud-based systems can be used for storing and processing highly confidential data. These threats create a chaotic situation that is restricting the adoption rate of cloud-based services. In this paper, we anticipate giving a proposal that identifies and handle the security issues present in the system. Our proposal would first find the potential threats to the cloud system, and then algorithms implemented by the existing systems are evaluated by calculating the security index to check if they can protect the system from identified threats. Security index is the metric representing the risk measure of live threats in the system.

Keywords Cloud computing · Cloud security · Cloud storage · Security requirements · Security engineering · Security index

1 Introduction

The National Institute of Standards and Technology (NIST) (Liu et al. 2011) defines cloud computing as a technology that provides computing resources to the customer on-demand, in time and in the economy friendly way. Cloud computing offers several benefits such as lower cost, fast deployment, pay for use, low-cost disaster recovery, scalability, and provides the high need of data storage solutions. Data security issues such as data privacy and data protection are the major concerns of cloud computing, restricting its growth. Providing security in cloud computing architecture is much more difficult and challenging as compared to a network system, because of underlying complex architecture that has a wider range of new concepts such as multi-location data placement, multi-tenancy, trust. Providing security in the cloud system requires effort from both cloud developer and cloud customer. Ko and Lee (2013) highlighted various security vulnerabilities such as Insecure Interfaces & APIs, Data Loss & Leakage, and Hardware Failure. Also, researchers are investigating security requirements and their implementation for a cloud system.

Security is defined as technological and managerial procedures applied to computer systems to ensure CIA of dedicated system resources. In CIA 'C' stands for Confidentiality that limits access to information by application of a set of rules, 'I' refers to Integrity that provides assurance that information is consistent, trustworthy and accurate. 'A' stands for Availability that guarantees the reliable access to information by authorized people. Increased penetration of ubiquitous devices in software systems has led to increased attack surface for attackers and so for the security practitioners to study and provide security to decrease the impact of attack on system resources. Therefore, security engineering community feels that to secure a software system, first security requirements should be identified along with functional and non-functional requirements and then they should be implemented based on environment constraints. Security requirements are defined by researcher Firesmith (2003) as high-level requirements that give detail specification of any system

✉ Shruti Jaiswal
dce.shruti@gmail.com

[1] Department of Computer Science and Engineering, Delhi Technological University, Delhi, India

Published online: 21 April 2017

behavior that is not acceptable, he has defined twelve security requirements. As the cause of security requirements are potential threats to the system, the developed system should be validated for extenuation of potential threats. This process of enacting security is called security engineering.

There are various proposals in the literature that address the security in cloud systems, for example, researcher Patrick (Honer 2013) describes various security requirements for cloud systems and available solutions for implementation and highlighted non-repudiation, physical protection, recovery, and prosecution as the under-researched areas. Similarly, proposals (Rong et al. 2013; Sun et al. 2011, 2014; Che et al. 2011) present literature survey of the security issues of the Cloud System and advised further research is required for delivering a secure cloud application. In (Ficco et al. 2015) authors are using the existing modeling languages such as misuse cases, abuse cases, secure tropos with slight modification for annotating the security requirements for cloud systems, they are suggesting the implementation of security requirements in an ad-hoc manner. In the proposals by researchers Islam et al. (2011) and Naveed et al. (2014) threats present in the cloud system with their protection (cryptographic algorithm) is proposed without considering the environment and design attributes.

Security testing is the process to determine the level of security provided by the software system with given set of intended functionalities. Proposals are present in the literature that perform the security testing, some (Felderer et al. 2014), (Schieferdecker et al. 2012) have generated test cases to identify the potential vulnerabilities present in the system based on different set of models (architectural, functional, risk). Arkin et al. (2005) proposal known as penetration testing, that identifies the threats present in the system. In (Basin et al. 2006) a model based security testing method is presented where they have combined system modeling languages with modeling languages for security and formalize access control requirements. In (Wang et al. 2007) researchers are creating threat traces to test the security concept at the time of testing by matching the execution trace with threat trace created with the help of sequence diagrams. A novel scenario-based testing known as security attack testing (SAT) method is proposed by researcher Mouratidis et al. (2007) that develops the security attacks scenarios during the design time and then save them for later testing after implementation. They are not actually validating the security implemented.

From above it is observed:

- Current proposals address security requirements independent of functional requirements. As most of the threats occur during the execution of functional requirements, hence there exists some dependencies between these two. Therefore, Security Requirements should be elicited based on functional requirements.
- Environment constraints play a crucial role in the selection of cryptography algorithms and these algorithms mitigates different attacks in different environments. In present scenario, the security requirements are implemented without considering these constraints.
- None of the proposals validates the security implemented in the system. Testing implemented security is an essential task when it comes to providing security to the cloud system, used for storage and processing.

Hence a security methodology is required that mitigates the above drawbacks to provide better security that deals with the security breaches occurring in the system. Our earlier works (Jaiswal and Gupta 2009; Chatterjee et al. 2013) tried to resolve the above mentioned issues by proposing a framework for web based systems, which includes security requirements elicitation and prioritization with the identification of security algorithms based on environment constraints. Unlike web-based systems, cloud systems have additional issues such as trust, lock-in, multi-location data placement, downtime; also they have predefined functionality and assets. Based on this difference between the two systems, we adapted our previous framework for cloud systems. Therefore, in this paper, a proposal is presented that identify and prioritize the security requirements along with functional requirements for cloud-based systems. Once the security requirements are implemented, the final system is validated for potential threats. During validation, a security index is generated that reveals the gap in the security of deployed algorithm. This metric value would act as a guide for a software developer to enhance/revise the existing cryptographic algorithm and also helps in evaluating the security of available cloud systems.

Therefore, the contribution of the paper are listed as follows:

- Elicitation of security requirements along with the functional and non-functional requirements, using the developed mapping tables for mapping of vulnerability to threats.
- Prioritization of security requirements based on risk analysis method implemented using the concept of fuzzy logic.
- The system is evaluated in terms of Security Index. The security index may guide cloud developers in developing a new secure cloud system. Also, helps users in the selection of appropriate cloud from the available list.
- Also, we have evaluated some existing cloud-based storage system.

The rest of the paper is organized as follows: In Sect. 2, presents a brief overview of security engineering process proposed in our previous work (Chatterjee et al. 2013); Sect. 3, presents our Proposed Methodology for the cloud-based system; Sect. 4 provides a detailed explanation of proposed methodology for Cloud storage model; Sect. 5 shows the evaluation of the existing cloud-based storage system; finally, Sect. 6 concludes the paper with direction for further research.

2 Security engineering

Security engineering is a new approach that identifies security concerns (threats) in a structured manner and provides an algorithm to implement the security requirements. Most developers enforce security during the design phase, that may result in unnecessary constraints and may make the system slow or leave loopholes in security because security concerns are not analyzed. Hence, handling of security concerns must start from the initial phases of development life cycle.

To achieve the goal of secure software development in our previous work (Chatterjee et al. 2013) a framework is proposed that handles the security related concerns parallel to SDLC activities. The proposed framework is shown in Fig. 1, and different phases of the framework are as follows:

(i) *Security requirements engineering* Security requirements applicable to the system are specified, analyzed and prioritized along with the functional and non-functional requirements. First, different functionality executed by involved actors in the system are identified. As functional requirements use assets, different threats on these assets are applicable. Therefore, threats are identified and represented in the form of security requirements. Also, threats are evaluated using risk analysis method and based on it prioritization of security requirements is done.

(ii) *Security design engineering* In this phase, design decisions are taken to implement the security requirements. Design decisions are the security algorithms mainly cryptography algorithms that are identified to mitigate the threats based on prioritized security requirements and environmental parameters namely encryption speed, bandwidth, memory requirements, and computational speed.

(iii) *Security requirements testing* In this phase deployed algorithms are tested to check if all the potential threats are mitigated. Overall security assessment and verification of the system is done.

Fig. 1 Security engineering process

In our earlier proposal, only first two phases are explored. Hence, in this paper, a proposal for security testing process is presented that completes our security engineering framework. Details of different phases of Security Engineering Process with advancement for cloud system are discussed in the subsequent sections.

3 Proposed methodology for cloud-based system

In cloud-based systems or any software system, when actors execute the functionalities they are directly or indirectly interacting or using system resources; these resources are called assets and are always a target for security attack by intruders. Therefore, it is necessary to identify all the assets that may get affected by the attack and ensure their security. This section describes a structured methodology that addresses the security of different assets in the cloud-based system. The proposed process is depicted in Fig. 2, consisting of three phases.

- Security requirements specification
- Security requirements prioritization
- Validation

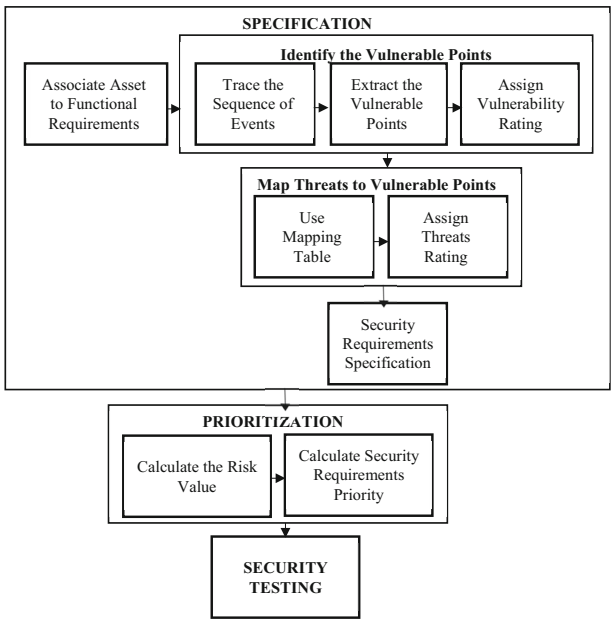

Fig. 2 Proposed methodology

3.1 Security requirements specification

In this phase, security requirements are identified along with functional and non-functional requirements based on threats to the system assets. In this phase, security requirements are generated by following activities as shown in the first part of Fig. 2.

- *Associate assets to functional requirements* Functional requirements work on assets during their execution. Therefore, different assets are associated with various functional requirements of cloud-based system. Assets are taken from a report (ENISA 2009) and list of functionality is built by studying various existing cloud-based systems.
- *Identify the vulnerable points* Vulnerability is the weakness in the system environment, where an attack is possible. So all the weakness known as Vulnerable Points that exist in the system are identified. Execution of functional requirements will give rise to vulnerable points, identify all such points associated with the functionality by the creation of a scenario. The scenario is created using the sequence diagram that represents the actors involved in the execution of functionality, their interaction, involved assets, type of data transmitted (private or secret). Vulnerabilities are taken from ENISA report (2009) which are stored in the database as shown in Tables 1 and 2. Figure 3 shows a sample scenario for 'Login' functionality, and extracted vulnerabilities is AAA (Authentication, Authorization, and Accounting).
  Identified Vulnerabilities are assessed, and vulnerability values are assigned in terms of Low (L), Medium (M), and High (H) showing the threat proneness of the vulnerable point. Vulnerability value is assigned by analyzing occurrence of threats at given weak point in vulnerability-threat mapping table presented in Tables 1 and 2. The fuzzy membership function is created for the vulnerability is depicted in Fig. 4, and membership function weights are given in Table 3.
- *Identify the threats* Threats are circumstances that have potential to cause harm to system assets, that occur at vulnerable points. Potential threats to cloud systems stored in the predefined repository assembled after doing the extensive literature review (ENISA 2009; Cloud Security Alliance 2010, 2013) and knowledge-based approach, and the repository is updated if new threat occurs. Threats corresponding to the vulnerable point are identified using the developed mapping tables shown in Tables 1 and 2. The mapping table entry represents the threat occurrence at vulnerable points. As various threats are present corresponding to the single vulnerable point, threats applicable to the particular functionality under consideration is extracted based on the information gained from the created scenario. Threats pertinent to vulnerability 'V.AAA' for Login functionality are T.Password Cracking, T.Impersonate; T.Password Reuse, extracted from the Vulnerability-Threat Mapping tables.
  Identified Threats are assessed by analyzing the system and are assigned a value in terms of Very Low (VL), Low (L), Medium (M), High (H), and Very High (VH) showing the occurrence frequency of threat. Therefore, the fuzzy membership function is created for threat rating as shown in Fig. 5 and membership function weights are given in Table 4. Weights are assigned by analyzing the threats occurrence at different vulnerable points in Vulnerability- Threat mapping table. A higher presence of threat on vulnerable points gives its higher weight.
- *Security requirements specification* Security Requirements defined by Researcher Firesmith (2003) expresses what functionality is needed to represent the threats of the system to protect the assets. Mapping of security requirements is done through analysis and experience of requirement engineers and team. For instance, security requirements to mitigate threats T.Password_Cracking, T.Impersonate and T.Password_Reuse are Identification and Authentication.

3.2 Security requirements prioritization

Prioritized security requirements would help in knowing which threat need to be handled immediately. Prioritization starts after the security requirements are specified as shown in Fig. 2. Priority is calculated by adding together the risk values of threats mitigated by the security requirements under consideration, higher the security requirement value higher is the priority. Following activities are followed for prioritization:

- *Calculate risk value for threats* The risk is a factor which shows the negative impact of threat on the system which can occur in future. Risk values corresponding to threats are calculated using fuzzy logic. The concept of Fuzzy logic is used because risk is the function of threat rating, vulnerability, and asset value. Risk function is given by Eq. (1)

$$\text{Risk} = f(\text{TR}, \text{V}, \text{AV}) \quad (1)$$

where, TR = threat rating; V = vulnerability value; AV = asset value

Threat rating and vulnerability value are fetched from the previous stage, and evaluation of identified assets is done by taking the view of interested stakeholder. The process of asset evaluation is:

Table 1 Vulnerabilities-threats mapping

Threats	Vulnerability							
	V.AAA	V.User_ Provisioning	V.User_De_ Provisioning	V.Remote_Access_ to_Management_ Interface	V.Hypervisor_ Vulnerabilities	V.Lack_of_ Resource_ Isolation	V.Lack_of_ Reputational_ Isolation	V.Communication_ Encryption_ Vulnerabilies
T.Password_Cracking	X							
T.Impersonate	X							
T.Sniffing								X
T.Social_Engineer		X				X		X
T.Disclose_Data	X							
T.Malicious code					X	X	X	
T.Repudiate	X							
T.Change_Data								X
T.Data_Theft	X							X
T.Password_Reuse	X							
T.Insider	X							
T.MITM	X							X
T.Replay_Attack								X
T.Network_Issues								
T.Resource_Exhaustion								
T.DDoS								
T.Sabotage								
T.Conflict_between_Customer_ Provider_Hardening_Process and Cloud_Environment								
T.Lock_In								
T.Loss_of_Governance								
T.Operational_Logs_Compromise	X	X	X					
T.Security_Log_Compromise	X	X	X					
T.Data_Deletion								
T.Supply_Chain_Failure								
T.Compliance_Challenges								
T.Legal_Issues						X		
T.Priviledge_Abuse	X	X	X		X			
T.Backup_Lost_Stolen	X	X	X					
T.Unauthorized_Physical_Access								
T.Natural_Disaster								
T.Malicious_Probes_Scans								
T.Data_Leakage	X							X
T.Side_Channel_Attack								
T.Cloud_Service_Termination								

Table 1 continued

Threats	Vulnerability							
	V.AAA	V.User_ Provisioning	V.User_De_ Provisioning	V.Remote_Access_ to_Management_ Interface	V.Hypervisor_ Vulnerabilities	V.Lack_of_ Resource_ Isolation	V.Lack_of_ Reputational_ Isolation	V.Communication_ Encryption_ Vulnerabilies
T.Loss_of_Encryption_Keys								
T.Cloud_Provider_Acquisition								
T.Management_Interface_Copmpromise	X			X				
T.Compromise_Service_Engine					X	X		
T.Modifying_Network_Trafic		X	X					X

Threats	Vulnerability							
	V.Lack_of_Weak_ Encryption_of_ Archive_and_ Data_in_Transit	V.Impossibility_of_ processing _Data_ in_encrypted_form	V.Poor_Key_ Management_ Procedures	V.Key_Generation: Low Entropy for Random Number Generation	V.Lack_of_ Standard_ Technologies_ and_Solutions	V.No_Source_ Escrow_ Agreement	V.Inaccurate_ Modelling_of_ Resource_ Usage	V.No_Contol_ of_Vunerability_ Assessment_ Process
T.Password_Cracking								
T.Impersonate			X					
T.Sniffing								
T.Social_Engineer								
T.Disclose_Data								
T.Malicious code								
T.Repudiate								
T.Change_Data	X							
T.Data_Theft	X							
T.Password_Reuse								
T.Insider		X						
T.MITM	X							
T.Replay_Attack	X							
T.Network_Issues								
T.Resource_Exhaustion							X	
T.DDoS								
T.Sabotage								
T.Conflict_between_Customer_Provider_ Hardening_Process and Cloud_ Environment								
T.Lock_In					X			
T.Loss_of_Governance					**X**	**X**		X

Table 1 continued

Threats	Vulnerability							
	V.Lack_of_Weak_ Encryption_of_ Archive_and_ Data_in_Transit	V.Impossibility_of_ processing _Data_ in_encrypted_form	V.Poor_Key_ Management_ Procedures	V.Key_Generation: Low Entropy for Random Number Generation	V.Lack_of_ Standard_ Technologies_ and_Solutions	V.No_Source_ Escrow_ Agreement	V.Inaccurate_ Modelling_of_ Resource_ Usage	V.No_Contol_ of_Vunerability_ Assessment_ Process
T.Operational_Logs_Compromise								
T.Security_Log_Compromise								
T.Data_Deletion								
T.Supply_Chain_Failure								
T.Compliance_Challenges					X			
T.Legal_Issues								
T.Priviledge_Abuse								
T.Backup_Lost_Stolen								
T.Unauthorized_Physical_Access								
T.Natural_Disaster								
T.Malicious_Probes_Scans								
T.Data_Leakage		X						
T.Side_Channel_Attack								
T.Cloud_Service_Termination								
T.Loss_of_Encryption_Keys			X	X				
T.Cloud_Provider_Acquisition								
T.Management_Interface_Copmpromise								
T.Compromise_Service_Engine								
T.Modifying_Network_Trafic								X

Threats	Vulnerability							
	V.Internal_Cloud_ Network_probing	V.Co-Residence_ Checks	V.Lack_ of_Forensic_ Rediness	V.Senstive_ Media_ Sanitization	V.Synchronizing_ Responsibility_ or_Contractual_ Obligation_ External to Cloud	V.Cross-Cloud_ Applications_ Creating_Hidden_ Dependency	V. SLA_ Clauses_ with_Conflicting_ Promises_ to_ different Stakeholders	V.SLA_Clauses_ Containing_ Excessive_ Business_Risk
T.Password_Cracking								
T.Impersonate								
T.Sniffing								
T.Social_Engineer								
T.Disclose_Data								
T.Malicious code								
T.Repudiate								
T.Change_Data								
T.Data_Theft								
T.Password_Reuse								
T.Insider								
T.MITM	X	X						

Table 1 continued

Threats	Vulnerability							
	V.Internal_Cloud_ Network_probing	V.Co-Residence_ Checks	V.Lack_ of_Forensic_ Rediness	V.Senstive_ Media_ Sanitization	V.Synchronizing_ Responsibility_ or_Contractual_ Obligation_ External to Cloud	V.Cross-Cloud_ Applications_ Creating_Hidden_ Dependency	V. SLA_ Clauses_ with_Conflicting_ Promises_ to_ different Stakeholders	V.SLA_Clauses_ Containing_ Excessive_ Business_Risk
T.Replay_Attack								
T.Network_Issues					X			
T.Resource_Exhaustion								
T.DDoS								
T.Sabotage								
T.Conflict_between_Customer_ Provider_Hardening_Process and Cloud_Environment							X	
T.Lock_In								
T.Loss_of_Governance					X	X	X	
T.Operational_Logs_Compromise			X					
T.Security_Log_Compromise			X					
T.Data_Deletion				X				
T.Supply_Chain_Failure						X		
T.Compliance_Challenges								
T.Legal_Issues								
T.Priviledge_Abuse								
T.Backup_Lost_Stolen								
T.Unauthorized_Physical_Access								
T.Natural_Disaster								
T.Malicious_Probes_Scans	X	X						
T.Data_Leakage	X	X						
T.Side_Channel_Attack	X	X						
T.Cloud_Service_Termination								
T.Loss_of_Encryption_Keys								
T.Cloud_Provider_Acquisition								
T.Management_Interface_Copmpromise								
T.Compromise_Service_Engine								
T.Modifying_Network_Trafic								

Table 2 Vulnerabilities Threats Mapping

Threats	Vulnerability							
	V.Audit_or_ Certification_ not_Available_ to_Customer	V.Certification_ Schemes_not_ Adapted_to_ Cloud_Infrastructure	V.Inadequate Resource Provisioning and Investments in Infrastructures	V.No Policies for Resource Capping	V.Storage of Data in Multiple Jurisdiction and Lack of Transparency about this	V.Lack of information on Jurisdictions	V.Lack of Completeness and Transparency in Terms of Use	V.Lack of Security Awareness
T.Password_Cracking								
T.Impersonate								
T.Sniffing								
T.Social_Engineer								X
T.Disclose_Data								
T.Malicious_Code								
T.Repudiate								
T.Change_Data					X			
T.Data_Theft								
T.Password_Reuse								
T.Insider								
T.MITM							X	
T.Replay_Attack								
T.Network_Issues			X					
T.Resource_Exhaustion			X	X				
T.DDoS				X				
T.Sabotage				X				
T.Conflict_between_Customer_ Provider_Hardening_Process and Cloud_Environment							X	
T.Lock_In							X	
T.Loss_of_Governance	X	X			X	X	X	
T.Operational_Logs_Compromise								
T.Security_Log_Compromise								
T.Data_Deletion								
T.Supply_Chain_Failure							X	
T.Compliance_Challenges	X	X			X	X	X	
T.Legal_Issues					X	X	X	
T.Priviledge_Abuse								
T.Backup_Lost_Stolen								
T.Unauthorized_Physical_Access								
T.Natural_Disaster								

Table 2 continued

Threats	Vulnerability							
	V.Audit_or_ Certification_ not_Available_ to_Customer	V.Certification_ Schemes_not_ Adapted_to_ Cloud_Infrastructure	V.Inadequate Resource Provisioning and Investments in Infrastructures	V.No Policies for Resource Capping	V.Storage of Data in Multiple Jurisdiction and Lack of Transparency about this	V.Lack of information on Jurisdictions	V.Lack of Completeness and Transparency in Terms of Use	V.Lack of Security Awareness
T.Malicious_Probes_Scans								
T.Data_Leakage								
T.Side_Channel_Attack								
T.Cloud_Service_Termination							X	
T.Loss_of_Encryption_Keys								
T.Cloud_Provider_Acquisition							X	
T.Management_Interface_Copmpromise								
T.Compromise_Service_Engine								
T.Modifying_Network_Trafic								

Threats	Vulnerability						
	V.Unclear Roles and Responsibilities	V.Poor Enforcement of Role Definitions	V.Need-To-Know Principle Not Applied	V.Inadequate Physical Security Procedures	V.Misconfiguration	V.System/OS Vulnerabilities	V.Lack of/Poor and Untested Business Continuity and Disaster Recovery Plan
T.Password_Cracking							
T.Impersonate							
T.Sniffing							
T.Social_Engineer				X			
T.Disclose_Data							
T.Malicious_Code							
T.Repudiate							
T.Change_Data							
T.Data_Theft							
T.Password_Reuse							
T.Insider							
T.MITM							
T.Replay_Attack							
T.Network_Issues					X	X	X
T.Resource_Exhaustion							
T.DDoS					X	X	
T.Sabotage							

Table 2 continued

Threats	Vulnerability						
	V.Unclear Roles and Responsibilities	V.Poor Enforcement of Role Definitions	V.Need-To-Know Principle Not Applied	V.Inadequate Physical Security Procedures	V.Misconfiguration	V.System/OS Vulnerabilities	V.Lack of/Poor and Untested Business Continuity and Disaster Recovery Plan
T.Conflict_between_Customer_Provider_Hardening_Process and Cloud_Environment	X						
T.Lock_In							
T.Loss_of_Governance	X	X					
T.Operational_Logs_Compromise						X	
T.Security_Log_Compromise						X	
T.Data_Deletion							
T.Supply_Chain_Failure							
T.Compliance_Challenges							
T.Legal_Issues							
T.Priviledge_Abuse	X	X	X		X		
T.Backup_Lost_Stolen				X			
T.Unauthorized_Physical_Access				X			
T.Natural_Disaster							X
T.Malicious_Probes_Scans							
T.Data_Leakage							
T.Side_Channel_Attack							
T.Cloud_Service_Termination							
T.Loss_of_Encryption_Keys							
T.Cloud_Provider_Acquisition							
T.Management_Interface_Copmpromise					X	X	
T.Compromise_Service_Engine							
T.Modifying_Network_Trafic							

Threats	Vulnerability						Threat Rating
	V.Unclear Asset Ownership	V.Poor Provider Selection	V.Lack of Supplier Redundancy	V.Application Vulnerabilities or Poor Patch Management	V.Lack of Policy or Poor Procedures for Log Collection and Retention	V.Inadequate/ Misconfigured Filtering Resources	
T.Password_Cracking							1
T.Impersonate							2
T.Sniffing							1
T.Social_Engineer							5

Table 2 continued

Threats	Vulnerability						
	V.Unclear Asset Ownership	V.Poor Provider Selection	V.Lack of Supplier Redundancy	V.Application Vulnerabilities or Poor Patch Management	V.Lack of Policy or Poor Procedures for Log Collection and Retention	V.Inadequate/ Misconfigured Filtering Resources	Threat Rating
T.Disclose_Data							1
T.Malicious_Code							3
T.Repudiate							1
T.Change_Data							3
T.Data_Theft							3
T.Password_Reuse							1
T.Insider							2
T.MITM							6
T.Replay_Attack							2
T.Network_Issues							5
T.Resource_Exhaustion			X				4
T.DDoS						X	4
T.Sabotage							1
T.Conflict_between_Customer_ Provider_Hardening_Process and Cloud_Environment							3
T.Lock_In							2
T.Loss_of_Governance							13
T.Operational_Logs_Compromise					X		6
T.Security_Log_Compromise					X		6
T.Data_Deletion							1
T.Supply_Chain_Failure		X	X				4
T.Compliance_Challenges							6
T.Legal_Issues							4
T.Priviledge_Abuse							8
T.Backup_Lost_Stolen							4
T.Unauthorized_Physical_Access							1
T.Natural_Disaster							1
T.Malicious_Probes_Scans							2
T.Data_Leakage				X			6
T.Side_Channel_Attack							2
T.Cloud_Service_Termination		X	X				3
T.Loss_of_Encryption_Keys							2

Table 2 continued

Threats	Vulnerability						Threat Rating
	V.Unclear Asset Ownership	V.Poor Provider Selection	V.Lack of Supplier Redundancy	V.Application Vulnerabilities or Poor Patch Management	V.Lack of Policy or Poor Procedures for Log Collection and Retention	V.Inadequate/ Misconfigured Filtering Resources	
T.Cloud_Provider_Acquisition							1
T.Management_Interface_Copmpromise				X			5
T.Compromise_Service_Engine							2
T.Modifying_Network_Trafic							4

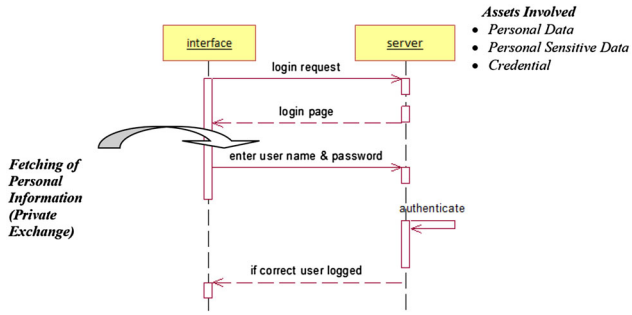

Fig. 3 Scenario using sequence diagram login functionality

- *Identify and evaluate the assets* Various assets associated with the functionality are determined and evaluated. The asset can be anything that has value to the organization; it may be tangible (infrastructure) or intangible (customer information, trust). Therefore, identification and evaluation of assets are important for providing security in the software systems. Asset evaluation is done to know its importance for the organization. Most of the risk analysis, methods such as CRAMM (2005), den Braber et al. (2007) assigns the asset value based on its importance for the organization. However, we conjure that if asset values are allocated by taking a view of each concerned stakeholders, it will be more accurate.

  (i) *Identify the assets associated with different functionality*. Assets related to the functionalities of direct stakeholders are identified. As stakeholders may need different assets, and different stakeholder can use an asset. Therefore, m:n mapping exists between them. So each stakeholder assigns a value to involved assets required for his functionality in the range (Very Low (VL), Low (L), Medium (M), High (H), Very High (VH)) representing the importance of asset for him. For illustration consider an asset 'User Login Information' is rated by the stakeholder's Customer as High (H), Bank Employee as Medium (M) and Bank DBMS as Medium (M).

  (ii) *Calculate final asset value* Final asset value is calculated by analyzing the view of different stakeholders using fuzzy rules listed in Table 5. A total of 125 rules are made for the calculation of final asset values. For example, asset 'User Login Information' value comes to be Medium (M) by application of created rules (Rule no. 5 of Table 5).

A fuzzy system for the above function where threat rating, vulnerability, and asset values are input, and risk value as the output is designed. Fuzzy rules are created for

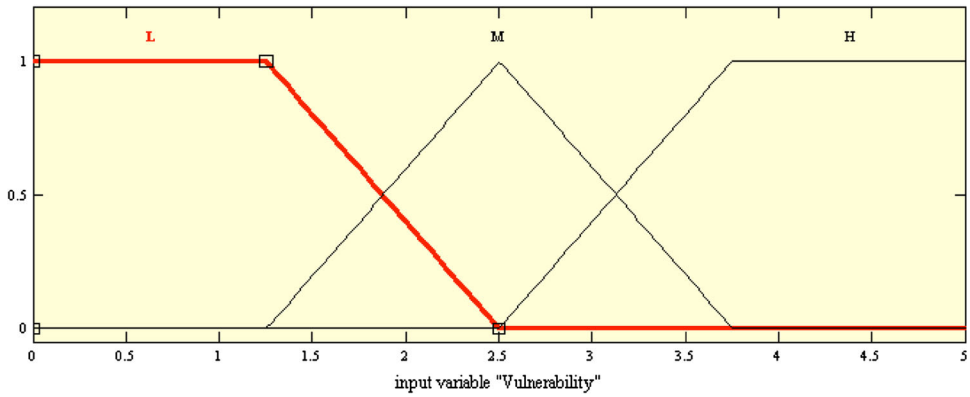

Fig. 4 Membership function for vulnerability

Table 3 Weights of vulnerability variables

Variable	Value
L	(0, 0, 1.25, 2.5)
M	(1.25, 2.5, 3.75)
H	(2.5, 3.75, 5, 5)

calculation of risk values. A Fuzzy Inference system designed to calculate the value of risk, corresponding membership functions, and its value are shown in Figs. 6, 7 and Table 6 respectively. For accurate calculation, ten different output membership functions are used for risk value.

Total 75 rules are formed for risk calculation some rules are shown in Table 7.

Based the calculated risk values threats are categorized in Essential, Important, Tolerable, and No Influence category, category and its detail are mentioned in Table 8. This categorization would help in choosing the optimal security algorithm for implementation.

- *Prioritize the security requirements* Priority of Security Requirements is calculated using risk values of threats mitigated by them. If the security requirement is mitigating three threats, then the security requirement value is simply the sum of risk values corresponding to threats mitigated. This value would act as security requirement priority; higher the security requirement value higher is the priority. For instance, risk values for threats, T.Password_Cracking is 2.74 and T.Impersonate is 4.22 then the value of security requirements Identification, and Authentication will be $(2.74 + 4.22 = 6.96)$. Similarly, other security requirements are prioritized based on the risk value of threats.

3.3 Security testing

The process of security testing starts once the prioritized security requirements are implemented using some security algorithms which is selected based on the environment constraints of the system. Security testing is the process of evaluation of selected security mechanism to mitigate potential threats in the system. For the purpose of assessment vulnerability metric values are generated that shows the remaining risk present in the system. Then a Security Index is calculated which estimates the security gap of cryptographic mechanisms. The metric value helps the software developer to enhance/revise the existing algorithm. Finally, a test report that contains all related information about security is generated. Proposed process of Security Testing is shown in Fig. 8, and various steps involved in the process are as follows:

- *Check threat mitigation* Potential threat identified for functionality is validated for its mitigation, from the attack analysis repository of deployed cryptography algorithms. Threats which are not mitigated are considered as live/active threats. Live threats analogous

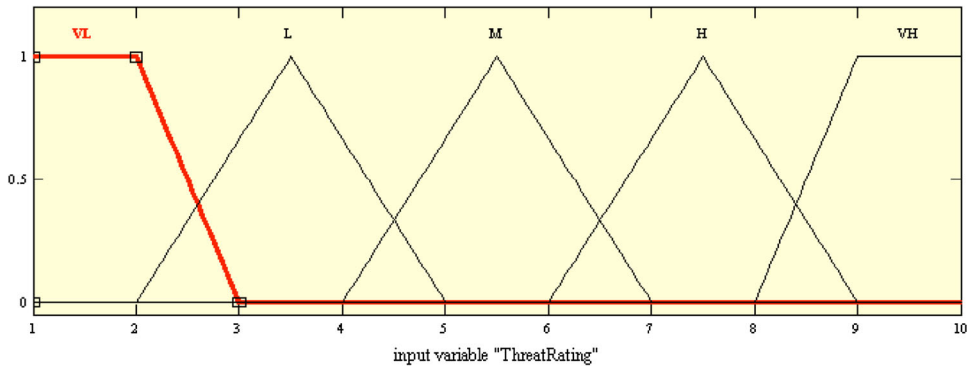

Fig. 5 Membership function for threat rating

to all functionalities are assembled by analyzing the scenario diagram. Finally, a vulnerability metric (V_i) is calculated for each active threat which is nothing but their corresponding risk values. Continuing our example both threats are mitigated by chosen security algorithm, so V_i becomes zero.

$$V_i = \sum f(\text{Risk Value of Live Threats for Functionality } F_i)$$

- *Calculate the security index* Security index shows the gap in the security of the system. Security index is calculated using Eq. (2). For our example, SI will be zero means no gap in security exists.

Table 4 Weights of variables for threat rating

Variable	Value
VL	(1, 1, 2, 3)
L	(2, 3.5, 5)
M	(4, 5.5, 7)
H	(6, 7.5, 9)
VH	(8, 9, 10, 10)

Table 5 Rules to calculate asset values

Rule. no.	Rule	Output
1.	If (ST1 is VL) and (ST2 is VL) and (ST3 is VL)	VL
2.	If (ST1 is L) and (ST2 is VL) and (ST3 is VL)	VL
3.	If (ST1 is M) and (ST2 is VL) and (ST3 is VL)	L
4.	If (ST1 is H) and (ST2 is VL) and (ST3 is VL)	L
5.	If (ST1 is H) and (ST2 is M) and (ST3 is M)	M
6.	If (ST1 is H) and (ST2 is H) and (ST3 is H)	H

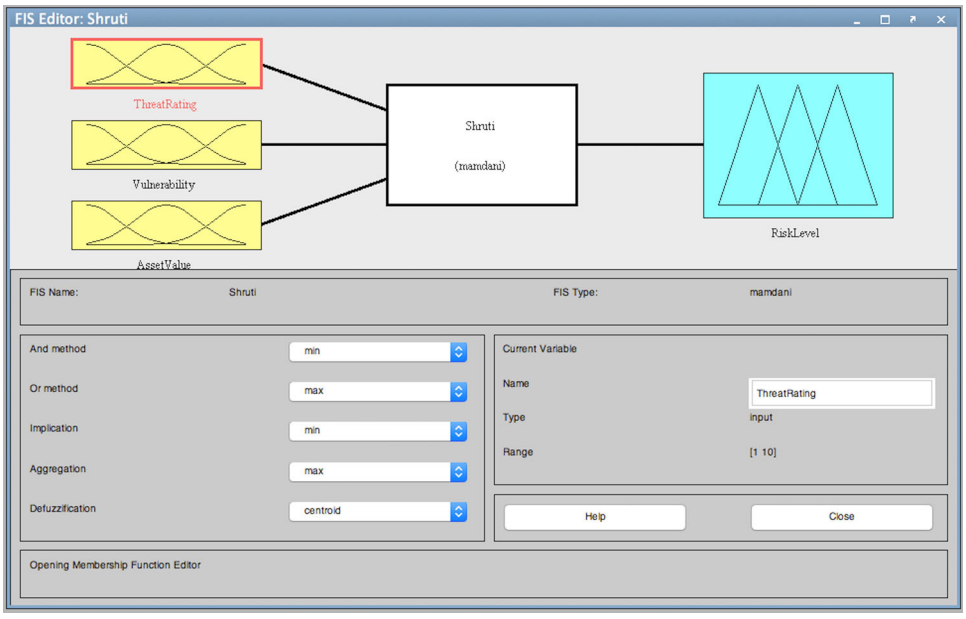

Fig. 6 Fuzzy inference system (FIS Editor) for risk calculation

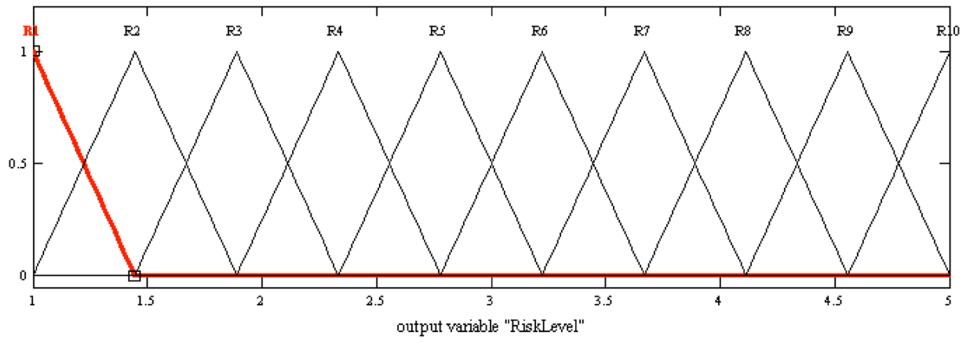

Fig. 7 Membership function for risk

Table 6 Weights of variables for risk

Variable	Value
R1	(0.5, 1, 1.4)
R2	(1, 1.4, 1.8)
R3	(1.4, 1.8, 2.3)
R4	(1.8, 2.3, 2.7)
R5	(2.3, 2.7, 3.2)
R6	(2.7, 3.2, 3.6)
R7	(3.2, 3.6, 4.1)
R8	(3.6, 4.1, 4.5)
R9	(4.1, 4.5, 5)
R10	(4.5, 5, 5)

$$\text{Security Index (SI)} = \sum_{1}^{n} f\left(\frac{V_i}{R_i}\right) \quad (2)$$

where V_i is the vulnerability metric of live threats for the functionality F_i; R_i is the total risk value of functionality F_i; n is number of Functionality considered.

The value of security index will act as a quality parameter showing the system proneness to various threats. Lower is the security index value higher is the security and vice versa. Hence the Security Index value indicates the effectiveness of chosen security algorithms.

- *Generate test report* The test report is generated for the system under test representing the summary of testing activities. The template will help the developer to decide further activities as it contains all the security related information such as threats implemented by algorithm, their associated risk value, unresolved threats, security index showing effectiveness of selected algorithms. A sample test report is shown in Table 9.

4 Application of proposed security methodology for cloud storage systems

In this section proposed methodology is applied and explained for evaluation of cloud-based storage system. Storage model is chosen for illustration among the available service models because it is the most widely used service and requires high security.

4.1 Security requirements specification

The security needs of the system are derived from functional requirements and represented in the form of security requirements. In a cloud-based storage system, different stakeholders are Cloud Customer, Cloud User, Cloud Service Provider. Here only one actor that is Cloud Customer is considered for illustration of further activities, as cloud user functionalities are the subset of it and provider is serving to customer's requests. Therefore, all security issues are dependent on the functionalities related to cloud customer. Functionality, associated asset, vulnerability, threats and security requirements for the system is given in Table 10.

Table 7 Showing rules to calculate risk value

S. no.	Rule	Output
1.	If (Threat Rating is VL) and (Vulnerability is L) and (Asset Value is VL)	R1
2.	If (Threat Rating is VL) and (Vulnerability is M) and (Asset Value is VL)	R4
3.	If (Threat Rating is VL) and (Vulnerability is H) and (Asset Value is VL)	R5
4.	If (Threat Rating is L) and (Vulnerability is L) and (Asset Value is VL)	R4
5.	If (Threat Rating is L) and (Vulnerability is M) and (Asset Value is VL)	R5
6.	If (Threat Rating is H) and (Vulnerability is M) and (Asset Value is M)	R6
7.	If (Threat Rating is H) and (Vulnerability is M) and (Asset Value is VH)	R8

Table 8 Category of threats based on risk values

Category	Risk range	Need of handling threat
Essential	Risk $\geq$ 10	Threats are critical as they are impacting various (greater than three) high-value assets, so need urgent handling
Important	10 > Risk $\geq$ 4	These threats are important as they are impacting: Various (greater than three) moderate assets Either single high-value asset or two moderate assets So require careful consideration
Tolerable	4 > Risk $\geq$ 2	These threats are impacting single, or two moderate value assets so can be considered or ignored
No Influence	Risk < 2	These threats are impacting single low-value asset, therefore ignore them

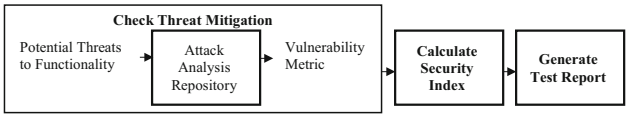

Fig. 8 Process of security testing

4.2 Security requirements prioritization

Security requirements identified in the previous phase are now prioritized. For calculation of priority first the asset values are calculated, calculation of asset value is shown in Table 11. Assets values are calculated using the fuzzy rules of Table 5, calculation of some assets are shown as the list is very vast. Then the risk value of threats is calculated using fuzzy rules defined in Table 7 and then based on these risk values Security requirement are prioritized. Table 12 shows the calculation of risk values for threats identified and Table 13 shows the priority of Security requirements based on risk values. Because of space limitation, only first two functionalities of Table 10 are considered namely Registration/Login/Update Login and Store Data/Download Data/Share Data.

After prioritization of security requirements, algorithms for implementation is chosen by considering the environment and other constraints as presented in our previous work (Chatterjee et al. 2013). Then testing is done by calculating the security index value, followed by generation of the test report. The testing process is explained in the next section for evaluation of existing cloud-based storage system.

5 Evaluation of the existing cloud storage

In this section existing cloud-based storage are evaluated to know the level of security provided by them to users. Various security incidents and threats are reported in the past (Kuppuswamy and Al-Khalidi 2014; Dropbox: Yes, We Were Hacked 2012; DropBox Storage Service 2016; Newton 2011) on cloud storage systems.

Different security algorithm implemented by primary cloud storage is shown in Table 14. Here we are only considering the login and storage part. Now the security index value is calculated for each cloud storage specified in Table 14 (main focus is on the authentication and encryption part).

5.1 Dropbox

5.1.1 Initial version

Dropbox provides TLS secure communication channel for both registration and login process. Customers are allowed to enter first and last name, email address and desired password during the registration process. Email address is used to login into Dropbox and password length should be of six characters. It shows the already registered e-mail address error warning to users during the registration process which in addition to weak password strength makes "T.Password_Cracking" threat easy and it would lead to "T.Password_Reuse" and "T.Social Engineering" threats. It also does not send any activation emails after the registration to customers, resulting in "T.Impersonate" threat possible on it.

It uses AES-128-bit encryption algorithm for the encryption of customer data stored on its servers, but only at server side using its encryption key to which the client is unaware. Hence, a "T.Change_Data" and "T.Data_Theft" threat applies on Dropbox.

$$SI = \left(\frac{2.94 + 6.44 + 2.94}{2.94 + 6.44 + 2.94} + \frac{3.22 + 18.03 + 15.24}{3.22 + 18.03 + 15.24 + 13.9 + 11.4 + 6.01 + 5.12 + 11.4 + 4.34}\right)$$

$$SI = (1 + 0.43) = 1.43$$

The SI value is divided by 2 as we have considered two functionalities. Therefore, the security index comes to be a combination of two functionalities.

SI is 0.715 that is 71.5% which is very high that shows system is not safe. As various security breaches are possible, so Dropbox has added new security feature in a later version.

Table 9 Sample test report

	System under test
Applied/chosen security algorithms	List of Algorithms chosen to implement the prioritized security requirements
Threats and risk	List of potential threats at different vulnerable points with their risk measure
Mitigated threats	List of threats mitigated by chosen algorithms
Live threats	List of threats not implemented by chosen security algorithms
Security index	The value of Security Index showing the level of protection
Suggestions	Any suggestion or recommendation required for enhancing the level of security in the system

Table 10 Vulnerabilities, threats, assets for customers functionalities

S. no.	Functionality	Vulnerabilities extracted	Threats	Affected assets	Security requirement
1.	Registration (new Customer)/ Login (Existing Customer) and Update Login Detail	V.AAA	1. T.Password_Cracking 2. T.Impersonate 3. T.Password_Reuse	Personal Data (2) Personal Sensitive Data (2) Credentials (1,3)	Identification Authentication
2.	Store data/ Download Data/ Share Data	V.Lack of Resource Isolation V.Lack of Reputational Isolation V.Communication Encryption Vulnerabilities V.Lack of or weak Encryption or Archives and Data in Transit V.Sensitive Media Sanitization V.Storage of Data in Multiple Jurisdictions and lack of Transparency about this V.Misconfiguration V.Lack of, or a poor and untested, Business Continuity and Disaster Recovery Plan	1. T.Social Engineer 2. T.Change_Data 3. T.Sniffing 4. T.Data_Theft 5. T.MITM 6. T.Replay Attack 7. T.Data_Leakage 8. T.Modifying_Network_Traffic 9. T.Data_Deletion 10. T.Loss_of_Governance 11. T.Compliance_Challenge 12. T.Legal_Issues 13. T.Network_Issues 14. T.DDoS 15. T.Priviledge_Abuse 16. T.Natural_Disaster	Company Reputation (10,11,12,16) Employee Loyalty and Experience (15) Personal Sensitive Data (2,3,4,5,7) Personal Data (2,3,4,5,7) HR Data (2,3,4,5) Service Delivery- real time services (14,16) Service Delivery (14) Credentials (1,6) User Directory (data) (2, 3,4,9,16) Cloud Service Management Interface (6,11) Network (connections, etc.) (2,3,5,8,13,16) Backup or Archive Data (2,3,4,7,9,10,11,12,16)	Identification Authentication Immunity Integrity Intrusion Detection Privacy Survivability Multi-Trust System Maintenance Authorization Physical Protection
3.	Manage automatic backup	V.Sensitive Media Sanitization V.Untrusted Software	1. T.Data_Deletion 2. T.Malicious_Code	User Directory (data) (1,2) Backup Archive Data (1,2)	Integrity Immunity Intrusion Detection
4.	Upgrade storage space	V.No Policies for Resource Capping V.Resource Consumption Vulnerabilities	1. T.DDoS 2. T.Resource Exhaustion	User Directory (data) (1) Backup or Archive Data (1,2)	Immunity Survivability
5.	Make payment	V.AAA	1. T.Password_Cracking 2. T.Impersonate 3. T.Password_Reuse 4. T.Insider	Personal Data (2,4) Credentials (1,3)	Identification Authentication Authorization

Table 10 continued

S. no.	Functionality	Vulnerabilities extracted	Threats	Affected assets	Security requirement
6.	Maintenance and Management of Identity Management System/ Authentication platform (including enforcing password policy)/ Data and Traffic monitoring for security risk avoidance	V.AAA	1. T.Password_Cracking 2. T.Impersonate 3. T.Disclose_Data 4. T.Repudiate 5. T.Data_Theft 6. T.Password_Reuse 7. T.Insider 8. T.Operational Log Compromise 9. T.Security Log Compromise 10. T.Priviledge_Abuse 11. T.Data_Leakage	Company Reputation (2,4) Employee Loyalty and Experience (3,4,7,10) Personal Sensitive Data (2,3,5,11) Personal Data (3,5,7,11) Credentials (1,2,4,6) User Directory (data) (5,11) Cloud Service Management Interface (14) Operational Logs (5,8) Security Logs (5,9) Backup or Archive Data (3,11)	Identification Authentication Privacy Immunity Non-Repudiation Authorization Security Auditing
7.	Delete Data from Cloud/ Migrate from one Cloud Provider to other/ End of Subscription	V.AAA V.User De-Provisioning	1. T.Repudiate 2. T.Data_Theft 3. T.Password_Reuse 4. T.Insider 5. T.Operational Log Compromise 6. T.Security Log Compromise 7. T.Backup_Lost_Stolen 8. T.Modifying_Network_Traffic	Employee Loyalty and Experience (1,4) Personal Sensitive Data (2,4,7) Personal Data (2,4,7) HR Data (2,7) Credentials (1,3) User Directory (data) (2,7) Operational Logs (5) Security Logs (6) Backup or Archive Data (2,7) Network (connections, etc) (8)	Non-Repudiation Privacy Authentication Authorization Security Auditing Integrity Physical Protection Intrusion Detection Survivability

Table 11 Evaluation of involved asset

Asset	Customer	User	Provider	Asset value
Credentials	H	H	H	H
Personal data	H	H	M	H
Personal sensitive data	VH	H	H	H
HR data	L	VL	M	L
User directory data	H	H	M	H
Network (connection, etc.)	L	L	H	M
Backup or archive data	M	M	M	M
Service delivery-real time services ()	H	H	H	H
Service delivery ()	H	M	M	M
Company reputation ()	H	M	H	H
Cloud service management interface	VL	VL	H	L

Table 12 Showing the risk value of threats

Threat	Threat rating	Vulnerability	Affected asset and asset value	Risk on various assets	Risk value
T.Password Cracking	VL	H	Credentials (H)	2.94	2.94
T.Impersonate	L	H	Personal data (H)	3.22	6.44
			Personal sensitive data (H)	3.22	
T.Password_Reuse	VL	H	Credentials (H)	2.94	2.94
T.Social Engineer	M	M	Credentials (H)	3.22	3.22
T.Sniffing	VL	M	Personal data (H)	2.39	13.9
			Personal sensitive data (H)	2.39	
			HR data (L)	1.95	
			User directory data (H)	2.39	
			Network (connection, etc.) (M)	2.39	
			Backup or archive data (M)	2.39	
T.Data Theft	L	H	Personal data (H)	3.22	15.24
			Personal sensitive data (H)	3.22	
			HR data (L)	2.79	
			User directory data (H)	3.22	
			Backup or archive data (M)	2.79	
T.Change Data	L	H	Personal data (H)	3.22	18.03
			Personal sensitive data (H)	3.22	
			HR data (L)	2.79	
			User directory data (H)	3.22	
			Network (connection, etc.) (M)	2.79	
			Backup or archive data (M)	2.79	
T.MITM	H	H	Personal sensitive data (H)	3.87	11.4
			Personal Data (H)	3.87	
			Network (connections, etc.) (M)	3.66	
T.DDoS	M	M	Service delivery-real time services (H)	3.22	6.01
			Service delivery (M)	2.79	
T.Replay attack	L	M	Credentials (H)	2.79	5.12
			Cloud service management interface (L)	2.33	
T.Data Leakage	H	H	Personal data (H)	3.87	11.4
			Personal sensitive data (H)	3.87	
			Backup or archive data (M)	3.66	
T.Data Deletion	VL	L	User directory data (H)	2.39	4.34
			Backup or archive data (M)	1.95	

Table 13 Prioritized security requirements

Security requirements	Threats mitigated	Risk value	Security requirement value	Priority
Identification	T.Password_Cracking	2.94	57	1
	T.Impersonate	6.44		
	T.Social_Engineer	3.22		
	T. Change Data	18.03		
	T.Data_Theft	15.24		
	T.DDoS	6.01		
	T.Replay_Attack	5.12		
Authentication	T.Password_Cracking	2.94	57	1
	T.Impersonate	6.44		
	T.Social_Engineer	3.22		
	T. Change Data	18.03		
	T.Data_Theft	15.24		
	T.DDoS	6.01		
	T.Replay_Attack	5.12		
Authorization	T.Change Data	18.03	37.62	3
	T.Data_Theft	15.25		
	T.Data_Deletion	4.34		
Integrity	T.Change_Data	18.03	58.58	2
	T.Data_Theft	15.25		
	T.Sniffing	13.9		
	T.Data_Leakage	11.4		
Immunity	T.DDoS	6.01	6.01	6
Intrusion Detection	T.Sniffing	13.9	13.9	5
Survivability	T.Natural Disaster	11.07	11.07	4

Table 14 Security algorithm employed by cloud storage systems

Storage Service	Personal encryption (user manage their encryption key or password; provider is not able to access user data)	Transmission	Storage encryption	2 Step authentication	SI value	Remarks
DropBox (initial version)	No	AES-128, SSL/TLS	AES-256	No	71.5	SI very high
DropBox (later version)	No	AES-128, SSL/TLS	AES-256	Yes	18.7	SI is not acceptable
MEGA	Yes	AES-256 TLS and RSA	AES-128	No	0	SI is nil but if the user lost the encryption key he is not able to retrieve its data.
Google Drive	No	256-SSL/TLS	AES-128	Yes	18.7	SI is not acceptable
iCloud	–	AES-128 SSL	AES-128	Yes	–	As all security algorithms are not known

5.2 Later version

$$SI = \left(\frac{0}{2.94 + 6.44 + 2.94} + \frac{18.03 + 15.24}{3.22 + 18.03 + 15.24 + 13.9 + 11.4 + 6.01 + 5.12 + 11.4 + 4.34}\right)$$

$$SI = (0 + 0.375) = .375$$

Again the SI value is not low (18.7%), so we can say that if the control of encryption key is with provider system is susceptible to a security breach which is not acceptable.

5.3 MEGA

Security Index = 0/64.98 = 0

In the case of MEGA encryption control is with the user, so it is secure. However, the problem with MEGA is that if the user forgets the key, he cannot make access to the storage system.

Hence from the Table 14 and calculated the value of security index, we can conclude that initial version of Dropbox lacks in security. Also, the later version is also not that much secure as it should be. As we can see from Table 14 that various other cloud providers are providing encryption to data at rest but are keeping the control of encryption key with them. That leads to severe threats and is not acceptable because we are storing our personal, private, financial data in these cloud storages.

6 Conclusions and further research directions

Our findings suggest that real world cloud storage services are not safe, several threats are still possible. As different cloud storage providers are using a different level of security means some of them are encrypting the stored data, some are encrypting data at the client side, and some are giving control of security to users while others are keeping it with providers. This mismatch in the system creates the serious security confusion to the user in the selection of cloud system for their use. Threats are possible only because of improper elicitation and handling of Security Requirements during the development process. However, if our proposed methodology is applied to developing similar Cloud-based Storage models, all possible threats are uncovered for functional requirements and represented in the form of security requirements during the initial phase. Knowing the security requirements beforehand would help the developer greatly during the implementation as well as it would reduce the cost of system development. As adding security after release or implementation require issue on new versions that incur a lot of cost and effort. Also, our proposal helps in the evaluation of security provided by the current cloud-based systems.

Further, as an extension of our proposal following issues needs investigation:

- Need to do more case studies to propose a generic method for security.
- Need to develop and test a configurable method for constrained domains such as mobile devices, new emerging technologies such as Internet of Things, Big Data.

References

Arkin B, Stender S, McGraw G (2005) Software penetration testing. Secur Priv 3(1):84–87

Basin D, Doser J, Lodderstedt T (2006) Model drive security: from UML models to access control infrastructures. ACM Trans Softw Eng Methodol (TOSEM) 15(1):39–91

Chatterjee K, Gupta D, De A (2013) A framework for development of secure software. CSI Trans ICT 1(2):143–157

Che J, Duan Y, Zhang T, Fan J (2011) Study on the security models and strategies of cloud computing. In: International conference on power electronic and engineering application. Proc Eng 23: 586–593

Cloud Security Alliance (2010) Top Threats to Cloud Computing. Version 1.0. http://www.cloudsecurityalliance.org/topthreats/csathreats.v1.0.pdf

Cloud Security Alliance (2013) The notorious nine: Cloud computing threats in 2013. http://www.cloudsecurityalliance.org/topthreats/

CRAMM (2005) United Kingdom Central Computer and Telecommunication Agency (CCTA) Risk analysis and management method, CRAMM user guide, *Issue 5.1*. United Kingdom

den Braber F, Hogganvik I, Lund MS, Stølen K, Vraalsen F (2007) Model-based security analysis in seven steps—a guided tour to the CORAS method. BT Technol J 25(1):101–117

DropBox storage service (2016) Consulté le March 2016, sur https://www.dropbox.com/

Dropbox: Yes, We Were Hacked (2012) Consulté le december 2015, sur http://gigaom.com/cloud/dropbox-yes-we-were-hacked/

ENISA (2009) Cloud Computing Benefits, risks and recommendations for information security http://www.enisa.europa.eu/

Felderer M, Zech P, Breu R, Buchler M, Pretschner A (2014) Model-based security testing: a taxonomy and systematic classification. Softw Test Verif Reliab 26:1–29

Ficco M, Palmieri F, Castiglione A (2015) Modeling security requirements for cloud-based system development. Concurr Comput 27(8):2107–2124

Firesmith DG (2003) Security use cases. J Obj Technol 2(3):53–64

Honer, P. (2013). Cloud computing security requirements and solutions: A systematic literature review. In: 19th twenty student conference on IT

Islam S, Mouratidis H, Edgar RW (2011) A goal-driven risk management approach to support security and privacy analysis of cloud- based system. In: Mario Piattini EF-M (ed) Security engineering for cloud computing. IGI Global, Hershey

Jaiswal S, Gupta D (2009) Security requirements prioritiztion. Softw Eng Res Pract 673–679

Ko R, Lee SS (2013) Cloud computing vulnerability incidents: A statistical overview. Retrieved from cloudsecurityalliance.org: https://cloudsecurityalliance.org/download/cloud-computing-vulnerability-incidents-a-statistical-overview/

Kuppuswamy P, Al-Khalidi S (2014) Analysis of security threats and prevention in cloud storage: review report. Int J Adv Res Eng Appl Sci 3:1–10

Liu F, Tong J, Mao J, Bohn R, Messina J, Badger L, Leaf D (2011) NIST cloud computing reference architecture: recommendations of the national institute of standards and technology. NIST Special Publication, Gaithersburg, pp 500–592

Mouratidis H, Giorgini P (2007) Security Attack Testing (SAT)—testing the security of information systems at design time. J Inform Syst 32:1166–1183

Naveed R, Abbas H (2014) Security requirements specification framework for cloud users. In: Future information technology, Lecture Notes in Electrical Engineering, vol 276, pp 297–305

Newton D (2011) Dropbox authentication: insecure by design. Récupéré sur dereknewton.com: http://dereknewton.com/2011/04/dropbox-authentication-static-host-ids/

Rong C, Nguyen S, Jaatun M (2013) Beyond lighting: a survey on security challenges in cloud computing. Comput Elect Eng 39(1):47–54

Schieferdecker I, Grossmann J, Schneider M (2012) Model-based security testing. Workshop on model-bsed testing 2012 (MBT 2012), pp 1–12

Sun D, Chang G, Sun L, Wang X (2011) Surveying and analyzing security, privacy and trust issues in cloud computing environments. Advances in control engineering and information science. Proc Eng 15:2852–2856

Sun Y, Zhang J, Xiong Y, Zhu G (2014) Data security and privacy in cloud computing. Int J Distrib Sens Netw 10(7):1–9

Wang L, Wong E, Xu D (2007) A threat model driven approach for security testing. In: Third international workshop on software engineering for secure systems (SESS 2007). IEEE Computer Society

Waste Biomass Valor
DOI 10.1007/s12649-017-9935-8

ORIGINAL PAPER

Experimental Studies on Utilization of *Prunus armeniaca* L. (Wild Apricot) Biodiesel as an Alternative Fuel for CI Engine

Ashok Kumar Yadav[1] · Amit Pal[2] · Alok Manas Dubey[1]

Received: 20 September 2016 / Accepted: 8 April 2017

Abstract In present research work, *Prunus armeniaca* L. (Wild Apricot) Seed oil has been investigated to produce biodiesel. The free fatty acid (FFA) content of the *Prunus armeniaca* oil (PAO) was <2%, so a single stage alkali catalyzed transesterification process was used to produce *Prunus armeniaca* methyl ester (PAME). The transesterification was conducted using optimum condition of 1% (w/w) potassium hydroxide as catalyst, 55 °C reaction temperature and 60 min reaction time with constant stirring at 400 rpm. Transesterification process gave a maximum yield of 96.5% by weight of *Prunus armeniaca* biodiesel. Fuel properties determined in the study conform to standards set for the ASTM D6751 and EN 14214. PAME exhibited a satisfying oxidative stability of 6.3 h and high cetane number (58.7) compared to petrodiesel (49.7). The experiments were conducted using various blends (B5, B10, B20 and B30) of the methyl ester of PAO with diesel in a single cylinder, four strokes, and direct injection diesel engine. The test results show that the brake thermal efficiency (BTE), in general, was found to be decreased and brake specific fuel consumption (BSFC) increased with increased volume fraction of *P. armeniaca* biodiesel (PAME) in the blends. A marginally higher BTE and lower BSFC noticed for B5 blend than diesel. At higher load conditions, CO, UHC and smoke opacity were found lower for all PAME blends in comparison to neat diesel. The NOx emissions were found to be increased for PAME based fuel in comparison to neat diesel. It may be concluded from the experimental investigations that PAME, can be an alternative for petrodiesel that can be used in a diesel engine without any major modification in the engine.

Keywords *Prunus armeniaca* L. oil · *Prunus armeniaca* methyl ester (PAME) · Transesterification · Physico-chemical characteristics · Engine performance and emission

Introduction

The exponential rise of petroleum consumption in industrial, transportation and technology developments has been leading to depletion of the limited fossil fuel resources in the world. Because of this, researchers have been giving more attention to find alternative energy resource such as biodiesel, which is renewable, biodegradable and non-toxic [8, 15]. Biodiesel can be produced from vegetable oil, animal fat and waste cooking oil [9, 17]. However feed stock type, availability and cost are the obstacles to the commercialization of biodiesel. It is, therefore, inevitable to look for non-edible but economically viable feed stocks as alternatives to edible vegetable oils. Several such feedstocks's, are Jatropha, *Calophyllum inophyllum*, Rubber seed, Neem, Tobacco, Karanja and Madhuca indica etc. are already under consideration and the worldover these feed stocks are considered as a potential source for biodiesel [2–4].

Substantial research work has been reported with regards to the production and performance of biodiesel derived from variety of vegetable oils. Cheikh et al. [5] reported production and performance of waste cooking oil (WCO) biodiesel and compared to diesel. The BSFC of B100 and its blends was almost higher, a noticeable increase in BSFC

✉ Amit Pal
amitpal@dce.ac.in

[1] Department of Mechanical Engineering, Raj Kumar Goel Institute of Technology, Ghaziabad 201003, India

[2] Department of Mechanical Engineering, Delhi Technological University, Delhi 110042, India

Published online: 22 April 2017

was observed when the biodiesel blend ratio raised from 50 to 100%. Dhar and Agarwal [6] reported maximum torque for 10 and 20% KOME blends which were higher than mineral diesel. Similarly, Raheman and Ghadge [13] found the comparable performance of Mahua biodiesel and its blends with petroleum-based diesel. Mufijur et al. [10] have also reported reduction in UHC and CO emissions but higher NOx emission. Ong et al. [12] reported an optimum yield of *C. monophylum* biodiesel at 9:1 methanol to oil ratio with 1 wt%. NaOH catalyst at 50 °C for 2 h. The performance and emission of 10% *C. inophyllum* biodiesel blends (CIB10) gave a satisfactory result in diesel engines. Also, biodiesel has good ignition ability in the engine due to its higher cetane number than for diesel fuel [1].

From above literature, it is evident that no reliable work has been done on the utilization of *Prunus armeniaca* oil as an alternate fuel for CI engine. Hence, the objective of the present study is to extract oil from *P. armeniaca* L. seeds, investigation of biodiesel production from "*P. armeniaca* oil" as the promising and novel feedstock using homogeneous alkaline catalysts KOH, physicochemical characterization and its performance and emission analysis on a CI engine.

Materials and Methods

The *P. armeniaca* L. fruits (Fig. 1) were collected from a village of Almora district of Uttrakhand, India. Pulps removed, seeds dried in sunlight, deshelled and the kernel crushed using a grinder prior to oil extraction. Solvents and other chemicals used in this research including potassium hydroxide (85%), methanol (99%) and n-hexane (98%) were purchased from a chemical store situated in New Delhi India.

Prunus armeniaca Seeds

Prunus armeniaca belongs to the family Rosaceae, is an important non-edible oil crop of mid hills and dry temperate

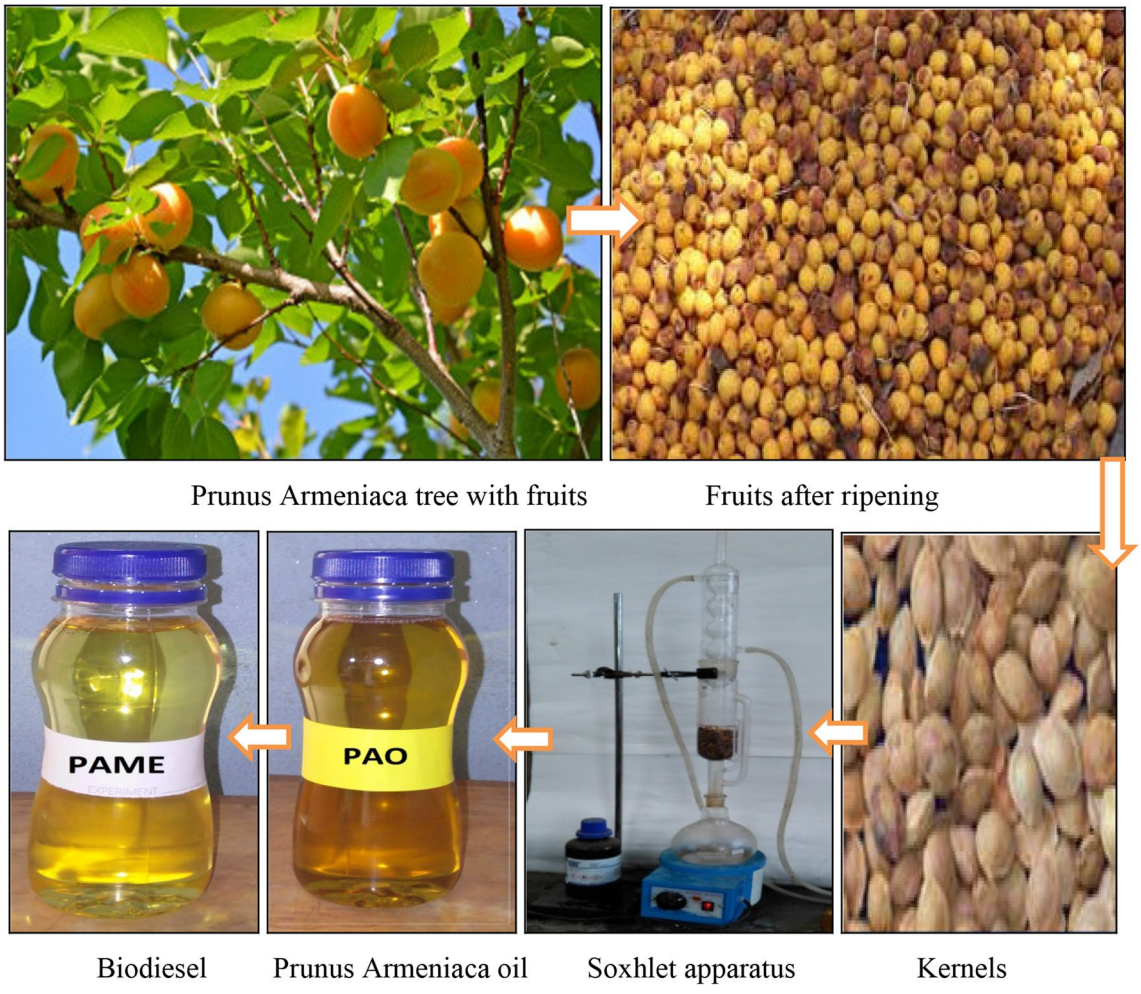

Fig. 1 *Prunus armeniaca* tree with fruits, fruits after ripening, kernels, oil, biodiesel and Soxhlet apparatus

regions of the India. In the Himalayan region of the country, local communities known it by different names viz. Chulli, Khurmani, Chulu, Aaroo, Zardhi, Khubani, Chuari and Chola. The cultivated *P. armeniaca* has its origin in North-Eastern China, whereas, *P. armeniaca* appears to be indigenous to India. It is found in the dry temperate regions of North-Western Himalayas particularly in the valleys of Jammu and Kashmir (especially Ladakh), Chenab; Kullu and Shimla regions of H.P. and Garhwal hills of Uttrakhand at altitudes up to 3000 m. In Kumaon region, *P. armeniaca* is found in all the three districts of Nainital, Almora and Pithoragarh. Pithorgarh district has a maximum density of *P. armeniaca* tree in the Kumaon region. The height of the tree is about 10–15 m with a reddish brown bark leaves. *P. armeniaca* fruits generally start maturing from last week of May and continue up to August end depending upon altitude and location. The tree starts bearing at the age of 4–5 years and continues to bear well for 50–60 years. The full bearing occurs at about 10–15 years when it yields about 100–150 kg. fruits per tree. The stone yield varies from 12 to 17% of fruits and the kernel yield ranges 3.14–4.81 kg/tree. The *P. armeniaca* fruits yield 22–38 percent kernels and 54.21% oil [7]. On the other hand, the press cake, left after oil extraction is considered unfit for human consumption and as cattle feed due to the presence of hydro-cyanic acid, however, can be utilized as fuel and fertilizer [16].

Methods

Oil Extraction

A Soxhlet apparatus (shown in Fig. 1) and n-hexane as extraction solvent were used for this work. The apparatus was initially charged with powdered *P. armeniaca* kernels, which was packed in a cloth. A round bottom flask was filled with the extraction solvent and the whole set up was heated up in a heating mantle at a temperature of 60–70 °C. The extraction solvent in the solvent–oil mixture was recovered and recycled by distillation. The oil was extracted with petroleum ether from the crushed kernel in a Soxhlet extractor. The solvent was then removed at 50 °C.

Biodiesel Production Method

A known quantity of the oil was measured and poured into a conical flask. The oil was pre heated to 105 °C. A specific amount of potassium hydroxide pellets was weighed and dissolved in the required amount of methanol. The KOH solution was then added to the pre-heated oil in a 250 ml three-neck glass flask and placed on a hot plate magnetic stirrer at a particular temperature with a constant speed of 400 rpm. The reaction was allowed to stand for a defined time and then stopped. The product of the reaction was kept overnight for the proper settling of the biodiesel produced. The PAME was separated from glycerol using a separating funnel. Then, 50 ml of water was measured and poured gently on the PAME sample to purify it. The mixture was gently stirred to avoid foam formation and was left overnight to settle into two phases namely; water-impurity phase and biodiesel phase. The two-phase mixture was separated using a separating funnel. The biodiesel layer was then heated to 100 °C for 1 h to evaporate the remaining water molecules present in it. The percentage of the biodiesel yield was determined by using Eq. 1.

$$\text{Biodiesel Yield (\%)} = \frac{\text{Weight of biodiesel produced} \times 100}{\text{Weight of raw oil}} \tag{1}$$

Fuel Properties Determination

Saponification Value (SV)

1 gram of each sample (oil and biodiesel) was dissolved in 25 ml of 0.5 M ethanolic potassium hydroxide solution, using 250 ml flask. The flask was heated in a steam bath under reflux for 30 min with occasional swirling. The resultant solution was heated with 0.5 M HCl using phenolphthalein indicator. A blank determination was carried out under similar conditions. The difference in the above two titration values gives the number in milliliters of HCl acid required to neutralize the alkali after saponification. The saponification value (SV) was determined by using Eq. 2.

$$\text{SV(mg KOH)} = \frac{56.1 \times \text{M(B} - \text{V)}}{\text{W}} \tag{2}$$

where M is the morality of standard HCl (0.5 M), B is the volume of HCl in ml used in the blank titration, V is the volume of HCl in ml used for oil and biodiesel titration respectively, 56.1 is the molar mass of potassium hydroxide, and W is the weight in gram of the oil sample.

Peroxide Value (PV)

One gram of oil sample and 1gram of powdered potassium iodide was added into two test tubes containing 20 ml of solvent mixture each (2 vol. glacial acetic acid + 1 vol. of chloroform) i.e. (60:30). Step 1 was carried out in a blank tube. The tubes were placed in a water bath and allowed to boil vigorously for 1 min. The contents were poured quickly into a conical flask containing 10 ml of 5% potassium iodide solution. The tubes were washed with 5 ml of water each and poured into each conical flask with contents, and four drops of phenolphthalein were then added into each conical flask and was titrated with 0.002 M thiosulphate until a color change was obtained. The Peroxide value (PV) was determined by using Eq. 3.

$$\mathrm{PV}\left(\mathrm{meq\ O_2/kg}\right) = \frac{(\mathrm{B\text{-}S}) \times 0.02 \times 1000}{\mathrm{W}} \quad (3)$$

where B = blank titre value, S = sample titre value and W is the weight in gram of the oil sample.

Iodine Value (IV)

One gram of each sample was dissolved in 15 ml of carbon tetrachloride. The solution was mixed with 25 ml Wiji's solution. The flask with the content was stoppered and allowed to stand in the dark for 30 min at room temperature, to enable oxidation to take place. Then 100 ml of distilled water and 20 ml of 10% potassium iodide solution were added to the content of the flask. The resultant mixture was titrated with 0.1 M sodium thiosulphate using 10% starch solution (weight by volume). A blank determination was carried out in the same manner under similar conditions. Its value was calculated by using Eq. 4.

$$\mathrm{IV}\left(\mathrm{gI_2/100\ g\ oil}\right) = \frac{12.69 \times \mathrm{M(B\text{-}V)}}{\mathrm{W}} \quad (4)$$

where M is the morality/strength of standard thiosulphate solution, B is the volume of $Na_2S_2O_4$ in ml used in the blank titration, V is the volume of $Na_2S_2O_4$ in ml used in test titration, and W is the weight in gram of the oil sample.

Acid Value (AV)

One gram of each sample was dissolved in a 25 ml neutral mixture of solvent (equal volume of diethy1 ether and absolute ethanol). The resultant oil solution was titrated with 0.1 M potassium hydroxide (KOH) solution, using phenolphthalein indicator. The titration continued until a pink colored solution was obtained, indicating the end point. The acid value was calculated using the expression below:

$$\mathrm{AV(mg\ KOH/g)} = \frac{56.1 \times \mathrm{M} \times \mathrm{V}}{\mathrm{W}} \quad (5)$$

M is the morality of standard KOH (0.1 M), V is the volume of KOH in ml, and 56.1 is the molar mass of potassium hydroxide. W is the weight in gram of the oil sample.

Determination of Free Fatty Acid (FFA)

One gram each of oil and biodiesel samples was dissolved in a 25 ml neutral mixture (equal volume of diethyl ether and absolute ethanol). The resultant oil solution was titrated with 0.1 M potassium hydroxide solution with a phenolphthalein indicator added in three drops. The titration continued until the end point was reached. The end point was recorded as the appearance of a permanent pink color. The free fatty acid was expressed in terms of oleic acid and computed using the Eq. 6.

$$\mathrm{FFA(\%)} = \frac{\mathrm{TV} \times 0.0282 \times 100}{\mathrm{W}} \quad (6)$$

where TV is the Titration value, 0.0282 = constant (weight of oleic acid neutralized by 1 mg of KOH) and W = Weight in gram of the oil sample.

Cetane Number (CN)

This is a measurement of the combustion quality of diesel fuel during compression ignition. The Cetane number was calculated using the expression 7.

$$\mathrm{Cetane\ Number} = 46.3 + (5458/\mathrm{S}) - (0.225 \times \mathrm{I}) \quad (7)$$

where S and I stand for saponification and iodine value respectively.

Viscosity

This is the resistance offered during the flow of a liquid. The viscosity of the oil and biodiesel was determined using Stabinger Viscometer-SVM 3000 (Anton Paar India Pvt. Ltd.).

Experimental Setup for Performance and Emission Testing

The experimental setup (Fig. 2) consists of a single cylinder, four strokes, water cooled diesel engine with 3.5 kW maximum power, 110 mm stroke and 87.5 mm bore connected to eddy current type dynamometer for loading. The performance characteristics were measured by using the software 'Engine Soft'. Table 1 shows the technical Specifications of the engine. The NOx, HC and CO was measured with AVL DIX Emission Diagnostic System. The range and accuracy of measurements of AVL DIX emission diagnostic system are shown in Table 2.

Results and Discussion

Fatty Acid Composition and Oxidation Stability

Gas chromatography (GC-FID) analysis of PAO revealed that it contains mainly oleic acid (71%), LINOLEIC acid (20.15%) and palmitic acid (4.2%) (Table 3). Any biofuel must be analyzed for its oxidative stability with time and thermal degradation before its implementation as an alternate fuel. The important characteristic for measuring the oxidative stability of fuel is its iodine value that is an indicator of the total number of double bonds in

Fig. 2 Experimental set-up

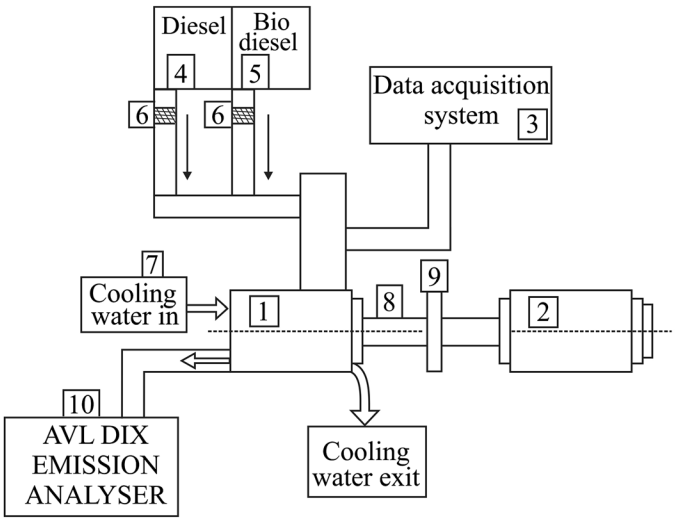

1. SINGLE CYLINDER KIRLOSKAR ENGINE 2. EDDY CURRENT DYNAMOMETER 3. DATA ACQUISTION SYSTEM
4. DIESEL TANK 5. BIODIESEL TANK 6. VALVES 7. COOLING WATER SYSTEM 8. ENGINE SHAFT
9. COUPLING FLANGE 10. AVL DIX EMISSION ANALYSER

Table 1 Technical Specifications of the test engine

S. No.	Component	Specification
1	Engine make	Kirloskar
2	Engine type	1 cylinder, 4 stroke, water cooled
3	Rated power	3.5 kW at 1500 rpm
4	Cylinder volume	661 cc
5	Compression ratio	18
6	Dynamometer	Eddy current, water cooled
9	Load sensor	Load cell, type strain gauge
10	Software	Engine soft

the chemical composition and fatty acid present in the oil. Almost all the biodiesels have significant amounts of esters of oleic, linoleic or linolenic acids and the trend of increasing stability is linolenic < linoleic < oleic [20]. All the samples from PAO showed a higher percentage of oleic acid than linoleic acid. Thus an increase in unsaturated acid constituents, decreases the oxidation stability of oil and hence of biodiesel.

Physico-Chemical Characteristics of *Prunus armeniaca* Seed Oil and It's Biodiesel

The various physiochemical characteristics of *P. armeniaca* oil (PAO) and *P. armeniaca* biodiesel (PAME) obtained from the experimental work are presented in Table 4.

It can be observed that the specific gravity of PAO decreased from 0.912 to 0.883 after transesterification and this was within the acceptable limit. Saponification value of PAO is 188.56 mg/g while that of PAME is 163.67 mg/g. Thus we can conclude that triglycerides of PAO have higher constituents of fatty acids. PAO had an initial acid value of 2.6 mg KOH/g, which was reduced to 0.32 mg KOH/g after treatment. The Higher acid value in biodiesel leads to fuel system deposits and corrosion. The iodine value for PAO was 90.3 mgI_2 and for PAME 100.7 mgI_2. The oxidative stability increases with increase of iodine value and hence the degree of unsaturation. Thus PAO is a good source of raw material for biodiesel production because its viscosity is low due to higher number of unsaturated double bonds in its molecular structure. Peroxide value involves an increase in cetane number and therefore may reduce ignition delay time and hence the rate of oxidation [11, 14]. The pour

Table 2 AVL DIX emission diagnostic systems specification

Measured variable	Measurement range	Resolution	Accuracy
CO	0–10 vol%	0.01 vol%	<0.6 vol%: ±0.03 vol%
HC	0–20,000 ppm	<2000: 1 ppm vol	<200 ppm vol: ±10 ppm
		>2000: 10 ppm	vol P200 ppm vol: ±5% of ind. val.
CO_2	0–20 vol%	0.1 vol%	<10 vol%: ±0.5 vol%
NO	0–5000 ppm	1 ppm vol	<500 ppm vol: ±50 ppm vol
Opacity	0–100%	0.001	±1%

Table 3 Fatty acid composition (wt%) of *Prunus armeniaca* oil comparison with some other oils

Type of fatty acids	Chemical formula	Degree of unsaturation	*Prunus armeniaca*	Jatropha (Atabani et al. [3])	Karanja (Atabani et al. [3])
Myristic	–	(14:0)	1.13	–	–
Palmitic	$C_{16}H_{32}O_2$	(16:0)	4.2	16.0	11.65
Stearic	$C_{18}H_{34}O_2$	(18:0)	2.32	6.5	7.50
Palmitoleic	$C_{16}H_{30}O_2$	(16:1)	–	–	–
Oleic	$C_{18}H_{32}O_2$	(18:1)	71	43.5	51.59
Linoleic	$C_{20}H_{40}O_2$	(18:2)	20.15	34.4	16.46
Linolenic	$C_{18}H_{30}O_2$	(18:3)	1.20	0.80	2.65
Arachidic	$C_{20}H_{38}O_2$	(20:0)	–	–	–
∑Saturated fatty acids			8.85	22.5	19.15
∑Unsaturated fatty acids			91.15	78.7	70.7

Table 4 Physio-chemical properties of *Prunus armeniaca* oil methyl esters (PAME) and comparison with other biodiesel and petro-diesel

Property	Test method	ASTM D6751 and EN 14214	PAO	PAME	Petro diesel
Density at 15 °C (kg/m^3)	D 1298	860–900	913	857	809
Specific gravity (g/cm^3) at 25 °C	D4052	0.87–0.90	0.912	0.883	0.851
Viscosity at 40 °C (mm^2/s)	D 445	1.9–6.0	20.53	5.2	2.91
Calorific value (MJ/kg)	D240	–	31.47	38.93	44.85
Flash point (°C)	D 93	Min 120	221	180	71.5
CFPP (°C)	D 6371	Max 19	–	8	−9
Pour point (°C)	D97	−15 to 16	4	−9	−2.0
Cloud point (°C)	D 2500	−3 to 12	13	−3	−5.0
Moisture content (wt%)	D2709	0.050 max	0.032	0.030	–
FFA (%)	D664	–	0.30	0.27	0.0014
Acid value (mg KOH/g)	D 664	Max 0.5	2.6	0.32	0.01
Iodine value (mgI_2/100 g)	EN 14214	Max 120	90.3	100.7	–
Saponification value (Mg/g)	–	–	188.56	163.67	–
Peroxide value (meq O_2/kg)	AOCS Cd 8 b-90	–	5.16	2.33	–
Carbon residue (mass %)	D4530	0.050 max	0.31	0.02	0.01
Cetane number	D 613	Min 51	–	58.7	51.3
Oxidation stability (h)	EN 14112	6 h	–	6.3	–

point of biodiesel prepared is −8 °C. Such a biodiesel is suitable for use in cold weather conditions prevailing in North-West Himalayan regions of India in winter. The density of PAME was found to be 857 Kg/m^3, which is closer to the density of diesel. The flash point of PAME was 180 °C, which is higher than that of diesel. The higher flash point of PAME ensures safe handling and storage. The Calorific value of *P. armeniaca* biodiesel obtained in the present study (38.93 MJ/kg) is quite comparable to diesel. As physico-chemical properties of the produced biodiesel were within the recommended limits according to the ASTM/EN standards, hence, *P. armeniaca* biodiesel can be used as an alternate fuel in diesel engines.

Engine Performance

Figures 3 and 4 describe the performance characteristics of an engine operated with *P. armeniaca* biodiesel and its blends with diesel. The variation of brake thermal efficiency (BTE) with respect to BMEP (brake mean effective pressure) is shown in Fig. 3. It was observed that BTE of mineral diesel is higher than any of the biodiesel blends except B5 blend which shows marginal increased BTE than diesel. This is due to the reduction in calorific value

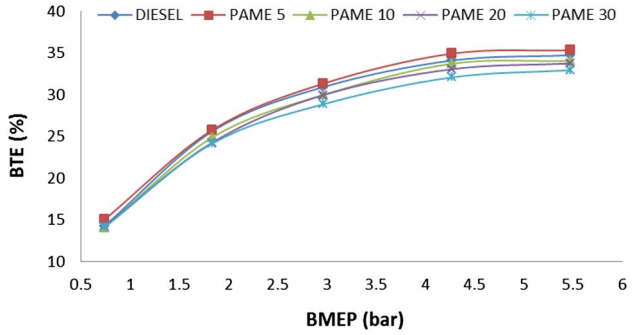

Fig. 3 Brake thermal efficiency versus brake mean effective pressure

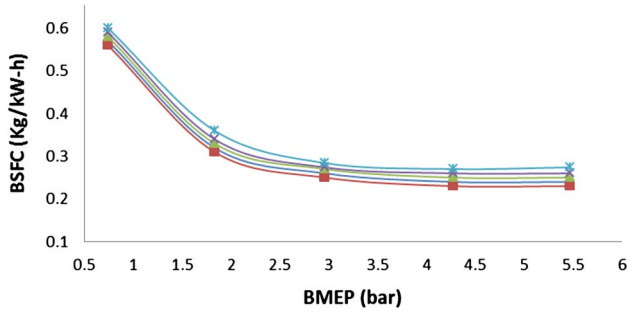

Fig. 4 Brake specific fuel consumption versus brake mean effective pressure

and increase in fuel consumption as compared to diesel [14]. The results are similar to the findings of Dhar and Agarwal [6] and Ong et al. [12]. The efficiency obtained for biodiesel blends B10, B 20 and B 30 are 34.06, 33.7 and 32.94% respectively as compared to the neat diesel (34.74%).

Figure 4 shows the BSFC with respect to BMEP. Blend B5 shows slightly lower BSFC than diesel fuels due to the reason that biodiesel has a relatively higher heat of vaporization than diesel, which affects the combustion, Raheman and Ghadge [13]. Besides, the BSFC of B5, other blends of *P. armeniaca* biodiesel shows higher BSFC than diesel fuel due to their lower calorific value. Some researchers have explained that the increase in BSFC in relation with the high density and viscosity of the biodiesel [12, 18]. The full load BSFC for blends B10, B20 and B30 were 0.25, 0.26 and 0.274 kg/kW h respectively as compared to 0.24 kg/kW h in case of baseline diesel. Previous researchers reported similar trends [10, 13].

Exhaust Emissions

Figures 5, 6, 7 and 8 describe the emission characteristics of *P. armeniaca* biodiesel and its blends with diesel. CO emissions for various test fuels were shown in Fig. 5.

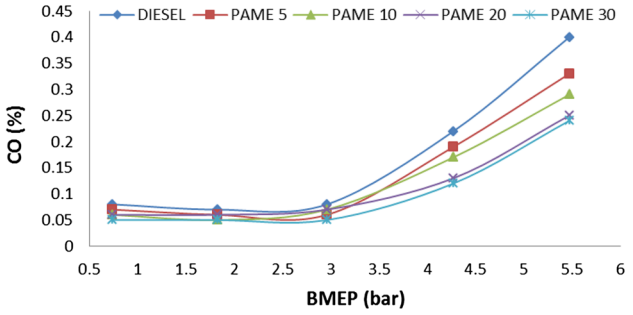

Fig. 5 CO Emission versus brake mean effective pressure

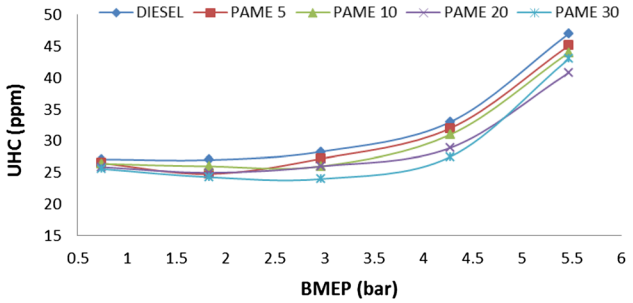

Fig. 6 UHC Emission versus brake mean effective pressure

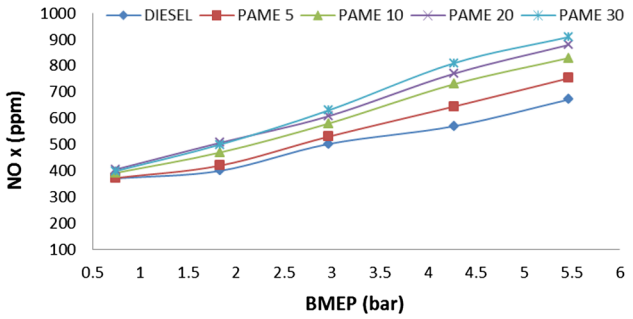

Fig. 7 NOx Emission versus brake mean effective pressure

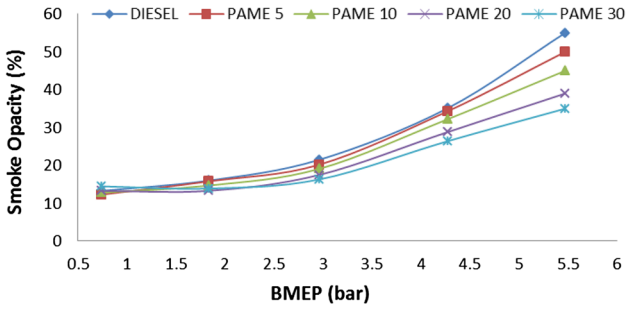

Fig. 8 Smoke opacity versus brake mean effective pressure

From graph it is clear that for all the biodiesel fuels and their blends, CO emissions were found to be lower. As the load is increased on the engine, there is an increase in CO emission for all the test fuels. The increase in CO emission levels at higher load is due to rich mixture at higher load condition than at lower load results in incomplete combustion of fuel. Within the experimental range, the lower CO emissions have been observed with blended biodiesel fuel and least in B30 samples. At full load, CO emissions of B5, B10, B20 and B30 were 0.33, 0.29, 0.25 and 0.24% respectively were lower than the baseline diesel. Similar results were reported by other researchers [1, 2, 5]. This is possible because of complete combustion of biodiesel based fuels since biodiesel contains more oxygen than diesel and as such carbon monoxide is converted into carbon dioxide.

Figure 6 shows that the UBHC emissions are found lower at partial load conditions and increases at higher engine load [10]. This is due to relatively less oxygen available for the reaction when more fuel is injected into the engine cylinder at higher engine load. The value of UBHC emission from no load to full load is higher in case of diesel compared to biodiesel based fuels. Hydrocarbons emissions are mainly caused due to the incomplete combustion of hydrocarbon fuel. The maximum reduction in UBHC was achieved for B30 biodiesel blend. At full load condition, B5, B10, B20 and B30 showed 45.1, 44, 40.8 and 43 ppm respectively as compared to 47 ppm in case of baseline diesel. These results are in agreement with results of previous researchers [2, 3, 13].

The variation of NOx emissions from *P. armeniaca* biodiesel and its blends with respect to diesel fuel are shown in Fig. 7. The NOx emissions increased with the increasing engine load, due to a higher combustion temperature [6]. The NOx emissions of biodiesel based fuels have been found higher than diesel on all load conditions. Similar results were obtained by Raheman and Ghadges [13] and Mofijur et al. [10]. At full load, B5, B10, B20 and B30 had NOx emissions of 753, 830, 880 and 910 ppm, as compared to 672 ppm for diesel. It is quite obvious, that with biodiesel addition in diese fuel, more amount of oxygen is present in combustion chamber, leading to formation of higher NOx in biodiesel fueled engines.

Figure 8 shows the variation of the smoke opacity of diesel and *P. armeniaca* biodiesel and its blends at different bmep. It can be seen that smoke is high mainly at high power outputs. High loads imply that more fuel is injected into the combustion chamber and hence incomplete combustion of fuel is amplified. Reduction of smoke emissions for biodiesel based fuels in comparison to diesel fuel has been achieved for all load conditions. With an increase of biodiesel blends, smoke decreases [5, 6] at most of the operating conditions. The full load smoke opacity of the baseline diesel operation was found to be 55.2% which continually dropped to 50.0, 45.1, 39.0 and 35.2% for B5, B10, B20 and B30 test fuels respectively. The reduction in smoke can be explained by the presence of lower hydrocarbons with biodiesel based fuels as compared to diesel. Similar trends of reducing smoke opacity for biodiesel blended fuel were reported by Yadav et al. [19] and Cheikh et al. [5].

Conclusions

A high quality Biodiesel with high yield (96.5%) has been prepared from *P. armeniaca* seed oil via transesterification process. All properties of PAME meet with ASTM D6751 and EN14214 standards.

The engine test results show that B5 gave good improvement in the engine performance with higher BTE. On the other hand, there is an improvement in fuel economy with lower BSFC by using B5 compared to diesel fuel. Furthermore, all tested blends of biodiesel reduced the CO, UHC and smoke opacity compared to diesel fuel but NOx emission is slightly increased. Thus, the present investigation has established the *P. armeniaca* seed oil as highly potential alternative feedstock of biodiesel.

References

1. Agarwal, A.K., Gupta, T., Shukla, P.C., Dhar, A.: Particulate emissions from biodiesel Fuelled CI engines. Energy Convers. Manage. **94**, 311–330 (2015)
2. Ashraful, A.M., Masjuki, H.H., Kalam, M.A., Fattah Rizwanul, I.M., Imtenan, S., Shahir, S.A., Mobarak, H.M.: Production and comparison of fuel properties, engine performance and emission characteristics of biodiesel from various non-edible vegetable oils: a review. Energy Convers. Manage. **80**, 202–228 (2014)
3. Atabani, A.E., Silitonga, A.S.: Non-edible vegetable oils: a critical evaluation of oil extraction fatty acid compositions, biodiesel production, characteristics, engine performance and emissions production. Renew. Sustain. Energy Rev. **18**, 211–245 (2013)
4. Bankovic, I.B., Stamenkovic, O.S., Veljkovic, V.B.: Biodiesel production from nonedible plant oils. Renew. Sustain. Energy Rev. **16**, 3621–3647 (2012)
5. Cheikh, K., Sary, A., Khaled, L., Abdelkrim, L., Mohand, T.: Experimental assessment of performance and emissions maps for biodiesel-fueled compression ignition engine. Appl. Energy. **161**, 320–329 (2016)
6. Dhar, A., Agarwal, A.K.: Performance, emissions and combustion characteristics of Karanja biodiesel in a transportation engine. Fuel **119**, 70–80 (2014)
7. Katea, A.E., Lohanib, U.C., Pandeyc, J.P., Shahid, N.C., Sarkar, A.: Traditional and mechanical method of the oil extraction from wild apricot kernel: a comparative study. Res. J. Chem. Environ. Sci. **2**, 54–60 (2014)
8. Knothe, G.: Biodiesel derived from a model oil enriched in palmitoleic acid, macadamia nut oil. Energy Fuels **24**, 2098–2103 (2010)

9. Maleki, E., Aroua, M.K., Sulaiman N.M.N.: the Improved yield of solvent free enzymatic methanolysis of palm and jatropha oils blended with castor oil. Appl Energy **104**, 905–909 (2013)
10. Mofijur, M., Masjuki, H.H., Kalam, M.A., Atabani, A.E.: Evaluation of biodiesel blending, engine performance and emissions characteristics of Jatropha curcas methyl ester: Malaysian perspective. Energy **55**, 879–887 (2013)
11. Mohammed, J., Atuman, J.S., Ugwu, E., Aboje, A.A.: Production and characterization of biodiesel from jatropha oil and neem oil. Int. J. Emerg. Trends Eng. Develop. **2**, 313–320 (2012)
12. Ong, H.C., Masjuki, H.H., Mahlia T.M.I., Silitonga, A.S., Chong, W.T., Leong, K.Y.: Optimization of biodiesel production and engine performance from high free fatty acid *Calophyllum inophyllum* oil in CI diesel engine. Energy Convers. Manage. **81**, 30–40 (2014)
13. Raheman, H., Ghadge, S.V.: Performance of compression ignition engine with mahua (*Madhuca indica*) biodiesel. Fuel **86**, 2568–2573 (2007)
14. Sahoo, P.K., Das, L.M.: Process optimization for biodiesel production from Jatropha, Karanja and Polanga oils. Fuel **88**, 1588–1594 (2009)
15. Satyarthi, J.K., Srinivas, D., Ratnasamy, P.: Estimation of free fatty acid content in oils, fats, and biodiesel by 1-H NMR spectroscopy. Energy Fuels. **23**, 2273–2277 (2009)
16. Sharma, R., Gupta, A., Abrol, G.S., Joshi, V. K.: Value addition of wild apricot fruits grown in North-West Himalayan regions: a review. J. Food Sci. Technol. (2012). doi 10.1007/s13197-012-0766-0
17. Yan, Y., Li, X., Wang, G., Gui, X., Li, G., Su, F.: Biotechnological preparation of biodiesel and its high-valued derivatives: a review. Appl Energy. **113**, 1614–1631 (2014)
18. Yadav, A.K., Khan, M.E., Pal, A.: Biodiesel production from oleander (Thevetia Peruviana) oil and its performance testing on a diesel engine. Korean J. **34**, 340–345 (2017)
19. Yadav, A.K., Khan, M.E., Pal, A.: Kaner biodiesel production through hybrid reactor and its performance testing on a CI engine at different compression ratios. Egypt. J. Pet. (2016). 10.1016/j.ejpe.2016.07.006
20. Yaakob, Z., Narayanan, B.N., Padikkaparambil, S., Unni, K.S., Akbar, P.M.: A review on the oxidation stability of biodiesel. Renew. Sustain. Energy Rev. **35**, 136–153 (2014)

Accepted Manuscript

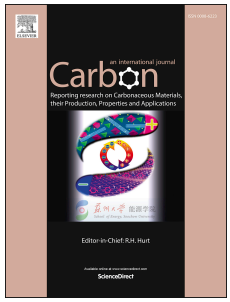

Filled-carbon nanotubes: 1 D nanomagnets possessing uniaxial magnetization axis and reversal magnetization switching

Reetu Kumari, Anshika Singh, Brajesh S. Yadav, Dipti Ranjan Mohapatra, Arnab Ghosh, Puspendu Guha, P.V. Satyam, Manoj Kumar Singh, Pawan K. Tyagi

PII: S0008-6223(17)30419-0

DOI: 10.1016/j.carbon.2017.04.053

Reference: CARBON 11962

To appear in: *Carbon*

Received Date: 29 December 2016

Revised Date: 7 April 2017

Accepted Date: 21 April 2017

Please cite this article as: R. Kumari, A. Singh, B.S. Yadav, D.R. Mohapatra, A. Ghosh, P. Guha, P.V. Satyam, M.K. Singh, P.K. Tyagi, Filled-carbon nanotubes: 1 D nanomagnets possessing uniaxial magnetization axis and reversal magnetization switching, *Carbon* (2017), doi: 10.1016/j.carbon.2017.04.053.

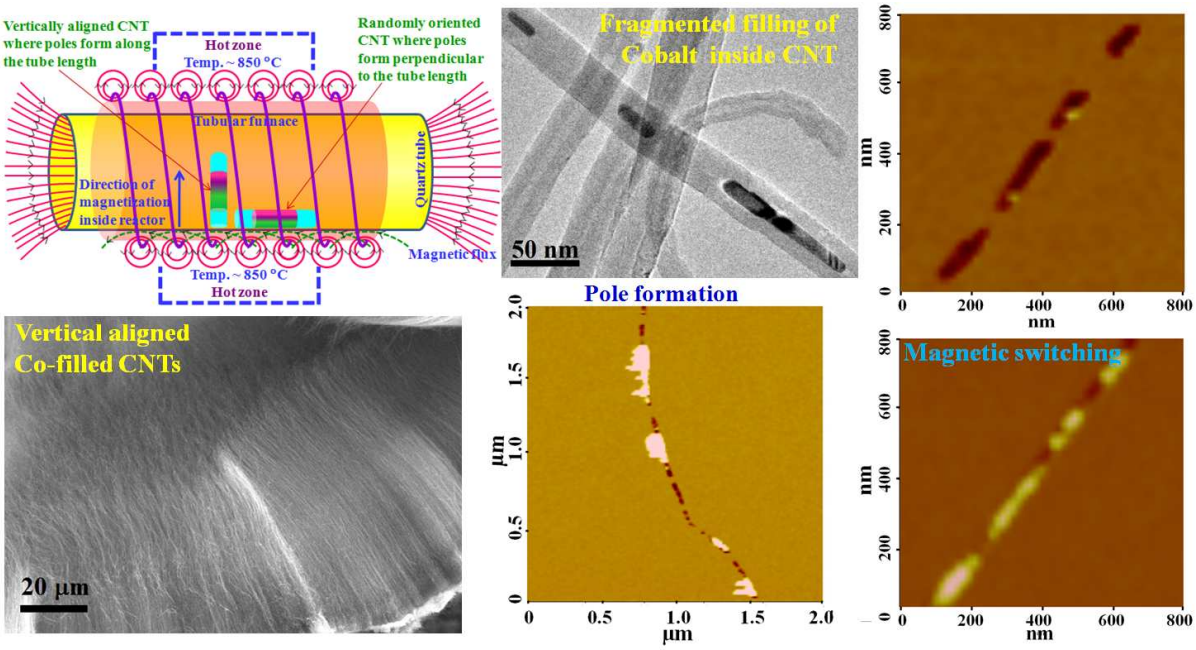

Filled-carbon nanotubes: 1 D nanomagnets possessing uniaxial magnetization axis and reversal magnetization switching

Reetu Kumari[1], Anshika Singh[1], Brajesh S. Yadav[2], Dipti Ranjan Mohapatra[3], Arnab Ghosh[4,5], Puspendu Guha[4,6], P V Satyam[4,6], Manoj Kumar Singh[7], Pawan K. Tyagi[1*],

[1]Deptartment of Applied Physics, Delhi Technological University, Delhi, India

[2]Solid State Physics Laboratory, Lucknow Road, Timarpur, Delhi-110054, India

[3]Department of Physics, Vikram Deb College, Jeypore Koaput, Odisha-764001, India

[4]Institute of Physics, Sachivalaya Marg, Bhubaneswar-751005, India

[5]Department of Physics, Indian Institute of Technology Kharagpur, Kharagpur 721302, India

[6]Homi Bhabha National Institute, Training School Complex, Anushakti Nagar, Mumbai-400085, India

[7]Centre for Mechanical Technology & Automation, Department of Mechanical Engineering, University of Aveiro, 3810-193 Aveiro, Portugal

The present study aims to control the direction of magnetization in Fe_3C, Co and Ni nanorods filled inside carbon nanotube (CNT). This control has been achieved during growth by modifying thermal chemical vapor deposition (CVD) system. As-grown *in situ* filled-CNTs were found to exhibit permanent magnetization. These CNTs have been characterized by using scanning electron microscopy (SEM), X-ray diffraction, Raman spectroscopy and transmission electron microscopy (TEM). Afterwards, direction of magnetization in Fe_3C, Co or Ni nanorod filled inside CNT has been further probed by using magnetic force microscopy (MFM). MFM measurements reveal that nanorod exhibits single domain behavior and direction of magnetization, instead of being controlled either by shape or magneto crystalline

* Corresponding Author: Tel:+91-11-27852212; Fax: +91-11- 27871023
E-mail address: pawan.phy@dce.edu , pawankumartyagi@gmail.com

anisotropy, has been found to be influenced by magnetic field gradient, produced in modified thermal CVD system. Direction of magnetization has been found either along tube axis in vertical grown CNTs or in radial direction i.e. perpendicular to the tube axis in randomly grown CNTs. Besides investigated structural and magnetic properties, plausible growth model of *in situ* filling as well as mechanism to understand unique magnetization behavior has been proposed.

Keywords: Filled carbon nanotubes, uniaxial magnetization, magnetic force microscopy, Magnetic switching.

Introduction:

The accomplishment of filling of carbon nanotube core with various materials has stimulated a large excitement as well as boosted research interest in various areas of nanotechnology such as magnetic resonance imaging[1], catalyst & energy storage[2], photothermal[3] and nano-biotechnological applications[4]. This has been attributed to the fact that in filled-CNT, tube-walls not only protect the filled nanomagnets against harsh environment but also prohibit coalescence and enhance the physical, chemical, magnetic or electronic properties of host nanotube as well as filled-nanomaterials. In recent reports, CNTs filled with magnetic materials have been proposed as a novel material and successfully demonstrated in innumerable potential applications in the thrust areas of research such as MFM tips [5,6], selective drug delivery [7, 8], spintronics[9] and magnetic data storage devices[10]. In addition to CNT-related research activity, one-dimensional, well-aligned and separated magnetic nanostructures exhibit numerous potential applications such as labelling and magnetic separation of cells[11], cancer treatment[12], sensing[13], data storage[14] and so on. Specifically, in data storage device well-ordered magnetic structures with either in or out of plane magnetization are highly desirable. In order to have nanostructures which possess out of plane magnetization, vertical aligned-CNTs were found to be promising. Generally, in filled-

CNT, direction of magnetization might be either along or perpendicular to tube axis, depending on the dominance of shape or magneto crystalline anisotropy, respectively[15]. If direction of magnetization can be controlled, filled-CNT could be novel material for data storage devices. Recently, Weissker *et al*. found the direction of magnetization in Fe nanowire was along the nanotube axis whereas it was in radial direction in case of Fe_3C[15]. This might have happened due the dominance of magnetocrystalline anisotropy in Fe_3C nanowire. Coexistence of Fe and Fe_3C phase has also been observed by some researchers[16,17,18]. To optimize the direction of magnetization in Fe_3C filled-CNT, the main challenge is limited formation of γ-Fe, and α-Fe phases, and ensuring the production of long continuous Fe_3C nanorod magnetized parallel to the tube axis. To the best of our knowledge, till date no reports have been published on controlling the magnetization direction in Co or Ni nanorod confined inside CNTs. However, magnetization direction has been probed in bare Co and Ni nanorod by using MFM[19]. Majetich et al. probed the magnetization direction in carbon coated ferromagnetic nanoparticles by using Lorentz microscopy reported in plane magnetization[20].

In present work, we report a method to make permanent cylindrical nanomagnets confined inside CNT. In these nanomagnets, direction of magnetization was controlled by applying a magnetic field gradient. Direction of magnetization was found to be dependent on the direction of magnetic field gradient. This approach has been tested in nanorod of Fe_3C, Co and Ni confined inside CNT and found to be consistent for all. In order to investigate the direction of magnetization, individual tubes were probed with magnetized tip in tapping as well as in lift height mode. We foresee that in future this study could be forwarding step to facilitate the applications of filled-CNT in data storage as well as spintronic devices.

Experimental details:

Fe_3C, Co or Ni filled-CNTs were grown by using modified thermal chemical vapour deposition (thermal CVD) technique. Here, we have used especially modified thermal CVD system in order to grow permanently magnetized CNTs. This system was designed in a way that magnetic field gradient was always applied in radial direction. In this system, a hand-wound coil furnace was used. More details of furnace as well as quartz tube reactor have been reported elsewhere[21]. In our procedure, a 50 mL solution of metallocene/benzene was taken, where ferrocene, cobaltocene and nickelocene were dissolved in benzene at a ratio of 0.02 g mL^{-1}, 0.013 g mL^{-1} and 0.013 gmL^{-1} in order to grow Fe_3C, Co and Ni-filled CNTs, respectively. The solution was first ultra-sonicated and then fed into a pre-heating zone at rate of 0.5 mL/minute. In order to ensure that argon/hydrogen gas mixture carried the vapors of metallocene/benzene, gas mixture in the ratio of 2:1 with total flow rate 150 sccm was optimized. This flow was found to be sensitive to inner diameter of the quartz reactor. To grow vertical aligned filled- CNT, SiO_2 (300 nm)/Si (500 μm) substrate was used. This substrate was first ultrasonicated in acetone for 20 minutes and then kept in the middle of the quartz tube. After completion of the synthesis process we found black powder as-deposited on the wall of quartz reactor and film of CNTs on SiO_2/Si substrate. We preserve both types of samples separately for further characterizations. As-grown samples were investigated by using X-Ray diffractometer (Bruker D8 Advance), Scanning Electron Microscopy (SEM), Hitachi S3100 and Micro Raman (Horiba HR Evolution confocal micro-Raman spectrometer, with an excitation wavelength of 532 nm Nd:YAG laser. In order to estimate the diameter and to confirm the filling of CNTs, HRTEM study was performed by using JEOL JEM 2010 (UHR model with URP22 pole piece) operated at 200 kV. The magnetic force microscopy (MFM) probing was performed by using scanning probe microscopy (SPM) system (Park system XE-100) with Co-Cr coated Si tip (Nsc18/Co-Cr). Small amount of sample has been dispersed in isopropyl alcohol (IPA) and then sonicated. After 20 minutes of ultrasonication,

one drop of the dispersion was cast on carbon coated Cu-grid and SiO_2 coated Si substrate in order to carry out the high-resolution TEM imaging and MFM measurements, respectively.

Results and discussion:

Structural characterization:

Surface morphology of as-synthesized sample having Fe_3C, Co and Ni-filled CNTs deposited on SiO_2/Si substrate was examined by using SEM, as shown in Fig.1 (a-c). It has been observed that Fe_3C-filled and Co-filled CNTs deposited on the substrate are vertical aligned whereas Ni-filled CNTs are randomly oriented. SEM micrographs of scratched powder reveal that it always consists the bundles of randomly oriented CNTs (Fig. 1d-f). Dense and straight CNTs are found if ferrocene was catalyst precursor whereas curly CNTs are obtained with low density if nickellocene is used.

In order to confirm the crystallinity and phase of nanorod, XRD measurements were carried out on all three scratched powder samples, as shown in Fig. 1(g-i). The diffraction peaks observed at 2θ positions at 26.0°, 26.34° and 26.37° for Fe_3C, Co and Ni filled-CNTs, respectively. These peaks were indexed as a characteristic peak of MWCNT representing the inter-wall spacing. The determined value of average d_0 is 3.423 ± 0.001 Å, 3.379 ± 0.001 Å, 3.375 ± 0.001 Å for Fe_3C, Co or Ni filled-CNT, respectively (PCPD file no: 89-8487). These values exhibit that compressive strain along c-axis is more in the walls of Ni-filled CNT. In addition to the signature peak of CNT, we have observed few more peaks reflected from encapsulated materials. These identified peaks are attributed to orthorhombic structure of Fe_3C (Fig. 1g) and face centered cubic (FCC) structure of cobalt (Fig. 1h) and nickel (Fig.1i) as mentioned in panels. However, in Fig. 1g the peak around 45° might have overlapped peaks of α-Fe or/and γ-Fe but no other peak related to these phases has been observed. Therefore possibility of coexistence of other phases of Fe might be ruled out. Furthermore, in the present case phases of Fe did not have influence on the field gradient and its induced pole

formation which is found to be independent of filled material. A slight downshift of ~ 0.2° has been observed in 2θ positions of peaks in comparison of reported values for bulk which may be associated with minimal presence of vacancies in nanorod[21].

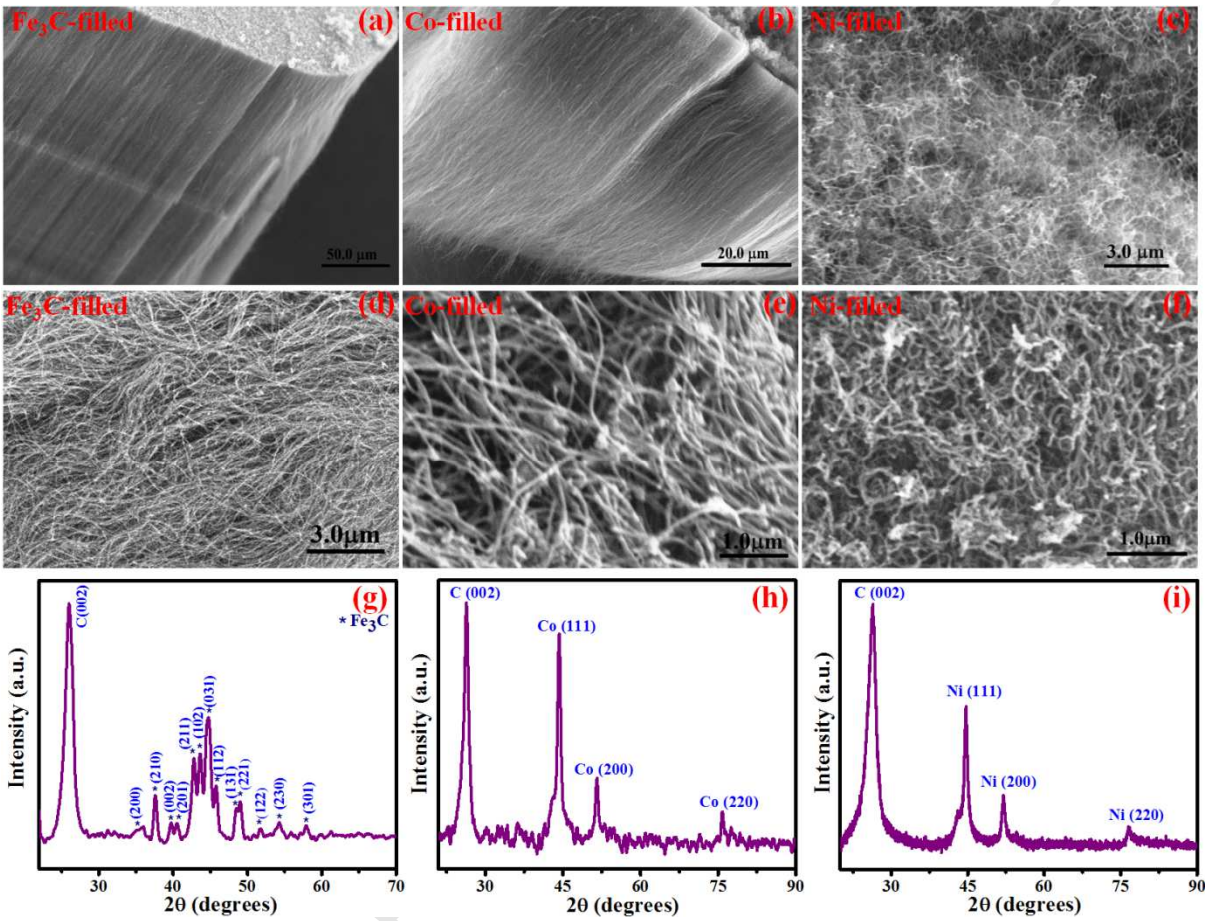

Figure 1. SEM images of (a-c) vertically oriented CNTs and (d-f) randomly grown (g-i) XRD patterns of sample containing randomly oriented Fe_3C, Co and Ni-filled CNTs, respectively.

In order to examine the detailed crystal structure of individul CNT, samples were further characterized by using high-resolution transmission electron microscope (HRTEM). The bright field TEM images of filled-CNTs as shown in Figs 2 (a-c) reveal that nanorod are confined in a fragmented manner. These nanorods were found to be single-crystalline as confirmed by lattice periodicity, present in the dark region in Fig. 2 d, e and f. The measured lattice spacings were found to be 0.207 ± 0.003 nm, 0.198 ± 0.004 nm, 0.175 ± 0.003 nm as

mentioned in Figs. 2(d-f), respectively and are in accordance with d-spacing values of (121), (200), (200) planes of respective crystal. The orthorhombic structure of the Fe_3C and FCC structure of both Co as well as Ni were further reconfirmed by indexing the fast Fourier transformation (FFT) patterns as shown in the inset of panels Figs. 2(d-f) as well as by XRD pattern (Fig. 1g-i).

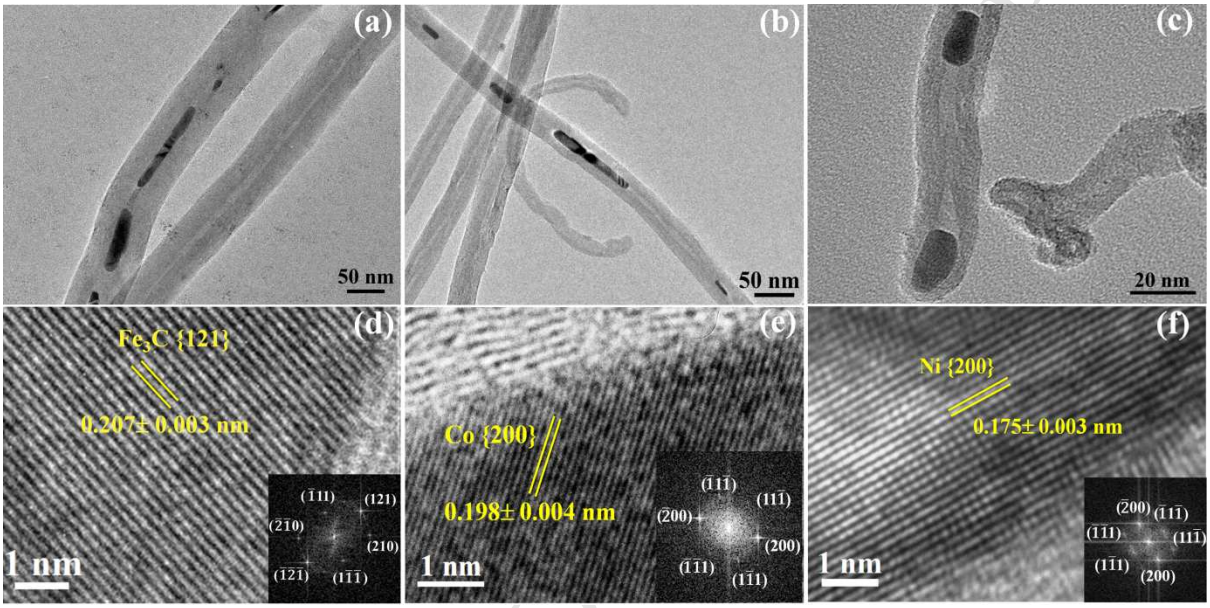

Figure 2. (a-c) Bright field TEM images of CNTs filled with Fe_3C, Co and Ni respectively. (d-f) High resolution lattice images of nanorod and inset of panels display the indexed FFT pattern of corresponding lattice image.

Raman spectra of all the samples (Fig. 3) show two major peaks located at ~ 1342 cm^{-1} and 1572 cm^{-1}, which are attributed to well known D- band and G- band. Asymmetric in the shape of both D-band and G-band suggest that multiple peak components are present in the spectra. The spectra were further deconvoluted by adpotinng Lorentzian fitting and represented by different colors and their possible identities has been mentioned in Figure 3. Besides two major G and D bands one more band which identified as D′ located at 1608 cm^{-1} was observed. In the sample containing Ni-filled CNTs, after deconvolution two more peaks at 1270 and 1490 cm^{-1} observed with characteristic peaks in D, G and D′ bands. Here, G-band derived from tangential breathing mode in MWCNTs (E_{2g} symmetry), originates due to bond

stretching vibration of all pairs of sp^2 atoms arranged in both olefinic chains or aromatic rings[22]. *D* band is due to breathing of sp^2 atoms in ring, originates from the finite size effects in sp^2 carbon atoms generally associated with the presence of disordered graphite[23]. This mode is forbidden in a perfect graphitic material and only actives in the presence of disorder. D′ band appeared at 1608-1611 cm^{-1} is another weak disorder-induced feature of graphitic carbon [24]. In case of Ni-filled CNTs, two weak bands at 1490 and 1270 cm^{-1} originated form M and K points, respectively are also known to be associated with disordered graphite[25]. In G-band, significantly blue shift of 14 cm^{-1} was observed in the sample of Ni-filled CNT as compared to others. This blue shift can be classified considering two main aspects: (i) lattice mismatch with Ni, and (ii) strength of the CNT-metal interaction, associated with electron-phonon coupling. S. Gayen et.al theoretically investigated that in a filled-CNT there may be an additional peak due to excitation of the phonon of the filling atom or molecule[26]. Positions, shapes and relative strengths of these Raman peaks depend on plasmon-phonon and phonon-phonon interactions. Furthermore, hybridization between the G-bands and the filling atom phonon is only strong when these two frequencies are close to each other[26]. If phonon frequency of the filling atom is far from the G-band frequencies, it gives modest effects on the G-band spectra. Since, phonon frequencies of Fe_3C, Co and Ni are lower than that of G band[27,28,29]. Hence, it can be concluded that a significant shifting found only in Ni filled-CNT does not occur due to phonon coupling rather it may be due to the strain in C-C bond streching and compressive strain present in a direction prependicular to tube axis[30]. The coefficient of thermal expansion (CTE) of Ni and Co is 13.4×10^{-6} and 13×10^{-6} K^{-1} respectively whereas it is 11.3×10^{-6} K^{-1} for c-axis of Fe_3C[31]. CTE for CNT in radial direction is reported to be 7.3×10^{-6} K^{-1} [32]. This difference in CTE of CNT and encapsulated nonorods causes compressive stress on CNT walls in radial direction while they were being coolled after growth. As evident from the XRD analysis, inter-wall spacing of CNT is found to be

largest for Fe_3C and then decreases for Co and Ni, respectively. The shift in inter-wall spacings for the three types of CNT is in well agreement with mismatch of CTE for Fe_3C, Co and Ni. Fe_3C having less CTE causes less stress on CNT wall as compared to Co and Ni which have comparatively higher CTE. During the cooling process, the negative value of CTE (α_{CNT}) in the axial direction further generates compression along the tube axis and strain in C-C bond streching which is present in the all sample. Hence, C-C bond stretching caused due to mismatch of CTE cannot significantly influence the G-band position. From the SEM micropgraphs, it was already observed that Ni-filled CNTs have tangled structure, which may produce the strain in C-C bonds. This bond streching along with compression in CNT walls ultimately results the blue shift of G band. Additionally, I_G/I_D ratio consistently decreased from Fe_3C to Co and Ni-filled CNT. This can also be associated with the twisted structure which give rise to more defective sites, eventually results in more intense D band. Moreover, the presence of two other bands which are also associated with the disorderness clearly indicates that Ni-filled CNTs are more defective.

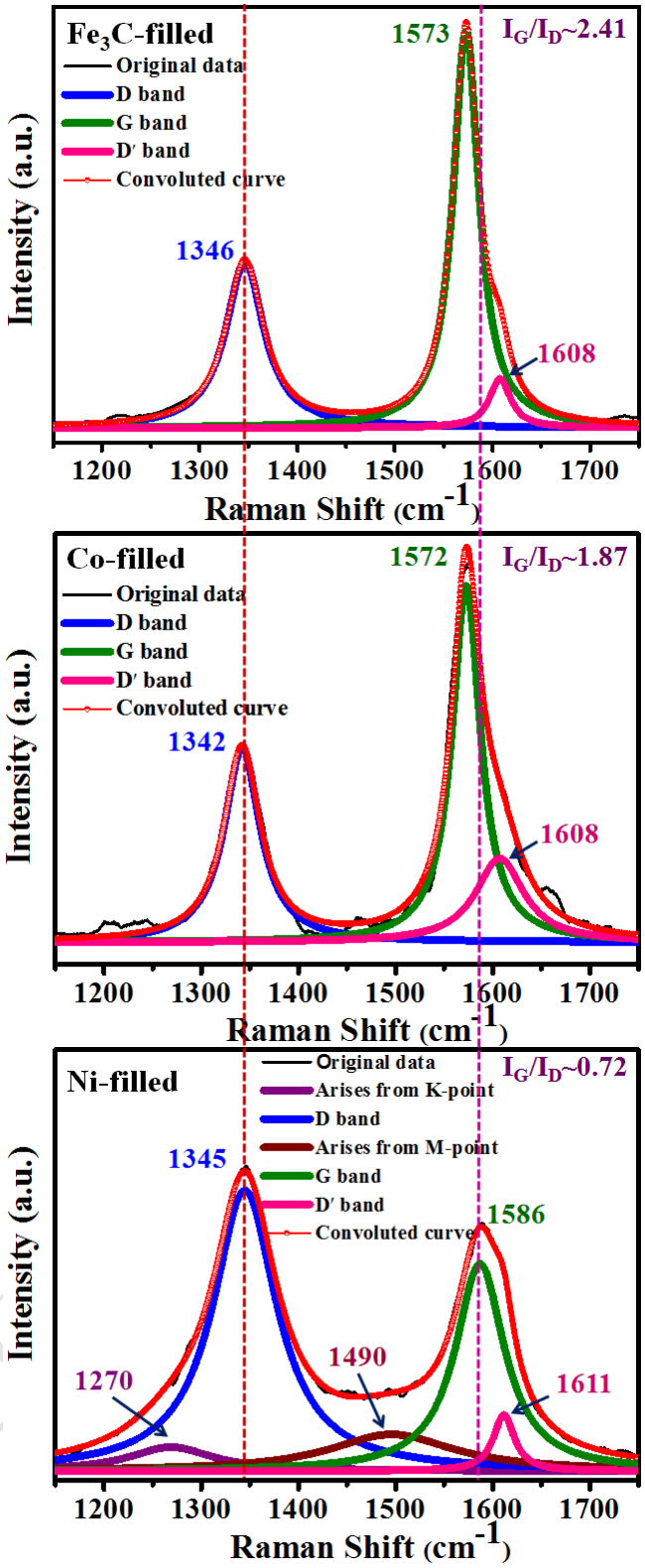

Figure 3. Raman spectra of sample containing unfilled/filled-CNT with Fe_3C, Co and Ni respectively.

We have performed the MFM measurement on as-grown Fe_3C, Co and Ni filled CNTs. These studies were performed on both types of filled-CNTs i.e. vertical aligned CNT where tube axis is parallel to the direction of radial magnetic field gradient and randomly grown where tube axis is perpendicular to field gradient i.e. along the radial direction. The topographical and phase images were captured in tapping mode and in lift height mode with 50 nm height, respectively. In the present study, a two-pass tapping/lift mode has been used to measure the relatively weak long-range magnetic interaction. In order to minimize the strong short-range Van der Waals force, magnetized tip was lifted-up to certain height. By keeping the probe–sample distance constant, it can be presumed that non-magnetic forces will only dominate during surface topography whereas magnetic forces dominate while phase image was captured. Figure 4 shows the topography as well as phase image of randomly grown Co-filled CNT. In the phase image (Fig. 4B), bright contrast appears in two parts for the same selected length of CNT in topography which is continuous as shown in Fig.4A. This is due to the partial filling of CNT as in phase imaging contrast represents the magnetic response between filled-part of CNT and MFM tip. The line profiles plotted in the filled-part shows the positive phase shifts in range of 45-70°. Furthermore, vertically aligned Co-filled CNTs were also probed. Phase image was again taken at same lift height 50 nm. The alternate bright and dark contrast was observed as shown in Fig. 5.The line profile of marked part by (b-i) in the filled-part shows positive and negative phase shifts in the range of 45-70° and -3 to - 4°.

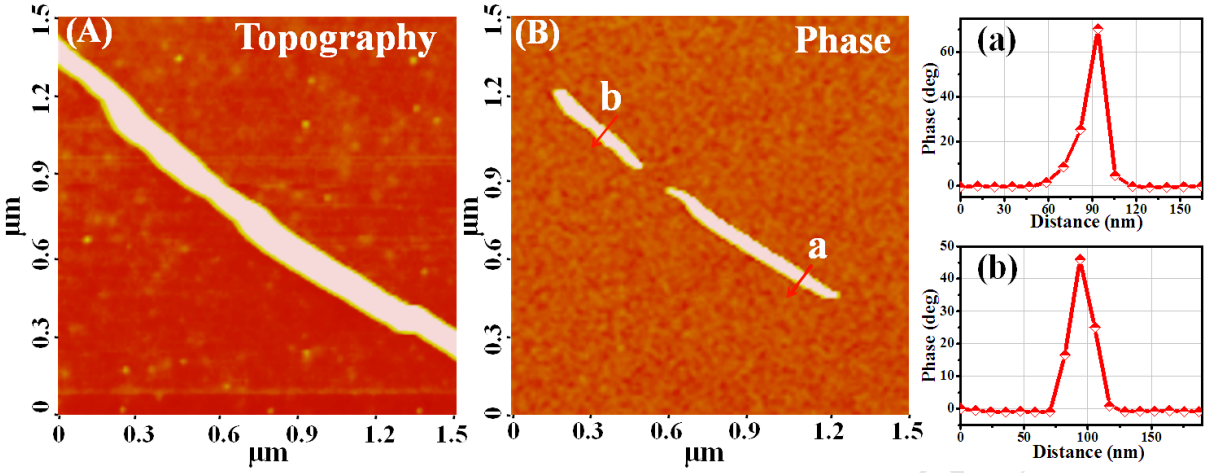

Figure 4. (A) Topography and (B) phase images of randomly oriented Co-filled CNT, (a) and (b) line profiles corresponding to the bright regions in the phase image.

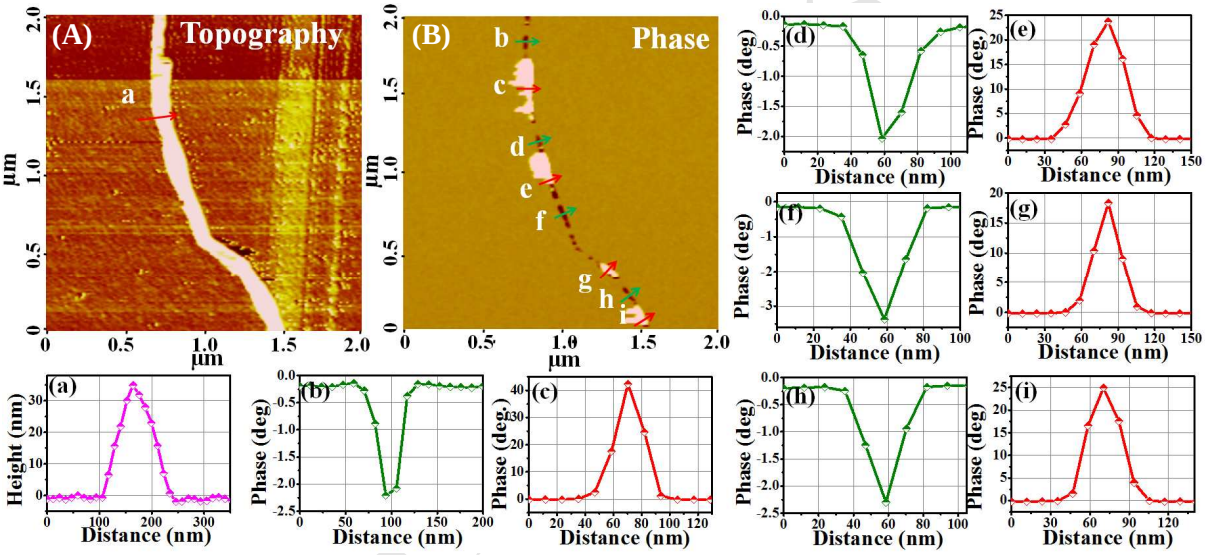

Figure 5. (A)Topography and (B) phase images of vertical aligned Co filled CNT, (a)-(b) line profiles corresponding to the alternate dark and bright regions in the phase image. Green line represents the negative phase shift whereas red line represents the positive phase shift.

These studies were further exteneded on randomly grown Fe_3C-filled CNT. We have observed three tyes of contrast formation one as evidenced from Figs. 6. We have observed either one type of contrast dark (Fig. 6B) and bright (Fig. 6D) or combination of both types of contrast prependicular to the length of the nanotube (Fig.6F). In phase image having combination of contrast, this is to be noted that conrtrast switching was found along the diameter of the tube. These phase images obtained from three different CNTs clearly signify

the same type of pole formation i.e. along the diameter. On the other hand, when probing was performed on vertically grown CNT, the filled-part depicted both type of the contrast along the direction of tube axis as shown in Fig. 7.

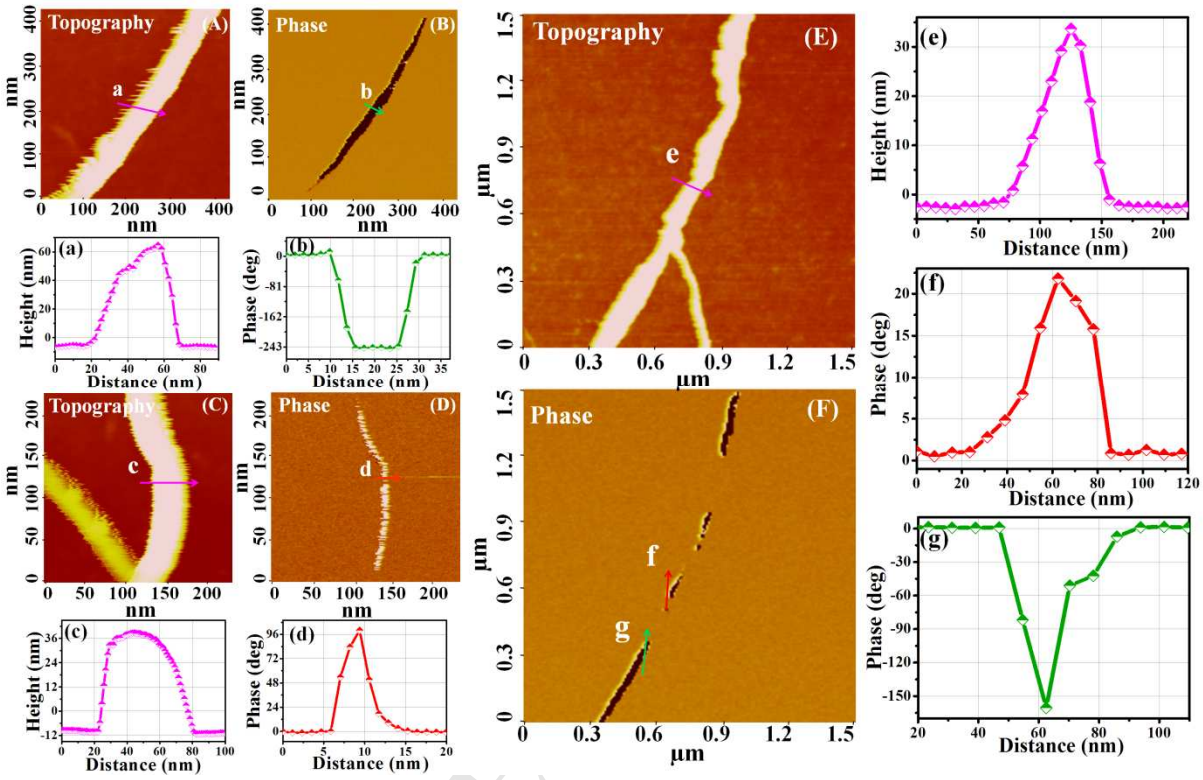

Figure 6. Topography (A, C & E) and (B, D & F) phase images of randomly grown Fe_3C filled CNTs. (a), (c) and (e) are the line profiles corresponding to the lines a drawn over topography of three CNTs; (b) & (d) line profiles corresponding to phase image (B) and (C) respectively; (f) & (g) line profiles corresponding to bright and dark regions of phase image (B) and (C). In this phase image both type of forces attractive as well as repulsive forces are acting between filled regions and the cantilever.

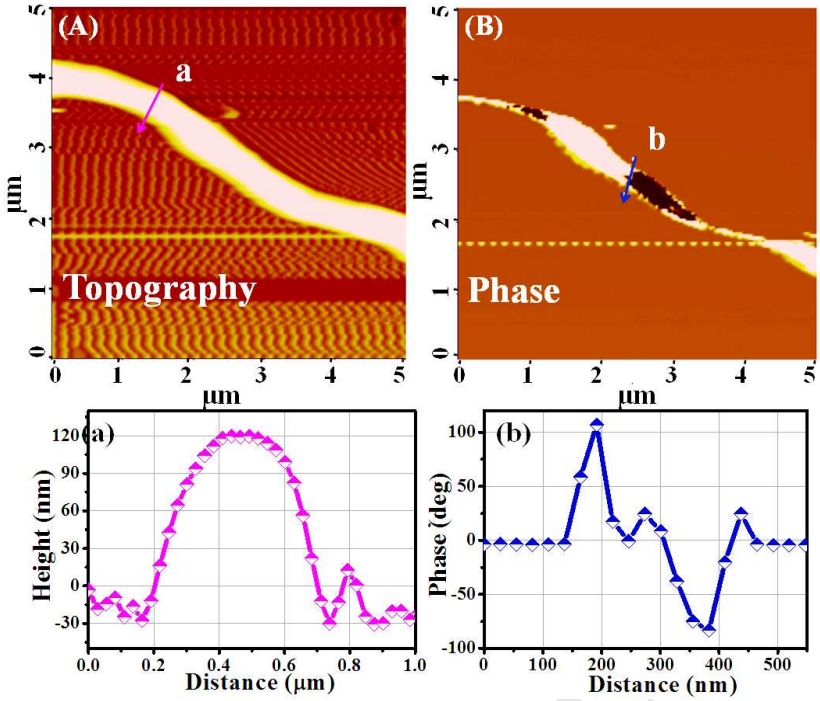

Figure 7. (A) Topography and (B) phase images of vertically aligned Fe_3C filled CNT, (b) and (c) line profiles correspond to the topography and phase image.

As evidenced from Fig. 1(c), as-grown Ni-filled CNTs were found to have curly structure with random orientation. The response of magnetic tip to such Ni-filled CNT was analogous to randomly grown CNT either filled with Fe_3C or Co, as shown in Fig. 8. The maximum positive phase shift along the diameter of the tube was found to be 28º.

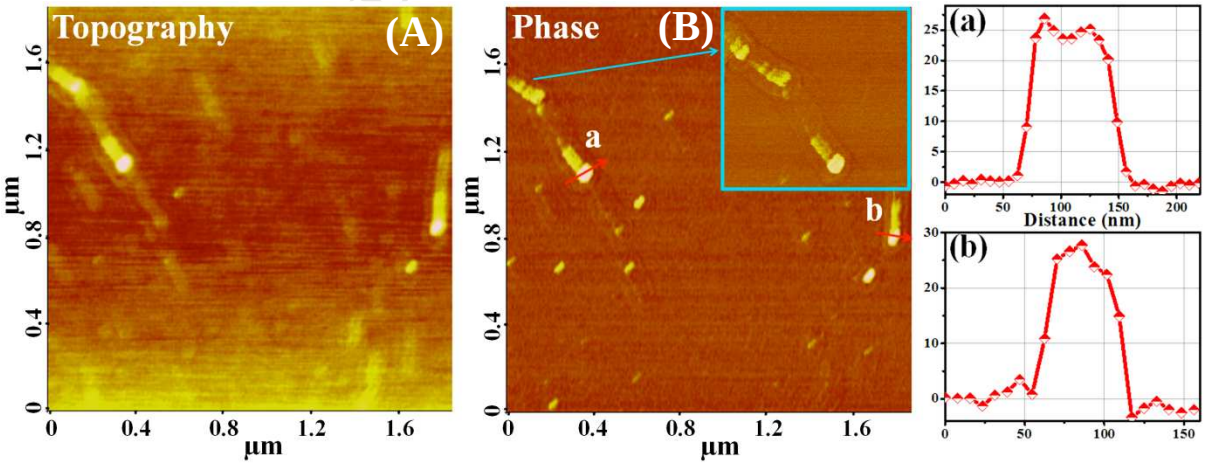

Figure 8. (A)Topography and (B) phase images of Ni-filled CNT which always grow with random orientation, (b) and (c) line profiles drawn on two different CNT.

Theoretically, in lift mode, phase variation is directly related to the local force derivative. Therefore, MFM does not directly measure the interaction energy, rather the force which is derived either from sample-tip interaction, or force gradient which ultimately results in contrast formation[33]. As demonstrated above, for vertically aligned CNTs contrast variation was observed along the tube axis whereas if CNTs grown randomly we have observed either one type of contrast or combination along the diameter of the tube. The darker contrast represents negative phase shift which is associated with the force of attraction while bright one showing positive phase shift appeared as a result of repulsive interaction. Here, it can be emphasized that phase images depict the magnetic state of nanorod, possessing single domain structure. Confined nanorods have different direction of magnetization hence the way of interaction would be specific. In order to attain an understanding about magnetic interaction between tip and filled region of CNT, a schematic representation has been shown in Fig.9. As it was probed that in magnetized CNT direction of magnetization is either along or perpendicular to the tube axis. Suppose, if pole formation is along the tube axis, then during scanning tip will alternatively experience both attractive and repulsive interaction, depending on the nature and location of the pole. Therefore, in such case bright and dark contrast will form along the axis of the tube as shown in the right part of Fig.9. On the other hand, if poles form in radial direction then only one type of interaction would be experienced again depending on the nature of pole, consequently, one type of contrast would appear as shown in left part of Fig.9. Furthermore, we have estimated magnetic moment of individual nanorod (m_s) which is determined to be 3.18×10^{-14} A m^2. This value was found to be 100 times higher than that of bulk and suggests that strong magnetization occurred in confined material. More details of calculation are given in supplementary information S1.

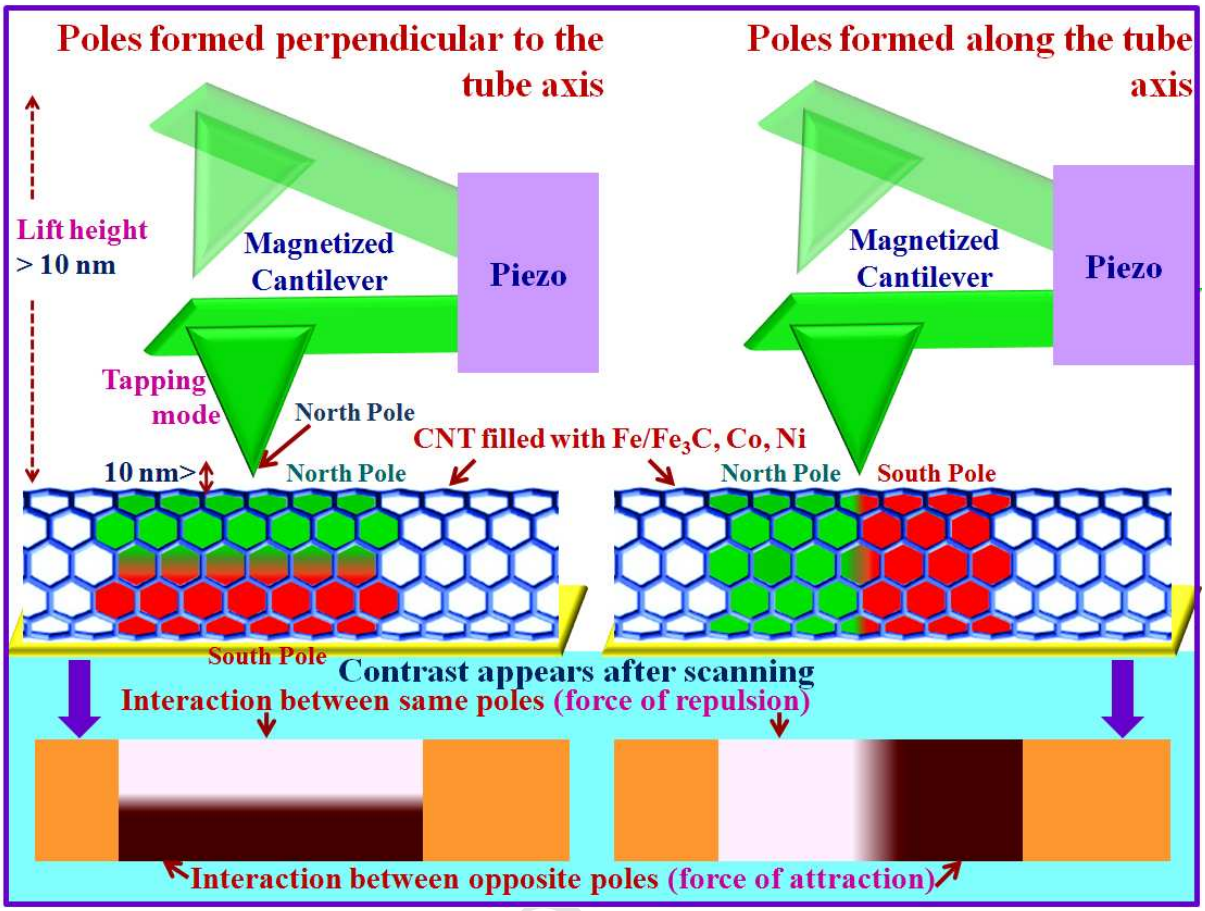

Figure 9. Schematic representation of contrast generation due to interaction between magnetized tip and filled-CNT. When magnetic poles form in CNT along tube axis it generates alternate contrast along the length of the tube whereas in case pole formation perpendicular to the tube contrast variation is perpendicular to the tube.

In order to further explore the feasibility of filled-CNTs to be used in data storage device, we have probed the standard hard disk drive (HDD) and results were compared. Phase image of HDD (see Fig.10) seems to be nearly same as we have observed in vertical aligned filled-CNT where alternate bright and dark contrast appears. Phase images of CNT and HDD reveals that shift was much higher in filled CNT, depending on nature of filler. Therefore, we propose that vertically aligned filled-CNTs could be promising material for data storage applications.

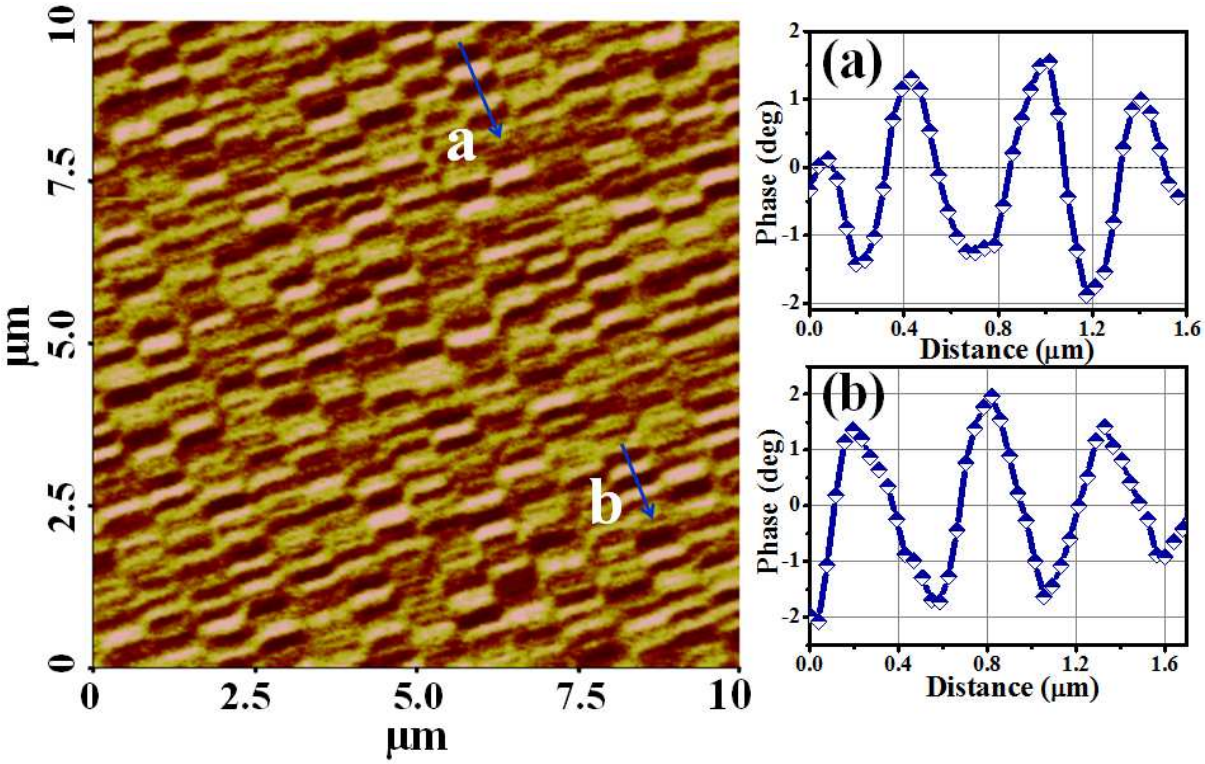

Figure 10. Phase image of hard disk drive, (b) and (c) phase shift profiles corresponding to the lines marked as a and b in phase image.

In the perspective of storage application, ability of writing as well as erasing which involves reversal switching of magnetization direction was studied. Here, we applied different bias voltages between confined nanorod and tip and subsequently scanned to capture phase images. As shown in Fig. 11, the magnetic switching in Co nanorod by applying bias voltage of 18 V and -18 V was achieved with total height of 25 nm from surface of filled-CNT. In this process, first, the MFM phase image with total height of 50 nm (30 nm lift height, 20 nm set point) has been captured without bias as shown in Fig. 11b and then a bias of +18 V was applied and filled-CNT was scanned. In second step, bias was removed and tip is lifted to 30 nm and then sample was scanned for MFM phase imaging. The phase images clearly demonstrate the switching of contrast which reflects the reversal of magnetization. In order to further confirm reversal switching, MFM phase image has been taken by applying bias of -18 V as shown in Fig. 11d. Since appropriate applied bias can efficiently allow the

reconstruction of spin structures and resulted in contrast switching. This electric field derived local switching of magnetization pave the way to use the filled-CNT in storage devices.

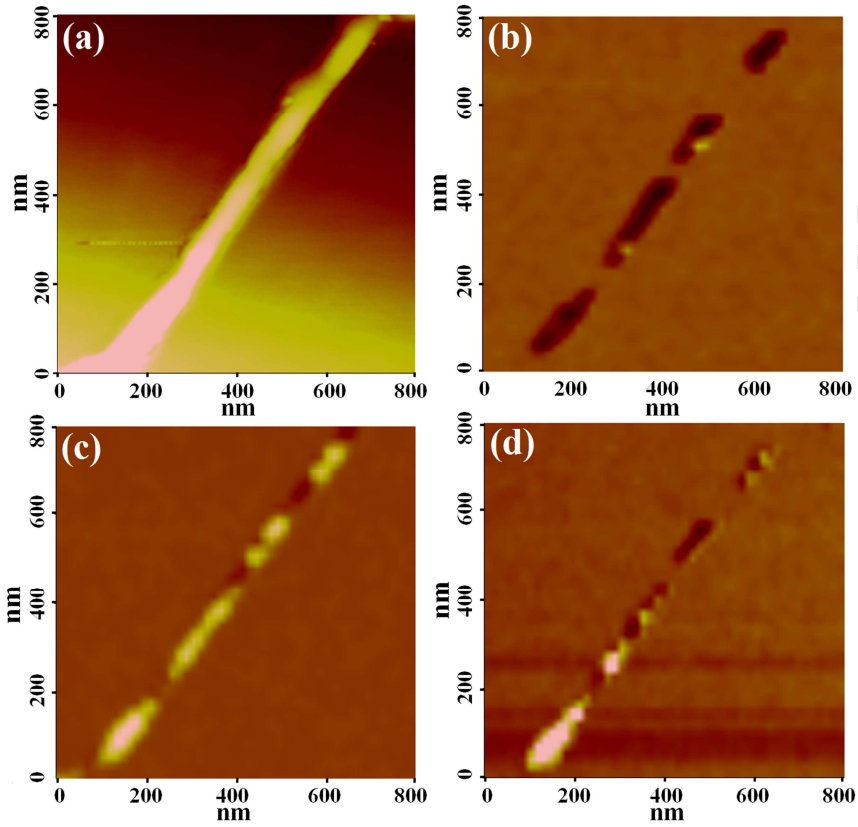

Figure 11. Electric field driven reversal switching of direction of magnetization (a) Topography of Co-filled CNT (randomly grown) having 42 nm outer and 18 nm inner diameter, (b) MFM phase image of filled part, (c-d) In order to demonstrate the switching of magnetization first, filled-CNT was first scanned by applying 18 V and then phase image was captured when voltage between tip and sample was 0 V. (d) -18 V was applied and then phase image was captured keeping voltage again 0 V.

Above-depicted analysis conclude that in vertical aligned CNT either filled with Fe_3C or Co, poles were always formed along the tube axis whereas in randomly oriented CNTs poles were formed in radial direction. Theoretically, direction of magnetization is governed by either shape or magnetocrystalline anisotropy. Since, Fe_3C possesses orthorhombic structure therefore magnetocrystalline anisotropy dominates in bulk as well as in nano-dimension[34], whereas shape anisotropy dominates in Co and Ni nanorods having FCC structure[35,36]. In literatures, it has been reported that if Co and Ni nanorods possess FCC structure, shape anisotropy always dominates whether they are bare or confined. In the present case, direction

of magnetization was not found to be dependent on the anisotropies. Here, it is being controlled by the magnetic field gradient produced inside the reactor as demonstrated in Fig. 12. This can be understood as during growth in order to maintain a constant temperature, a constant current is passed through the coils turned around the periphery of reactor. This current always produces heat and magnetic field gradient in the radial direction as shown in Fig.12. The current supply raises temperature to the set point (850 °C) and is maintained till completion of the growth. Thereafter, the current supply is turned off in order to cool down the reactor due to which magnetic field is not present during cooling. The as-described process results *in situ* filling and permanent magnetization of CNTs by formation of magnetic poles in filled nanorods. We propose that during the *in situ* filling, magnetic dipoles in metal cluster/nanorod are formed in such a manner that the poles are always directed from bottom to center of the reactor. This can be further explained as in case of nano-sized one-dimensional objects like CNTs, a small section of the current carrying coil near the bottom of the quartz reactor is supposed to behave as a straight wire and produce a magnetic field gradient in the radial direction which controls the direction of magnetization along the radial direction of reactor i.e. along the axis of the nanorod in vertically grown CNT and perpendicular in randomly grown CNT as demonstrated in Fig. 12.

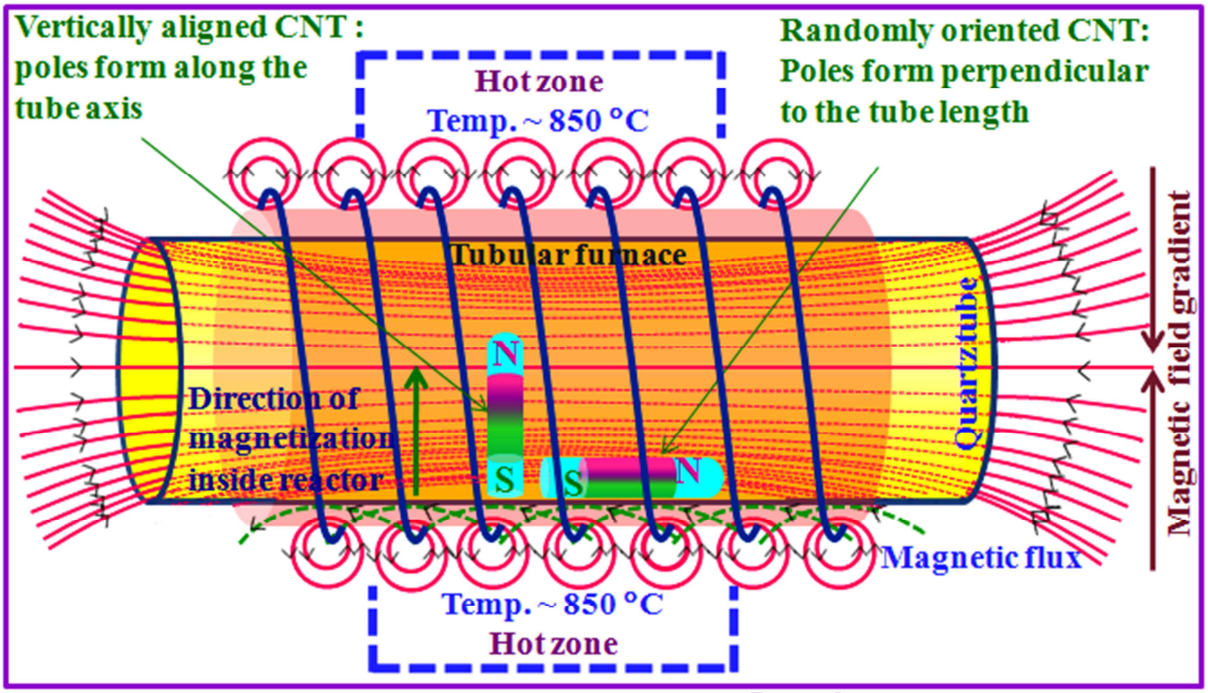

Figure 12. Mechanism of pole formation in CNT during synthesis.

Growth mechanism

As demonstrated above, all three as-grown samples possess different morphological as well as structural properties depending on the catalyst. We have observed that CNTs grown by using Fe as a catalyst were more dense and of good quality with high yield whereas in case of Co catalyst these CNTs exhibits I_G/I_D ratio > 1, with low yield in comparison of Fe_3C-filled CNTs. Furthermore, in case of Ni catalyst, CNTs were randomly grown and quality is low even if experimental conditions were kept similar as in case Fe and Co. Moreover, if Fe was used as a catalyst, CNTs were filled with Fe_3C. On the other hand, in case of Co and Ni we did not observe any carbide formation. In order to understand the catalyst dependent growth behavior and encapsulation phenomena, a complete growth mechanism is needed. The schematic of growth mechanism is depicted in Fig. 13. The following steps were described to enlighten the growth mechanism of filled-CNT. First, metallocene decomposes before entering into the hot zone in temperature range of 350-550 °C depending on the metal. Among all three used metallocene, ferrocence is most stable as compared to other. Their

thermal stability can be ordered as Cp_2Fe (550 °C) > Cp_2Co (450 °C) > Cp_2Ni (360 °C)[37]. The thermal decomposition of metallocene is considered to be associated with both thermodynamic factors as well as electronic structure factors. Low thermal stability of both cobaltocene and nickelocene is due to the presence of one electron on the anti-bonding orbital in former one and two electrons in later one[37]. In this experiment, benzene not only supplies carbon atoms but also facilitates the dissociation of metallocene by releasing atomic hydrogen. At 850 ºC, first complete decomposition of metallocene occurred and afterwards metal atoms released. These free atoms can easily diffuse on the inner wall of the quartz reactor and then form clusters on the surface of reactor wall. These clusters not only serve as a catalyst for nucleation of CNT but also act as a source of metal atoms for the encapsulation inside the core of CNT. During the nucleation of CNT, carbon diffusion in/on the metal cluster plays a decisive role in order to grow MWCNT/SWCNT because during single walled carbon nanotubes (SWCNT) growth, surface diffusion dominates while in the case of MWCNT, sub surface diffusion or bulk diffusion dominates which is in agreement with the previous reports[39]. As reported earlier, for growth of inner walls of the tubes, supply of carbon is accomplished through sub surface diffusion or bulk diffusion[38]. Energy barriers for surface diffusion of carbon atoms on (111) plane of Fe, Co and Ni are reported as 0.45 eV, 0.40 eV, 0.40 eV, respectively[39,40]. Activation energies for sub-surface diffusion of carbon atoms in Fe, Co, Ni were reported to be 0.73 eV, 0.83, 1.0 eV respectively[39-41] whereas for bulk diffusion energy barriers are 0.83 eV, 1.51eV, 1.6 eV respectively[42-44]. After the formation of cluster, in/on diffused C atoms first nucleate the graphitic layer on the cluster surface and then this layer lifts off from cluster surface in order to start the nucleation of CNT walls. During the growth of CNT, metal atoms also diffuse on the inner surface of the CNT as surface diffusion is favorable due to weak interactions between Fe, Co, Ni and graphite. The migration energy of Fe, Co, Ni atoms to diffuse on graphene has been reported to be

nearly 0.404 eV, 0.468 eV and 0.222 eV respectively[45]. During growth of CNT, these metals start to diffuse inside the tube and then trapped at energetically favored sites. This leads to clustering metal atoms inside core of CNT and eventually nanorod forms. In present case, filling occurs through solid state diffusion of metal atoms not via capillary action as evident by fragmented filling and such diffusion accomplished due to the continuous supply of metal atoms thorough dissociation of catalyst precursor. This assumption agrees the mechanism reported by Xiang *et al.* where they suggests that filling of CNT achieved through solid state diffusion of metal atoms through root of CNT on optimum feeding of catalyst[46]. However, it has also been reported that small nanoparticles can diffuse inside the core through open end of CNT and can form rod like structure[47]. Both possible ways of filling corroborate our proposed mechanism that filling is accomplished via solid diffusion inside CNT core.

In general, Fe, Co or Ni metals tend to form metastable carbides above 350 ºC. Interestingly, in present case carbide formation is found to occur only in case of Fe whereas pure FCC phase of Co and Ni were formed. This might be possible because Fe_3C phase can exist up to 900 ºC but Co_3C and Ni_3C decompose nearly at 468 ºC and 418 ºC respectively[48]. It can be presumed that Co_3C and Ni_3C were formed as intermediate compound but in present growth process, vapors of nickelocene or cobaltocene were introduced after desired growth temperature (850 ºC) was achieved and at such high temperature which is far above their decomposition temperature these carbides will decompose. Therefore, we can believe that these carbide phases could not exist as final products along with pure metal phases. However, in Fe, the carbide formation as an intermediate phase along with FCC and BCC phases is possible. But the possibility of carbide formation is insignificant as it has been reported that at high temperature Fe_3C decomposes in argon atmosphere[49]. Among all, BCC phase was reported to be the most active for CNT nucleation and atomic Fe can easily diffuse inside CNT. Subsequent diffusion of Carbon atoms inside the CNT core led the formation of Fe_3C.

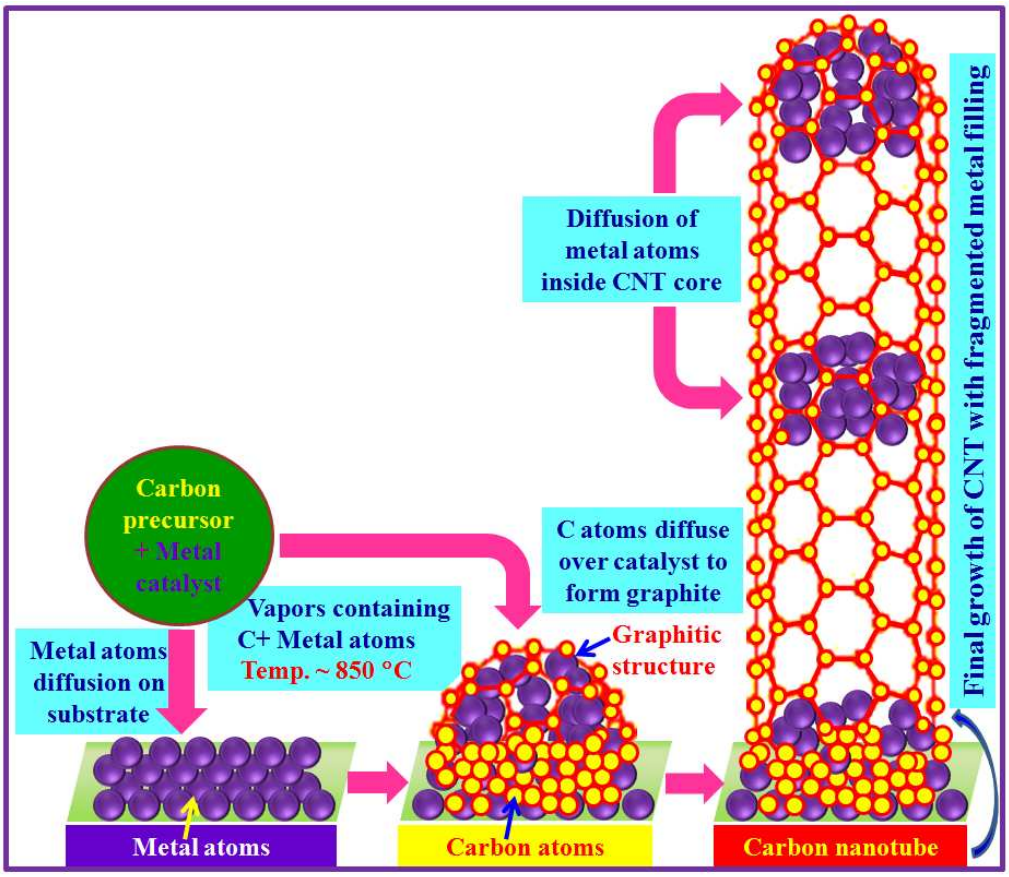

Figure 13. Schematic of growth mechanism filled CNT.

Conclusion:

We conclude that direction of magnetization in Fe_3C, Co and Ni nanorod filled inside the CNT was controlled by magnetic field gradient which is always present in radial direction of the reactor. Direction of magnetization does not depend on shape or magnetocrystalline anisotropy, rather field gradient is found to control the pole formation in nanorod. Furthermore, structural properties of filled-CNT are found to be significantly influenced by catalyst nature. Here a comprehensive model is presented in order to understand the growth as well as direction of magnetization. Probed MFM study reveals that filled-CNT possess superior magnetic properties than that of existing HDD in terms of phase angle even if nanorod of diameter 20 nm exhibits large phase angle than that of ~ 0.4 μm of HDD. We

envision that present study will be forwarding step for the application of magnetized CNT in spintronics and storage devices.

Acknowledgments

MKS and PKT would like to thank Bilateral Cooperação Científica e Tecnológica FCT/INDIA-2015/2017; between University of Aveiro, Portugal and Delhi Technological University, India (INT/PORTTUGAL/P-13/2013) sponsored by DST-FCT. Authors are thankful to Prof. F. Banhart for his valuable comments and scientific discussion.

References

1. W. Ding, J. Qiu, Z. Zhao, Q. Zhou, M. Liang, Z. Ji, S.Yang, D. Xing, Targeted Fe-filled carbon nanotube as a multifunctional contrast agent for thermoacoustic and magnetic resonance imaging of tumor in living mice, Nanomedicine 12 (2016) 235-44.
2. C. Guangli, B.B. Lakshmi, C.R. Martin, E.R. Fisher, Metal-Nanocluster-Filled Carbon Nanotubes: Catalytic Properties and Possible Applications in Electrochemical Energy Storage and Production, Langmuir. 15 (1999) 750-758.
3. F. Rossella, C. Soldano, V. Bellani, M. Tommasini, Metal-Filled Carbon Nanotubes as a Novel Class of Photothermal Nanomaterials, Adv. Mater. 24 (2012) 2453–2458.
4. R. Marega, D. Bonifazi, Filling carbon nanotubes for nanobiotechnological applications, New J. Chem. 38 (2014) 22-27.
5. F. Wolny, U. Weissker, T. Mühl, M.U. Lutz, C. Müller, A. Leonhardt B. Büchner, Stable magnetization of iron filled carbon nanotube MFM probes in external magnetic fields, J. of Physics Conference Series, 200 (2010) 112011.

6. F. Wolny, T. Mühl, U. Weissker, K. Lipert, J. Schumann, A. Leonhardt, B. Büchner, Iron filled carbon nanotubes as novel monopole-like sensors for quantitative magnetic force microscopy, Nanotechnology 21 (2010) 435501.
7. W. Zhang, Z. Zhong, Y. Zhang, The application of carbon nanotubes in target drug delivery systems for cancer therapies, Nano Resea. Lett. 6 (2011) 555.
8. M.L. Chen, Y.J. He; X.W. Chen, J.H. Wang, Quantum Dots Conjugated with Fe_3O_4-Filled Carbon Nanotubes for Cancer-Targeted Imaging and Magnetically Guided Drug Delivery, Langmuir 28 (2012) 16469–16476.
9. F. Rossella, C. Soldano, P. Onorato, V. Bellani, Nanoscale, Tuning electronic transport in cobalt-filled carbon nanotubes using magnetic fields, 21 (2014) 788-94.
10. Y.W. Tyson, Magnetic storage medium formed of carbon nanotube arrays, U.S. Patent 11, 278, 879, Mar 30, 2010.
11. R.S. Molday, D. Mackenzie, Immunospecific ferromagnetic iron-dextran reagents for the labeling and magnetic separation of cells, J. Immun. Meth. 52 (1982) 353-367.
12. J. Kosel, T. Ravasi, M. Fernanda, C. Gerenas, Biofunctionalized magnetic nanowires, U.S. Patent, 13, 919, 552, Dec 19, 2013.
13. S. Nath, C. Kaittanis, V. Ramachandran, N.S. Dalal, J.M. Perez, Synthesis, Magnetic Characterization, and Sensing Applications of Novel Dextran-Coated Iron Oxide Nanorods, Chem. Mater. 21 (2009) 1761–1767.
14. Y.C. Stephen, S.W. Mark, R.K. Peter, P.B. Fischer, Single domain magnetic pillar array of 35 nm diameter and 65 Gbits/in.2 density for ultrahigh density quantum magnetic storage, J. Appl. Phys. 76 (1994) 6673.
15. M.U. Lutz, U. Weissker, F. Wolny, C. Müller, M. Löffler, T. Mühl, A. Leonhardt, B. Büchner, R. Klingeler, Magnetic properties of α-Fe and Fe_3C nanowires, Journal of Physics: Conference Series. 200 (2010) 072062.

16. S. Karmakar, S.M. Sharma, M.D. Mukadam, S.M. Yusuf, A.K. Sood, Magnetic behavior of iron-filled multiwalled carbon nanotubes. J. Appl. Phys. 97 (2005) 054306-01-054306-05.

17. R. Bhatiya, V. Prasad, Synthesis of multiwall carbon nanotubes by chemical vapor deposition of ferrocene alone, Sol. Sta. Commun. 150 (2010) 311-15,

18. A.G. Osorio, L.G. Pereira, J.B.M. Cunha da, C.P. Bergmann, Controlling the magnetic response of carbon nanotubes filled with iron-containing material. Mater. Rese. Bull., 48 (2013) 4168-4173.

19. P. Aprelev, Y. Gu, R. Burtovyy, I. Luzinov, K.G. Kornev, Synthesis and characterization of nanorods for magnetic rotational spectroscopy, J. App. Phy. 118 (2015) 074901.

20. S.A. Majetich, Y. Jin, Magnetization Directions of Individual Nanoparticles, Science 284 (1999) 470-473.

21. R. Kumari, L. Krishnia, V. Kumar, S. Singh, H. K. Singh, R. K. Kotnala, et. al. Fe_3C-filled carbon nanotubes: permanent cylindrical nanomagnets possess exotic magnetic properties, Nanoscale, 8 (2016) 4299-4310.

22. M.S. Dresselhaus, G. Dresselhaus, A. Jorio, A.G. Souza Filho, R. Saito, Raman spectroscopy on isolated single wall carbon nanotubes, carbon 40 (2002) 2043.

23. A.C. Ferrari, J. Robertson, Interpretation of Raman spectra of disordered and amorphous carbon, Phy. Rev. B 61 (1999)14095-99.

24. A.M. Rao, A. Jorio, M.A. Pimenta, M.S.S. Dantas, R. Saito, G. Dresselhaus, M.S. Dresselhaus, Polarized Raman Study of Aligned Multiwalled Carbon Nanotubes, Phys. Rev. Lett. 84 (2004) 1820-23.

25. C. Thomsen, S. Reich, Double Resonant Raman Scattering in Graphite. Phy. Rev. Lett. 80 (2004) 5214-5217.

26. S. Gayen, S. N. Behera, S. M. Bose, Raman spectra of unfilled and filled carbon nanotubes: theory, Phys. Rev. B 76 (2007) 165433.

27. C. Jiang, S. G. Srinivasan, A. Caro, S. A. Maloy, Structural, elastic, and electronic properties of Fe_3C from first principles, J. Appl. Phys. 103 (2008), 043502.

28. O.P. Gupta, Crystal dynamics of face centered cubic cobalt, Sol. Stat. Comm. 42 (1982) 31-32.

29. R.J. Blrgeneau, J. Cordes, F.G. Dolling, A.D.B. Woods, Normal Modes of Vibration in Nickel. Physical Review 136 (1964) A1359.

30. A.S. Paipetis, V. Kostopoulos, Carbon nanotube enhanced eerospace composite materials: A new generation of multifunctional hybrid structural composites, Springer Netherlands, 2012, pp186-211.

31. N.Y. Rokhmanov, A.F. Sirenko, S.A. Bakharev, Thermal expansion of cementite in hypereutectoid iron - Carbon alloy, Met. Sci. Hea. Treat. 39 (1997) 1 -2.

32. F.Y. Wu, H.M. Cheng, Structure and thermal expansion of multi-walled carbon nanotubes before and after high temperature treatment, J. Phys. D: Appl. Phys. 38 (2005) 4302–07.

33. A. Hubert, W. Rave, Imaging magnetic charges with magnetic force microscopy. Phys. Stat. Sol. 204 (1997) 817.

34. U. Weissker, M. Löffle, F. Wolny, M.U. Lutz; N. Scheerbaum, Perpendicular magnetization of long iron carbide nanowires inside carbon nanotubes due to magnetocrystalline anisotropy, J. Appl. Phys. 106 (2009) 054909-5.

35. N. Cordente, Synthesis and Magnetic Properties of Nickel Nanorods, Nanoletters, 1 (2001) 565-568.

36. P. Aprelev, Y. Gu, R. Burtovyy, I. Luzinov, K.G. Kornev, Synthesis and characterization of nanorods for magnetic rotational spectroscopy, J. Appl. Phy. 118 (2015) 074901.

37. L.M. Dy-Agileva, V.P. Mar'in, E.I. Tsyganova, Reactivity of the first transition row metallocenes in thermal decomposition reaction, Journal Of Organometallic Chemistry, 175 (1979)63-72.

38. J.P. Tessonnier, D.S. Su, Recent progress on the growth mechanism of carbon nanotubes: a review, Chem. Sus. Chem. 4 (2011) 824-47.

39. X.W. Liu, Y.W. Li, J.G. Wang, C.F. Huo, First-principles study of the mechanism of carbon deposition on Fe(111) surface and subsurface. J. Fuel. Chem. Tech., 40 (2012) 202-9.

40. S. Hofmann, G. Csanyi, A.C. Ferrari, M.C. Payne, J. Robertson, Surface Diffusion: The Low Activation Energy Path for Nanotube Growth, Phy. Rev. Lett. 95 (2005) 036101.

41. L. Qiao, X. Zhang, S. Wang, S. Yu, X. Hu, L. Wang, Y. Zeng, First-principles investigations on the adsorption and diffusion of carbon atoms on the surface and in the subsurface of Co (111) related to the growth of graphene, RSC Adv. 4 (2014) 34237–34243.

42. C.J. Smithells, Smithells metals reference book. Seventh edition ed. Brandes EA, Brook G, editors. Oxford: Butterworth-Heinemann; 1992.

43. H. Mehrer, Landolt-Börnstein: Numerical data and functional relationships in science and technology. 26. Berlin: Springer-Verlag; 1992. p. 471.

44. J.H. Byeon, J.H. Park, K.Y. Yoon, J. Hwang, Ambient spark generation to synthesize carbon-encapsulated metal nanoparticles in continuous aerosol manner, Nanoscale, 1 (2009) 339–343.

45. X. Liu, C. Z. Wang, Y. X. Yao, W. C. Lu, M. Hupalo, M. C. Tringides, K. M. Ho, Bonding and charge transfer by metal adatom adsorption on graphene, Phy. Rev. B, 83 (2011) 235411.

46. R. Xiang, G. Luo, W. Qian, Q. Zhang, Y. Wang, F. Wei, Q. Li, A. Cao, Encapsulation, Compensation, and Substitution of Catalyst Particles during Continuous Growth of Carbon Nanotubes, Adv. Mater. 19 (2007) 2360–2363.

47. A. Cao, X. Zhang, J. Wei, Y. Li, C. Xu, J. Liang, D. Wu, Macroscopic Three-Dimensional Arrays of Fe Nanoparticles Supported in Aligned Carbon Nanotubes, J. Phys. Chem. B 105 (2001) 11937-11940.

48. K. Tokumitsu, Synthesis of metastable Fe_3C, Co_3C and Ni_3C by mechanical alloying method, Materials Scence Forum. 235-238 (1997) 127-132.

49. T. Miki, K. Ishi, Decomposition Behavior of Fe_3C under Ar atmosphere, ISIJ International, 54 (2014) 29-31.

50. X. Li, W. Lu, Y. Song, Y. Wang, A. Chen, B. Yan, S. Yoshimura, H. Saito, Quantitatively probing the magnetic behavior of individual nanoparticles by an AC field modulated magnetic force microscopy, Scientific Reports 6 (2016) 22467 (1-8).

Supplementary information (S1):

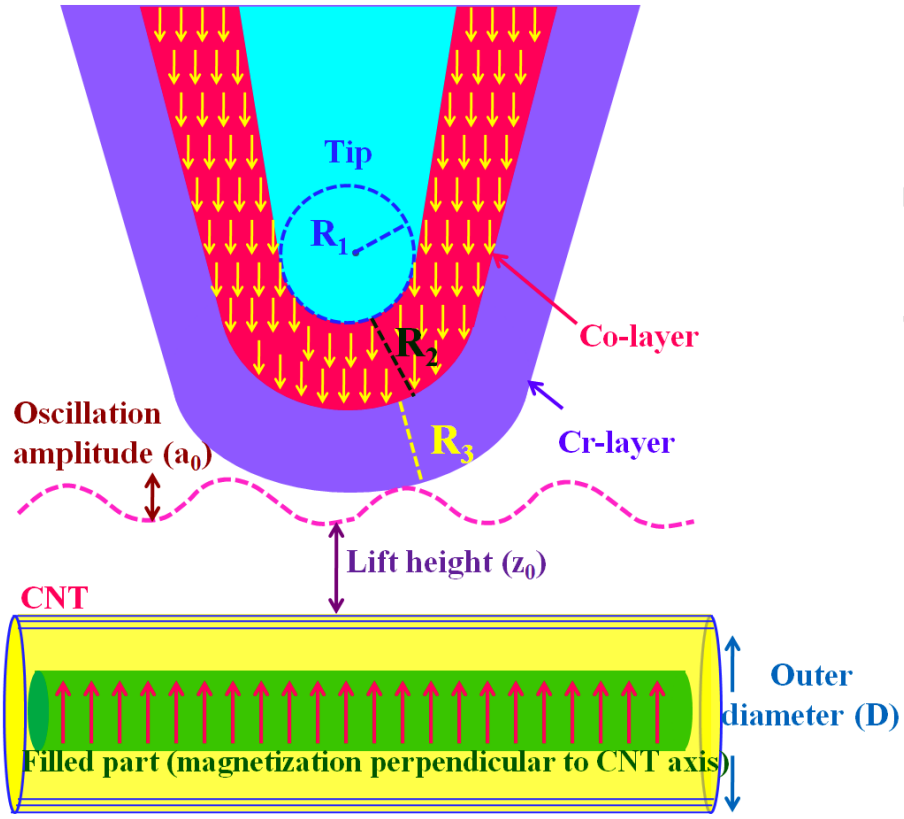

Figure S1. Schematic of magnetic interaction between the MFM tip and magnetic nanord confined inside CNT with spin orientations along z direction.

We have estimated the magnetic strength of individual nanorod by taking in to account of magnetostatic interaction between tip cylindrical nanorod. In this evolution, curved tip of Si coated with a magnetic layer of Co/Cr was used as probe and set into oscillation at a frequency *f* close to its resonance frequency (f_0). Probe was lifted-up to certain height (h) from sample surface in order to ensure that the force gradient along the *z* axis was produced only due to the magnetic force between rod and tip. Hence the resulted phase shift can be expressed as[1]:

$$\varphi = \frac{Q}{K_c}\frac{\partial^2 F_z}{\partial z^2} \quad (1)$$

Where Q and K_c are the cantilever quality factor and spring constant of tip, respectively and Fz is the component of the force acting between tip and sample along the z direction. The force acting on the tip can be obtained by integrating the tip–sample force density and expressed as:

$$F = \mu_0 \nabla(\vec{m}_t \cdot \vec{H}_s) \quad (2)$$

Where μ_0 is the vacuum permeability, H_s is the stray field of the sample and m_t is the magnetic moment of the tip. Magnetic moment (m_t) of the tip can be calculated by using Equation 3 and determined to be 1.52×10^{-16} Am^2.

$$m_t = \frac{4}{3}\pi\left[(R_1 + R_2)^3 - {R_1}^3\right]M_t \quad (3)$$

$$M_t = 1.4 \times 10^6 \text{ A/m}$$

It is presumed that the tip is uniformly magnetized in the z direction; consequently the z component of interacting force is considered as acting force. Hence eq. (2) becomes

$$F_z = \mu_0 \frac{\partial}{\partial z}(\vec{m}_t \cdot \vec{H}_s) \quad (4)$$

Here, H_s for the nanorod was calculated by considering it as a small cylinder of radius 'a' and length 'l'. This presumed that direction magnetization (M_s) is perpendicular to the cylinder axis as shown in Figure S1. In such case, H_s at distance r from the cylinder can be expressed as.

$$H_s = \frac{M_s a^2 \cos\theta}{2r^2} \quad (5)$$

Here θ is angle between M_s and $\hat{r}$. In this case, we have measured the phase shift when $Ms \parallel M_t$ and $Ms \parallel \hat{r}$. In this case, θ = 0° and r is the total distance between nanorod and center of tip dipole. Hence the relation (5) becomes

$$H_s = \frac{M_s a^2}{2z^2}$$

Where $M_s = \frac{m_s}{\pi a^2 l}$

Now expression for H_s, F_z and φ becomes

$$H_s = \frac{1}{2\pi}\frac{m_s}{z^2 l}$$

$$F_z = \mu_0 \frac{\partial}{\partial z}\left(\frac{1}{2\pi}\vec{m}_t \cdot \frac{\vec{m}_s}{z^2}\right)$$

Putting the expression for F_z, Eq.1 becomes:

$$\varphi = \frac{Q}{K_c}\frac{\mu_0}{2\pi l}\frac{\partial^2}{\partial z^2}\left(\frac{1}{z^2}\right) m_t m_s \frac{180}{\pi}$$

$$\varphi = \frac{Q}{K_c}\frac{\mu_0}{2\pi l}\left(\frac{6}{z^4}\right) m_t m_s \frac{180}{\pi} \quad (6)$$

Here, z is the total distance from centre of sample to centre of tip dipole is taken as:

$$z = \frac{D}{2} + R_1 + R_2 + R_3 + z_0 + a_0$$

Where D, R_1, R_2, R_3, z_0, a_0 have been represented in Fig.S1

The total z is found to be 130 nm by taking values of D = 40 nm, R_1 =10 nm, R_2 =20 nm, R_3 =20, z_0 =50 nm and a_0 =10 nm.

By taking $\varphi = 70^0$ and length of nanorod $l = 300$ nm as shown in Fig. 4, we have determined m_s to be 3.18×10^{-14} A m^2. This value was found to be 100 times higher than that of bulk and suggests that strong magnetization occurred in confined material.

References:

51. X. Li, W. Lu, Y. Song, Y. Wang, A. Chen, B. Yan, S. Yoshimura, H. Saito, Quantitatively probing the magnetic behavior of individual nanoparticles by an AC field modulated magnetic force microscopy, Scientific Reports 6 (2016) 22467 (1-8).

International Journal of Sustainable Built Environment (2017) xxx, xxx–xxx

HOSTED BY

ELSEVIER

Gulf Organisation for Research and Development

International Journal of Sustainable Built Environment

ScienceDirect
www.sciencedirect.com

Original Article/Research

Fuzzy decision approach for selection of most suitable construction method of Green Buildings

Sunita Bansal [a,*], Srijit Biswas [b], S.K. Singh [c]

[a] Uttarakhand Technical University, Dehradun, India
[b] Department of Civil Engineering, Manav Rachna International University, Faridabad, India
[c] Department of Environmental Engineering, Delhi Technological University, Delhi, India

Received 15 December 2015; accepted 10 February 2017

Abstract

A big challenge in sustainable projects is selection of appropriate construction method and is considered to be the decisive factor for its success. Many environment friendly prefabricated elements are entering into the market at an increasing pace. This has increased the workload and inquisitiveness of the stakeholders who will need information about their environmental, technical and esthetic aspects. The use of prefabrication in sustainable construction is advantageous but appropriate decision criteria and their weightage for applicability assessments for a project from every stakeholder's perspective is found to be deficient. Decisions to use prefabricated elements are still largely based on anecdotal evidence or cost-based evaluation rather than holistic sustainable performance. But authenticated information is seldom available and suitability within the project requirements is always debatable. Environmental decisions, being closely coupled with society's built-in uncertainties and risks, are uncertain since ecological systems as well as social systems change in the future. Thus the selection of a suitable construction method has been perceived as a multi-criteria decision-making problem highly intensive in knowledge with partial information and uncertainty. This knowledge or perception base from the minds of experts has to be collected and processed for a decision. Fuzzy synthetic evaluation method using analytic hierarchy process by Saaty has been adopted to provide an analytical tool to evaluate the applicability of prefabricated or on-site construction method.

Keywords: Buildings; Cast-in-situ construction; Precast construction environment; Mathematical modeling; Sustainability

1. Introduction

With mounting threats of environmental pollution, natural resource depletion and accompanying social problems, sustainable development in construction has become a growing concern (Neama, 2012). Construction of Green Buildings has now become a flagship of Sustainable Development in construction sector and offers an opportunity to create environmentally responsible and occupant friendly buildings. However, definition, scope and various approaches of Green Buildings compared to conventional buildings is still not well understood. Also, little emphasis has been laid on the importance of selecting more environment friendly designs during the project appraisal stage

* Corresponding author at: Department of Civil Engineering, Manav Rachna International University, Faridabad, India.
E-mail addresses: sunitabansal.fet@mriu.edu.in, sunitabansal221@gmail.com (S. Bansal), srijitbiswas@yahoo.com (S. Biswas), sksinghdce@gmail.com (S.K. Singh).
Peer review under responsibility of The Gulf Organisation for Research and Development.

http://dx.doi.org/10.1016/j.ijsbe.2017.02.005

Please cite this article in press as: Bansal, S. et al. Fuzzy decision approach for selection of most suitable construction method of Green Buildings. International Journal of Sustainable Built Environment (2017), http://dx.doi.org/10.1016/j.ijsbe.2017.02.005

Notation

$u_1,u_2,\ldots,u_n$ are a set of evaluation factors or criteria
$v_1,v_2,\ldots,v_m$ are a set of evaluation grades
V_i is a probable evaluation which can be described as excellent, good, normal, poor or very poor
R fuzzy relation matrix from U to V
r_{ij} is the membership degree ($i = 1,2,\ldots..n$; $j = 1,2,\ldots\ldots m$)
N is the number of appraisal stakeholders
x_{ij} is the number of the appraisal commissioners
W is the weight set
$w_1, w_2,\ldots..w_n$ weights for evaluation criteria
D is called the decision making set
CM is the construction method
W_{ECO} is the Weight vector for economic criteria
W_{ENV} is the Weight vector for environmental criteria
W_{SOC} is the Weight vector for Social criteria
D_{PC1}, D_{PC2} and D_{PC3} are the decision making sets for Precast
D_{CS1}, D_{CS2}, D_{CS3} are the decision making sets for Cast in Situ
$R_{PC\text{-}ECO}$, $R_{PC\text{-}ENV}$, $R_{PC\text{-}SOC}$ are the Fuzzy Relation Sets for Precast construction
$R_{CS\text{-}ECO}$, $R_{CS\text{-}ENV}$, $R_{CS\text{-}SOC}$ are the Fuzzy Relation Sets for Cast in Situ construction

when environmental matters are best incorporated. Project appraisal based on a multi-dimensional approach would need a sustainability model to allow the alternatives to be ranked (Ding, 2008).

Conventional on-site construction methods have long been criticized for non-sustainability, low productivity, poor quality and safety records, long construction time, and large quantities of waste in the industry (Abioye, 2015; Agamuthu, 2008). Prefabrication is a manufacturing process, taking place at a specialized facility, to form component parts of the final installation. Several benefits of applying prefabrication technology in construction are commonly listed as- shortened construction time, lower overall construction cost, improved quality, enhanced durability, better architectural appearance, enhanced occupational health and safety, material conservation, less construction site waste, less environmental emissions, and reduction of energy and water consumption (Yee and Hon, 2001; Blismas et al., 2006).

Pasquire demonstrated that decisions to use precast elements are still largely based on anecdotal evidence rather than rigorous data, as no formal measurement criteria are available (Blismas et al., 2006). Gluch and Baumann also indicated that holistic and methodical assessments of the precast applicability to a particular project have been found to be deficient, and common methods of evaluation simply take material, time, labor and transportation costs into account when comparing various construction methods, without explicit regard for the sustainability, long-term cost or soft issues, such as health and safety of workers, energy consumption, and environmental impacts of a project (Gluch and Baumann, 2004). Also, for individual building projects, precast technology is not always the only available option, nor is it always better than on-site construction method due to various project characteristics and available resources. If not employed appropriately, change orders, severe delays in production, erection schedules, substantial cost overruns, and constructability problems may be encountered in the use of precast concrete systems (Sacks et al., 2004). The selection of appropriate construction method of a project, considered to be a decisive factor for its success, is perceived as a knowledge problem. The construction companies do not have formal systems to collect, process and manage this knowledge held in the minds of the professionals (Murtaza et al., 1993; Ferrada and Serpell, 2014). Ying Chen identified 33 performance criteria based on the sustainable triple bottom line and requirements of different project stakeholders, consisting of 16 economic criteria, 8 social criteria, and 9 environmental criteria (Chen et al., 2010). Wei Pan and Andrew Dainty developed 50 criteria grouped under cost, time, quality, health and safety, sustainability, etc. but cost was again ranked most important and sustainability, process and procurement were weighted lower. All of these demonstrate that criteria for decisions regarding construction methods are unclear and unrecorded. But considering the relative importance or weightage of each criteria from the perspective of every stakeholder in the decision making process is a difficult task. Thus the selection of a CM among alternative CMs is a multicriteria decision-making problem including both quantitative and qualitative criteria. In decisions related to environment and social factors, the values of the qualitative criteria are often imprecisely defined for the decision-makers. The conventional approaches to CM selection problem tend to be less effective in dealing with the imprecise or vague nature of the linguistic assessment. Thus we have a mix of both tangibles like cost and time and intangibles relating to subjective ideas and beliefs of the individual and the world of experience. So we need to use a coherent theory that can deal with both these worlds of reality without compromising either (Saaty, 1987). The Analytical Hierarchy Process formulates and analyzes decisions by simplifying a complex multi-criteria decision problem and uses the numerical ratings from the pair-wise comparisons to establish an importance weight for each criterion. The aim of this paper is to solve CM selection problem using approach of fuzzy synthetic evaluation group decision-making (Kahraman et al., 2003). Criteria derived from prior studies have been employed in the model developed to support and automate

Please cite this article in press as: Bansal, S. et al. Fuzzy decision approach for selection of most suitable construction method of Green Buildings. International Journal of Sustainable Built Environment (2017), http://dx.doi.org/10.1016/j.ijsbe.2017.02.005

the complex considerations of precast and Cast in Situ CM on Green building projects. This will assist the integrated design team members in the selection of appropriate construction methods in concrete buildings during early project stages. As a result, the likelihood of sustainable construction is enhanced, both to meet society's environmental goals and account for the social and economic impacts of Buildings and thus earn higher credits according to Green Building Rating Systems (Bansal, 2015; Kuncheva, 2001).

2. Literature review

Zuo and Zhao presented a systematic review of existing studies and found that focus is mainly on environmental aspects and social sustainability is being largely overlooked (Zuo and Zhao, 2014). Among all sectors, buildings are one of the largest sources of carbon dioxide and greenhouse gas (GHG) emissions. Developing a low carbon society is a global trend to achieve sustainability and counter the climate change issue (Zuo et al., 2012). Green building Rating systems (Smith, 2015) provide an effective framework for assessing Green Quotient of buildings. The advantages and industrialization of construction sector provide opportunities for prefabrication to better serve sustainable building projects. Worldwide, the highest precast construction levels in 1996 were located in Denmark (43%), the Netherlands (40%), Sweden and Germany (31%) (Jaillon and Poon, 2009). In the United States, the share of precast reinforced concrete construction is only 6% while the average across the European Union is 18% (Sacks et al., 2004). Although the U.S. precast concrete industry produces technologically and architecturally complex building elements, such as double tees, inverted tee and ledger beams, hollow-core slab elements, and façade panels, in building construction market, the percentage of precast concrete systems is pretty low (approximately 1.2%) (Sacks et al., 2004). The construction industry in India is around USD 500 million and precast has only 2% share vis-à-vis the traditional method of cast-in situ construction. However, a gradual shift is occurring and precast construction technology is rapidly gaining a foothold in the Indian construction market and primary among them is the need for affordable housing (VanGeem, 2006). Studies have been made comparing carbon emissions of Precast and conventional cast-in-situ construction methods for high rise buildings (Dong et al., 2015). A lack of incorporation of innovative sustainable technology into corporate strategy was reflected (Pan et al., 2012). The indicators collected from existing literatures and construction sector-based respondents recommend development of practical and simple tools for decisions ensuring sustainability. Govindan et al. (2016) perceived the selection of sustainable materials as a hybrid multi criteria decision making problem with a specific examination of UAE. Si et al. evaluated the application of Multi Criteria Decision making methods to the selection of Green technologies for retrofitting existing buildings. They also suggested that social criteria are as important as environmental or economic criteria which are based on rather quantitative data (Si et al., 2016). Another research on delivering sustainable buildings in context of China identified that additional cost, incremental time and limited availability of green suppliers and information are critical barriers to foster sustainable construction practices (Shi et al., 2013). A recent research analyzing econometric data from Qatar identified characteristics and organizational behavior attributes for Sustainable Construction Adoption. The factors internal to the firms like their risk taking tendencies, claimed competitive advantages or history of changes in modus operandi etc were reflected (Hassan et al., 2016). The problem of CM selection for sustainability involves Economic, Environmental and Social criteria out of which, some can be measured quantitatively and some can be estimated qualitatively. AHP allows decision-makers to make qualitative decisions objectively, enables systematic decision-making by expressing the interaction and hierarchy of factors, thus reducing the risk of a rough estimation. The hierarchy can be complex enough to capture the situation and also sensitive to any small changes (Saaty, 2008). This paper lays the groundwork for automated tools to help make project level decisions regarding prefabrication strategies and facilitates the achievement of a healthy built environment.

3. Research methodology

3.1. Analytic hierarchy process (AHP)

Choosing the appropriate construction method satisfying the triple bottom line of sustainability viz. Environmental, Economic and Social criteria from every stakeholder's perspective is a multi criteria Group Decision making problem. Saaty's analytic hierarchy process (AHP) (Thiranun and Xu, 2015), (Saaty, 1987) is being used to solve this problem which is an intuitively simple method to formulate and analyze decisions. AHP uses the numerical ratings from the pair-wise comparisons of criteria to establish a priority or importance weight. AHP allows decision-makers to make qualitative decisions objectively enabling systematic decision-making by expressing the hierarchy of factors in order of their weightage, thus reducing the risk of a rough estimation (Alonso & Lamata, 2006). Hence, this study adopted AHP to analyze client/developer, contractor et al. preferences in adoption of either precast or on-site construction method.

The three steps of AHP are decomposition into important criteria, comparative judgment of each with respect to another and finally synthesis into an aggregate form. In the first step, a hierarchical structure is established to present the problem of choosing most apt CM. The next step compares criteria at the same level in pairs and measures their comparative contribution to higher Green Building rating. A comparison matrix was set up by

Please cite this article in press as: Bansal, S. et al. Fuzzy decision approach for selection of most suitable construction method of Green Buildings. International Journal of Sustainable Built Environment (2017), http://dx.doi.org/10.1016/j.ijsbe.2017.02.005

comparing pairs of criteria or alternatives. A scale of values ranging from 1 (equally important) to 9 (extreme more important) was used to express stakeholders' preferences. This pair wise comparison enabled the decision-maker to measure the contribution of each criterion to the objective independently, thereby simplifying the decision-making process. The final step conducts synthesis of preferences to calculate a composite weight for each alternative (Saaty, 2008).

3.2. Fuzzy synthetic evaluation

Fuzzy theory (Goguen, 1973; Negoita, 1988) was developed to provide decision-making capabilities in the presence of imprecise and uncertain information, which is usually expressed in linguistic terms. An important application of the fuzzy transform used in developing the extension principle is synthetic evaluation. Fuzzy synthetic evaluation uses fuzzy mathematics to transform and fathom unclear data, and has various attributes concerning evaluation of objects. Thus, a comprehensive assessment and general appraisal must be performed on related factors to produce the overall assessment (Saaty, 2008).

For both Precast and On-site construction method, suppose that domain $U = \{u_1,u_2,\ldots,u_n\}$ denotes a set of evaluation factors or criteria (shortened construction time, lower overall construction cost, improved quality, enhanced durability, better architectural appearance, enhanced occupational health and safety, material conservation, less construction site waste, less environmental emissions); $V = \{v_1,v_2,\ldots,v_m\}$ denotes a set of evaluation grades, where V_i denotes a probable evaluation which can be described as excellent, good, normal, poor or very poor. Every appraisal object has a fuzzy relation matrix R from U to V.

$R = (r_{ij})_{nxm}$ where r_{ij} denotes the membership degree $(i = 1,2,\ldots..n;\ j = 1,2,\ldots\ldots..m)$ and the appraisal object is measured as v_j considering attribute u_i.

If N appraisal stakeholders make appraisal v_j aiming at various factors in U separately, where x_{ij} denotes the number of the appraisal commissioners who determine u_i as v_j, then the sum of each list of numbers in the table equals N.

If $r_{ij} = x_{ij}/N$, then the appraisal matrix of the stakeholders to a particular CM is obtained as $(r_{ij})_{ixj}$.

However the obtained appraisal matrix R is not enough to appraise the CM yet; a fuzzy subset W in U called weight set that is, $W = (w_1,\ w_2,\ldots..w_n)$ in which $w_i > 0$ and $\sum w_i = 1$ should be obtained from AHP (The analytic hierarchy process: Applications and studies, 1993). The weight W denoted the relative importance of the various criteria expressed by the decision makers or the stakeholders in this study. Moreover, a fuzzy subset D in V called the decision making set is also introduced and denotes the overall fuzzy appraisal of the stakeholder to the particular CM.

$$\boldsymbol{D} = \boldsymbol{W} \circ \boldsymbol{R} = [\boldsymbol{d}_1, \boldsymbol{d}_2 \ldots \boldsymbol{d}_m]$$

3.3. Questionnaire and data collection

First, stakeholders in decision making were interviewed to create the research model and questionnaire. For evaluation, criteria based on triple bottom line were employed. Chen projected 33 performance criteria (Chen et al., 2010) based on the sustainable triple bottom line and requirements of different project stakeholders, consisting of 16 economic criteria, 8 social criteria, and 9 environmental criteria. Wei (Pan et al., 2012) also developed 50 criteria out of which some were taken for this study. A nine-point Likert scale ranging from 1 (least important) to 9 (most important) was adopted. Ten experts were interviewed to formulate the hierarchy with the evaluation category and the criteria for each category. From many criteria, Saaty (MacCormac, 1983; Wasil and Golden, 2003) pointed out that human beings can simultaneously compare up to seven items. All of the criteria were weighed and top 7 criteria from each category were taken so that each level's set of criteria does not exceed seven items (Fig. 1).

The second questionnaire (AHP questionnaire) was designed according to the analytic hierarchy structure. The various criteria under each level in the questionnaire were compared pair wise, producing values from 1 to 9 scale ratings. Experienced contractors and engineers validated questionnaire. The questionnaire was sent to industry practitioners within the construction industry who are primary participants in the precast concrete supply chain, including construction clients/developers, engineers, contractors, environmentalists, social workers and precast concrete manufacturers. All of them have different opinions and focus on construction method selection. Trends showed that clients were changing the way of their thinking taking "long-term cost" and environmental and social factors into account when selecting a construction method. In the Integrated Design of Green Buildings, every stakeholder is a part of decision making and he will have his own concerns depending upon his expertise. E.g. "Constructability" is the criterion that contractors may care most about, and clients may value "construction costs and time". "Influence on job market" and "Pollution generation" are other social and environmental criteria as shown in Table 1.

3.4. Fuzzy analysis of data

Here we want to compare two main CMs – Precast and Cast-in situ. The evaluation criteria are based on the triple bottom line of economic, social and Environmental criteria as listed in Fig. 1.

The CMs are measured against these economic Criteria and given ratings as "Excellent(E)", "Superior(S)", "Adequate(A)" and "Inferior(I)". "Excellent" means that CM is the best available with respect to the particular criterion. "Superior" means that the CM is among the best with respect to this criterion. "Adequate" means that, although not superior, CM can meet the minimum acceptable

Please cite this article in press as: Bansal, S. et al. Fuzzy decision approach for selection of most suitable construction method of Green Buildings. International Journal of Sustainable Built Environment (2017), http://dx.doi.org/10.1016/j.ijsbe.2017.02.005

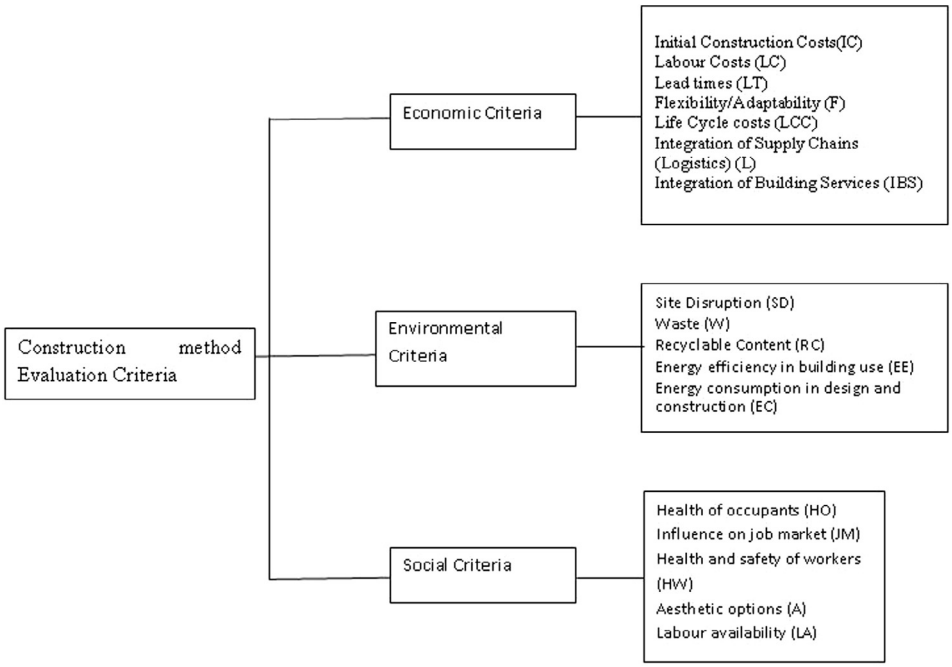

Fig. 1. The AHP model.

Table 1
Sustainable performance criteria for construction method selection in concrete buildings (Chen et al., 2010), (Pan et al., 2012).

	Economic criteria	Social criteria	Environmental criteria
Focus of Clients/Engineers	E1: Construction time E2: Initial construction costs E3: Maintenance costs E4: Disposal costs E5: Life cycle costs E6: Defects and damages E7: Durability E8: The speed of return on investment	S1: Health of occupants (Indoor Air Quality) S2: Influence on job market S3: Physical space S4: Esthetic options	P1: Site disruption P2: Recyclable/Renewable contents P3; Energy Efficiency in building use (thermal mass) P4: Reusable/Recyclable elements P5: Material consumption P6: Energy consumption in design and construction
Focus of Contractors/ Precasters	E10: Loading capacity E11: Integration of building services E12: Lead times E13: Material costs E14: Labor costs E15: Constructability(buildability) E16: Integration of supply chains (logistics)	S5: Workers' health and safety S6: Labor availability S7: Community disturbance S8: Traffic congestion	P7: Waste P8: Pollution generation P9: Water consumption

requirements for this criterion. "Inferior" means that the CM cannot meet the requirements for the particular criterion.

3.4.1. Economic criteria

The relations based on the consensus of the group of decision-makers with respect to different economic criteria are given in Table 2.

Now the criterion weight vector W_{ECO}, will be obtained by using Saaty's analytic hierarchy process. The matrix of relative weights of subjective estimates is given in Table 3. The elements of each column are divided by the sum of that column (i.e., normalize the column) and the elements in each resulting row are added and this sum is divided by the number of elements in the row as shown in Table 4.

Using the matrix of subjective attribute weights in Table 3 and Saaty's method, the following weight vector is obtained:

$W_{ECO} = (0.342015, 0.239171, 0.166521, 0.118594, 0.068718, 0.046063, 0.018918)$

Consistency checking: Consistency ratio (CR) checking is required to be checked whether the weights assigned based on expert reasoning is correct or not, usually its value is less than 0.1 which shows that the weights are consistent. A relative importance matrix to assign weights for comparing criteria with criteria as in Table 3, in this matrix

Please cite this article in press as: Bansal, S. et al. Fuzzy decision approach for selection of most suitable construction method of Green Buildings. International Journal of Sustainable Built Environment (2017), http://dx.doi.org/10.1016/j.ijsbe.2017.02.005

Table 2
Fuzzy relations between alternatives and evaluation criteria (Economic).

Criteria/alternatives	CM-I(Precast)(R_{PC-ECO})				CM-II(Cast-in situ) (R_{CS-ECO})			
	E	S	A	I	E	S	A	I
Initial construction costs (IC)	0.8	0.4	0.3	0.1	0.2	0.5	0.4	0.3
Labor costs (LC)	0.9	0.5	0.4	0.1	0.6	0.5	0.4	0.2
Lead times (LT)	0.2	0.3	0.4	0.6	0.9	0.8	0.5	0.2
Flexibility/adaptability(F)	0.1	0.2	0.5	0.8	0.9	0.8	0.7	0.2
Life cycle costs(LCC)	0.7	0.6	0.4	0.1	0.7	0.5	0.4	0.3
Integration of supply chains (logistics) (L)	0.9	0.8	0.4	0.1	0.2	0.3	0.5	0.6
Integration of building services (IBS)	0.5	0.4	0.3	0.2	0.6	0.4	0.3	0.1

Table 3
The matrix of subjective attribute weights (Matrix: $A_{1:7X7}$) (Economic).

	IC	LC	LT	F	LCC	L	IBS
IC	1	3	3	3	5	7	7
LC	1/3	1	3	5	3	5	7
LT	1/3	1/3	1	3	3	5	9
F	1/3	1/5	1/5	1	3	5	7
LCC	1/9	1/3	1/7	1/5	1	3	7
L	1/9	1/5	1/7	1/7	1/5	1	7
IBS	1/9	1/7	1/9	1/9	1/9	1/7	1

diagonal elements are always 1 because criteria compared with same will always be 1.

With the help of above subjective attribute weights matrix as in Table 3, we can calculate geometric mean (GM) as follows:

$GM_1 = (1 * 3 * 3 * 3 * 5 * 7 * 7)^{1/7} = 3.513905$
$GM_2 = (1/3 * 1 * 3 * 5 * 3 * 5 * 7)^{1/7} = 2.443265$
$GM_3 = (1/3 * 1/3 * 1 * 3 * 3 * 5 * 9)^{1/7} = 1.717616$
$GM_4 = (1/3 * 1/5 * 1/5 * 1 * 3 * 5 * 7)^{1/7} = 1.047736$
$GM_5 = (1/9 * 1/3 * 1/7 * 1/5 * 1 * 3 * 7)^{1/7} = 0.5772$
$GM_6 = (1/9 * 1/5 * 1/7 * 1/7 * 1/5 * 1 * 7)^{1/7} = 0.346829$
$GM_7 = (1/9 * 1/7 * 1/9 * 1/9 * 1/9 * 1/7 * 1)^{1/7} = 0.161533$

Hence total Geometric mean (GM) $= GM_1 + GM_2 + GM_3 + GM_4 + GM_5 + GM_6 + GM_7 = 9.808084$

Calculating normalized weights ($[A_2]_{7X1}$ as weight matrix)

$W_1 = GM_1/GM = 3.513905/9.808084 = 0.358266$
$W_2 = GM_2/GM = 2.443265/9.808084 = 0.249107$
$W_3 = GM_3/GM = 1.717616/9.808084 = 0.175123$
$W_4 = GM_4/GM = 1.047736/9.808084 = 0.106824$
$W_5 = GM_5/GM = 0.5772/9.808084 = 0.058849$
$W_6 = GM_6/GM = 0.346829/9.808084 = 0.035362$
$W_7 = GM_7/GM = 0.161533/9.808084 = 0.016469$

Consistency can now be checked using following formulae:

$[A_3] = [A_1] * [A_2]$,

where A_1 is relative importance matrix and A_2 is weight matrix

Also $[A_4] = [A_3]/[A_2]$,

The calculations are tabulated in Table 5.

Calculating average of $[A_4]$ i.e. $??_{??????}$

$??_{??????} = (7.280872 + 7.609021 + 6.838682 + 7.288072 + 7.607827 + 8.23268 + 8.087247)/7 = 7.563486$

Then Consistency Index $= (??_{??????} - ??)/?? - 1$, where n is size of matrix

Consistency Index $= 0.093914$

And Consistency Ratio (CR) = Consistency Index/Random Index

CR $= 0.093914/1.32 = 0.071147 < 0.1$ where Random index is already given for specified number of criteria and for seven criteria, its value is 1.32. Since value of CR is less than 0.1, hence the weights are consistent.

3.4.2. Environmental criteria

Similarly weight vector has to be generated for Environmental criteria and weights allocated have to be checked for consistency (see Table 6).

Using the matrix of subjective attribute weights in Table 7 and Saaty's method, the following vector is obtained: Tables 8–10

Table 4
Normalized subjective attribute weights.

Normalized column values							Sum of rows	Sum/7
0.431034	0.576923	0.395257	0.240964	0.326584	0.267789	0.155556	2.394107	0.342015
0.142241	0.192308	0.395257	0.401606	0.19595	0.191278	0.155556	1.674196	0.239171
0.142241	0.063462	0.131752	0.240964	0.19595	0.191278	0.2	1.165647	0.166521
0.142241	0.038462	0.02635	0.080321	0.19595	0.191278	0.155556	0.830158	0.118594
0.047414	0.063462	0.018445	0.016064	0.065317	0.114767	0.155556	0.481024	0.068718
0.047414	0.038462	0.018445	0.011245	0.013063	0.038256	0.155556	0.32244	0.046063
0.047414	0.026923	0.014493	0.008835	0.007185	0.005356	0.022222	0.132428	0.018918

Please cite this article in press as: Bansal, S. et al. Fuzzy decision approach for selection of most suitable construction method of Green Buildings. International Journal of Sustainable Built Environment (2017), http://dx.doi.org/10.1016/j.ijsbe.2017.02.005

Table 5
Calculations for consistency ratio (Economic Criteria).

Matrix [A_1]							Matrix [A_2]	Matrix [A_3] = [A_1] * [A_2]	Matrix [A_4] = [A_3]/[A_2]
1	3	3	3	5	7	7	0.358266	2.60849	7.280872
1/3	1	3	5	3	5	7	0.249107	1.895463	7.609021
1/3	1/3	1	3	3	5	9	0.175123	1.197607	6.838682
1/3	1/5	1/5	1	3	5	7	0.106824	0.778539	7.288072
1/9	1/3	1/7	1/5	1	3	7	0.058849	0.447716	7.607827
1/9	1/5	1/7	1/7	1/5	1	7	0.035362	0.29112	8.23268
1/9	1/7	1/9	1/9	1/9	1/7	1	0.016469	0.133192	8.087247

Table 6
Fuzzy relations between alternatives and evaluation criteria (Environmental).

Criteria/alternatives	CM-I(Precast) ($R_{PC\text{-}ENV}$)				CM-II(Cast-in situ) ($R_{CS\text{-}ENV}$)			
	E	S	A	I	E	S	A	I
Site Disruption(SD)	0.8	0.4	0.3	0.1	0.2	0.5	0.4	0.3
Waste(W)	0.9	0.5	0.4	0.1	0.4	0.3	0.2	0.2
Recyclable Content(RC)	0.2	0.3	0.4	0.6	0.9	0.8	0.5	0.2
Energy efficiency in building use(EE)	0.5	0.4	0.3	0.2	0.9	0.8	0.7	0.2
Energy consumption in design and construction(EC)	0.7	0.6	0.4	0.1	0.5	0.4	0.3	0.2

Table 7
The matrix of subjective attribute weights (Matrix: $A_{1:5X5}$).

	SD	W	RC	EE	EC
SD	1	3	3	3	5
W	1/3	1	3	5	3
RC	1/3	1/3	1	3	3
EE	1/3	1/5	1/5	1	3
EC	1/9	1/3	1/7	1/5	1

Table 8
Normalized subjective attribute weights.

Normalized column values					Sum	Sum/5
0.47619	0.617284	0.408719	0.245902	0.333333	2.081429	0.416286
0.157143	0.205761	0.408719	0.409836	0.2	1.38146	0.276292
0.157143	0.067901	0.13624	0.245902	0.2	0.807186	0.161437
0.157143	0.041152	0.027248	0.081967	0.2	0.50751	0.101502
0.052381	0.067901	0.019074	0.016393	0.066667	0.222416	0.044483

Table 9
Calculations for consistency ratio (Environmental Criteria).

Matrix [A_1]					Matrix [A_2]	Matrix [A_3] = [A_1] * [A_2]	Matrix [A_4] = [A_3]/[A_2]
1	3	3	3	5	0.433362	2.215166	5.111589
1/3	1	3	5	3	0.278695	1.455889	5.223955
1/3	1/3	1	3	3	0.161822	0.775166	4.790235
1/3	1/5	1/5	1	3	0.085177	0.439123	5.15542
1/9	1/3	1/7	1/5	1	0.040945	0.220274	5.379811

$W_{ENV} = (0.416286, 0.276292, 0.161437, 0.101502, 0.044483)$

Consistency checking: Consistency ratio (CR) checking is again required for Environmental criteria to check whether the weights assigned based on expert reasoning is correct or not. If its value is less than 0.1, it shows that the weights are consistent. With the help of above subjective attribute weights matrix as in Table 7. We can calculate geometric mean (GM) as follows:

$$GM_1 = (1 * 3 * 3 * 3 * 5)^{1/5} = 2.667269$$
$$GM_2 = (1/3 * 1 * 3 * 5 * 3)^{1/5} = 1.715321$$
$$GM_3 = (1/3 * 1/3 * 1 * 3 * 3)^{1/5} = 0.995988$$
$$GM_4 = (1/3 * 1/5 * 1/5 * 1 * 3)^{1/5} = 0.524251$$

Please cite this article in press as: Bansal, S. et al. Fuzzy decision approach for selection of most suitable construction method of Green Buildings. International Journal of Sustainable Built Environment (2017), http://dx.doi.org/10.1016/j.ijsbe.2017.02.005

Table 10
Fuzzy relations between alternatives and evaluation criteria.

Criteria/alternatives	CM-I(Precast)($R_{PC\text{-}SOC}$)				CM-II(Cast-in situ) ($R_{CS\text{-}SOC}$)			
	E	S	A	I	E	S	A	I
Health of occupants(HO)	0.5	0.4	0.3	0.1	0.5	0.4	0.3	0.2
Influence on job market(JM)	0.5	0.4	0.3	0.1	0.7	0.6	0.5	0.3
Health and safety of workers (HW)	0.8	0.6	0.4	0.2	0.4	0.3	0.2	0.1
Esthetic options(A)	0.8	0.7	0.6	0.5	0.6	0.5	0.4	0.1
Labor availability(LA)	0.4	0.3	0.2	0.1	0.6	0.5	0.3	0.2

Table 11
The matrix of subjective attribute weights.

	HO	JM	HW	A	L
HO	1.00	3.00	3.00	5.00	5.00
JM	1/3	1.00	3.00	5.00	5.00
HW	1/3	1/3	1.00	3.00	3.00
A	1/3	1/5	1/5	1.00	3.00
LA	1/9	1/3	1/7	1/5	1.00

Table 12
Normalized subjective attribute weights.

Normalized column values					Sum	Sum/5
0.47619	0.617284	0.408719	0.352113	0.294118	2.148424	0.429685
0.157143	0.205761	0.408719	0.352113	0.294118	1.417854	0.283571
0.157143	0.067901	0.13624	0.211268	0.176471	0.749022	0.149804
0.157143	0.041152	0.027248	0.070423	0.176471	0.472436	0.094487
0.052381	0.067901	0.019074	0.014085	0.058824	0.212264	0.042453

Table 13
Calculations for Consistency Ratio (Social Criteria).

Matrix [A_1]					Matrix [A_2]	Matrix [A_3] = [A_1] * [A_2]	Matrix [A_4] = [A_3]/[A_2]
1	3	3	5	5	0.445829	2.342639	5.254568
1/3	1	3	5	5	0.286713	1.470509	5.128857
1/3	1/3	1	3	3	0.150309	0.743495	4.94643
1/3	1/5	1/5	1.00	3.00	0.079117	0.42774	5.40641
1/9	1/3	1/7	1/5	1.00	0.038032	0.218555	5.746659

Table 14
Fuzzy relation set of precast CM for economic criteria ($R_{PC\text{-}ECO}$).

Criteria/alternatives	CM-I(Precast)($R_{PC\text{-}ECO}$)			
	E	S	A	I
Initial Construction Costs(IC)	0.8	0.4	0.3	0.1
Labor Costs(LC)	0.9	0.5	0.4	0.1
Lead times(LT)	0.2	0.3	0.4	0.6
Flexibility/Adaptability(F)	0.1	0.2	0.5	0.8
Life Cycle costs(LCC)	0.7	0.6	0.4	0.1
Integration of Supply Chains(Logistics)(L)	0.9	0.8	0.4	0.1
Integration of Building Services(IBS)	0.5	0.4	0.3	0.2

$GM_5 = (1/9 * 1/3 * 1/7 * 1/5 * 1)^{1/5} = 0.252007$

Hence total Geometric mean (GM) = $GM_1 + GM_2 + GM_3 + GM_4 + GM_5 = 6.154835$

Calculating normalized weights ($[A_2]_{5X1}$ as weight matrix)

$W_1 = GM_1/GM = 2.667269/6.154835 = 0.433362$
$W_2 = GM_2/GM = 1.715321/6.154835 = 0.278695$
$W_3 = GM_3/GM = 0.995988/6.154835 = 0.161822$
$W_4 = GM_4/GM = 0.524251/6.154835 = 0.085177$
$W_5 = GM_5/GM = 0.252007/6.154835 = 0.040945$

Please cite this article in press as: Bansal, S. et al. Fuzzy decision approach for selection of most suitable construction method of Green Buildings. International Journal of Sustainable Built Environment (2017), http://dx.doi.org/10.1016/j.ijsbe.2017.02.005

Table 15
Total scores for the construction methods.

CM/criteria	Economic	Environmental	Social
Precast	79.01565	90.66453	91.7136
Cast in Situ	74.16898	86.35065	95.05778

Consistency can now be checked using following formulae:

$A_3 = A_1 * A_2$ Where A_1 is relative importance matrix and A_2 is weight matrix

Also $A_4 = A_3/A_2$

Calculating average of A_4 i.e. $??_{??????}$

$??_{??????} = 5.111589 + 5.223955 + 4.790235 + 5.15542 + 5.379811/5 = 5.132202$

Then Consistency Index $= (??_{??????} - ??)/?? - 1$, where n is size of matrix

Consistency Index = 0.033051

And Consistency Ratio (CR) = Consistency Index/Random Index

$=0.033051/1.12 = 0.029509 < 0.1$

Where Random index is already given for specified number of criteria and for five criteria, its value is 1.12. Since value of CR is less than 0.1, the weights are consistent.

3.4.3. Social criteria

Weight vector has to be generated for Social criteria also.

Using the matrix of subjective attribute weights in Table 11 and Saaty's method, the following vector is obtained: Tables 12–15

$W_{SOC} = (0.429685, 0.283571, 0.149804, 0.094487, 0.042453)$

Consistency checking: Consistency ratio (CR) is checked whether the weights assign based on expert reasoning is correct or not. If its value is less than 0.1, it shows that the weights are consistent. With the help of above subjective attribute weights matrix as in Table 11, we can calculate geometric mean (GM) and normalized weights as follows:

$GM_1 = (1 * 3 * 3 * 5 * 5)^{1/5} = 2.954177$
$GM_2 = (1/3 * 1 * 3 * 5 * 5)^{1/5} = 1.899831$
$GM_3 = (1/3 * 1/3 * 1 * 3 * 3)^{1/5} = 0.995988$
$GM_4 = (1/3 * 1/5 * 1/5 * 1 * 3)^{1/5} = 0.524251$
$GM_5 = (1/9 * 1/3 * 1/7 * 1/5 * 1)^{1/5} = 0.252007$

Hence total Geometric mean (GM) $= GM_1 + GM_2 + GM_3 + GM_4 + GM_5 = 6.626254$

$W_1 = GM_1/GM = 2.954177/6.626254 = 0.445829$
$W_2 = GM_2/GM = 1.899831/6.626254 = 0.286713$
$W_3 = GM_3/GM = 0.995988/6.626254 = 0.150309$
$W_4 = GM_4/GM = 0.524251/6.626254 = 0.079117$
$W_5 = GM_5/GM = 0.252007/6.626254 = 0.038032$

Consistency can now be checked using following formulae:

$A_3 = A_1 * A_2$, where A_1 is relative importance matrix and A_2 is weigh matrix

Also $A_4 = A_3/A_2$

Calculating average of A_4 i.e. $??_{??????}$

$??_{??????} = (5.254568 + 5.128857 + 4.94643 + 5.40641 + 5.746659)/5 = 5.296585$

Then Consistency Index $= (??_{??????} - ??)/?? - 1$, where n is size of matrix

Consistency Index = 0.074146

And Consistency Ratio = Consistency Index/Random Index

$=0.074146/1.12 = 0.066202 < 0.1$

where Random index is already given for five number of criteria as 1.12. Since value of CR is less than 0.1, the weights are consistent.

3.5. Composition of weight set and Fuzzy relation

Every CM Decision set can be obtained by composition of the weight set and Fuzzy relation set as follows – Out of the two composition techniques – Fuzzy max–min composition and Fuzzy max-product composition, Fuzzy max–min composition has been employed for this problem.

The max–min composition of $R(x, y)$ and $S(y, z)$ denoted by

$$\boldsymbol{R}(\boldsymbol{x},\boldsymbol{y}) \circ \boldsymbol{S}(\boldsymbol{y},\boldsymbol{z})$$

Is defined by $T(x, z)$ *as* $\mu_t(x, z) = \mu_{R \circ S}(x, z) = max\{min[\mu_R(x, y), \mu_S(y, z)]\}$

The CM decision making set for Precast can be D_{PC1}, D_{PC2} *and* D_{PC3} and for Cast in Situ can be D_{CS1}, D_{CS2}, D_{CS3} on economic, Environmental and Social criteria respectively.

$$D_{PC1} = W_{ECO} \circ R_{PC\text{-}ECO} \quad D_{CS1} = W_{ECO} \circ R_{CS\text{-}ECO}$$
$$D_{PC2} = W_{ENV} \circ R_{PC\text{-}ENV} \quad D_{CS2} = W_{ENV} \circ R_{CS\text{-}ENV}$$
$$D_{PC3} = W_{SOC} \circ R_{PC\text{-}SOC} \quad D_{CS3} = W_{SOC} \circ R_{CS\text{-}SOC}$$

The calculations for one of them is shown below and the rest five can be calculated similarly-

$$\boldsymbol{D_{PC1}} = \boldsymbol{W_{ECO}} \circ \boldsymbol{R_{PC-ECO}}$$

$W_{ECO} = (0.342015, 0.239171, 0.166521, 0.118594, 0.068718, 0.046063, 0.018918)$

$\mu_T(x_1, z_1) = \max\{\min(0.342015, 0.8), \min(0.239171, 0.9), \min(0.166521, 0.2), \min(0.118594, 0.1), \min(0.068718, 0.7), \min(0.046063, 0.9), \min(0.018918, 0.5)\}$
$\mu_T(x_1, z_2) = \max\{\min(0.342015, 0.4), \min(0.239171, 0.5), \min(0.166521, 0.3), \min(0.118594, 0.2), \min(0.068718, 0.6), \min(0.046063, 0.8), \min(0.018918, 0.4)\}$
$\mu_T(x_1, z_3) = \max\{\min(0.342015, 0.3), \min(0.239171, 0.4), \min(0.166521, 0.4), \min(0.118594, 0.5), \min(0.068718, 0.4), \min(0.046063, 0.4), \min(0.018918, 0.3)\}$
$\mu_T(x_1, z_4) = \max\{\min(0.342015, 0.1), \min(0.239171, 0.1), \min(0.166521, 0.6), \min(0.118594, 0.8), \min(0.068718, 0.1), \min(0.046063, 0.1), \min(0.018918, 0.2)\}$

Please cite this article in press as: Bansal, S. et al. Fuzzy decision approach for selection of most suitable construction method of Green Buildings. International Journal of Sustainable Built Environment (2017), http://dx.doi.org/10.1016/j.ijsbe.2017.02.005

$D_{PC1} = (0.342015, 0.342015, 0.3, 0.166521)$ Similarly,
$D_{PC2} = (0.416286, 0.4, 0.3, 0.161437)$
$D_{PC3} = (0.429685, 0.4, 0.3, 0.149804)$
$D_{CS1} = (0.239171, 0.342015, 0.342015, 0.3)$
$D_{CS2} = (0.276292, 0.416286, 0.4, 0.3)$
$D_{CS3} = (0.429685, 0.4, 0.3, 0.283571)$

Defuzzification means calculating the crisp value of fuzzy number. The crisp value will approximately represent the deterministic characteristics of the fuzzy reasoning process based on the assessment matrix, and thus help convert the uncertainty into an applicable action when solving real world problems. The defuzzification way is as follows.

$$K = D \bullet S$$

where K is a defuzzification score, D is the decision making set, and S is the appraisal grade set. Here in this paper taken as- Excellent (E), Superior(S), Adequate (A), inferior (I) can be defined in appraisal grading as 100, 75, 50, and 25 respectively. Using this scale, the CM Precast and Cast in situ scores on Economic, Environmental and social criteria are shown in the table below.

The above table shows a crisp score in every criteria domain for both the construction methods. These values have been derived based on experts' opinions on the weightage of one criteria upon another and to what extent a particular CM satisfies that criteria again opined by the field expert/ Stakeholder. Depending upon the significance of economic vs. environmental vs. social criteria in the domain of a particular project, a particular CM can be adopted.

4. Discussion

The scores show the collective inclination of current knowledge perception of different stakeholders toward particular criteria in economic, environmental and social domains. Precast CM scores higher than Cast-in-situ for Environmental criteria but scores less for social criteria. Both CMs are at par as far as economic criteria are concerned and this small parity can be borne if other two legs of sustainability tripod are satisfied. Precast construction directly and adversely affects the job market and thus scores less whereas Cast-in-situ or conventional construction is a major employment avenue in a country. Also the scores show that social awareness and environmental concerns are considered to be increasingly important when selecting construction methods. Workers' health and safety, health of occupants, water and energy efficiency in building use, and reusability/recyclability issues are rated with higher priorities. Since Governments are giving incentives to projects with higher Green Building ratings, the stake holders would put more emphasis on criteria related to rating scheme points. As the Green Building rating schemes become more popular, increased environmental consideration in CM selection is an inevitable trend in the future. Though most of the Green Building Rating schemes allocate higher credits toward environmental criteria and specify lesser credit points to social and economic criteria but CM selection cannot ignore these criteria. The industrialization of construction elements has social implications relating to wage fixation, availability of technical and general labor etc.

Successful implementation of the CM selection tool proposed requires genuine and systematic process of opinion collection and early decision-making based on project factors. Adoption of Precast construction may appear to be more viable with recent advances in design and information technologies but the decision has to be supported by experts' knowledge domain. The proposed tool provides transparency in invoking decision-makers' judgment on relative importance of decision factors and helps users sort out what factors drive or impede its use on the project under consideration.

5. Conclusion

This research work deals with multi-criteria decision making problem of an expert during selection of suitable construction method of a green building. The contemporary industry emphasis on the apparent advantages of precast construction over cast-in-situ method in the era of industrialization and sustainable development needs to be proven. Holistic criteria considering both "hard" and "soft" factors capturing the sustainable performance of construction methods instead of traditional measures of cost, time and quality need to be employed. Since no formal and authenticated data on the applicability of construction methods are available, this study employed Zadeh's Fuzzy synthetic evaluation technique to develop an analytical tool based on the experts' collective preferences in the Integrated Green Building Design. An appropriate balance between economic, social, and environmental issues of sustainable construction has been attempted reflecting the concerns of different experts/project stakeholders. The weightage allocated to each criteria has been obtained from pair wise comparisons and then the weights checked by finding the consistency ratio. The optimum construction method selected will satisfy all the project stakeholders and also the criteria being evaluated requires minimal information usually available in the early stages of conceptualization. Since the results give crisp score for different set of criteria, decision can easily be made giving due consideration to social, economic or environmental aspects as per project constraints. This paper lays the foundation for automated tools to help make project level decisions and strategies toward a healthy built environment. Same analytical model may be applied if some other criteria are adopted and the experts' opinions change according to their perspective and requirements. Further empirical studies should be carried out for different type of projects to widen knowledge of the near-future market potential for industrialization of construction sector.

Please cite this article in press as: Bansal, S. et al. Fuzzy decision approach for selection of most suitable construction method of Green Buildings. International Journal of Sustainable Built Environment (2017), http://dx.doi.org/10.1016/j.ijsbe.2017.02.005

References

Abioye, A.O.U., 2015. Sustainable approach to managing construction and demolition waste: An opportunity or a new challenge? Int. J. Innov. Res. Sci. Eng. Technol. 4 (11), 10368–10378.

Agamuthu, P., 2008. Challenges in sustainable management of construction and demolition waste. Waste Manage. Res. 26 (6), 491–492.

Alonso, Lamata, M.T., 2006. Consistency in the analytic hierarchy process-a new approach. Int. J. Uncertain. Fuzz. Knowledge-Based Syst. 14 (04), 445–459.

Bansal, S., 2015. Selection of most economical green building out of N-alternatives: approach of vague fuzzy logic. Int. J. Res. Eng. Technol. 04 (02), 164–168.

Blismas, N., Pasquire, C., Gibb, A., 2006. Benefit evaluation for off-site production in construction. Construct. Manage. Econ. 24 (2), 121–130.

Chen, Y., Okudan, G.E., Riley, D.R., 2010. Sustainable performance criteria for construction method selection in concrete buildings. Auto. Construct. 19 (2), 235–244.

Ding, G.K., 2008. Sustainable construction—The role of environmental assessment tools. J. Environ. Manage. 86 (3), 451–464.

Dong, Y.H., Jaillon, L., Chu, P., Poon, C.S., 2015. Comparing carbon emissions of precast and cast-in-situ construction methods – A case study of high-rise private building. Constr. Build. Mater. 99, 39–53.

Ferrada, X., Serpell, A., 2014. Selection of construction methods for construction projects: a knowledge problem. J. Construct. Eng. Manage. 140 (4), B4014002.

Gluch, P., Baumann, H., 2004. The life cycle costing (LCC) approach: a conceptual discussion of its usefulness for environmental decision-making. Build. Environ. 39 (5), 571–580.

Goguen, J.A., 1973. Zadeh L. A. Fuzzy sets. Information and control, vol. 8 (1965), pp. 338–353. Zadeh L. A. Similarity relations and fuzzy orderings. Information sciences, vol. 3 (1971), pp. 177–200. J. Symbol. Logic 38 (04), 656–657.

Govindan, K., Shankar, K.M., Kannan, D., 2016. Sustainable material selection for construction industry – A hybrid multi criteria decision making approach. Renew. Sustain. Energy Rev. 55, 1274–1288.

Hassan, M.E., Kandil, A., Senouci, A., Al-Derham, H., 2016. Organizational behavior attributes and sustainable construction adoption: an econometric analysis using data from Qatar. J. Construct Eng. Manage. 05016016

Jaillon, L., Poon, C.S., 2009. The evolution of prefabricated residential building systems in Hong Kong: a review of the public and the private sector. Auto. Construct. 18 (3), 239–248.

Kahraman, C., Ruan, D., Doğan, I., 2003. Fuzzy group decision-making for facility location selection. Inf. Sci. 157, 135–153.

Kuncheva, L.I. 2001. Fuzzy logic with engineering applications. In: Timothy J. Ross, (ed.), McGraw hill, New York, 1995, pp. 592, ISBN 0-07-053917-0. Neurocomputing, 41 (1-4), 187.

MacCormac, E.R., 1983. Review of: 'THE ANALYTIC HIERARCHY PROCES' by Thomas L. Saaty, New York, McGraw-Hill Inc, 1980, xiii + 287 pp., list $37.50*. Eng. Econ. 28 (3), 263–264.

Murtaza, M.B., Fisher, D.J., Skibniewski, M.J., 1993. Knowledge-Based approach to modular construction decision support. J. Construct. Eng. Manage. 119 (1), 115–130.

Neama, W.A., 2012. Protect the planet through sustainability rating systems with local environmental criteria - LEED in the middle east. Proc. Soc. Behav. Sci. 68, 752–766.

Negoita, C.V., 1988. Fuzzy sets, uncertainty and information, by George J. Klir and Tina A. Folger, Prentice hall, Englewood cliffs, NJ, 1988. Syst. Res. 5 (4), 355–356.

Pan, W., Dainty, A.R., Gibb, A.G., 2012. Establishing and weighting decision criteria for building system selection in housing construction. J. Construct. Eng. Manage. 138 (11), 1239–1250.

Saaty, R.W., 1987. The analytic hierarchy process—what it is and how it is used. Math. Modell. 9 (3–5), 161–176.

Saaty, T.L., 2008. Decision making with the analytic hierarchy process. Int. J. Serv. Sci. 1 (1), 83.

Sacks, R., Eastman, C.M., Lee, G., 2004. Process model perspectives on management and engineering procedures in the Precast/Prestressed concrete industry. J. Construct. Eng. Manage. 130 (2), 206–215.

Shi, Q., Zuo, J., Huang, R., Huang, J., Pullen, S., 2013. Identifying the critical factors for green construction – an empirical study in china. Habitat Int. 40, 1–8.

Si, J., Marjanovic-Halburd, L., Nasiri, F., Bell, S., 2016. Assessment of building-integrated green technologies: a review and case study on applications of multi-criteria decision making (MCDM) method. Sustainable Cities Soc. 27, 106–115.

Smith, R.M., 2015. "Green" building in India: a comparative and spatial analysis of the LEED-India and GRIHA rating systems. Asian Geogr., 1–12

The analytic hierarchy process: Applications and studies, 1993. Comput. Oper. Res. 20 (5), 562–563.

Thiranun, M., Xu, H., 2015. Evaluating teachers of international business education in NUAA based on efficacy using AHP. Adv. Soc. Sci. Res. J. 2 (11).

VanGeem, M., 2006. Achieving sustainability with Precast concrete. PCI J. 51 (1), 42–61.

Wasil, E., Golden, B., 2003. Celebrating 25 years of AHP-based decision making. Comput. Oper. Res. 30 (10), 1419–1420.

Yee, A.A., Hon, D., 2001. Structural and economic benefits of Precast/Prestressed concrete construction. PCI J. 46 (4), 34–42.

Zuo, J., Zhao, Z.-Y., 2014. Green building research–current status and future agenda: a review. Renewable Sustainable Energy Rev. 30, 271–281.

Zuo, J., Read, B., Pullen, S., Shi, Q., 2012. Achieving carbon neutrality in commercial building developments – perceptions of the construction industry. Habitat Int. 36 (2), 278–286.

Please cite this article in press as: Bansal, S. et al. Fuzzy decision approach for selection of most suitable construction method of Green Buildings. International Journal of Sustainable Built Environment (2017), http://dx.doi.org/10.1016/j.ijsbe.2017.02.005

Composites Communications 4 (2017) 20–23

Contents lists available at ScienceDirect

Composites Communications

journal homepage: www.elsevier.com/locate/coco

Mesoporous silica as amine immobiliser for endowing healing functionality to epoxy resin

Manorama Tripathi[a,b], Devendra Kumar[b], Prasun Kumar Roy[a,*]

[a] Centre for Fire, Explosive and Environment Safety, DRDO, Timarpur, Delhi 110054, India
[b] Department of Applied Chemistry and Polymer Technology, Delhi Technological University, Delhi 110042, India

ARTICLE INFO

Keywords:
Mesoporous
Microcapsules
Self-healing

ABSTRACT

Feasibility of physical entrapment approach towards the immobilisation of amine hardener in mesoporous silica has been demonstrated for potential applications in the perspective of self-healing. A representative mesoporous silica (SBA-15) was synthesised using polymer-templated technique and employed as a substrate for immobilizing triethylene tetramine, a conventional epoxy hardener. Polymeric composites containing microencapsulated epoxy microcapsules and amine loaded SBA-15 were prepared by room temperature curing. The autocatalytic nature associated with the curing of epoxy remained unaltered due to introduction of either SBA-15 or epoxy loaded microcapsules, as confirmed by calorimetric studies. Healing efficiency, as quantified in terms of the ratio of impact strength before and after healing, was found to increase proportionally with increasing loading of healing additives in the formulation, with complete healing (100%) being exhibited at 20% microcapsule loading.

1. Introduction

Self-healing materials are an emerging class of smart responsive materials, which are finding increasing applications in varied fields, e.g anti-corrosive, scratch resistant coatings, structural fiber-reinforced composites to name a few [1]. As is suggestive, these materials possess an innate ability to regain their structural integrity in the event of damage, which can be initiated by any external stimulus e.g. light, mechanical force, surrounding pH-variations etc. Extrinsic self-healing functionality can be bestowed to any composite by the inclusion of healant loaded microcapsules in the formulation. In a conventional self-healing organization, an encapsulated liquid healing agent and a solid phase hardener or catalyst is dispersed homogenously throughout the polymeric matrix. Crack propagation leads to the rupture of microcapsules lying within the crack plane, which result in the release of the healant to subsequently undergo polymerization and restrict the crack growth.

The first generation self-healing systems were based on monomeric healants capable of undergoing ring opening polymerization, e.g. endodicyclopentadiene, 5-ethylidene-2-norbornene [2]. Lately, this elementary theme has been extended to encompass diverse healing chemistries, e.g. unsaturated polyester [3], siloxane [4], epoxy-amine system [5,6] with the latter being most extensively studied in view of the associated economic factors. It is imperative to mention here that though there exist a number of successful methodologies for encapsulation of liquid epoxy, but encapsulation of the liquid hardener still remains a major challenge in view of its hydrophilic nature. To address this issue, several strategies have been adopted including encapsulation of amine in polyurea shells using reverse emulsion technique [7] and interfacial polymerization [8]. Alternatively, hollow microballoons of poly(urea-formaldehyde) and silica have also been explored as amine containment structures [9,10]. However, these microcapsules usually exhibit low core contents, which has led researchers to explore other alternatives.

Surprisingly, porous siliceous substrates e.g. SBA-15, MCM 41, which are routinely employed towards enzyme immobilization [11–13] have not yet been explored for immobilizing amines. In view of their extremely high surface areas, and suitable pore sizes, these materials apparently possess excellent candidature as amine containments. In this paper, we adopt a “physical” entrapment technique for immobilisation of triethylene tetramine hardener for potential application in self-healing applications. Here, the liquid amine remains immobilized within the extended interconnected channels of SBA-15, and is made available to the flowing epoxy in the event of crack propagation. The feasibility of such a system has also been experimentally demonstrated.

* Corresponding author.
E-mail address: pk_roy2000@yahoo.com (P.K. Roy).

http://dx.doi.org/10.1016/j.coco.2017.03.002
Received 18 November 2016; Received in revised form 9 February 2017; Accepted 10 March 2017

2. Materials and methods

Urea, formalin (37% formaldehyde in water), sodium hydroxide, conc. HCl, ammonium chloride and resorcinol were obtained from CDH and poly(ethylene-alt-maleic anhydride) (EMA), P-123 amphiphilic block-copolymer poly (ethylene oxide)-poly (propylene oxide)-poly (ethylene oxide) ($EO_{20}PO_{70}EO_{20}$), tetraethyl orthosilicate (TEOS) were purchased from Sigma-Aldrich. Epoxy monomer, (Araldite CY 230; epoxy equivalent 200 eq/g) and triethylene tetramine (TETA) based curing agent (HY 951; amine content 32 eq/kg) were obtained from Ciba Geigy. Distilled water was used throughout the course of this work.

3. Amine Immobilization in mesoporous silica (SBA-15)

The detailed procedure for preparation of mesoporous silica (SBA-15) has been discussed in our previous paper [14]. N_2 adsorption-desorption profile, PXRD pattern and SEM image of SBA-15 is presented in the Supplementary section (Figs S1 and S2). Liquid hardener was entrapped within the pores of SBA-15 by vacuum infiltration technique [9,10]. For this purpose, an accurately weighed amount of SBA-15, thermally activated at 200 °C for 12 h, was placed in excess triethylene tetramine under vacuum at 25 °C. The hardener infiltrated into the pores of SBA-15, which led to its settling to the bottom of the vessel. After 24 h, the sample was centrifuged at 600 rpm for 5 min, filtered and washed with ethanol to remove excess amine adhering to the surface. The ratio of entrapped amine to the initial mass of SBA-15 was estimated to quantify the extent of loading (Supplementary section).

The vaporization of the entrapped amine from SBA-15 was assessed through isothermal thermogravimetric analysis. For this purpose, amine loaded silica was subjected to isothermal conditions (40, 70 and 100 ° C) for extended time periods and the mass loss profile as a function of time is presented in Fig. 1. Interestingly, even at temperature as high as 100 °C, complete loss of the amine could not be effected, with ~40% amine entrapped within the pores of the substrate.

4. Epoxy microencapsulation

The procedure for encapsulation of epoxy in poly(urea-formaldehyde) microcapsules has been discussed previously [15,16]. In brief, urea and formaldehyde were allowed to undergo dispersion polymerization over the surface of stabilized dispersed epoxy droplets. Microcapsules with an average diameter of 190 ± 49 μm with a core content of 56 ± 2% were used for demonstrating self-healing in composites.

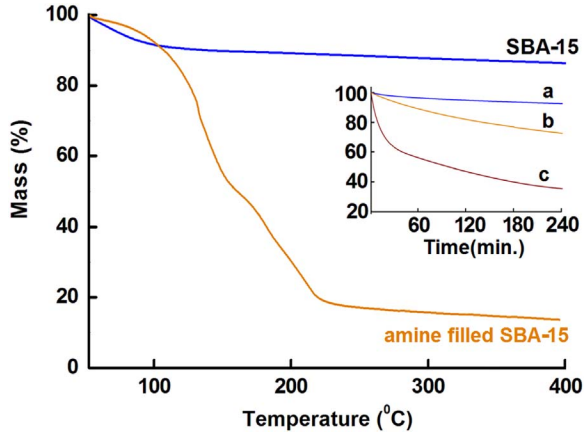

Fig. 1. TG traces of SBA-15 and amine immobilized SBA-15. Isothermal TG traces at different temperatures a) 40 °C, b) 70 °C and c) 100 °C.

5. Results and discussion

We have demonstrated the potential of mesoporous silica (SBA-15) as an immobiliser for TETA for potential in self healing application. Studies reveal that the dimensions of TETA (0.307 nm × 0.294 nm × 1.173 nm) are sufficiently small so as to permit its diffusion within the pores of SBA-15 (pore size 5.4 nm, Supplementary section, Fig. S3). Vacuum infiltration of TETA led to its entrapment within the porous structure of SBA-15 (Loading ~5 g/g). Such high loadings could be attributed to the presence of surface hydroxyl functionalities, which led to strong chemical interactions between the siliceous substrate and the amine, particularly hydrogen bonding and acid–base interactions. TG traces of SBA-15, both before and after amine entrapment is presented in Fig. 1, which clearly reveal the high loadings. In the TG trace of the neat SBA-15, ~3% w/w mass loss was observed initially (T < 150 °C), which could be attributed to the removal of condensed water present within its pores.

6. Healant delivery

The amount of healant delivered in the event of rupture is proportional to the diameter of the microcapsule as well as microcapsule loading [17]. A plot of the healant delivery (on crack plane) as a function of microcapsule loading is presented in Fig. 2. It has been reported that ~4.5 mg/cm^2 healant delivery is required for complete healing purposes. SEM image of a representative batch of microcapsule and the reservoir type internal morphology is also included in the inset. The rough external appearance of the microcapsules can be attributed to the deposition of small poly(urea-formaldehyde) particles formed during the encapsulation process [2].

7. Curing studies

Curing of epoxy with triethylene tetramine, being an exothermic reaction (Supplementary section, Fig. S4), was followed by non-isothermal DSC studies. For this purpose, epoxy and amine, in stoichiometric ratio were transferred to a DSC pan and subjected to a controlled heating program at 10 °C/min. A single exothermic peak was observed (Fig. 3a), with an onset temperature of ~70 °C. DSC studies were also performed, where the amine was derived from TETA entrapped in SBA-15 (Fig. 3b). A third set of experiment was performed in the presence of crushed microcapsules, which served as the epoxy source and TETA loaded SBA-15 which served as the amine source (Fig. 3c). In all the cases, similar profile was observed, with the only difference being the amount of heat liberated.

In view of the envisaged application of the developed additives (microcapsules and SBA-15) in the field of self healing, it was

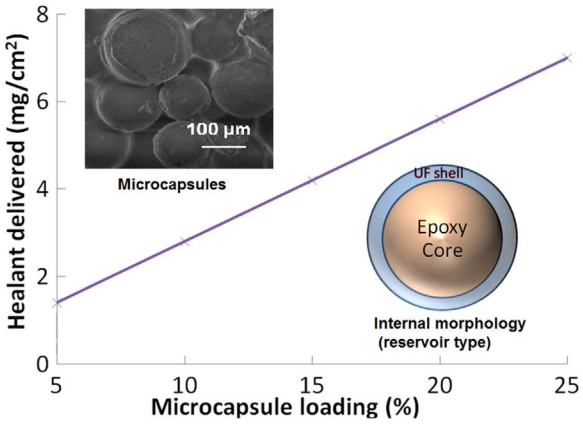

Fig. 2. Epoxy delivery into a crack plane as a function of microcapsule loading (diameter = 200 μm). SEM image and reservoir type internal morphology of the microcapsule.

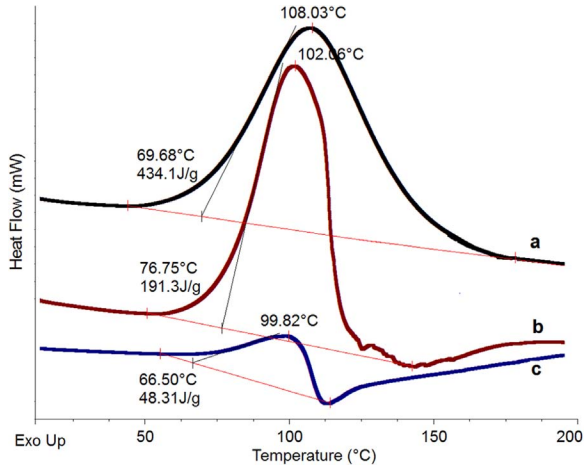

Fig. 3. DSC trace associated with the curing behavior (a) epoxy-hardener (b) encapsulated epoxy- hardener and (c) encapsulated epoxy- immobilized hardener.

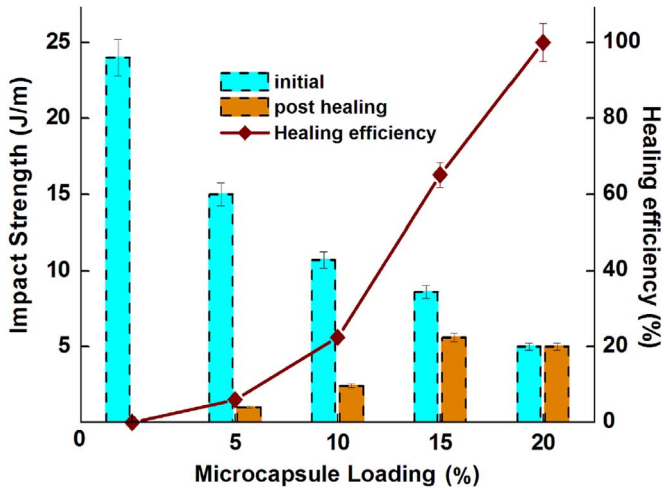

Fig. 4. Healing efficiency as a function of microcapsule loading. The impact strength of samples before and after healing is also shown.

considered of interest to investigate their effect on the curing behavior of epoxy [14]. For this purpose, non-isothermal DSC studies were performed on representative formulations at different heating rates (β = 3–10 °C/min), and the degree of conversion (α) was determined as a function of temperature. Plots for neat epoxy and a representative formulation (Epoxy: microcapsules: amine loaded SBA15:100:10:2) is presented in the supplementary section (Fig. S5), which clearly indicate that the curing kinetics remain practically unaffected due to introduction of the additives developed.

8. Effect of increasing microcapsule loading on mechanical properties

Epoxy composites containing varying amounts of poly(urea-formaldehyde) microcapsules (5 - 20% w/w) were prepared by dispersing epoxy-loaded microcapsules and SBA-15 immobilized amine within the polymeric resin and ultrasonicated to obtain a viscous slurry. Subsequently, stoichiometric amount of TETA hardener (13% w/w) was added. Post-degassing, the slurry was transferred to greased silicone molds and allowed to cure at room temperature for 24 h. Neat epoxy specimens were also prepared for comparison purposes. The effect of increasing microcapsule loading on the impact strength of epoxy is presented in supplementary section (Fig. S6). It can be seen that inclusion of fragile microcapsule lead to a pronounced decrease in the mechanical properties, which is proportional to the microcapsule loading. The effect of adding amine immobilised SBA-15 (1% w/w) is also included in the figure. It is clear from the figure that the contribution of TETA loaded SBA-15 towards decrease in the mechanical properties is rather negligible.

9. Self healing efficiency

Healing efficiency was determined as the ratio of impact strength of healed and virgin sample as per established procedure [18]. The Izod impact strength was determined as per ASTM D 256. Post-fracture, both faces were aligned and gently pressed and clamped to ensure close contact for a period of 6 h at 70 °C (Fig. S7). Healed specimens were resubjected to impact tests after 24 h. A control set of experiments was performed with an aim to quantify the intrinsic healing ability of neat epoxy in the absence of microcapsules. For this purpose, fractured epoxy samples were exposed to conditions mentioned previously and the impact strength both before and after fracture was compared. Preliminary studies revealed that a period of 6 h was sufficient for the samples to regain mechanical integrity; hence quantification of healing efficiency was performed under these conditions. The increase in healing efficiency as a function of microcapsule loading is presented in Fig. 4. Fractured epoxy samples, prepared in the absence of microcapsules, did not exhibit any healing, thereby negating the possibility of residual intrinsic healing in the resin.

It is to be noted that the self healing efficiency is dependent on several factors, and is directly proportional to the size and loading of microcapsule. Our studies revealed that healing efficiency increased with microcapsule loading and reached a maximum (100%) at 20% loading. Similar self-healing efficiency based on epoxy-amine chemistry has been reported by Jin et. al. [9], where average self-healing efficiency was reported to be 91 ± 2% for 17.5 wt% capsules, with the amine and epoxy were both being compartmentalized in urea-formaldehyde microcapsules. In another study, healing efficiency of ~93% has been reported at 15% microcapsule loading, nonetheless with much larger epoxy loaded glass balloons (255.7 ± 39.4 μm) and amine loaded glass balloons of 66.9 ± 8.2 μm [10].

Utilizing a similar epoxy-hardener system where the latter remains in the latent form, the healing efficiency has been reported to be 100% for 30% microcapsule loading where metal imidazole complexes have been used as latent hardener for encapsulated epoxy [16]. In a separate study, 70% healing efficiency has been reported for samples containing 20% epoxy encapsulated microcapsule loading and 2% BF_3-amine complex [19]. It is to be noted that the dynamics of healing in a fiber reinforced system is different where the microcapsule loading required for healing can vary substantially. In this context, 68% recovery of the interlaminar fracture toughness has been reported for glass fabric reinforced epoxy using 10% epoxy loaded microcapsules and 2% latent hardener [5]. In the present study, introduction of 20% microcapsules lead to complete healing, which clearly highlight the potential of mesoporous silica as amine carriers in the context of self healing.

10. Conclusion

Triethylene tetramine hardener was filled within the pores of mesoporous silica (SBA-15) by vacuum infiltration technique. The extent of amine immobilisation was determined gravimetrically to be 5 g/g. Epoxy was encapsulated in poly(urea-formaldehyde) shell and the microcapsules were characterized for their morphological, structural as well as thermal properties. Non-isothermal calorimetric studies show that these fillers (microcapsules and amine immobilized on SBA-15 (2% of microcapsule loading)) do not affect the curing behavior of epoxy but nonetheless bestow healing functionality to the base matrix. Complete healing (~100%) could be effected at 20% microcapsule loading.

Acknowledgements

The authors would like to thank DRDO for funding this work through ST/14-15/CFE-1311.

Appendix A. Supporting information

Supplementary data associated with this article can be found in the online version at doi:10.1016/j.coco.2017.03.002.

References

[1] B.J. Blaiszik, S.L.B. Kramer, S.C. Olugebefola, J.S. Moore, N.R. Sottos, S.R. White, Self-Healing Polymers and Composites, Annu. Rev. Mater. Res. 40 (1) (2010) 179–211.
[2] E.N. Brown, M.R. Kessler, N.R. Sottos, S.R. White, In situ poly(urea-formaldehyde) microencapsulation of dicyclopentadiene, J. Microencapsul. 20 (6) (2003) 719–730.
[3] M. Tripathi, R. Dwivedi, D. Kumar, P.K. Roy, Application of microencapsulated unsaturated polyester toward temperature-triggered healing in epoxy composites, J. Intell. Mater. Syst. Struct. (2015).
[4] S.H. Cho, H.M. Andersson, S.R. White, N.R. Sottos, P.V. Braun, Polydimethylsiloxane-based self-healing materials, Adv. Mater. 18 (8) (2006) 997–1000.
[5] T. Yin, M.Z. Rong, M.Q. Zhang, G.C. Yang, Self-healing epoxy composites – Preparation and effect of the healant consisting of microencapsulated epoxy and latent curing agent, Compos. Sci. Technol. 67 (2) (2007) 201–212.
[6] L. Yuan, G.-Z. Liang, J.-Q. Xie, L. Li, J. Guo, The permeability and stability of microencapsulated epoxy resins, J. Mater. Sci. 42 (12) (2007) 4390–4397.
[7] D.A. McIlroy, B.J. Blaiszik, M.M. Caruso, S.R. White, J.S. Moore, N.R. Sottos, Microencapsulation of a reactive liquid-phase amine for self-healing epoxy composites, Macromolecules 43 (4) (2010) 1855–1859.
[8] S.L. Poe, M. Kobašlija, D.T. McQuade, Microcapsule enabled multicatalyst system, J. Am. Chem. Soc. 128 (49) (2006) 15586–15587.
[9] H. Jin, C.L. Mangun, D.S. Stradley, J.S. Moore, N.R. Sottos, S.R. White, Self-healing thermoset using encapsulated epoxy-amine healing chemistry, Polymer 53 (2) (2012) 581–587.
[10] H. Zhang, P. Wang, J. Yang, Self-healing epoxy via epoxy–amine chemistry in dual hollow glass bubbles, Compos. Sci. Technol. 94 (2014) 23–29.
[11] S. Hudson, E. Magner, J. Cooney, B.K. Hodnett, Methodology for the immobilization of enzymes onto mesoporous materials, J. Phys. Chem. B 109 (41) (2005) 19496–19506.
[12] B. Karimi, S. Emadi, A.A. Safari, M. Kermanian, Immobilization, stability and enzymatic activity of albumin and trypsin adsorbed onto nanostructured mesoporous SBA-15 with compatible pore sizes, RSC Adv. 4 (9) (2014) 4387–4394.
[13] H.H.P. Yiu, P.A. Wright, N.P. Botting, Enzyme immobilisation using SBA-15 mesoporous molecular sieves with functionalised surfaces, J. Mol. Catal. B Enzym. 15 (1–3) (2001) 81–92.
[14] V. Meynen, P. Cool, E.F. Vansant, Verified syntheses of mesoporous materials, Microporous Mesoporous Mater. 125 (3) (2009) 170–223.
[15] M. Tripathi, Rahamtullah, D. Kumar, C. Rajagopal, P. Kumar Roy, Influence of microcapsule shell material on the mechanical behavior of epoxy composites for self-healing applications, J. Appl. Polym. Sci. 131 (15) (2014) 40572.
[16] M. Tripathi, R. Dwivedi, D. Kumar, P.K. Roy, Thermal activation of mendable epoxy through inclusion of microcapsules and imidazole complexes, Polym.-Plast. Technol. Eng. 55 (2) (2016) 129–137.
[17] J.D. Rule, N.R. Sottos, S.R. White, Effect of microcapsule size on the performance of self-healing polymers, Polymer 48 (12) (2007) 3520–3529.
[18] Ce Yuan, M.Q. Zhang, M.Z. Rong, Application of alkoxyamine in self-healing of epoxy, J. Mater. Chem. A 2 (18) (2014) 6558–6566.
[19] Y.X. Song, X.J. Ye, M.Z. Rong, M.Q. Zhang, Self-healing epoxy with a fast and stable extrinsic healing system based on BF3-amine complex, RSC Adv. 6 (103) (2016) 100796–100803.

Accepted Manuscript

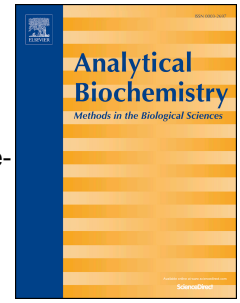

Moderate reagent mixing on an orbital shaker reduces the incubation time of enzyme-linked immunosorbent assay

Saroj Kumar, Rajesh Ahirwar, Dr, Ishita Rehman, Pradip Nahar

PII: S0003-2697(17)30162-8

DOI: 10.1016/j.ab.2017.04.004

Reference: YABIO 12671

To appear in: *Analytical Biochemistry*

Received Date: 24 September 2016

Revised Date: 10 February 2017

Accepted Date: 13 April 2017

Please cite this article as: S. Kumar, R. Ahirwar, I. Rehman, P. Nahar, Moderate reagent mixing on an orbital shaker reduces the incubation time of enzyme-linked immunosorbent assay, *Analytical Biochemistry* (2017), doi: 10.1016/j.ab.2017.04.004.

Moderate reagent mixing on an orbital shaker reduces the incubation time of enzyme-linked immunosorbent assay

Saroj Kumar[1,3,$], Rajesh Ahirwar[1,2,$], Ishita Rehman[1], Pradip Nahar[1,2,4,*]

[1]CSIR-Institute of Genomics and Integrative Biology, Delhi, India

[2]Academy of Scientific and Innovative Research, New Delhi, India

[3]Department of Biotechnology, Delhi Technological University, Delhi, India

[$]These authors contributed equally.

[†]Present address of Dr. Rajesh Ahirwar: Department of Biochemistry, ICMR- National Institute for Research in Environmental Health, Kamla Nehru Hospital Building, Bhopal-462001, India

[†]Present address of Ishita Rehman: Laboratory of Molecular Biology, Indian Association for the Cultivation of Science, Kolkata-700032, India

[*]**Corresponding Author**

Dr. Pradip Nahar

E-mail: pnahar@igib.res.in; pradip_nahar@rediffmail.com

Abstract

Rapid diagnostic tests can be developed using ELISA for detection of diseases in emergency conditions. Conventional ELISA takes 1-2 days, making it unsuitable for rapid-diagnostics. Here, we report the effect of reagents mixing via shaking or vortexing on the assay timing of ELISA. A 48-min protocol of ELISA involving 12-min incubations with reagent mixing at 750 rpm of for every step was optimised. Contrary to this, time-optimized control ELISA performed without mixing produced similar results in 8 hours, leaving a time gain of 7 h using the developed protocol. Collectively, these findings suggest development of ELSIA-based rapid diagnostics.

Keywords

Enzyme-linked immunosorbent assay; Microplate shaker; Mixing; Human IgG; Human IgE; Concanavalin A

Emergence of the enzyme-linked immunosorbent assay (ELISA) for detection and quantification of substances such as peptides, proteins, antibodies and hormones have proven extremely beneficial in clinical laboratories because of its vast diagnostic applications [1]. A typical ELISA involves immobilization of an antigen of interest to the assay plate through direct adsorption or via a capture antibody that has been attached previously to the plate. The antigen is then detected using an enzyme labelled primary antibody (directly ELISA) or a labelled secondary antibody (indirect ELISA). A chromogenic substrate is used as an indicator of presence or absence of the antigen, wherein the color or fluorescence intensity measures the level of antigen concentrations in the assayed sample.

With first appearance in 1971 for quantitative measurement of IgG in rabbit serum [2], the ELISA has rapidly gained importance in basic and clinical research. Though the basic principle of ELISA has remained same, the strenuous research efforts to adapt to high-throughput and rapid operation and automation have enabled the development of miniaturized and rapid ELISA protocols. Multiplex technology using spatially separated and bead immobilization processes allows the detection and measurement of multiple targets in a single ELISA. However, the cost and availability of robotic machines for such multiplex experiments limit its application to high end laboratories. Majority of the clinical laboratories especially those with limited resources still employ the conventional ELISA that takes 1-2 days to detect a diseased condition. Such procedures are not ideal for the emergency medical conditions. The next generation diagnostics requires ELISA procedures that are simple and rapid, yet efficient and affordable to make the most use of it for rapid-diagnostics.

Factors that affect the outcome of an ELISA experiment mainly include the incubation conditions, pH and ionic strength of buffer, and concentrations of antigen and antibody [3, 4]. Usually, it is the time of incubation that determines the total assay time of ELISA. Efforts to reduce the assay timing of the conventional ELISA were made using various energies and

incubation strategies [5-10], assay formats and supports [11-13] and immobilization and detection strategies [14-16]. Requirement of specific instruments, accessories and trained manpower are still the major limitation of many of instrumentally- advanced ELISA protocols.

In the present study, we have probed the effect of controlled shaking of antigenic reagents on the outcome of ELISA for development of ELISA-based rapid diagnostic tests. Shaking instruments such as biological shakers and vortex mixers are commonly used for uniform mixing during biochemical reactions and incubations [17,18]. Shaking facilitates better and uniform fluid mixing, allowing more interactions among the assay components per unit time. As miniaturized shakers (e.g. microplate shaker) employ the same principle of mechanical agitation for mixing of assay components within microplate, controlled mixing via shaking may provide ideal conditions for binding interactions during an ELISA.

To probe the beneficial effect of reagent mixing on the assay timing of ELISA, we carried out the study in two stages- optimization of mixing speed and comparative assessment of the developed mixing to without-mixing ELISA protocols. Checkerboard experiments were performed to optimize effective speed of reagent mixing during various incubations viz. coating, blocking, antigen-antibody binding and target detection. The experiments were performed in a sandwich format on 96-well polystyrene microtiter plates (Greiner Bio-One, Germany) with all incubation performed on a shaker mixer (Eppendorf ThermoMixer C, max Speed 3000 rpm, orbit- 3.0 mm) agitating at a constant speed of 0 -1500 rpm. Washings between incubations were performed with PBST (10 mM PBS, pH 7.4, 0.1% tween-20) as per the conventional procedure of ELISA.

The optimization of mixing speed for individual step of ELISA was carried out by performing the rest of steps by conventional procedure. In first set of experiment, mixing conditions were optimized for the immobilization of capture antibody. The capture antibody

(anti-human IgG, 0.1 µg/ 100 µL in 10 mM PBS, pH 7.4; Sigma-Aldrich, USA) was coated onto the untreated wells and 1-fluoro-2-nitro-4-azidobenzene (FNAB)- treated wells of polystyrene microtiter plates [19] by 30 min incubation on a microtiter plate shaker set at 0, 500, 750, 1000 and 1500 rpm mixing speeds in five separate experiments. The remaining steps were performed as per conventional procedure (blocking- 3 h, antigen binding- 3 h, detection antibody binding- 1 h; all steps at room temperature of 25±2ºC). The time interval of 30 min for incubation with mixing was selected based on preliminary experiments performed for immobilization of HRP (Sigma-Aldrich, USA) onto microtiter plates. Mixing speed for BSA blocking step was optimized in second set of experiment. For this, the capture antibody was coated on microtiter plates by overnight incubation at 4ºC (conventionally) followed by blocking (2% BSA in 10 mM PBS; Sigma-Aldrich, USA) for 30 min on a microtiter plate shaker set at mixing speeds of 0- 1500 rpm. Again, the remaining steps were performed conventionally. Similarly, the antigen binding step (human IgG; 0.05 µg/ 100 µL; (Sigma-Aldrich, USA)) and target detection step (using anti-human IgG-HRP; 1:15,000 dilution; Sigma-Aldrich, USA) were optimized for optimal mixing speed.

As shown in Fig. 1a, the IgG detection by ELISA performed with reagent mixing on incubator shaker produced maximum absorbance read at 750 rpm. The observations were consistent for all four incubation steps of coating, blocking, antibody binding and detection antibody binding performed on both the FNAB treated and untreated microtiter plates. The observed bell-shaped curve suggests the influence of reagent mixing on the outcome of ELISA. Both the low speed (≤ 500 rpm) and high speed (≥ 500 rpm) shaking of ELISA reaction mixture produced significantly low absorbance reads in 15 min as compared to those obtained at 750 rpm in same time. Shaking speed of ≥ 1500 rpm was found to cause spilling of reaction mixture, resulting in the error prone outcomes.

After optimizing the speed of mixing for various steps of an ELISA, we determined the optimal incubation time for each step of the assay. This was achieved by performing similar checkerboard experiments for antibody coating, BSA blocking, antigen binding and detection antibody binding. Incubation of 3- 30 min at fixed mixing speed of 750 rpm on a microplate shaker was used in these assays. In each set of experiment, the individual steps were performed for specified time, while the remaining steps were performed as per conventional procedure. As shown in Fig. 1b, the 12 min time was found to produce optimal results in all the experiments. Further increase in the incubation time to 15 or 30 min yield an insignificant improvement in the obtained absorbance reads. This may suggest that mechanical shaking affects the antigenic reactions by altering the rate at which equilibrium is attained.

Figure 1. Optimization of mixing speed and incubation time for rapid (mixing)-ELISA. (**a**) The effect of reagent mixing during an ELISA for detection of human IgG is studied by performing incubations at 0- 1500 rpm for 30 min, while rest of steps were performed as per conventional procedure. Readings are shown for experiments performed on FNAB treated microtiter plates. (**b**) Time of incubation for rapid-ELISA is optimized at 750 rpm. (**c**) Time gain in rapid-ELISA is estimated by performing a control ELISA without mixing. The absorbance reads of test sample (human IgG) are plotted after normalizing against control sample (rabbit IgG). The +L and -L represents the FNAB-activated and untreated wells of microtiter plate, respectively. Error bars indicate standard deviation of triplicate experiment.

To assess the advantages of mixing, we compared the rapid-ELSIA with time-optimized control ELISA (without mixing). Control ELSIA experiments were performed using similar checkerboard analysis wherein each step of an ELISA is carried out without reagent mixing

and for an incubation time of 15 min to 240 min in separate experiments. As shown in Fig. 1c, we found that unlike the 48 min protocol of rapid-ELISA (12 min incubation for each step), the time-optimized control ELISA without mixing produced significant absorbance reads in 8 hour (each incubation of 2 h). Accordingly, a time gain of 7 hour is observed in the rapid-ELISA protocol in comparison to time-optimized control assay performed at room temperature without mixing.

After these preliminary studies, we compared the rapid-ELISA with the conventional ELISA for detection of homogenous analytes including human IgG (Sigma-Aldrich, USA), human IgE (Bethyl Laboratories, USA) and Concanavalin A protein (Sigma-Aldrich, USA). The rapid-ELISA procedure involved coating of capture antibodies (anti human IgG- 0.1 µg/100 µl, anti-human IgE- 1.0 µg/100 µl; anti-lectn Con A- 0.2 ng/ 100 µl) onto the untreated wells of microtiter plates followed by blocking with BSA (2% BSA), antigen binding (human IgG- 0.05 µg/100 µl; human IgE- 0.05 µg/100 µl; Con A- 0.05 µg/100 µl) and binding of detection antibodies (anti-human IgG- HRP and anti-human IgE- HRP: 1:15,000 dilution; anti-rabbit IgG- HRP: 1:2000 dilution). All the incubations were performed for 12 min with mixing at 750 rpm on a microplate shaker.

The conventional ELISA was performed by coating capture antibodies to microtiter plates by overnight incubation at 4ºC, followed by blocking with 2% BSA for 3 h at room temperature, binding of respective antigens for 3 h at room temperature and binding of HRP conjugated detection antibodies at room temperature for 1 hour.

Both the protocols of ELISA were performed using same concentration of analytes. Appropriate sample control (rabbit IgG for both human-IgG and human-IgE; BSA for Con A) were taken to confirm the specificity of ELISA experiments. As shown in Fig. 2, the rapid-ELISA carried out in 48 min has produced significantly similar results to those obtained in conventional ELISA which takes almost two days. The conventional ELISA for IgG

produced four fold high absorbance read for test (1.244±0.1) as compared to control sample (rabbit IgG: 0.349±0.031 A). For same analyte, the rapid-ELISA produced a five folds significant difference in test (1.03±0.012) and control (0.196±0.04) samples (Fig. 2a). Similar results were obtained for human IgE and Con A through conventional and rapid- ELISA (Fig. 2a-c).

Figure 2. Comparison of rapid-ELISA with conventional ELISA for detection of human IgG, IgE and Concanavalin A. In first set of experiment, three homogenous analytes IgG (**a**), IgE (**b**) and Con A (**c**) were detected using the optimized protocol of rapid-ELISA and conventional ELISA. Rabbit IgG is taken as antigen control in these assays. These experiments were performed on FNAB activated (+L) and non-activated (-L) wells of microtiter plates. (**d**) In another experiment, heterogeneous extracts of Garbanzo bean, Black gram, Pigeon pea, Kidney bean and Jack bean were tested to detect the Con A. This experiment was performed on untreated (-L) microplates; purified Con A (2.5 µg) and BSA (2 mg) were taken as positive and negative control samples. (**e**) Sensitivity of the rapid ELISA was analyzed by detecting various dilutions of HIgG (0, 10, 25, 50, 100, 200, 1000 ng/mL).

In further attempts, the rapid-ELISA was compared with conventional ELISA for detection of heterogeneous samples. For this, the extracts of Garbanzo bean (*Cicer arietinum*), Black gram (*Vigna mungo*), Pigeon pea (*Cajanus cajan*), Kidney bean (*Phaseolus vulgaris*) and Jack bean (*Canavalia ensiformis*) were isolated and detected for presence of Concanavalin A, which is a potential food allergen. As shown in Fig. 2d, the high absorbance values in control sample and jack bean extract suggest the selective detection of analytes by the developed protocol of rapid-ELISA. Sensitivity of the rapid-ELISA protocol was further

confirmed by comparing it with the conventional ELISA (Pearson Correlation; R^2= 0.9486, p value < 0.0001) for detection of serial dilutions (0.1 -1000 ng/mL) of human IgG (Fig. 2e).

In conclusion, this preliminary study highlights the potential of controlled mixing of reagents during ELISA incubation to speed up the binding interactions and as a result, decreasing the assay timing of an ELISA. Results obtained in 48 min rapid- ELISA with moderate reagent mixing at 750 rpm matched those obtained in time-optimized 8 h ELISA (without reagent mixing). These results matches the outcome of conventional ELISA carried out in almost two days. Contrary to this, control ELISA performed in 48-min but without reagent mixing failed to produced significant results. The experiments carried out on non-modified and modified (through FNAB) ELISA plates were significantly similar in their outcomes. Though we have examined only a limited number of samples using the rapid-ELISA, we expect to obtain similar results for most antigen-antibody interactions. The possible chances of cross-contamination due to spill over and other errors during the protocol of rapid-ELISA can be minimized by using microtiter plate sealing films and calibrated shakers that maintain steady-state mixing. As the rapid-ELISA detects antigens without compromising the specificity or sensitivity of the assay, it can provide a valuable technique for rapid diagnostics.

Acknowledgments

SK thanks the SERB-Department of Science and Technology, Government of India, for the award of Fast Track Young Scientist. RA thanks the Council of Scientific and Industrial Research for the award of a research fellowship. This work is supported by fund from CARDIOMED project (BSC0122) of Council of Scientific and Industrial Research, Government of India.

The authors declare no competing interests.

Author Contributions

SK, RA and IR designed and performed the assay. SK, RA, IR and PN analysed the results.

SK, RA and PN wrote the manuscript.

References

[1] R.M. Lequin, Enzyme Immunoassay (EIA)/Enzyme-Linked Immunosorbent Assay (ELISA), Clinical Chemistry, 51 (2005) 2415-2418.
[2] E. Engvall, P. Perlmann, Enzyme-linked immunosorbent assay (ELISA) quantitative assay of immunoglobulin G, Immunochemistry, 8 (1971) 871-874.
[3] R. Reverberi, L. Reverberi, Factors affecting the antigen-antibody reaction, Blood Transfusion, 5 (2007) 227-240.
[4] S.D. Flynn, D.F. Keren, B. Torretti, R.C. Dieterle, S. Grauds, Factors affecting enzyme-linked immunosorbent assay (ELISA) for insulin antibodies in serum, Clinical Chemistry, 27 (1981) 1753-1757.
[5] U. Bora, K. Kannan, P. Nahar, Heat-mediated enzyme-linked immunosorbent assay procedure on a photoactivated surface, Journal of immunological methods, 293 (2004) 43-50.
[6] S. Kumar, L. Ghosh, S. Kumar, B. Ghosh, P. Nahar, A rapid method for detection of cell adhesion molecules (CAMs) on human umbilical vein endothelial cells (HUVECs), Talanta, 73 (2007) 466-470.
[7] P. Sharma, P. Nahar, Ultrasound wave-mediated enzyme-linked immunosorbent assay technique, Anal Chim Acta, 650 (2009) 241-246.
[8] D.K. Kannoujia, P. Nahar, Pressure: a novel tool for enzyme-linked immunosorbent assay procedure, BioTechniques, 46 (2009) 468-472.
[9] P. Nahar, U. Bora, G.L. Sharma, D.K. Kannoujia, Microwave-mediated enzyme-linked immunosorbent assay procedure, Analytical Biochemistry, 421 (2012) 764-766.
[10] R. Ahirwar, S. Tanwar, U. Bora, P. Nahar, Microwave non-thermal effect reduces ELISA timing to less than 5 minutes, RSC Advances, 6 (2016) 20850-20857.
[11] S. Parween, P. Nahar, Image-based ELISA on an activated polypropylene microtest plate--a spectrophotometer-free low cost assay technique, Biosensors & bioelectronics, 48 (2013) 287-292.
[12] C.-C. Lin, J.-H. Wang, H.-W. Wu, G.-B. Lee, Microfluidic Immunoassays, Journal of the Association for Laboratory Automation, 15 (2010) 253-274.
[13] M.D. Richardson, A. Turner, D.W. Warnock, P.A. Llewellyn, Computer-assisted rapid enzyme-linked immunosorbent assay (ELISA) in the serological diagnosis of aspergillosis, Journal of immunological methods, 56 (1983) 201-207.
[14] C.K. Dixit, S.K. Vashist, B.D. MacCraith, R. O'Kennedy, Multisubstrate-compatible ELISA procedures for rapid and high-sensitivity immunoassays, Nat. Protocols, 6 (2011) 439-445.
[15] S.K. Vashist, E. Marion Schneider, E. Lam, S. Hrapovic, J.H.T. Luong, One-step antibody immobilization-based rapid and highly-sensitive sandwich ELISA procedure for potential in vitro diagnostics, Scientific Reports, 4 (2014) 4407.
[16] R.H. Yolken, F.J. Leister, Investigation of enzyme immunoassay time courses: development of rapid assay systems, Journal of clinical microbiology, 13 (1981) 738-741.

[17] R.I. Freshney, R.I. Freshney, Culture of Specific Cell Types, Culture of Animal Cells, John Wiley & Sons, Inc.2005.
[18] N. Muller, P. Girard, D.L. Hacker, M. Jordan, F.M. Wurm, Orbital shaker technology for the cultivation of mammalian cells in suspension, Biotechnology and Bioengineering, 89 (2005) 400-406.
[19] P. Nahar, N.M. Wali, R.P. Gandhi, Light-induced activation of an inert surface for covalent immobilization of a protein ligand, Anal Biochem, 294 (2001) 148-153.

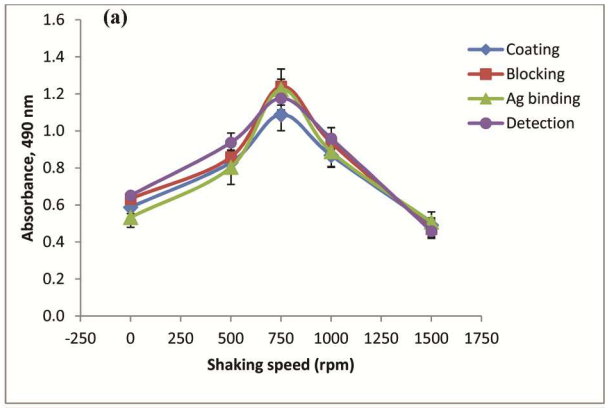

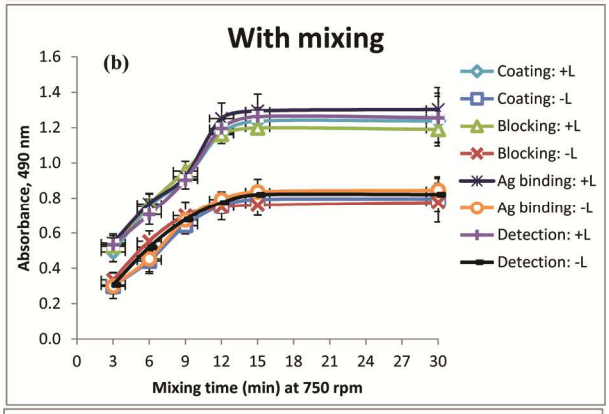

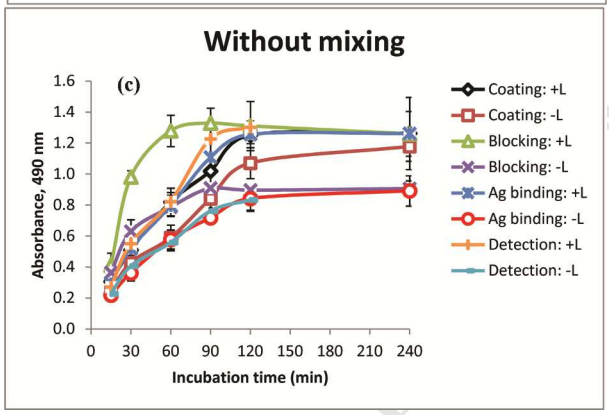

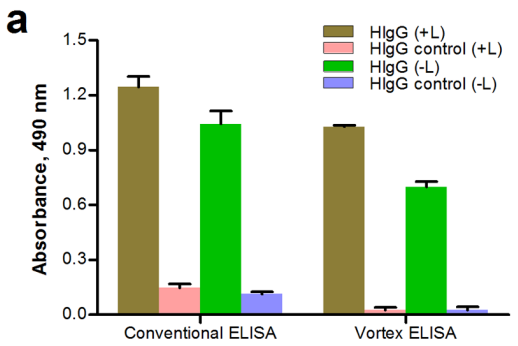
a
HIgG (+L)
HIgG control (+L)
HIgG (-L)
HIgG control (-L)
Absorbance, 490 nm
1.5
1.2
0.9
0.6
0.3
0.0
Conventional ELISA
Vortex ELISA

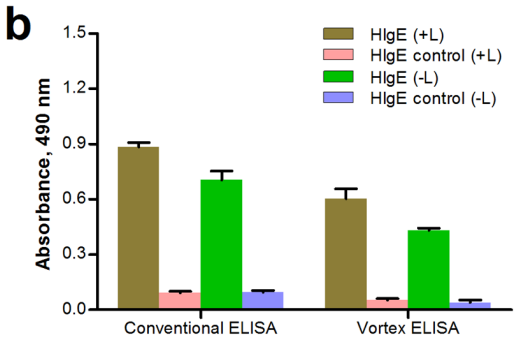
b
HIgE (+L)
HIgE control (+L)
HIgE (-L)
HIgE control (-L)
Absorbance, 490 nm
1.5
1.2
0.9
0.6
0.3
0.0
Conventional ELISA
Vortex ELISA

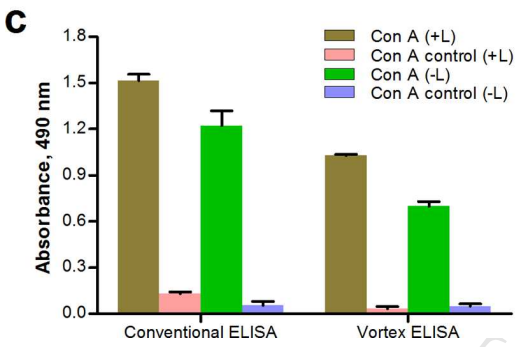
c
Con A (+L)
Con A control (+L)
Con A (-L)
Con A control (-L)
Absorbance, 490 nm
1.8
1.5
1.2
0.9
0.6
0.3
0.0
Conventional ELISA
Vortex ELISA

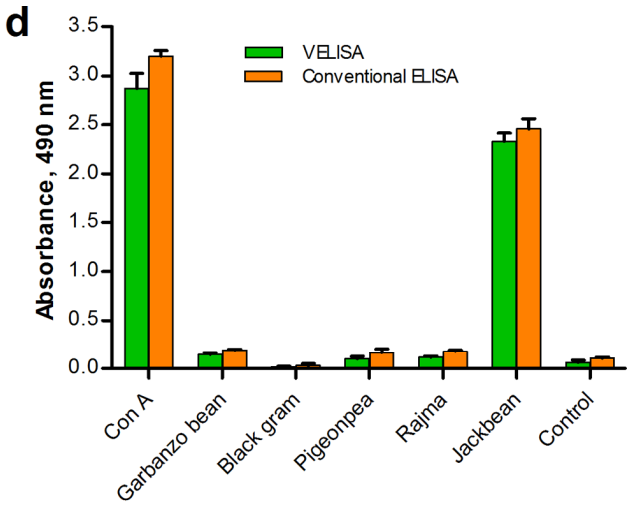
d
VELISA
Conventional ELISA
Absorbance, 490 nm
3.5
3.0
2.5
2.0
1.5
1.0
0.5
0.0
Con A
Garbanzo bean
Black gram
Pigeonpea
Rajma
Jackbean
Control

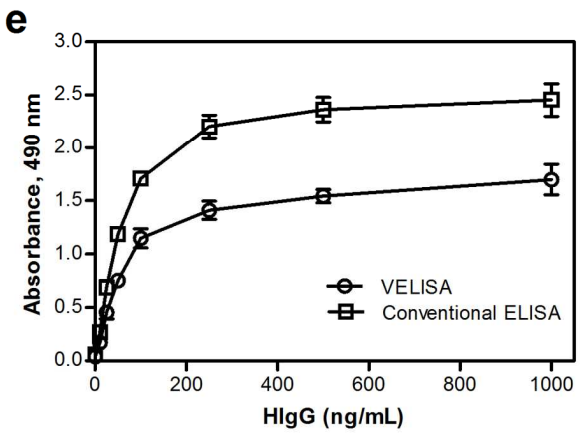
e
Absorbance, 490 nm
3.0
2.5
2.0
1.5
1.0
0.5
0.0
VELISA
Conventional ELISA
0
200
400
600
800
1000
HIgG (ng/mL)

Haritash et al. Ecological Processes (2017) 6:12
DOI 10.1186/s13717-017-0079-3

Ecological Processes

RESEARCH Open Access

Phosphate uptake and translocation in a tropical *Canna*-based constructed wetland

Anil Kumar Haritash*, Sarbari Dutta and Ashish Sharma

Abstract

Introduction: Considering the problem of eutrophication of the water bodies, phosphate removal from water has emerged as a research of topical interest. The present study aims to investigate the efficacy of *Canna* lily-based constructed wetland to remove phosphate from wastewater. The translocation of phosphate in plant tissue and its biochemical transformation in sediments is also studied to understand its accumulation and recirculation within the system.

Results: The removal of phosphate stabilized at around 50% in the present study and plant uptake was found to be the major removal mechanism. Average removal was 167 mg/m^2 day for total phosphate and 84 mg/m^2 day for available phosphate for an initial loading rate of 200 mg/m^2 day and 85 mg/m^2 day, respectively, at a HRT of 24 h. Most of the phosphate concentrated in above ground tissue of plant and its relative accumulation was maximum in flowers. Fractionation of phosphate in sediments confirmed removal by sediments with an accumulation of apatite phosphate (Ca and Mg bound), but release of non-apatite form (Fe and Al bound).

Conclusion: The study concludes that *Canna*-based constructed wetland can be an effective tool for phosphate removal from wastewater and sediments particularly under tropical conditions. Regular harvesting of above ground tissue of *Canna* can result in nutrient export from the system, whereas autochthonous addition may result in recirculation.

Keywords: Phosphate removal, *Canna lily*, Wetland, Sediments, Wastewater

Introduction

Phosphate is a critical parameter to establish the wholesomeness of water in respect of its quality and treatment strategy. Conventional treatment of wastewater removes a significant fraction of suspended impurities and organic carbon, but the removal of nutrients like nitrogen and phosphorus remains limited. Advanced treatment techniques like chemical precipitation, ion exchange, and reverse osmosis are either energy or cost intensive or result in production of secondary sludge (Joshi and Srivastava 2006; Haritash et al. 2015). In such a case, discharge of partially treated wastewater may result in nutrient excess and eutrophication in water bodies (Yadav et al. 2015). Phosphate being an integral component of food and plant waste, fertilizers, detergents etc. is continuously discharged in wastewater, and it reaches to water bodies through various routes leading to a eutrophic state of water body every 10–15 years (Jeppesen et al. 2005). Measures towards restoration of such eutrophic water bodies include chemical application of lime, alum, and ferric salt and introduction of planktons, macrophytes (Gao et al. 2009), and higher organisms to restore a functional biological cycling of phosphorus (Jeppesen et al. 2007). Application of constructed wetlands (CWs) for stabilization of secondarily treated wastewater (Vymazal 2007), and bioretention systems for stormwater, prior to discharge in a water body, has resulted in substantial removal and mobilization of nutrients and restoration of functional nutrient cycling (Sack 2013; Hseih and Davis 2005). Regular harvesting of fish or plants from an under-restoration water body results in export of nutrients, but on-site death and decomposition may lead to recirculation of nutrients in the same environment. Phosphorus being a key limiting nutrient for algal growth in freshwater regulates the biochemical health of a water body (Padma and Nair 2010). Most of the studies report that total phosphorus concentration may not be adequate to determine the ecological risks associated with it. The retention or release of phosphate and its bioavailability are regulated by the chemical state of phosphorus and environmental conditions (Zhang et al. 2012). The release of bound phosphorus to free soluble

* Correspondence: akharitash@dce.ac.in
Department of Environmental Engineering, Delhi Technological University, Bawana Road, Shahbad Daulatpur, Delhi 110042, India

form, as regulated by pH and redox conditions, is reported in several studies (Kim et al. 2003). Many authors have reported phosphate removal from wastewater by *Phragmites*, *Typha*, *Eichhornia*, etc., but the ultimate treatment/disposal of such plants by composting is difficult. Whereas *Phragmites* and *Typha* are hard-stem plants, *Eichhornia* is an invasive weed and is difficult to harvest. In such a case, *Canna lily*, a plant with soft tissue, is identified as a potential candidate for phosphate removal without compromising the treatment efficiency, aesthetics, and option of its composting. Some studies on *Canna spp*. have reported its ability to remove nitrogen and phosphorus efficiently (Polomski et al. 2007), as a result of its higher evapotranspiration rates against other ornamental plants. The rate of dry weight accumulation was also reported high owing to high rate of nutrient accumulation in plant tissue. Analysis of different plant parts confirmed maximum storage in shoots and roots. Other important factors responsible for nutrient removal are sediments and microorganisms. Gravel-based sediments and plant roots offer suitable substrate for microbial growth. Root exudates in the form of carbohydrates, amino-acids, enzymes, etc. offer oxidizing conditions and support nitrifying conditions during decomposition of organic matter (Gersberg et al. 1986). The chemistry of sediments too compliments the removal of nutrients, especially phosphate. Fragmented limestone waste used as packing material in a phragmites-based CW demonstrated removal efficiency of around 62% for phosphate (Mateus et al. 2012). Calcium and magnesium present in sediments can bind to phosphate to immobilize it temporarily under alkaline conditions, whereas iron and aluminium can dominantly remove phosphate at neutral pH (VanBeusekom and DeJonge 1997). Thus, pH plays an important role in regulating availability of phosphate in an aquatic system. Reducing/acidic conditions may favour resolubilization of phosphate, making a water body prone to eutrophication. Therefore, it is important to monitor the total load, and fractionation of phosphate in a water body to comment upon its trophic status, and to determine the actual efficiency of plants towards removal of phosphate. The present study, therefore, aimed to study the removal of phosphate by plants and sediments, to characterize the different fractions of phosphate in sediments and water, and to quantify the distribution of phosphate in different plant tissues during phytoremediation.

Methods

The study was carried out in a pilot-scale vertical-flow constructed wetland cell constructed in the campus of Delhi Technological University during April–May 2013 (summer season). The temperature profile during the period was monitored along with other meteorological conditions (Table 1) to relate the uptake of nutrients to prevalent weather conditions. The CW cell was packed with a 35-cm-thick layer of sand-gravel substrate. The cell had dimensions of length 1.1 m, width 0.8 m, and depth 0.45 m and rectangular tank made up of brick and masonry. The influent was fed from the top, and effluent was collected from an outlet placed opposite to the inlet at the bottom of the tank (Fig. 1). The supporting matrix consisted of sand- and gravel-packed bed with a height of 0.35 m corresponding to a total volume of 0.325 m^3. The bulk density of the packing medium was 1.82 g/cm^3, and d_{10}, d_{30}, and d_{60} computed from particle size distribution were 0.42, 2.36, and 9.0 mm, respectively. The supporting matrix was classified as well-graded medium with a value of 21.43 for coefficient of uniformity (C_u) and 1.47 for coefficient of curvature (C_c). The void ratio was determined as 0.77 with porosity of 0.44. The classification of packing medium represented conditions suitable for easy percolation of water and penetration of plant roots. The CW cell was vegetated with 90 (stem count) healthy plants of *Canna* lily with an average shoot length of 43.2 cm. The initial concentration of phosphate in different tissues of plant (roots, stem, leaves, and flowers) was determined to compare it with the final plant-tissue phosphate level to confirm uptake by plants and subsequent accumulation as a process of removal. The CW cell was initially flushed with water at a hydraulic loading rate (HLR) of 400 L/day for 5 days, and later, the plants were irrigated, on daily basis, with HLR of 30 L/day of simulated wastewater. Synthetic wastewater was prepared by dissolving 21.74 mg of potassium-dihydrogen-orthophosphate in groundwater to obtain a concentration of 5.0 mg/L of PO_4^{3-}-P. The *Canna*-based CW cell was fed with this synthetic wastewater on daily basis (for 30 days) maintaining the hydraulic retention time (HRT) of 24 h on plug-flow basis. The concentration of available (AP) and total phosphate (TP) was determined regularly (for 30 days) in the influent and effluent using standard methods (APHA) (Eaton et al. 1995). Phosphate present in dissolved form was determined as available phosphate, and the sample was acid-digested for extraction of TP. Different fractions of phosphate, i.e. apatite phosphate (bound to Ca and Mg), non-apatite inorganic phosphate (NAIP bound to Fe, Al, and Mn), organic phosphate (OP-bound to biomass), were determined in the sediments, in triplicate ($n = 3$), before initiating the experiments and after the completion using standard prescribed procedure (Williams et al. 1980). The total phosphate accumulated in different plant tissues was also determined initially and finally in five ($n = 5$) samples of each tissue. All the experiments were carried out using analytical (AR) grade chemicals and double glass distilled water in triplicates. The glassware and plasticware used in the experiments were soaked in 0.3% HCl and rinsed with deionized water prior to use. The meteorological

Table 1 Concentration of total and available phosphate and its removal rate in *Canna*-based constructed wetland

Day	Total phosphate (TP) (mg/l)		Removal rate (mg/m^2 day)	Available phosphate (AP) (mg/l)		Removal rate (mg/m^2 day)
	Influent	Effluent		Influent	Effluent	
1	8.43	0.92	252.62	2.12	0.92	76.16
2	5.28	1.19	158.04	0.97	0.28	34.89
3	4.67	0.66	139.90	2.02	0.28	72.74
4	4.56	0.82	136.55	2.12	0.30	76.34
5	6.64	0.41	199.08	2.03	0.31	73.10
6	6.33	0.99	189.60	2.00	0.46	71.97
7	6.17	1.01	184.80	3.26	0.36	117.43
8	6.66	1.24	199.43	4.09	0.77	147.23
9	6.30	1.32	188.60	4.51	0.95	162.32
10	7.50	1.83	224.45	4.64	1.37	166.88
11	6.00	2.52	179.24	4.15	1.72	149.10
12	4.81	2.48	143.55	2.14	1.03	76.84
13	6.21	3.27	185.32	2.26	1.08	81.16
14	4.31	1.99	128.70	2.23	1.27	80.02
15	7.07	2.12	211.46	1.75	1.05	62.78
16	5.84	1.59	174.72	1.76	0.97	63.16
17	7.40	2.62	221.21	1.72	0.74	61.79
18	5.84	2.49	174.45	1.20	0.73	43.04
19	5.21	1.39	155.88	2.00	1.00	71.81
20	6.89	2.12	206.06	2.04	1.12	73.21
21	4.51	2.09	134.67	2.10	1.10	75.38
22	5.32	2.72	158.78	2.01	1.15	72.12
23	4.68	1.42	139.97	2.21	1.22	79.31
24	3.91	1.88	116.74	1.71	1.04	61.34
25	3.12	1.05	93.28	1.47	0.83	52.75
26	5.01	2.23	149.63	2.09	1.20	74.99
27	4.11	1.70	122.79	2.05	1.18	73.55
28	3.87	1.80	115.56	2.01	1.15	72.12
29	5.33	2.56	159.13	3.59	1.80	128.89
Mean	5.59	1.74	167.04	2.35	0.94	84.57
SD (±)	1.26	0.71	37.65	0.95	0.40	34.19

observations during the study were obtained from the weather station of Delhi Pollution Control Committee (DPCC). Statistical analysis of the obtained results was done over MS-Excel software to calculate mean, standard deviation, removal rate, etc.; to plot the normalized curve for removal efficiency; and to plot the graphs.

Results and discussion

Based on the values of ambient temperature and solar insolation during the study, it was observed that the study area represents tropical to sub-tropical weather conditions which favour optimum activity and growth of vegetation. Average ambient temperature was 30 °C ranging from 24.5 °C (minimum) to 40.2 °C (maximum) during the study. Such conditions promote good rate of uptake of nutrients and hence maximum efficiency towards removal. In order to highlight the role of vegetation and sediments in removal of phosphate from wastewater, this paper discusses the uptake, transformation, and translocation of different chemical forms of phosphate in detail.

Phosphate removal from wastewater

Significant removal of phosphate from wastewater in a *Canna*-based constructed wetland was observed in the

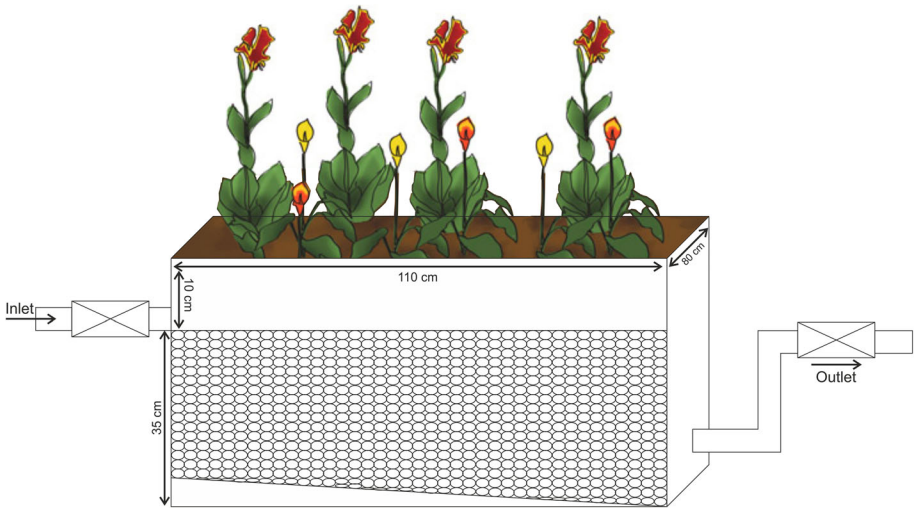

Fig. 1 Schematic description of configuration of constructed wetland cell used in the study

present study. The percent removal of TP was slightly higher than the removal of available phosphate (AP) (Table 1). Average removal of TP was around 68% as against 57% for AP. Percent TP removal was initially higher and went decreasing to stabilize at around 55% in the later stage (after 20 days) (Fig. 2a). On the other hand, the percent removal of AP ranged from 39 to 89% with an average value of 57%. It was low for first 2 days but increased to about 86% on the third day and fluctuated around the same value for 10 days. Later, it decreased and stabilized around 45% by the 20th day (Fig. 2b). Chemical transformation of bound phosphate to orthophosphate (AP) by microorganisms and enzymes secreted by plant roots results in higher removal efficiency for TP. Percent removal of P has been reported in the similar range (24.1–61.55) in another study on nutrient removal from wastewater by 15 wetland species including *Canna* (Jiang et al. 2011). In the present study, average removal rate of TP (167 mg/m^2 day) was higher than that of AP (84 mg/m^2 day) as against the loading rate of 200 mg/m^2 day for TP and 85 mg/m^2 day for AP. In a similar study on treating dairy industry wastewater using a *Canna*-based CW (DeBusk et al. 1995), removal rate of 173 mg/m^2 day has been reported. The present

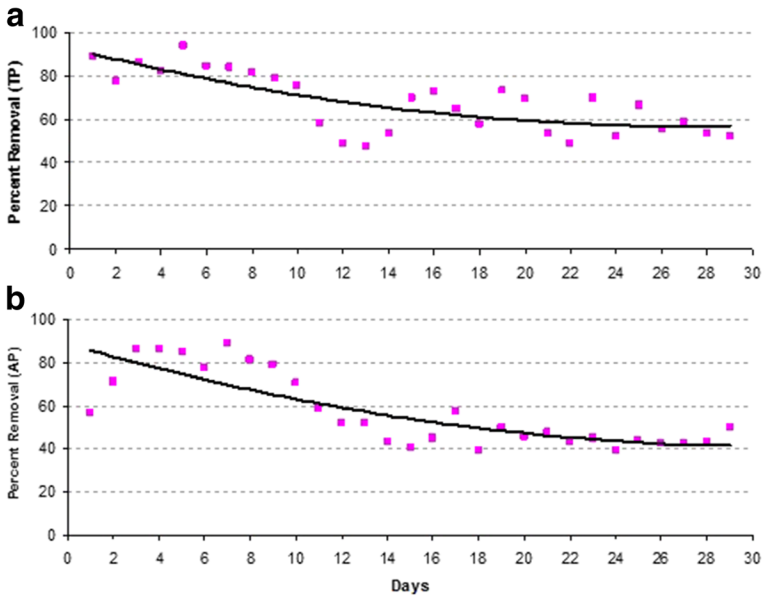

Fig. 2 Percent removal (curve represents normalized removal) of total phosphate (**a**), and available phosphate (**b**) from wastewater in Canna-based constructed wetland

study reports slightly higher removal rates owing to the climatic differences and chemical composition of wastewater in the study. The major mechanisms for phosphate removal are reported as uptake by plants and adsorption over supporting matrix in the study and its efficiency is dependent on plant-uptake rate and sediment binding. In the present study, initially higher percent removal of phosphate could be attributed to higher activity of plants and sediments in the initial phase as reported in other studies too (Haritash et al. 2015). Later, the decrease in removal efficiency is observed in wetlands and bioretention systems with saturation of sediments (Kadlec and Knight 1996).

Phosphate in plant tissue

Since removal of phosphate depends on plant uptake, it is important to study the accumulation of phosphate in various plant tissues. It was determined in various parts (roots, shoots, stem, and flowers) of *Canna* to ascertain its point of accumulation and investigate the possibility of recirculation. Maximum increase in phosphate concentration was observed in leaves, followed by flowers, roots, and stem respectively. The tissue phosphate concentration increased to about 1.7, 1.2, 22, and 4.2 times that of initial phosphate concentration in roots, shoots, leaves, and flowers, respectively (Fig. 3). It confirms that phosphate is taken up by the plants and is accumulated throughout the tissue via metabolism. Similar results have been reported by Polomski et al. (2007) in a study to remove nutrients from nursery run-off in a lab-scale gravel-based system employing seven garden plants individually. The study reported 40% more accumulation of P in shoots than roots at an influent level of 6.77 mg/L phosphate. In a similar study (Jiang et al. 2011), 15 wetland plants were observed to accumulate higher concentration of phosphate in shoots than roots with maximum accumulation by *Canna* among the plants. If relative fraction of initial and final phosphorus in different tissues is compared, flowers accumulated relatively more concentration, and it would result in recirculation of phosphate in the form of organic phosphate (OP) with the fall of flowers into the wetland system. Observations similar to the fact have been reported by Menon and Holland (2014) in a vegetated constructed wetland. In the present study, the higher concentration and overall accumulation of phosphate is observed in stem, leaves, and flowers (above ground tissue), and its recirculation via leaf fall, plant death, and degradation can be avoided by harvesting the above ground tissue at regular intervals, thus facilitating nutrient export from the wetland. Since the nutrients taken up by the plant take part in growth and metabolism, it is important to monitor the physical growth of wetland plants. In the present study, the root length, shoot length, and plant density were found to increase by a factor of 3.69, 3.67, and 2.04, respectively. The shoot-root ratio remained almost the same throughout the study indicating that there was no significant effect over the plant health. It stresses on application of *Canna*-based wetland systems for the removal of nutrients from wastewater.

Phosphate in sediments

Since adsorption of phosphate by sediments is a major removal pathway, its removal and fractionation was studied in the supporting matrix before initiating the experiments and after the completion of study. An increase in the concentration of total phosphate (TP) was observed from 5.14 to 5.88 mg/g confirming to its adsorption by sediments (Fig. 4). Since the root system of *Canna* is strong and extensive, it removes phosphate from sediments too. As a result, the increase of phosphorus in sediments is not as significant. This strengthens the idea

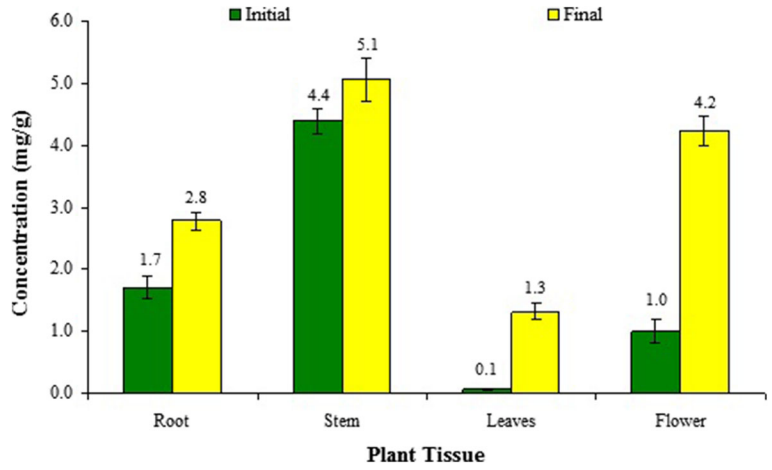

Fig. 3 Average concentration of phosphorus (mgP/g) in different plant tissues of Canna before and after the treatment (n=5)

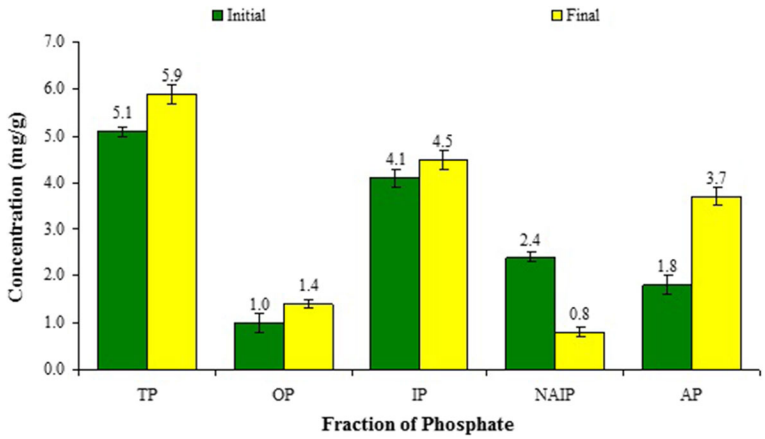

Fig. 4 Average concentration (mg/g) of different fractions of phosphate in sediments before and after the treatment (n=3)

that the removal of P in *Canna*-based wetland is predominantly by plant uptake, and sediments too play a role in it. Apart from it, the chemical composition and mineral profile of sediments may also be the reason for relatively less adsorption over sediments. The fraction of organic phosphate (OP) was observed to increase from 1.0 to 1.37 mg/g indicating to the role of microorganisms and organic matter in phosphate removal via biomass accumulation. Some addition of biomass as a result of leaf fall or dead tissue of old roots may also be the reason for an increase of OP in sediments. The concentration of inorganic phosphate (IP) too increased in sediments indicating chemical binding/precipitation of phosphate with its binding to Ca and Mg (AP) or Fe, Al, and Mn (NAIP). The Ca and Mg bound phosphate (AP) increased during the study indicating the binding of phosphate to Ca and Mg present in sediments. Similar observations have been presented by Gu and Dreschel (2008) in a constructed wetland in Florida. The NAIP concentration decreased during the study from 2.37 to 0.76 mg/g. It may be attributed to release of phosphate bound to Fe, Al, and Mn in sediments during higher oxygen demand of wetland for respiration. During high oxygen demand, ferric bound phosphate is released to water with reduction of Fe^{3+} to Fe^{2+} because iron is an alternate terminal electron acceptor during deficiency of dissolved oxygen (Kortmann and Rich 1994). Studies have confirmed that AP will be trapped in sediments for a longer duration and is regarded as non-available. It will not be released to water easily. On the other hand, NAIP can be released to water column easily particularly during summers depending on the redox conditions present (Zhang et al. 2012). Apart from it, the phosphorus concentration in sediments in rooted macrophyte-based system decreases since the plants use sediment too as source of phosphorus (Carignan and Kalff 1980). It further strengthens the objective of using a *Canna*-based wetland since it not only removes phosphate from wastewater but also removes a fraction of NAIP. Based on the results obtained, it was observed that major plant uptake of phosphate is from wastewater and sediment NAIP during oxygen-stressed conditions.

Conclusions

Based on the observations of the present study, *Canna lily*-based constructed wetland is found to be an effective treatment option for phosphate from wastewater. The removal of sediment bound phosphate is also facilitated by *Canna*, but the available phosphate accumulates in sediments which may be released in hypolimnion if pH is acidic or conditions are reducing. Apart from it, though phosphate is translocated to all the tissues, its relative accumulation is observed to be more in flowers which may cause recirculation. Most of the fraction of removed phosphate is accumulated in above ground tissue, and hence, regular harvesting of aerial tissue can result in nutrient export. Considering the nutrient accumulation of harvested tissue, it may be used as raw material for composting if ultimate disposal is aimed at. Within the sediments, AP is accumulated whereas NAIP is released. It confirms easy release of Fe and Al bound phosphate to water though the redox conditions play a crucial role in it. The study concludes that *Canna lily* removes phosphorus not only from wastewater but also from sediments. Hence, *Canna lily*-based wetlands are effective in phosphate removal from wastewater especially under tropical conditions.

Authors' contributions

AKH designed the study, participated in the experimental work, and drafted the manuscript. SD carried out the analysis of phosphate in wastewater and plant. AS did the analysis of sediments and helped prepare the wetland cell for the study. All authors have read and approved the final manuscript.

Competing interests

The authors declare that they have no competing interests.

Received: 17 January 2017 Accepted: 23 February 2017
Published online: 03 April 2017

References

Carignan R, Kalff J (1980) Phosphorus sources for aquatic weeds: water or sediments. Science 207:987–989
Debusk TA, Peterson JE, Rameshreddy K (1995) Use of terrestrial and aquatic plants for removing phosphorus from dairy wastewaters. Ecol Eng 5:371–390
Eaton AD, Clesceri LS, Greenberg AE (1995) Standard methods for the examination of water and wastewater, 19th edn. American Public Health Association (APHA), New York
Gao J, Xiong Z, Zhang J, Zhang W, Mba FO (2009) Phosphorus removal from water of eutrophic lake Donghu by five submerged macrophytes. Desalination 242:193–204
Gersberg RM, Elkins BV, Lyon SR, Goldman CR (1986) Role of aquatic plants in wastewater treatment in artificial wetlands. Water Res 20:363–368
Gu B, Dreschel T (2008) Effects of plant community and phosphorus loading rate on constructed wetland performance in Florida, USA. Wetlands 28(1):81–91
Haritash AK, Sharma A, Behal K (2015) The potential of *Canna lily* for wastewater treatment under Indian conditions. Int J Phytoremediation 17(10):999–1004
Hseih C, Davis AP (2005) Evaluation and optimization of bioretention media for treatment of urban storm water runoff. J Environ Eng 131:1521–1531
Jeppesen E, Meerhoff M, Jacobsen BA, Hansen RS, Sondergaard M, Jensen JP, Lauridsen TL, Mazzeo N, Branco CWC (2007) Restoration of shallow lakes by nutrient control and manipulation—the successful strategy varies with lake size and climate. Hydrobiol 581(1):269–285
Jeppesen E, Sondergaard M, Jensen JP, Havens K, Anneville O, Carvalho L, Covene MF, Deneke R, Dokulil MT, Foy B, Gerdeaux D, Hampton SE, Hilt S, Kangur K, Kohler J, Lammens E, Lauridsen TL, Manca M, Miracle R, Moss B, Noges P, Perrson G, Phillips G, Portielje R, Romo S, Schelske CL, Straile D, Tatrai I, Willen E, Winder M (2005) Lakes' response to reduced nutrient loading—an analysis of contemporary data from 35 European and North American long term studies. Freshw Biol 50:1747–1771
Jiang FY, Chen X, Luo AC (2011) A comparative study on growth and nitrogen and phosphorus uptake characteristics of 15 wetland species. Chem Ecol 27(3):263–272
Joshi M, Srivastava RK (2006) Removal of iron from waste water by using non-conventional ecofriendly material. Pollut Res 25(1):185–188
Kadlec RH, Knight RL (1996) Treatment wetlands. Lewis Publishers, Boca Raton
Kim LH, Choi E, Stenstrom MK (2003) Sediment characteristics, phosphorus types and phosphorus release rates between river and lake sediments. Chemosphere 50:53–61
Kortmann RW, Rich PH (1994) Lake ecosystem energetics: the missing management link. Lake Reservoir Manage 8(2):77–97
Mateus DMR, Vaz MMN, Pinho HJO (2012) Fragmented limestone wastes as a constructed wetland substrate for phosphorus removal. Ecol Eng 41:65–69
Menon R, Holland M (2014) Phosphorus release due to decomposition of wetland plants. Wetlands 34:1191–1196
Padma P, Nair SM (2010) Assessing the phosphorus fractionation in a tropical river-estuarine system of South India. Chem Ecol 26(6):453–466
Polomski FR, Bielenberg DG, Whitwell T, Taylor MD, Bridges WC, Klaine SJ (2007) Nutrient recovery by seven aquatic garden plants in laboratory-scale subsurface-constructed wetland. Hortic Sci 42(7):1674–1680
Sack C (2013) Landscape architecture and novel ecosystems: ecological restoration in an expanded field. Ecol Process 2(35):1–9
Vanbeusekom JEE, Dejonge VN (1997) Transformation of phosphorus in the Wadden sea: apatite formation. Ger J Hydrogr 49:297–305
Vymazal J (2007) Removal of nutrients in various types of constructed wetlands. Sci Total Environ 380:48–65
Williams JDH, Mayer T, Nriagu JO (1980) Extractability of phosphorus from phosphate minerals common in soils and sediments. Soil Sci Soc Am J 44: 462–465
Yadav A, Kataria A, Singh K, Mathur K, Goswami S, Haritash AK (2015) Seasonal assessment of trophic status of a palustrine water body. Int J Eng Res Technol 4(3):37–40
Zhang B, Fang F, Guo J, Chen Y, Li Z, Guo S (2012) Phosphorus fractions and phosphate sorption-release characteristics relevant to the soil composition of water-level-fluctuating zone of Three Gorges Reservoir. Ecol Eng 40:153–159

Spectroscopic studies of Pr 3+ doped lithium lead alumino borate glasses for visible reddish orange luminescent device...

Article *in* Journal of Alloys and Compounds · March 2017

DOI: 10.1016/j.jallcom.2017.03.020

CITATIONS
0

READS
79

7 authors, including:

Dr. SK. Mahamuda
K L University
21 PUBLICATIONS **242** CITATIONS
SEE PROFILE

Haranath Divi
CSIR-National Physical Laboratory - India
164 PUBLICATIONS **1,986** CITATIONS
SEE PROFILE

Gaddam Vijaya Prakash
Indian Institute of Technology Delhi
105 PUBLICATIONS **1,566** CITATIONS
SEE PROFILE

Journal of Alloys and Compounds 708 (2017) 911–921

Contents lists available at ScienceDirect

Journal of Alloys and Compounds

journal homepage: http://www.elsevier.com/locate/jalcom

Spectroscopic studies of Pr^{3+} doped lithium lead alumino borate glasses for visible reddish orange luminescent device applications

Nisha Deopa [a], A.S. Rao, Dr. [a, *], Sk. Mahamuda [b], Mohini Gupta [c], M. Jayasimhadri [a], D. Haranath [d], G. Vijaya Prakash [c]

[a] Department of Applied Physics, Delhi Technological University, Bawana Road, New Delhi, 110 042, India
[b] Department of Physics, K L University, Green Fields, Vaddeswaram, 522 502, Guntur (Dt), A.P, India
[c] Nanophotonics Lab, Department of Physics, Indian Institute of Technology-Delhi, Hauz Khas, New Delhi, 110016, India
[d] CSIR-National Physical Laboratory, Dr. K.S. Krishnan Marg, Pusa Road, New Delhi, 110012, India

ARTICLE INFO

Article history:
Received 1 December 2016
Received in revised form
28 February 2017
Accepted 4 March 2017
Available online 6 March 2017

Keywords:
Praseodymium
Glasses
Raman spectra
Judd-Ofelt parameters
Photoluminescence
Confocal images

ABSTRACT

Lithium Lead Alumino Borate (LiPbAlB) glasses doped with Pr^{3+} ions were prepared via melt quenching technique to study their luminescence behavior using absorption, excitation, photoluminescence (PL) and decay spectral studies. A broad hump observed in XRD confirms the amorphous nature of the as-prepared glass. The glass transition temperature (T_g) and thermal stability (ΔT) were measured from Differential Scanning Calorimetry (DSC). FT-IR and Raman studies were performed to understand the network functional groups involved in the host glass. Various radiative parameters for the prominent fluorescent levels of Pr^{3+} were evaluated with in the frame work of Judd-Ofelt theory. PL and confocal images recorded under 445 nm Continuous Wave (CW) diode laser excitation were used to understand the visible emission characteristic features of the as-prepared glasses. The decay profiles of $^1D_2 \rightarrow {}^3H_4$ show single exponential for lower concentration and non-exponential for higher concentration resulting decrease in experimental lifetime (τ_{exp}) with increase in concentration. Such decrease in τ_{exp} and decay conversion from single to non-exponential with increase in rare earth ion concentration has been attributed to the cross-relaxation processes and subsequent concentration quenching observed. From the emission cross-sections, branching ratios, quantum efficiency, CIE coordinates and confocal images, it was concluded that 1 mol % Pr^{3+} ion concentration is optimum in LiPbAlB glasses to develop visible reddish orange luminescent devices.

1. Introduction

Nowadays, Rare Earth (RE) doped glasses have attracted a great deal of attention among the researchers because of their versatile use and potential applications in diversified fields of Science and Technology [1–4]. The advancement in optical glasses doped with RE ions has caused revolution in optical communication and electronic industries. To elucidate the effect of host glass on lasing potentialities of the doped RE ions, various glassy materials such as borates, fluoroborates, phosphates, tellurites and fluorophosphates etc. were investigated [5–8]. Quite recently, glasses doped with RE ions are said to be superior over phosphors owing to their special characteristic features such as broad inhomogeneous bandwidths, simple manufacturing process, cheap production cost, good thermal stability and high doping capacity [9,10]. The spectroscopic characteristic of RE ions depends on its concentration, ambient temperature and composition of the host glass [11]. A host glass having low phonon energy is aptly suitable in designing the luminescent materials capable of reducing the non-radiative decay rates and thereby to enhance quantum efficiency to a greater extent [12].

Among all the conventional glass formers, boric acid (B_2O_3) is said to be one of the best glass formers, owing to its superior characteristic features such as good transparency, lower melting point, thermal stability, chemical durability and high RE ion solubility [13]. Nevertheless, in borate glasses, the presence of stretching vibrations of network forming oxides usually makes them to possess high phonon energies around 1300 cm^{-1} resulting in enhancing the non-radiative decay processes there by reducing the luminescence efficiency drastically [14]. However, such

* Corresponding author.
E-mail address: drsrallam@gmail.com (A.S. Rao).

http://dx.doi.org/10.1016/j.jallcom.2017.03.020
0925-8388/

redundant phonon energies possessed by borate glasses can be effectively reduced by adding Heavy Metal Oxides (HMO) such as lead and bismuth [15,16]. Further glasses containing HMOs are extremely robust in shielding the radioactive radiation penetration because of their high density and atomic number. Addition of lead oxide to a borate glass not only reduces the redundant phonon energies, but also enhances its transparent window from visible to near infrared regions. It is well known that, the presence of PbO in glasses enhances the chemical durability, resistance against devitrification and lowers the melting temperature [17]. In literature it was reported that, PbO can act as a network former or modifier depending on its content in glass [18]. The presence of Al_2O_3 in RE doped glasses not only improves chemical durability, mechanical strength and emission properties, but also works as network modifier [19]. It is worth to note that Al^{3+} ions can improve the optical response of the material by occupying tetrahedral and octahedral sites in the host glass [20]. Recently, borate glasses containing lithium oxides are showing immense scientific interest because of its network forming ability as well as best chemical durability [21]. There are only three coordinated boron atoms present in B_2O_3 vitreous and addition of alkali oxide (Li_2O) to this form changes it into four coordinated tetrahedral. Therefore an alkali metal oxide in B_2O_3 forms non bridging oxygen and modifies physical and chemical properties [22]. The aforementioned various scientific patronages offered by B_2O_3, PbO, Al_2O_3 and Li_2O have prompted us to prepare a germane system namely Lithium Lead Alumino Borate (LiPbAlB) glass to study the luminescence properties possessed by RE ions doped in them. The prime aim of the present work is to develop chemically and thermally more stable RE doped glassy system preferably with less phonon energies and better suited for fabricating a visible luminescent device with relatively good emission cross-section and quantum efficiency.

RE elements are attracting scientists continuously because of the special spectroscopic characteristic feature possessed by electrons present in 5f and 4d orbitals, which makes them as promising candidates in designing the luminescence devices. Among the RE elements, praseodymium is the most preferred one because of the presence of various metastable states like $^3P_{0,\ 1,\ 2,}$ $^1D_2$, $^1G_4$ in its energy level structure, which results emission in UV and infrared regions. Pr^{3+} doped glasses are also useful in up-conversion laser processes and suitable to develop 1.3 μm optical communication window [23]. Further, some energy levels of Pr^{3+} ions shows concentrating quenching with increase in the doped RE ion content. It has been investigated that, Pr^{3+} doped glasses possess lasing action from $^1D_2 \rightarrow {}^3H_4$ transition around 600 nm [24,25]. In the backdrop of the aforementioned reasons, Pr^{3+} doped glasses with low phonon energies are said to be potential candidates for solid state lasers in visible region. The absorption spectra of RE doped glassy matrices have been analyzed with the help of Judd-Ofelt (J-O) theory [26,27]. Recently much work has been done in the field of RE doped glasses for the luminescent device applications using J-O theory [28–31]. Due to small energy difference between ground ($4f^2$) and excited states (4f 5d) of Pr^{3+}, sometimes the J-O theory fails to explain intensity measurements successfully. To overcome this difficulty Goldner and Auzel [32] have used the standard J-O theory and adopted the normalization method for getting reliable J-O intensity parameters with proper scaling of intensity measurement by keeping hypersensitive transition ($^3H_4 \rightarrow {}^3P_2$) aside in the fitting procedure.

In the present study, LiPbAlB glasses doped with different concentration of Pr^{3+} were synthesized. Different spectroscopic characterization tools like XRD, DSC, FT-IR and Raman were used to understand glassy nature, thermal and structural properties of the as-prepared glass. Absorption, excitation, PL, confocal images and Time Resolved Photoluminescence (TR-PL) spectral profiles were used to understand the suitability of the as-prepared glasses along with optimization of the doped praseodymium ion concentration for better luminescence efficiency.

2. Experimental

Pr^{3+} doped LiPbAlB glasses were synthesized by using conventional melt quenching technique using the following chemical composition.

$$10Li_2O - 10PbO - (10\text{-}x)\,Al_2O_3 - 70B_2O_3 - xPr_6O_{11}$$

where, x = 0.05, 0.1, 0.5, 1.0, 1.5, 2.0 mol %; these glasses are designated as glass A, B, C, D, E and F. Analar grade chemicals of Li_2O, PbO, Al_2O_3, B_2O_3 and Pr_6O_{11} were purchased from Sigma Aldrich and about 8 g of these samples were mixed and crushed in an agate mortar until homogeneous mixture is obtained. Such mixture was collected into a silica crucible and heated at 1100° C in an electrical furnace for about 5 h and desired melts were prepared. Such melts removed from the furnace were quenched quickly between two pre-heated brass plates to form glass sample of uniform thickness. The glass samples thus prepared are annealed for 4 h in another electrical furnace at 350 °C to eliminate thermal strains. Finally, Pr^{3+} doped LiPbAlB glass samples were obtained to study their luminescent properties.

Refractive indices of the as-prepared glasses were measured with the help of Brewster's angle method by using He-Ne laser (650 nm line) with ±0.01 accuracy. Archimedes principle was employed to determine the density of the glasses taking water as an immersion liquid with an accuracy of ±0.01 gm/cm^3. XRD measurement for an un-doped glass was recorded by using high-resolution X-ray diffractometer (Bruker; Model D8 advance) in the 2θ range from 10° to 70° using nickel-filtered CuKα radiation (λ = 1.5406 Å). The FT-IR spectrum was recorded by using Perkin Elmer's Frontier FT-IR Spectrometer and the pellet was prepared by mixing an un-doped glass in powdered form with KBr pellet and then compressed mechanically at 1.5 ton. Raman spectral studies were performed with the help of Renishaw Invia Raman Microscope. Thermal analysis was recorded by using Perkin Elmer Differential Scanning Calorimetry (DSC) equipment with a heating rate of 10 °C/min starting from the ambient temperature to 500 °C in presence of N_2 atmosphere.

The optical absorption spectra were recorded by using Shimadzu 3600 UV–vis–NIR spectrophotometer having a spectral resolution of 0.1 nm. The excitation spectrum for glass D was recorded using Shimadzu RF-5310 PC-Spectrofluorophotometer with a spectral resolution of 0.5 nm. The steady state PL spectra for all the LiPbAlB glasses were recorded by using a home build setup with 445 nm CW diode laser as an excitation source. The emission was dispersed into a monochromator (Acton SP2300) coupled to a PMT through appropriate lenses and filters. TR-PL spectral recordings were done using an Edinburgh FLSP900 Fluorescence Spectrometer with a spectral resolution of 0.1 nm, where xenon lamp is used as an excitation source and data was analyzed by using origin 9 software. The confocal images were recorded by using a modified laser scanning confocal microscope (Olympus BX51) equipped with XY piezo state under 445 nm CW diode laser excitation.

3. Results and discussion

3.1. XRD spectral measurement analysis

In order to check the amorphous nature of the un-doped LiPbAlB glass, XRD spectral analysis was carried out and it was shown

in Fig. 1(a). As shown in Fig. 1(a), a broad hump observed in the XRD spectrum without any sharp peaks confirms the amorphous nature of the as-prepared glass.

3.2. Thermal characterization

The DSC curve recorded for an un-doped glass is shown in Fig. 1(b). The DSC curve shows three peaks at 325 °C, 352 °C and 452 °C corresponding to glass transition temperature (T_g), onset crystallization temperature (T_x) and peak crystallization temperature (T_p) respectively. The thermal stability of glass was evaluated by using following expression [33].

$$\Delta T = T_X - T_g \quad (1)$$

For better thermal stability, the ΔT value should be relatively large for a given glass. In the present work for an un-doped LiPbAlB glass the value of ΔT was observed to be around 27 °C.

Thermal stability of a glassy material can also be estimated using Hurby's parameter using following equation [34].

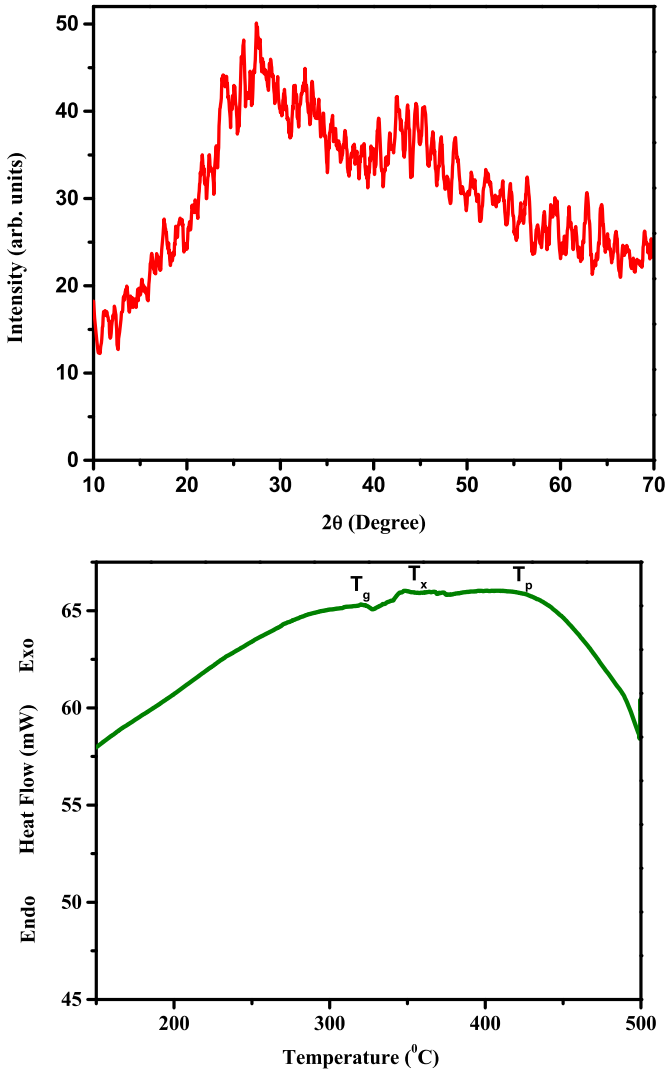

Fig. 1. (a): XRD spectrum of an un-doped LiPbAlB glass. **(b)**: DSC spectrum of an un-doped LiPbAlB glass.

$$K_H = \frac{T_X - T_g}{T_m - T_g} \quad (2)$$

where, K_H is Hruby's parameter of the glass. The higher the value of Hruby's parameter for a given glass the better will be the thermal stability. For better thermal stability the value of K_H should be greater than 0.1 [33,34]. In the present work for an un-doped LiPbAlB glass, the value of K_H was found to be 0.15, which confirms that the as-prepared glass is relatively stable thermally.

3.3. Physical properties characterization

From the experimentally measured density and refractive index values, various other physical properties were evaluated using suitable expression that are given in literature [35] and are presented in Table 1. The physical properties of the as-prepared glasses changing with increase in Pr^{3+} ions concentration indicates the transformed environment around the doped RE ion. From Table 1, it can be observed that with increasing the RE ion concentration from glass A to F, the average molecular weight, mean atomic volume, molar refraction, field strength, reflection losses and optical dielectric constant values are increasing and on the other hand the physical properties such as polaron radius, optical basicity, inter atomic distance and molecular electronic polarizability are decreasing. The low field strength values observed for the present glasses shows high RE ion solubility in these glasses. Further, optical basicity of the titled glasses denotes the capacity of the host glass to donate negative charges to the doped RE ion. It is observed form Table 1 that the titled glasses possess low molecular electronic polarizability that makes them more stable.

3.4. FT-IR and Raman spectral studies

To identify the functional groups present and local structure, FT-IR and Raman spectra of an un-doped LiPbAlB glass have been recorded and are shown in Figs. 2 and 3 respectively. The proper assignment of different function groups corresponding to the wavenumbers are given in Table 2. The FT-IR spectral vibrations of an un-doped glass consists of six infrared active modes around 3483, 2853, 2929, 2664, 544 and 462 cm^{-1}. It is reported that the presence of broad band in the FT-IR spectrum is because of the mixture of high degeneracy vibrational states, mechanical scattering and thermal broadening of the lattice dispersion within the sample [36]. Two broad bands observed around 3483 cm^{-1} and 2664 cm^{-1} are attributed to the symmetric stretching of O–H bond and the presence of molecular water. The bands observed at 2853 cm^{-1} and 2929 cm^{-1} shows the presence of organic contaminants and existence of hydrogen bonding respectively. The band present at 544 cm^{-1} attributes to B–O–B bond bending vibrations mixed with covalent Pb–O vibrations. The peak position around 462 cm^{-1} assigned for O–B–O bond bending vibrations Li–O bond vibrations. These FT-IR assignments are in good agreement with the reported once in borate glasses [17,37]. FT-IR spectral studies are also useful in evaluating the OH content present in the glass [38]. Estimation of OH content present in a glass is important because, its presence in a glass can reduce radiative decay process, resulting decrease in quantum efficiency. The OH content in an amorphous matrix can be evaluated by using the following expression

$$\alpha_{OH} = \frac{\ln\left(\frac{T_0}{T_D}\right)}{l} \quad (3)$$

here, T_0 is the highest transmission, T_D is the glass transmission at

Table 1
Various physical properties of Pr^{3+} ions in LiPbAlB glasses.

S.No	Physical Property	Glass A	Glass B	Glass C	Glass D	Glass E	Glass F
1	Refractive index (n_d)	2.13	2.24	2.38	2.49	2.59	2.68
2	Density (gm/cm^3)	3.32	3.33	3.34	3.36	3.38	3.41
3	Average molecular weight (g)	85.32	85.49	86.92	88.7	90.48	92.25
4	Pr^{3+} ion concentration, N (10^{22} ions/cm^3)	0.12	0.22	1.16	2.28	3.38	4.45
5	Mean atomic volume (g/cm^3/atom)	5.71	5.72	5.73	5.76	5.79	5.81
6	Dielectric constant (ε)	4.52	5.03	5.68	6.24	6.71	7.17
7	Optical dielectric constant ($\varepsilon - 1$)	3.52	4.03	4.68	5.24	5.71	6.17
9	Reflection losses (R %)	12.96	14.69	16.71	18.34	19.63	20.81
10	Molar refraction (R_m) (cm^{-3})	13.86	14.75	15.85	16.77	17.53	18.23
11	Polaron radius (r_p) (Å)	3.82	3.04	1.78	1.42	1.25	1.14
12	Inter-atomic distance (r_i) (Å)	9.48	7.53	4.42	3.53	3.09	2.82
13	Molecular electronic polarizability (10^{-23}cm^3)	10.99	5.847	1.257	0.665	0.463	0.361
14	Field Strength F (x10^{15} cm^{-2})	2.05	3.26	9.45	14.86	19.30	23.18
15	Optical basicity (Λ_{th})	0.448	0.447	0.446	0.436	0.434	0.429

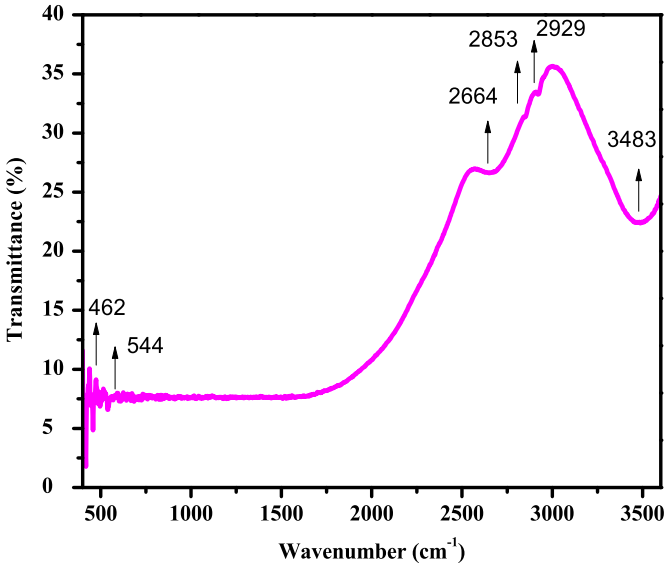

Fig. 2. FT-IR spectrum of an un-doped LiPbAlB glass.

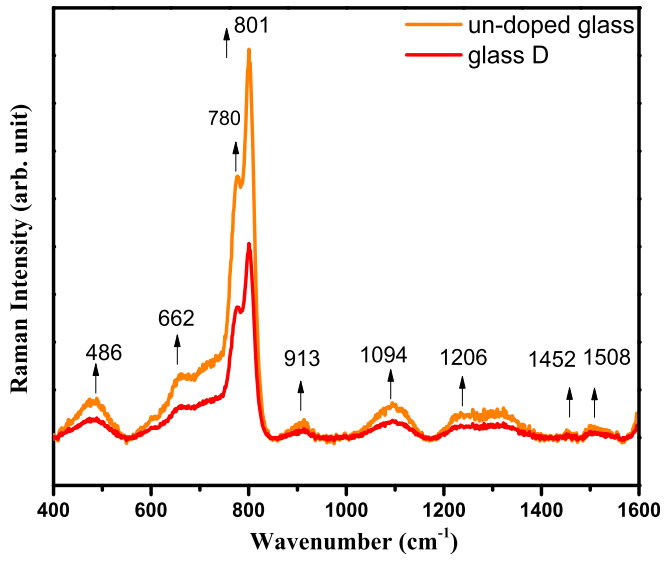

Fig. 3. Raman spectrum of an un-doped LiPbAlB glass along with glass D.

3000 cm^{-1} and *l* is thickness of glass sample. For the present glass, the estimated OH content is 58.79 ppm which is lower than ZnAlBiB glass (65.48 ppm) [20], GeS_2 (175.5 ppm) [39], LHG-8L (128 ppm) [40], KBS (133 ppm) [41] and LBTAF glass (120.00 ppm) [42]. Relatively smaller amount of OH content present in the as-prepared glass speaks its superiority in acting as an efficient luminescent device.

The Raman spectrum is a very significant tool for identifying the presence of different functional groups involved in a glassy matrix. The Raman spectrum of an un-doped glass was recorded in the wavelength range 400–1600 cm^{-1} and is shown in Fig. 3. The spectrum represents one dominant band corresponding to 801 cm^{-1}, which is assigned for symmetric breathing vibrations of boroxol rings. In addition to this dominant band, seven more peaks with one small shoulder of lower intensity also observed and presented in Table 2. The peak observed at 1094 cm^{-1} ascribed to di-borate group while 1206 cm^{-1} to pyro-borate group. The peak located at 1452 cm^{-1} and 1508 cm^{-1} ascribed to BO_2O triangle linked to BO_4 units and BO_2O triangle linked to other borate triangular units respectively. Further, the peak positioned at 780 cm^{-1} indicates the symmetric breathing vibrations of six-member rings with one or two BO_3 triangle replaced by BO_4 tetrahedral. A band observed at 662 cm^{-1} indicates the presence of ring type metaborate units and the in plane bending mode of BO_3 units while band located at 486 cm^{-1} ascribed to isolated di-borate groups as well as Li–O and Pb–O bond vibrations. These Raman peaks matches well with some of the reported values of borate glasses in literature [43,44].

3.5. Absorption spectral studies

Optical absorption spectra of LiPbAlB glasses doped with different concentration of Pr^{3+} were recorded at room temperature in UV–vis–NIR region and is shown in Fig. 4. The spectra exhibit seven absorption peaks centered around 444, 470, 482, 590, 1436, 1514 and 1926 nm. Each absorption spectrum consists of three peaks in the blue region arising from $^3H_4 \rightarrow {}^3P_{2,1,0}$ transitions, single intense peak corresponds to visible region from $^3H_4 \rightarrow {}^1D_2$ transition while three peaks in near infra-red region from $^3H_4 \rightarrow {}^3F_{4,3,2}$ transitions. Identification and assignment of bands observed in the present work are done as per the procedure outlined by Carnall et al. [45]. Transition observed in blue ($^3H_4 \rightarrow {}^3P_2$) region is hypersensitive, which strongly depends on the local environment of the RE ions and affects the J-O intensity parameters. Such hypersensitive transitions are governed by a selection rules $|\Delta S| = 0$, $|\Delta L| \leq 2$, and $|\Delta J| \leq 2$ [46]. It is shown in Fig. 4 that with increase in the RE ion concentration, the peak position of the

Table 2
Assignment of FT-IR and Raman peaks for an un-doped LiPbAlB glass.

FT-IR Wavenumber (cm^{-1})	FT-IR assignments	Raman Wavenumber (cm^{-1})	Raman assignments
462	O–B–O bond Bending vibrations Li–O bond vibrations	486	Isolated diborate groups, Li–O, Pb–O bond vibrations
544	B–O–B bond Bending vibrations mixed with covalent Pb–O vibrations	662	Presence of ring type metaborate units and the in plane bending mode of BO_3 units, Pentaborate groups
2664	Symmeytric stretching of the O–H bond, molecular water	780	Symmetric breathing vibrations of six-member rings with one or two BO_3 triangle replaced by BO_4 tetrahedra
2853, 2929	Presence of organic contaminants	801,913	Symmetric breathing vibrations of boroxol rings
3483	Symmeytric stretching of the O–H bond, molecular water	1094	Diborate group
		1206	Pyroborate group
		1452	BO_2O-triangle linked to BO_4- units
		1508	BO_2O-triangle linked to other borate Triangular units

hypersensitive transition shifts slightly toward shorter wavelength side and this may be due to nephelauxetic effect [47]. In order to know nature of bonding in the as-prepared glasses, nephelauxetic ratio ($\bar{\beta}$) and bonding parameters (δ) were evaluated using the relevant expression given in literature [48,49]. The bonding parameter (δ) thus evaluated for all the glasses are given in Table 3. Depending on the ligand field distribution around the RE ions, the bonding parameter may be positive or negative indicating covalent or ionic bonding respectively. From Table 3, it is conspicuous that, the magnitude of bonding parameter (δ) is negative for all the glasses indicating the bonding nature predominantly ionic. Such ionic nature of bonding decreases with increase in Pr^{3+} ion concentration in these glasses.

The energies of the absorption bands are calculated in terms of experimental oscillator strength (f_{exp}) using the area under the absorption curve employing the equation given in literature [50] and are given in Table 3. From the experimental oscillator strengths (f_{exp}) the J-O intensity parameters (Ω_2, Ω_4, Ω_6) and calculated oscillator strengths (f_{cal}) are evaluated by least square fit method using the J-O theory [26,27]. Root mean square deviation (δ_{rms}) was used to evaluate the quality of fit between calculated and experimental oscillator strength by using the following expression.

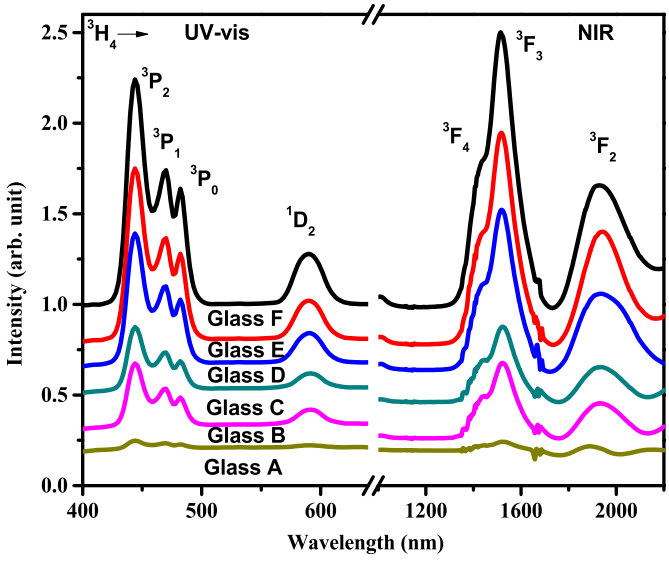

Fig. 4. Absorption Spectra of Pr^{3+} ions doped LiPbAlB glasses in UV–vis–NIR regions.

$$\delta_{rms} = \left[\frac{\sum \left(f_{exp} - f_{cal}\right)^2}{p}\right]^{\frac{1}{2}} \quad (4)$$

here, p represents the total number of energy levels present in the fitting procedure.

The experimental and calculated oscillator strengths along with δ_{rms} are given in Table 3. From Table 3, it can be observed that, exclusion of hypersensitive transition gives more reasonable δ_{rms} between calculated and experimental oscillator strengths. Hence, the J-O intensity parameters have been calculated by excluding hypersensitive transition and are given in Table 4 along with the values reported in literature [4,6,14,37–40,42].

From Table 4, it can be seen that the J-O parameters follows the same trend ($\Omega_4 > \Omega_6 > \Omega_2$) for all the glasses. The Ω_2 J-O parameter represents covalent nature between Pr^{3+} ions and ligand anions because this parameter directly connects to the asymmetry of the local environment around the trivalent RE ions (Pr^{3+} ions). In the present series of glasses, the Ω_2 parameter values are small when compared with Ω_4 and Ω_6. Similar trend has been observed in literature for other glasses [51–54]. The small values of Ω_2 parameter show the asymmetrical behavior of ion site i.e., the ionic nature is dominating the covalent nature between the ligands. The degree of covalency present in a glass can be evaluated using the following expression [55].

$$C_{covalent}\% = \exp\left[-25\,(\Delta\aleph)^2\right] \times 100. \quad (5)$$

where, $\Delta\aleph$ is the host glass's electro negativity value which is nothing but the difference between the anion's and cation's electronegativity values. For the present series of glasses, the estimated value of covalent character is 35.24% and ionic character is approximately 65%. The lowest percentage value of covalent character is an evidence for the low values of Ω_2 parameter. Hence in the present series of glasses, the ionic nature is more predominant when compared with the covalent nature. This is also well confirmed by the higher values of Ω_4 and Ω_6 parameters. Moreover, this result is also in consistent with the bonding nature (δ) evaluated from the nephelauxetic ratio ($\bar{\beta}$). The Ω_4 and Ω_6 parameters represent the rigidity of the host material in which RE ions are situated. Binnemans et al. [56] reported that increase in Ω_6 J-O parameter with increasing RE ion concentration may be due to tightening of the structure along with the formation of BO_4 units in the matrix. The spectroscopic quality factor ($\chi = \frac{\Omega_4}{\Omega_6}$) is also evaluated for the present series of glasses and are presented in Table 4

Table 3
Experimental oscillator strengths (f_{exp}) (10^{-6}), calculated oscillator strengths (f_{cal}) (10^{-6}) along with rms deviation (δ_{rms}) and bonding parameters (δ) of Pr^{3+} ions in LiPbAlB glasses.

Transition $^3H_4 \rightarrow$	Glass A (0.05 mol %)		Glass B (0.1 mol %)		Glass C (0.5 mol %)		Glass D (1 mol %)		Glass E (1.5 mol %)		Glass F (2 mol %)	
	f_{exp}	f_{cal}	f_{exp}	f_{cal}	f_{exp}	f_{cal}	f_{exp}	f_{cal}	f_{exp}	f_{cal}	f_{exp}	f_{cal}
$^3P_2$[c]	5.97	2.44	6.85	2.82	7.19	3.03	8.19	3.58	6.81	2.61	5.63	1.71
$^3P_1$	1.31	2.84	1.33	3.08	1.84	3.19	2.30	3.94	2.08	2.97	1.71	2.75
$^3P_0$	1.18	2.79	1.36	3.03	1.59	3.14	1.81	3.88	1.65	2.93	1.31	2.71
$^1D_2$	2.05	0.76	3.00	0.87	3.91	0.93	2.38	1.11	1.46	0.80	0.32	0.53
$^3F_4$	1.10	2.31	1.35	2.69	1.72	2.91	1.98	3.42	1.55	2.46	0.48	1.47
$^3F_3$	5.17	4.61	5.80	5.22	6.03	5.58	7.31	6.66	5.17	4.84	3.74	3.34
$^3F_2$	2.93	2.96	2.98	3.00	3.18	3.19	3.97	3.99	2.69	2.69	1.82	1.82
δ_{rms} (10^{-6})	±1.73[a] ±1.20[b]		±2.03[a] ±1.46[b]		±2.14[a] ±1.58[b]		±2.15[a] ±1.37[b]		±1.75[a] ±0.81[b]		±1.70[a] ±0.85[b]	
δ	−0.89		−0.86		−0.66		−0.57		−0.54		−0.49	

[a] Including hypersensitive transition ($^3H_4 \rightarrow {}^3P_2$).
[b] Excluding hypersensitive transition ($^3H_4 \rightarrow {}^3P_2$).
[c] Hypersensitive transition.

Table 4
Judd-Ofelt intensity parameters [Ω_2, Ω_4 and Ω_6 (10^{-20} cm^2)] for Pr^{3+} ions in LiPbAlB glasses.

Glass System	Ω_2	Ω_4	Ω_6	χ	Trend	References
Glass A	1.42	2.96	2.21	1.33	$\Omega_4 > \Omega_6 > \Omega_2$	present work
Glass B	1.09	2.91	2.36	1.23	$\Omega_4 > \Omega_6 > \Omega_2$	present work
Glass C	1.07	2.69	2.15	1.24	$\Omega_4 > \Omega_6 > \Omega_2$	present work
Glass D	1.29	3.01	1.99	1.51	$\Omega_4 > \Omega_6 > \Omega_2$	present work
Glass E	0.62	2.12	1.51	1.40	$\Omega_4 > \Omega_6 > \Omega_2$	present work
Glass F	0.05	1.83	1.74	1.05	$\Omega_4 > \Omega_6 > \Omega_2$	present work
ZnAlBiB	7.36	4.46	4.17	1.06	$\Omega_2 > \Omega_4 > \Omega_6$	[4]
CFBSm10	1.92	6.35	3.44	1.84	$\Omega_4 > \Omega_6 > \Omega_2$	[6]
PbFB	0.13	3.289	1.92	1.71	$\Omega_4 > \Omega_6 > \Omega_2$	[14]
Li–P–Al	2.41	5.89	5.60	1.41	$\Omega_4 > \Omega_6 > \Omega_2$	[37]
ZANP10	12.28	13.69	10.89	1.25	$\Omega_4 > \Omega_6 > \Omega_2$	[38]
OXFB	1.14	2.28	1.33	1.71	$\Omega_4 > \Omega_6 > \Omega_2$	[39]
ZBLAN	2.9	6.4	5.5	1.16	$\Omega_4 > \Omega_6 > \Omega_2$	[40]
MgTP	2.69	11.87	8.39	1.41	$\Omega_4 > \Omega_6 > \Omega_2$	[42]

along with the reported values for other glasses. From Table 4, it can be observed that, the "χ" values are in comparable with other reported values. In the present series, Glass D possesses maximum value of "χ" indicating the superiority of that glass in giving higher stimulated emission cross-sections than the others [57].

3.6. Photoluminescence spectral studies

In order to analyze the PL spectra, it is very much essential to know about the suitable excitation wavelength. For this reason, the excitation spectrum for glass D was recorded in the wavelength range 420–500 nm by fixing the emission at 602 nm and is shown in Fig. 5. As shown in Fig. 5, the excitation spectrum consists of three excitation bands 445, 470 and 485 nm corresponding to the transition $^3H_4 \rightarrow {}^3P_2$, $^3P_1$ and $^3P_0$ respectively. Among them, $^3H_4 \rightarrow {}^3P_2$ transition observed at 445 nm is very intense and is more suitable as an excitation wavelength to record the emission spectra of the titled glasses. We have recorded PL spectra for all the LiPbAlB glasses by using 445 nm CW diode laser as an excitation source as it can effectively excite more number of atoms to the desired metastable state than the conventional excitation source. Fig. 6 shows the PL spectra recorded for the titled glasses using 445 nm CW diode laser as an excitation source. From Fig. 6, it is observed that the PL spectra consists of three bands at 572, 602, 644 nm corresponding to $^3P_1 \rightarrow {}^3F_2$, $^1D_2 \rightarrow {}^3H_4$ and $^3P_1 \rightarrow {}^3F_3$ transitions respectively. Among all, $^1D_2 \rightarrow {}^3H_4$ observed in reddish orange region of the electromagnetic spectrum (602 nm) is very

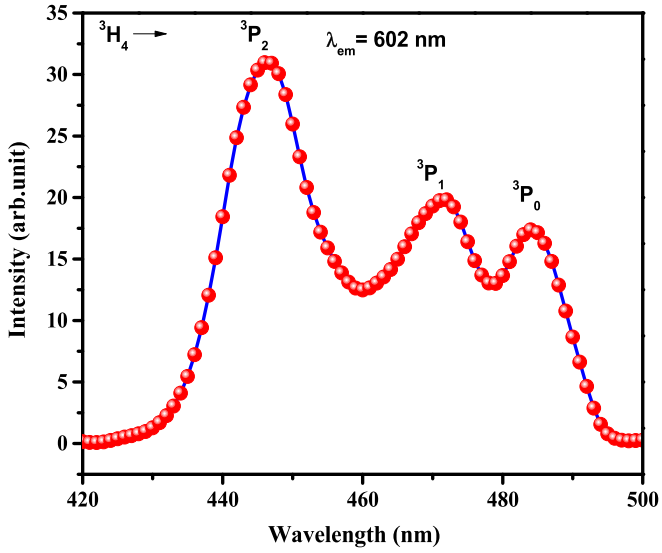

Fig. 5. Excitation spectrum of 1 mol% of Pr^{3+} ions in LiPbAlB glass (Glass D).

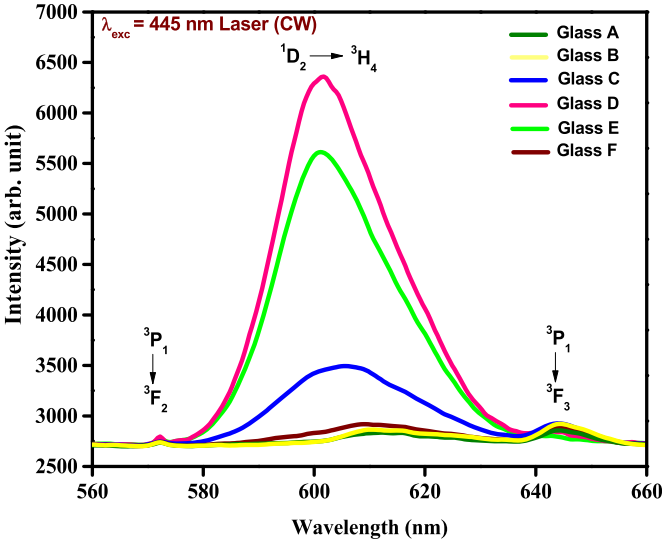

Fig. 6. PL spectra of LiPbAlB glasses under 445 nm CW diode laser excitation.

Cross relaxation channels	Donor emission channels	Acceptor absorption channels
CR1 ($^3P_0$)	$^3P_0 \rightarrow {}^1D_2$ (3910 cm^{-1})	$^3H_4 \rightarrow {}^3H_6$ (4300 cm^{-1})
	$^3P_0 \rightarrow {}^1G_4$ (10,850 cm^{-1})	$^3H_4 \rightarrow {}^1G_4$ (9700 cm^{-1})
	$^3P_0 \rightarrow {}^3H_6$ (16,250 cm^{-1})	$^3H_4 \rightarrow {}^1D_2$ (16,640 cm^{-1})
CR2 ($^3P_1$)	$^3P_1 \rightarrow {}^1D_2$ (4460 cm^{-1})	$^3H_4 \rightarrow {}^3F_2$ (5000 cm^{-1})
CR3 ($^1D_2$)	$^1D_2 \rightarrow {}^1G_4$ (6940 cm^{-1})	$^3H_4 \rightarrow {}^3F_4$ (6667 cm^{-1})
	$^1D_2 \rightarrow {}^3F_4$ (9890 cm^{-1})	$^3H_4 \rightarrow {}^1G_4$ (9700 cm^{-1})
ET ($^1D_2$)	$^1D_2 \rightarrow {}^3H_4$ (16,640 cm^{-1})	$^3H_4 \rightarrow {}^1D_2$ (16,640 cm^{-1})

intense than the remaining two. The intensity of $^1D_2 \rightarrow {}^3H_4$ transition increases with Pr^{3+} ions concentration up to 1 mol % and decreases beyond showing concentration quenching. The feasible cross-relaxation channels for concentration quenching are given below [58].

The above cross relaxation channels are depicted in energy level diagram shown in Fig. 7 along with excitation and emission wavelengths observed for glass D. Dexter's theory [59,60] explains the role of cross relaxation channels in emission quenching and lifetime shortening. According to this theory, emission and absorption spectra of doped glasses should have an overlap. Fig. 8 shows the perfect spectral overlap between emission and absorption spectra of $^1D_2$ transition in visible region along with cross relaxation channel. Such spectral overlap observed helps to us understand the energy migration produced from excited to unexcited Pr^{3+} ions through resonant energy transfer process.

The PL performance of titled glasses can be further understood with the help of radiative parameters like radiative transition probability (A_R), total transition probability (A_T), luminescence branching ratio (β_R) and radiative lifetime (τ_R) for all the fluorescent levels observed in the PL spectra using the expressions given literature [4,61]. Stimulated emission cross-section (σ_{se}) is another significant parameter for a glassy material to act as a good host for laser. The "σ_{se}" for a transition from an initial to final manifold can be evaluated by using the following expression [62,63].

$$\sigma_{se}(a_j, b_{j'}) = \left[\frac{\lambda_p^4}{8\pi c n^2 \Delta\lambda_p}\right] A_R(a_j, b_{j'}) \quad (6)$$

here, λ_P is wavelength of emission peak, $\Delta\lambda_p$ is the effective linewidth (FWHM) of the transition.

A_R, A_T, β_R and τ_R values evaluated for all the emission transitions of Pr^{3+} ions in LiPbAlB glasses are given in Table 5. The emission peak wavelength (λ_P), effective band widths ($\Delta\lambda_P$), radiative and experimental branching ratios (β_R & β_{exp}), σ_{se}, gain band width (σ_{se} x $\Delta\lambda_p$) and optical gain parameter (σ_{se} x τ_R) for the intense $^1D_2 \rightarrow {}^3H_4$ emission transition of Pr^{3+} ions doped LiPbAlB glasses are given in Table 6. Luminescence branching ratio (β_R) is another important parameter and for best lasing potentiality its value should be higher (around 0.5). From Table 6 it is observed that the value of β_R for $^1D_2 \rightarrow {}^3H_4$ transition in LiPbAlB glasses increases with increasing Pr^{3+} ion concentration up to 1 mol % and beyond deceases. This might be due to fluorescence quenching of the $^1D_2 \rightarrow {}^3H_4$ transition beyond 1 mol% of Pr^{3+} ions. The values of β_R obtained for all the glasses in the present work are in good agreement with the reported values [4,46,57,64]. The β_{exp} values are evaluated by measuring the relative areas of the emission transitions and these values are found to be in good agreement with β_R. From Table 6, it is observed that glass D with 1 mol% of Pr^{3+} ions in LiPbAlB glass is having highest radiative as well as experimental branching ratios suggests that this glass can act as a best luminescent device under 445 nm excitation. Stimulated emission cross-section, gain band width and optical gain parameter are

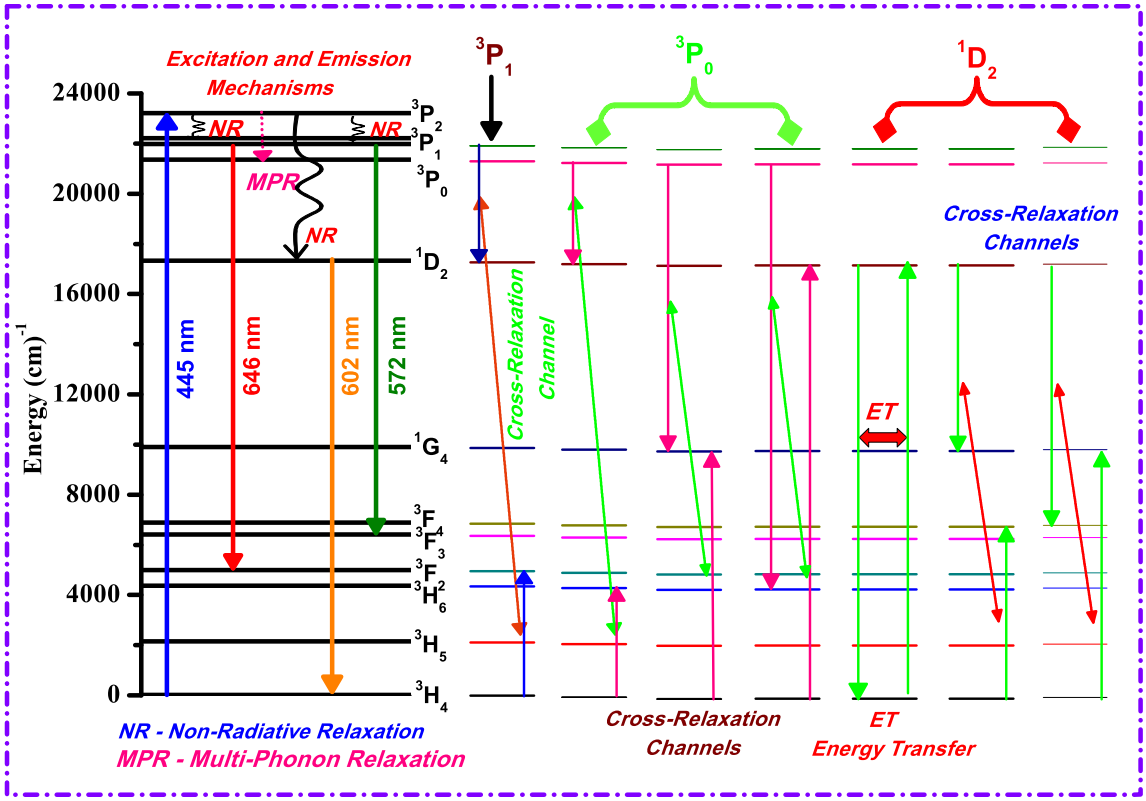

Fig. 7. Energy level diagram of 1 mol% of Pr^{3+} ions in LiPbAlB glass (glass D) with excitation, emission and cross-relaxation channels.

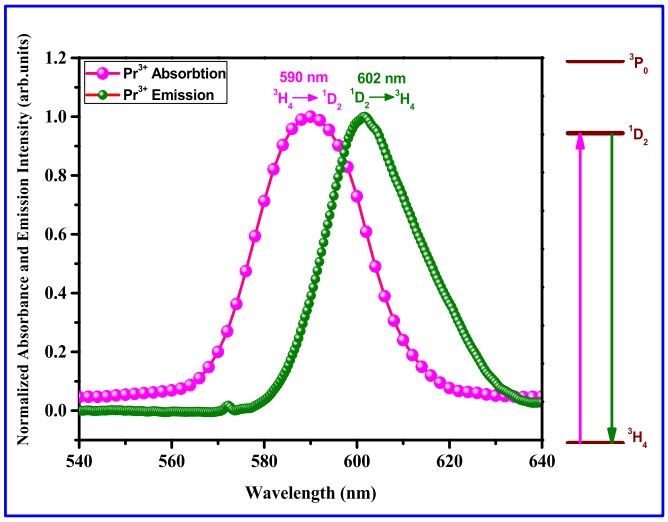

Fig. 8. Spectral overlap of emission and absorption spectra of $^1D_2$ transitions of Pr^{3+} ions in LiPbAlB glasses.

Table 5
Transition probability (A_R) (s^{-1}), total transition probability (A_T) (s^{-1}), branching ratio (β_R) and radiative lifetimes (τ_R) (μs) for the observed emission transitions of Pr^{3+} ions in LiPbAlB glasses.

Name	Transition	A_R	A_T	β_R	τ_R
Glass A	$^3P_1 \rightarrow {}^3F_2$	3831.16	54628.14	0.0701	18
	$^1D_2 \rightarrow {}^3H_4$	1166.92	4013.99	0.2907	230
	$^3P_1 \rightarrow {}^3F_3$	10934.67	54628.14	0.2001	18
Glass B	$^3P_1 \rightarrow {}^3F_2$	3559.08	63913.24	0.0556	15
	$^1D_2 \rightarrow {}^3H_4$	1386.92	4543.92	0.3272	202
	$^3P_1 \rightarrow {}^3F_3$	11474.62	63913.24	0.1795	15
Glass C	$^3P_1 \rightarrow {}^3F_2$	4469.67	76005.48	0.0588	13
	$^1D_2 \rightarrow {}^3H_4$	1902.14	5499.22	0.3277	167
	$^3P_1 \rightarrow {}^3F_3$	13911.10	76005.48	0.1830	130
Glass D	$^3P_1 \rightarrow {}^3F_2$	6544.64	103585.76	0.0631	9
	$^1D_2 \rightarrow {}^3H_4$	2951.41	7530.50	0.4122	122
	$^3P_1 \rightarrow {}^3F_3$	19656.71	103585.76	0.1897	9
Glass E	$^3P_1 \rightarrow {}^3F_2$	3491.74	78758.73	0.0443	13
	$^1D_2 \rightarrow {}^3H_4$	1831.02	5348.68	0.3423	171
	$^3P_1 \rightarrow {}^3F_3$	12996.95	78758.73	0.1650	13
Glass F	$^3P_1 \rightarrow {}^3F_2$	6966.36	64905.50	0.1099	15
	$^1D_2 \rightarrow {}^3H_4$	1282.21	3432.08	0.3735	262
	$^3P_1 \rightarrow {}^3F_3$	7392.65	64905.50	0.1138	15

another set of important parameters for a better luminescent material. From Table 6, it can be seen that these parameters are highest for glass D indicating the superior nature of glass D over the other glasses studies in the present investigation.

3.7. Time resolved photoluminescence spectral studies

The Time Resolved Photoluminescence (TR-PL) decay profiles for $^1D_2 \rightarrow {}^3H_4$ emission transition of Pr^{3+} ions in LiPbAlB glasses under 445 nm excitation are shown in Fig. 9. From Fig. 9 it can be observed that, the decay profile is single exponential for lower concentration and non-exponential for higher concentration. The experimental lifetimes (τ_{exp}) measured from the decay curves for all the glasses under investigation are given in Table 7 along with radiative lifetimes (τ_R). From Table 7, it can be observed that, the τ_{exp} values are decreasing with increase in Pr^{3+} ion concentration in these glasses. This decrease in τ_{exp} and conversion of decay curves from exponential to non-exponential with increase in RE ion concentration can be attributed to the cross-relaxation processes (As shown in Fig. 7) and the subsequent concentration quenching observed. From Table 7 it can also be observed that, the τ_{exp} are less than τ_R. This small inconsistency between τ_{exp} and τ_R can be attributed to the multi photon relaxation processes observed. In such a case, the τ_{exp} of an emitting state relates with τ_R and non-radiative decay rate (W_{NR}) through

$$\frac{1}{\tau_{exp}} = \frac{1}{\tau_R} + W_{NR} \tag{7}$$

The W_{NR} thus calculated by using the above expression are placed in Table 7.

The quantum efficiency (η %) is another important parameter used to evaluate the luminescence efficiency of a material under investigation. The value of η% can be evaluated by taking the ratio between τ_{exp} and τ_R. The value of η % increases with increase in Pr^{3+} ion concentrations up to 1 mol % (glass D) and deceases beyond. The η% values measured for all the titled glasses are presented in Table 7. Among all the glasses studied in the present work, glass D with 1 mol % of Pr^{3+} ions possesses highest quantum efficiency than the other glasses. Hence glass D is best suitable for lasing emission in reddish orange region under 445 nm excitation.

An amorphous material doped with RE ions can also acts as a good optical fiber, if the gain bandwidth (σ_{se} x $\Delta\lambda_p$) and optical gain parameters (σ_{se} x τ_R) are having relatively higher values. Particularly gain bandwidth parameter is more important to achieve a highly stable laser host material. From Table 6 it is observed that glass D (1 mol % Pr^{3+}) possesses highest values of gain band width and optical gain parameter among all the glasses. Hence glass D with 1 mol % Pr^{3+} ions in LiPbAlB glass is best suited for optical fiber amplification as well as visible reddish orange laser emission at 602 nm.

3.8. Inokuti-Hirayama model analysis

It is well known that the lifetime of a molecule or ion is the average time that it can spend in the excited state prior to its return to the ground state with the emission of a photon [49]. A molecule/ion in the excited state (donor ion) can relax to the lower energy states via two different mechanisms. Firstly donor ions/molecules can migrate energy between the donor ions prior to the energy reaches to the acceptor ions (un excited molecule/ion); secondly they can transfer energy directly to the acceptor ions [65]. In some cases, when donor and acceptor ions are distributed homogeneously in host matrix and if energy migration between the donor ions are negligible, then the decay curves obtained can be fitted well with the help of Inokuti-Hirayama (I-H) model [66] to understand the predominant energy transfer mechanism. Hence I-H model can be applicable when the energy transfer between donor and acceptor ions is faster than the energy migration between donor ions. The luminescence intensity decay in such a case is given by

$$I_t = I_0 \exp\left\{ -\frac{t}{\tau_0} - Q\left(\frac{t}{\tau_0}\right)^{\frac{3}{S}} \right\} \tag{8}$$

where, t is time after excitation, τ_0 is intrinsic decay time of donors in absence of acceptors and Q is energy transfer parameter which can be expressed as follows

$$Q = \frac{4\pi}{3}\, \Gamma\left(1 - \frac{3}{S}\right) N_0 R_0^3 \tag{9}$$

here, N_0 is concentration of acceptor ions, R_0 is critical energy transfer distance which can be obtained as the distance between donor and acceptor when energy transfer rate is equal to rate of

Table 6
Emission peak wavelength (λ_P) (nm), effective band width ($\Delta\lambda_P$) (nm), measured and experimental branching ratios (β_R & β_{exp}), stimulated emission cross-section (σ_{se}) (cm^2), gain band width ($\sigma_{se} \times \Delta\lambda_P$) ($cm^3$) and optical gain parameter ($\sigma_{se} \times \tau_R$) ($cm^2$ s) for $^1D_2 \rightarrow {}^3H_4$ emission transition of Pr^{3+} ions in LiPbAlB glasses.

Spectral Parameters	Glass A	Glass B	Glass C	Glass D	Glass E	Glass F
$^1D_2 \rightarrow {}^3H_4$ (Reddish Orange)						
λ_P = 602 nm						
$\Delta\lambda_P$	15.13	15.52	17.28	18.09	20.03	23.06
β_R	0.29	0.33	0.33	0.41	0.34	0.37
β_{exp}	0.33	0.32	0.45	0.51	0.45	0.54
$\sigma_{se}(\times 10^{-22})$	30.1	31.3	34.2	46.1	23.9	13.6
$\sigma_{se} \times \Delta\lambda_P$ ($\times 10^{-26}$)	0.46	0.49	0.59	0.83	0.48	0.31
$\sigma_{se} \times \tau_R$ ($\times 10^{-25}$)	6.93	6.89	6.19	7.50	4.44	3.96

intrinsic decay. Interactions involved in the mechanism can be of different types depending on the values of *S* and gamma function Γ(X). It can be dipole-dipole (S = 6, Γ(X) = 1.77) dipole-quadrupole (S = 8, Γ(X) = 1.43) and quadrupole-quadrupole interactions (S = 8, Γ(X) = 1.3). The energy transfer probability and donor acceptor interaction parameter can be evaluated by using the following expression.

$$C_{DA} = R_0^{(S)} \tau_0^{-1} \text{ and } W_{ET} = C_{DA} R_0^{(S)} \quad (10)$$

In the present work, non-exponential decay curves were fitted to I-H model by taking S = 6 as show in Fig. 9; which confirms

Table 7
Experimental (τ_{exp}) (μs), radiative (τ_R) (μs) lifetimes, quantum efficiencies (η) and non-radiative decay rates (W_{NR}) for $^1D_2 \rightarrow {}^3H_4$ transition of Pr^{3+} in LiPbAlB glasses.

Name of sample	τ_{exp}	τ_R	η (%)	W_{NR}
Glass A	165	230	71	1713
Glass B	160	202	79	1300
Glass C	136	167	81	1365
Glass D	106	122	86	1237
Glass E	101	171	58	4053
Glass F	94	262	38	6822

dipole-dipole interaction between Pr^{3+} ions. As the concentration increases, distance between donor and acceptors decreases and there may be a chance for increased energy transfer due to instant fluorescence decay [67]. From Table 8 it is observed that energy transfer parameter increases while critical distance between donor and acceptor decreases with increase in Pr^{3+} ions concentration. This is because of the enhanced energy transfer between Pr^{3+} ions via cross-relaxation. Fig. 10 shows the variation of energy transfer parameter (Q) and τ_{exp} with increase in Pr^{3+} ion concentration. From Fig. 10 it is conspicuous that, as Pr^{3+} ion concentration increases, the magnitude of Q increases while τ_{exp} decreases.

3.9. CIE chromaticity co-ordinates

The chromaticity coordinates which are useful to know the color

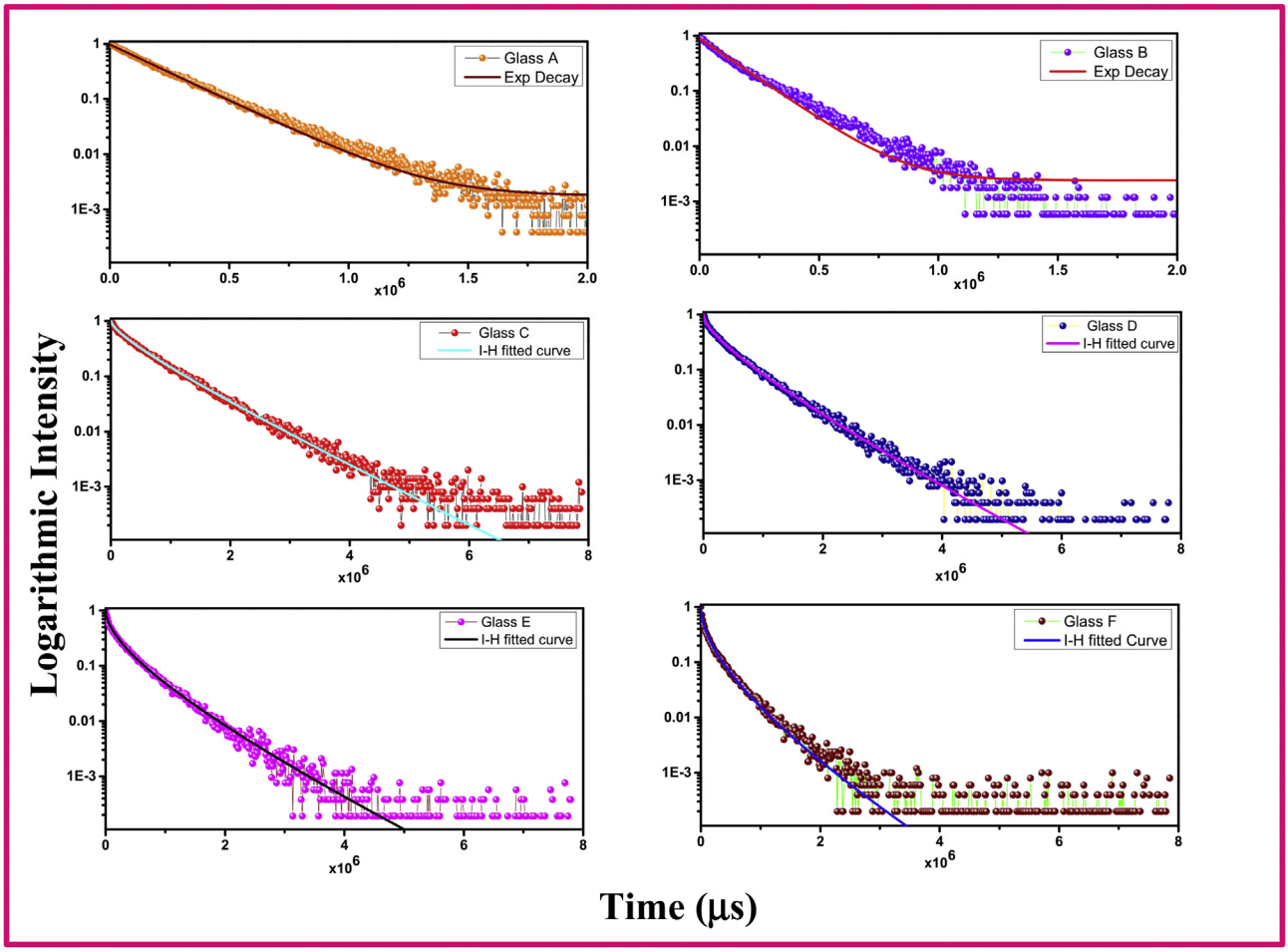

Fig. 9. Decay spectral profiles of $^1D_2 \rightarrow {}^3H_4$ (602) nm emission transition of Pr^{3+} ions in LiPbAlB glasses under 445 nm excitation along with I-H Fitting.

Table 8
Energy transfer parameter (Q), critical transfer distance (R_0) (Å), donor acceptor interaction parameters (C_{DA}, 10^{-41} cm^6 s^{-1}) of Pr^{3+} ions in LiPbAlB glasses.

Name of glass	Q	R_0	C_{DA}
Glass A	–	–	–
Glass B	–	–	–
Glass C	3.29	3.95	2.97
Glass D	3.58	3.25	0.91
Glass E	3.85	2.92	0.47
Glass F	4.69	2.85	0.42

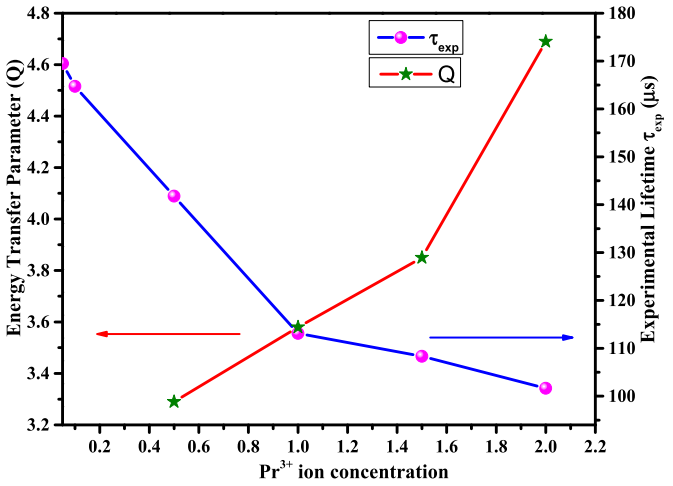

Fig. 10. Variation of energy transfer parameter (Q) and experimental lifetime (τ_{exp}) with increasing Pr^{3+} ions concentration in LiPbAlB glasses.

emitted by the material can be calculated from PL spectra shown by the material under suitable excitation wavelength by using Commission International de l'Eclairage France CIE system [68]. The PL spectra of the as-prepared glasses consist of three parts which is yellow to orange, orange to red, and pure red. Fig. 11 shows CIE chromaticity co-ordinates evaluated for Pr^{3+} doped LiPbAlB glasses under 445 nm CW diode laser excitation along with confocal PL images recorded for all the LiPbAlB glasses under the same excitation wavelength. CIE color co-ordinates for all the glass samples

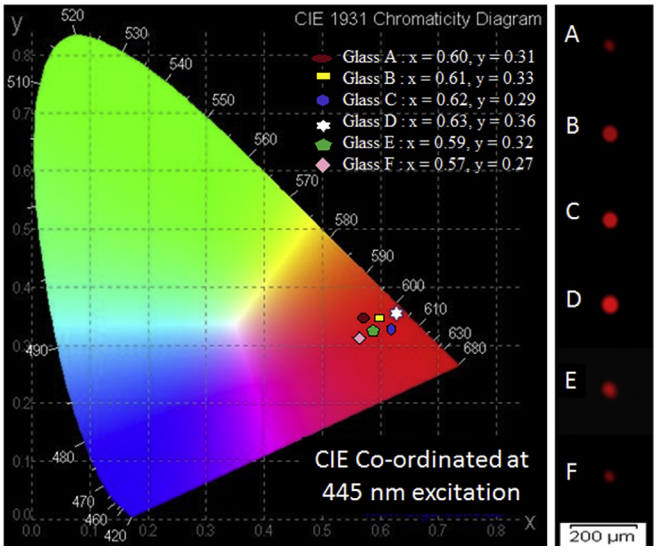

Fig. 11. CIE chromaticity coordinates and confocal images of Pr^{3+} ions in LiPbAlB glasses.

were found to be in orange red to red regions. Among all the glasses, the color co-ordinates evaluated for glass D (x = 0.630, y = 0.360) falls exactly in the reddish orange region of CIE chromaticity diagram. Therefore glass D with 1 mol% of Pr^{3+} concentration in LiPbAlB glass is more suitable for reddish orange light emission under 445 nm excitation. This result is also in consonance with the confocal PL images recorded for glass D emitting intense Reddish Orange light than the other glasses under investigation.

4. Conclusions

Lithium Lead Aumino Borate glasses doped with different concentrations of Praseodymium ions were synthesized using conventional melt quenching techniques to understand their structural as well as luminescence behavior using spectroscopic techniques such as XRD, FT-IR, Raman, absorption, excitation, PL, confocal images and TR-PL spectral profiles. The best fit J-O parameters evaluated from the absorptions spectral features allowed us to evaluate various radiative parameters for the observed fluorescent levels of Pr^{3+} ions in LiPbAlB glasses. Under 445 nm CW diode laser excitation, the titled glasses show three emission bands, of which $^1D_2 \rightarrow {}^3H_4$ emission is more intense and for which the emission cross-section and branching ratios are evaluated. The intensity of $^1D_2 \rightarrow {}^3H_4$ transition increases with Pr^{3+} ion concentration up to 1 mol % and decreases beyond showing concentration quenching. The decay profiles of $^1D_2 \rightarrow {}^3H_4$ transition show single exponential for lower concentration and non-exponential for higher concentration resulting decrease in experimental lifetimes with increase in concentration. Such decrease in experimental lifetimes and conversion of decay curves from exponential to non-exponential with increase in RE ion concentration has been attributed to the cross-relaxation processes and subsequent concentration quenching observed. From the observed branching ratios, spectroscopic quality factor, stimulated emission cross-section, CIE chromaticity co-ordinates and quantum efficiency, it was finally concluded that LiPbAlB glasses doped Pr^{3+} ions are quite suitable for the development of visible reddish orange luminescent devices. Among all, glass D with 1 mol% of Pr^{3+} ion concentration in LiPbAlB glass is superior in all respects to act as a best reddish orange luminescent device to operate at 602 nm. This result is also in consistent with the confocal PL image captured for glass D showing more bright reddish orange emission than the other titled glasses.

Acknowledgement

This work is partly supported by High Impact Research Initiative of IIT-Delhi, UK-India Education and Research Initiative and Department of Science and Technology, Govt. of India, New Delhi. Two of the authors, Dr.A.S.Rao and Dr.Sk.Mahamuda are thankful to DST, Govt. of India, New Delhi for the award of a major research project to them (File Number: ECR/2016/000376).

References

[1] Z. Wang, H. Guo, X. Xiao, Y. Xu, X. Cui, M. Lu, B. Peng, A. Yang, Z. Yang, S. Gu, Synthesis and spectroscopy of high concentration dysprosium doped GeS_2-Ga_2S_3-CdI_2 chalcohalide glasses and fiber fabrication, J. Alloy. Compd. 692 (2017) 1010–1017.
[2] K. Jha, M. Jayasimhadri, Structural and emission properties of Eu^{3+}-doped alkaline earth zinc-phosphate glasses for white LED applications, J. Am. Ceram. Soc. (2017) 1–10, http://dx.doi.org/10.1111/jace.14668.
[3] Ch.B. Annapurna, Sk. Mahamuda, M. Venkateswarlu, K. Swapna, A.S. Rao, G. Vijaya Prakash, Dy^{3+} ions doped single and mixed alkali fluoro tungsten tellurite glasses for LASER and white LED applications, Opt. Mater 62 (2016) 569–577.
[4] Sk. Mahamuda, K. Swapna, A.S. Rao, T. Sasikala, L.R. Moorthy, Reddish-orange emission from Pr^{3+} doped zinc alumino bismuth borate glasses, Phys. B 428 (2013) 36–42.

[5] S. Kang, X. Wang, W. Xu, X. Wang, D. He, L. Hu, Effect of B_2O_3 content on structure and spectroscopic properties of neodymium-doped calcium aluminate glasses, Opt. Mater. 66 (2017) 287–292.

[6] J.S. Kumar, K. Pavani, T. Sasikala, A.S. Rao, N.K. Giri, S.B. Rai, L.R. Moorthy, Photoluminescence and energy transfer properties of Sm^{3+} doped CFB glasses, Solid State Sci. 13 (2011) 1548–1553.

[7] W.A. Pisarski, J. Pisarska, G. Dominiak-Dzik, W. Ryba-Romanowski, Transition metal (Cr^{3+}) and rare earth (Eu^{3+}, Dy^{3+}) ions used as a spectroscopic probe in compositional-dependent lead borate glasses, J. Alloy. Compd. 484 (2009) 45–49.

[8] G. Lakshminarayana, J. Qiu, Photoluminescence of Pr^{3+}, Sm^{3+} and Dy^{3+} doped $SiO_2 - Al_2O_3 - BaF_2 - GdF_3$ glasses, J. Alloy. Compd. 476 (2009) 470–476.

[9] S. Liu, G. Zhao, X. Lin, H. Ying, J. Liu, J. Wang, G. Han, White luminescence of Tm – Dy ions co-doped aluminoborosilicate glasses under UV light excitation, J. Solid State Chem. 181 (2008) 2725–2730.

[10] H.J. Lozykowski, W.M. Jadwisienczak, I. Brown, Cathodoluminescence of GaN doped with Sm and Ho, Solid State Commun. 110 (1999) 253–258.

[11] H.J. Lozykowski, W.M. Jadwisienczak, I. Brown, Photoluminescence and cathodoluminescence of GaN doped with Pr, J. Appl. Phys. 88 (2000) 210–222.

[12] Y.G. Choi, J. Heo, 1.3 μm emission and multiphonon relaxation phenomena in $PbO-Bi_2O_3-Ga_2O_3$ glasses doped with rare-earths, J. Non Cryst. Solids 217 (1997) 199–207.

[13] G. Lakshminarayana, S. Buddhudu, Spectral analysis of Eu^{3+} and Tb^{3+};: B_2O_3–ZnO – PbO glasses, Mater. Chem. Phys. 102 (2007) 181–186.

[14] S. Arunkumar, K. Marimuthu, Concentration effect of Sm^{3+} ions in B_2O_3 – PbO – PbF_2 – Bi_2O_3 – ZnO glasses-structural and luminescence investigations, J. Alloy. Compd. 565 (2013) 104–114.

[15] M. Peng, L. Wondraczek, Photoluminescence of $Sr_2P_2O_7$: Bi^{2+} as a red phosphor for additive light generation, Opt. Lett. 35 (2010) 2544–2546.

[16] M. Peng, C. Zollfrank, L. Wondraczek, Origin of broad NIR photoluminescence in bismuthate glass and Bi-doped glasses at room temperature, J. Phys-Condens Mat. 21 (2009) 285106–285112.

[17] R.C. Lucacel, C. Marcus, V. Timar, I. Ardelean, FT-IR and Raman spectroscopic studies on B_2O_3-PbO-Ag_2O glasses dopped with manganese ions, Solid State Sci. 9 (2007) 850–854.

[18] M. Ganguli, K.J. Rao, Structure role of PbO in Li_2O – PbO – B_2O_3 glasses, J. Solid State Chem. 145 (1999) 65–76.

[19] G. Lakshminarayana, R. Yang, M. Mao, J. Qiu, Spectral analysis of RE^{3+} (RE = Sm, Dy, and Tm): $P_2O_5 - Al_2O_3 - Na_2O$ glasses, Opt. Mater. 31 (2009) 1506–1512.

[20] K. Swapna, Sk. Mahamuda, A.S. Rao, S. Shakya, T. Sasikala, D. Haranath, G. Vijaya Prakash, Optical studies of Sm^{3+} ions doped zinc alumino bismuth borate glasses, Spectrochim. Acta - Part A Mol. Biomol. Spectrosc. 125 (2014) 53–60.

[21] A. Pan, A. Ghosh, Dynamics of lithium ions in bismuthate glasses, J. Chem. Phys. 112 (2000) 1503–1509.

[22] D.L. Griscon, in: I.D. Pye, V.D. Frechette, N.J. Kreidl (Eds.), Borate Glasses, Structure, Properties, Application, Plenum, New York, 1978.

[23] K. Wei, D.P. Machewirth, J. Wenzel, E. Snitzer, G.H.S. Jr., Pr^{3+}-doped Ge-Ga-S glasses for 1.3 μm optical fiber amplifiers, J. Non Cryst. Solids 182 (1995) 257–261.

[24] F. Varsanyi, Surface lasers, Appl. Phys. Lett. 19 (1971) 169–171.

[25] J. Hegarty, D.L. Huber, W.M. Yen, Fluorescence quenching by cross relaxation in LaF_3:Pr^{3+}, Phys. Rev. B 25 (1982) 5638–5645.

[26] B.R. Judd, Optical absorption intensities of rare-earth ions, Phys. Rev. 127 (1962) 750–761.

[27] G.S. Ofelt, Intensities of crystal spectra of rare earth ions, J. Chem. Phys. 37 (1962) 511–520.

[28] Sk. Mahamuda, K. Swapna, A.S. Rao, M. Jayasimhadri, T. Sasikala, K. Pavani, L.R. Moorthy, Spectroscopic properties and luminescence behavior of Nd^{3+} doped zinc alumino bismuth borate glasses, J. Phys. Chem. Solids 74 (2013) 1308–1315.

[29] Sk. Mahamuda, K. Swapna, P. Packiyaraj, A.S. Rao, G. Vijaya Prakash, Visible red, NIR and Mid-IR emission studies of Ho^{3+} doped ainc alumino bismuth borate glasses, Opt. Mater 36 (2013) 362–371.

[30] K. Swapna, Sk. Mahamuda, A.S. Rao, T. Sasikala, P. Packiyaraj, L.R. Moorthy, G. Vijaya Prakash, Luminescence characterization of Eu^{3+} doped zinc alumino bismuth borate glasses for visible red emission applications, J. Lumin 156 (2014) 80–86.

[31] K. Swapna, Sk. Mahamuda, A.S. Rao, T. Sasikala, L.R. Moorthy, Visible luminescence characteristics of Sm^{3+} doped zinc alumino bismuth borate glasses, J. Lumin 146 (2014) 288–294.

[32] P. Goldner, F. Auzel, Application of standard and modified Judd-Ofelt theories to a praseodymium-doped fluorozirconate glass, J. Appl. Phys. 79 (1996) 7872–7877.

[33] R.T. Karunakaran, K. Marimuthu, S.S. Babu, S. Arumugam, Structural, optical and thermal investigations on Dy^{3+} doped NaF–Li_2O – B_2O_3 glasses, Phys. B 404 (2009) 3995–4000.

[34] A. Hruby, Evaluation of glass-forming tendency by means of DTA, Czechoslov. J. Phys. 22 (1972) 1187–1193.

[35] A.S. Rao, Y.N. Ahammed, R.R. Reddy, T.V.R. Rao, Spectroscopic studies of Nd^{3+}-doped alkali fluoroborophosphate glasses, Opt. Mater. 10 (1998) 245–252.

[36] K. Jha, M. Jayasimhadri, Spectroscopic investigation on thermally stable Dy^{3+} doped zinc phosphate glasses for white light emitting diodes, J. Alloy. Compd. 688 (2016) 833–840.

[37] K. Annapoorani, C. Basavapoornima, N.S. Murthy, K. Marimuthu, Investigations on structural and luminescence behavior of Er^{3+} doped lithium zinc borate glasses for lasers and optical amplifier applications, J. Non Cryst. Solids 447 (2016) 273–282.

[38] H.E. Heidepriem, W. Seeber, D. Ehrt, Dehydration of phosphate glasses, J. Non Cryst. Solids 163 (1993) 74–80.

[39] B.B. Kale, A. Jha, S.K. Apte, P.V. Adhyapak, D.P. Amalnerkar, Removal of OH impurities from GeS_2 by reactive atmosphere and its glass preparation, Mater. Chem. Phys. 78 (2002) 330–336.

[40] T.I. Suratwala, R.A. Steele, G.D. Wilke, J.H. Campbell, K. Takeuchi, Effects of OH content, water vapor pressure and temperature on sub-critical crack growth in phosphate glass, J. Non Cryst. Solids 264 (2000) 23–227.

[41] T. Som, B. Karmakar, Nephelauxetic effect of low phonon antimony oxide glass in absorption and photoluminescence of rare-earth ions, Spectrochim. Acta - Part A Mol. Biomol. Spectrosc. 79 (2011) 1766–1782.

[42] T. Suhasini, B.C. Jamalaiah, T. Chengaiah, J.S. Kumar, L.R. Moorthy, An investigation on visible luminescence of Ho^{3+} activated LBTAF glasses, Phys. B 407 (2012) 523–527.

[43] S. Saravanan, S. Rajesh, R. Palani, Thermal and structural properties of mixed alkali and transition metal ions in sodium borate glass, Int. J. Recent Res. Rev. 8 (2015) 1–9.

[44] G. Padmaja, P. Kistaiah, Infrared and Raman spectroscopic studies on alkali borate glasses: evidence of mixed alkali effect, J. Phys. Chem. A 113 (2009) 2397–2404.

[45] W.T. Carnall, P.R. Fields, K. Rajnak, Electronic energy levels in the trivalent lanthanide aquo ions. I. Pr^{3+}, Nd^{3+}, Pm^{3+}, Sm^{3+}, Dy^{3+}, Ho^{3+}, Er^{3+}, and Tm^{3+}, J. Chem. Phys. 49 (1968) 4424–4442.

[46] M. Venkateswarlu, M.V.V.K.S. Prasad, K. Swapna, Sk. Mahamuda, A.S. Rao, A.M. Babu, D. Haranath, Pr^{3+} doped lead tungsten tellurite glasses for visible red lasers, Ceram. Int. 40 (2014) 6261–6269.

[47] C.K. Jorgensen, The nephelauxetic series, Prog. Inorg. Chem. 4 (1962) 73.

[48] M.B. Saisudha, J. Ramakrishna, Optical absorption of Nd^{3+}, Sm^{3+} and Dy^{3+} in bismuth borate glasses with large radiative transition probabilities, Opt. Mater. 18 (2002) 403–417.

[49] Sk. Mahamuda, K. Swapna, M. Venkateswarlu, A.S. Rao, S. Shakya, G. Vijaya Prakash, Spectral characterisation of Sm^{3+} ions doped oxy-fluoroborate glasses for visible orange luminescent applications, J. Lumin 154 (2014) 410–424.

[50] P. Babu, C.K. Jayasankar, Spectroscopic properties of Dy^{3+} ions in lithium borate and lithium fluoroborate glasses, Opt. Mater. 15 (2000) 65–79.

[51] H. Takabe, Y. Nageno, K. Morinaga, Compositional dependence of Judd-Ofelt parameters in silicate, borate, and phosphate glasses, J. Am. Ceram. Soc. 78 (1995) 1161–1168.

[52] K. Brahmachary, D. Rajesh, S. Babu, Y.C. Ratnakaram, Investigations on spectroscopic properties of Pr^{3+} and Nd^{3+} doped zinc-alumino-sodium-phosphate (ZANP) glasses, J. Mol. Struct. 1064 (2014) 6–14.

[53] K.K. Mahato, D.K. Rai, S.B. Rai, Optical studies of Sm^{3+} doped oxyfluoroborate glass, Solid State Commun. 108 (1998) 671–676.

[54] F.B. Xiong, Z.D. Luo, Y.D. Huang, Spectroscopic properties of Pr^{3+} in anisotropic $PbWO_4$ crystal, Appl. Phys. B Lasers Opt. 80 (2005) 321–328.

[55] M.V.V. Kumar, K.R. Gopal, R.R. Reddy, G.V.L. Reddy, N.S. Hussain, B.C. Jamalaiah, Application of modified Judd-Ofelt theory and the evaluation of radiative properties of Pr^{3+}-doped lead telluroborate glasses for laser applications, J. Non Cryst. Solids 364 (2013) 20–27.

[56] K. Binnemans, R.V. Deun, C.G. Walrand, J.L. Adam, Spectroscopic properties of trivalent lanthanide ions in fluorophosphate glasses, J. Non Cryst. Solids 238 (1998) 11–29.

[57] D.V.R. Murthy, B.C. Jamalaiah, T. Sasikala, L.R. Moorthy, M. Jayasimhadri, K. Jang, H.S. Lee, S.S. Yi, J.H. Jeong, Optical absorption and emission characteristics of Pr^{3+} doped RTP glasses, Phys. B 405 (2010) 1095–1100.

[58] V. Naresh, B.S. Ham, Influence of multiphonon and cross relaxations on $^3P_0$ and $^1D_2$ emission levels of Pr^{3+} doped borosilicate glasses for broad band signal amplification, J. Alloy. Compd. 664 (2016) 321–330.

[59] D.L. Dexter, Theory of sensitized luminescence in solids, J. Chem. Phys. 21 (1953) 836–850.

[60] D.L. Dexter, J.H. Schulman, Theory of concentration quenching in inorganic phosphors, J. Chem. Phys. 22 (1954) 1063–1070.

[61] R. Cases, M.A. Chamarro, R. Alcala, V.D. Rodriguez, Optical properties of Nd^{3+} and Dy^{3+} ions in ZnF_2-CdF_2 based glasses, J. Lumin 48 (1991) 509–514.

[62] R.D. Peakcock, The intensities of lanthanide f-f transitions, Struct-Bond 22 (1975) 83–122.

[63] W. Krupke, Induced-emission cross sections in neodymium laser glasses, IEEE J. Quant. Electron 10 (1974) 450.

[64] G. Lakshminarayana, K.M. Kaky, S.O. Baki, S. Ye, A. Lira, I. V Kityk, M.A. Mahdi, Concentration dependent structural, thermal and optical features of Pr^{3+}-doped multicomponent tellurite glasses, J. Alloy. Compd. 686 (2016) 769–784.

[65] B.C. Jamalaiah, M.V.V. Kumar, K.R. Gopal, Fluorescence properties and energy transfer mechanism of Sm^{3+} ion in lead telluroborate glasses, Opt. Mater. 33 (2011) 1643–1647.

[66] M. Inokuti, F. Hirayama, Influence of energy transfer by the exchange mechanism on donor luminescence, J. Chem. Phys. 43 (1965) 1978–1988.

[67] K.S. Lim, N. Vijaya, C.R. Kesavulu, C.K. Jayasankar, Structural and luminescence properties of Sm^{3+} ions in zinc fluorophosphate glasses, Opt. Mater. 35 (2013) 1557–1563.

[68] F.W. Billmeyer, M. Saltzman Jr., Principles of Colour Technology, Wiley, New York, 1981.